LANCASTER UNIVERSITY

On the Modelling and Consequence of Small-Scale Magnetic Phenomena in the Saturnian System

by

Carley J. Martin

This thesis is submitted in partial fulfilment of the requirements
for the degree of Doctor of Philosophy

in the
Faculty of Science and Technology
Department of Physics

February 2019

Declaration of Authorship

I, Carley J. Martin, declare that this thesis titled 'On the Modelling and Consequence of Small-Scale Magnetic Phenomena in the Saturnian System' and the work presented in it are my own. I confirm that:

- This work was done wholly or mainly while in candidature for a research degree at this University.
- Where any part of this thesis has previously been submitted for a degree or any other qualification at this University or any other institution, this has been clearly stated.
- Where I have consulted the published work of others, this is always clearly attributed.
- Where I have quoted from the work of others, the source is always given. With the exception of such quotations, this thesis is entirely my own work.
- I have acknowledged all main sources of help.
- Where the thesis is based on work done by myself jointly with others, I have made clear exactly what was done by others and what I have contributed myself.

Signed:

Date:

'I see now that the circumstances of one's birth are irrelevant. It is what you do with the gift of life that determines who you are.'

Mewtwo - Pokémon: The First Movie

'I wish there was a way to know you're in the good old days before you've actually left them'

Andy Bernard - The Office Season 9 Episode 23

'We feel cold, but we don't mind it, because we will not come to harm. And if we wrapped up against the cold, we wouldn't feel other things, like the bright tingle of the stars, or the music of the aurora, or best of all the silky feeling of moonlight on our skin. It's worth being cold for that.'

Philip Pullman - Northern Lights

'The Stone Age didn't end because the world ran out of stones'

Niels Bohr

Abstract

This thesis presents an analysis of Cassini magnetometer data in two different regions of the Kronian system. An evaluation of aperiodic waves on the equatorial current sheet is presented; the waves are fitted to a model of a Harris current sheet deformed by a Gaussian wave pulse. This analysis allows examination of the parameters relating to the waves, where amplitude of waves is found to increase with radial distance. In addition, the direction of propagation of the waves is found by resolving the wave numbers in 2-dimensions, where a general outwards propagation is found.

The use of the Harris current sheet also allows the resolution of current sheet parameters, and it is found that the scale height of the current sheet increases with radial distance. Additionally, values of the magnetic field in the lobes are found using the model, which are then used along with the scale heights to estimate the current density in the azimuthal and radial directions. These values can also be used to calculate, using the divergence of current, the field aligned currents entering and leaving the ionosphere where a current entering the ionosphere pre-noon and a current exiting the ionosphere post-midnight are shown. This current density is then converted to an electron flux in the upward current region, and could produce an additional 1-11 kR of auroral emission which is seen in other infrared and ultraviolet data sets.

Additionally, irregular magnetic signatures, such as the aperiodic waves, are found in the entire system including Titan's ionosphere. At Titan, a statistical study of the position of flux ropes finds no spatial dependence other than an increased number of flux ropes in the sun-lit regions and ram-side regions. A comparison of force-free and non-force free models is utilised to extract the radii and axial magnetic field of the flux ropes, and compare the assumptions required for both models. Additionally, deformations to the models are used to model common asymmetries seen in the magnetometer data and find that bending a force-free flux rope solves the problem of the direction ambiguity of using minimum variance analysis and using elliptical cross-sections of flux ropes allows for a asymmetric flux rope signature.

All together, this thesis explores the varied magnetic phenomena in the Kronian system and uses them to understand the surrounding environment.

Declaration

The following publications have been published during the duration of this doctoral degree and constitute part of this thesis.

Martin, C.J. and Arridge, C.S. (2017). Cassini observations of aperiodic waves on Saturn's magnetodisc. Journal of Geophysical Research: Space Physics, 122(8), pp.8063-8077. DOI: 10.1002/2017JA024293

Martin, C.J. and Arridge, C.S. (2018). Current density in Saturn's equatorial current sheet: Cassini magnetometer observations. Journal of Geophysical Research: Space Physics, 124, pp.279-292. DOI: 10.1029/2018JA025970

Acknowledgements

I'd like to start by thanking my most recent friends and colleagues at Lancaster University. Thanks to Joe, Gareth, Nathan, Ben and more recently Dave, for putting up with me asking countless questions about Python and Matlab. Thanks to Maria and Becky for giving me tea and chats when I needed it. Big thanks to Sarah and Licia, for always being there when I needed help, support and grammatical aid and of course Marianna, my PhD big sister, for being just that.

I'd like to thank my supervisor, Chris Arridge, for firstly giving me the opportunity to do this PhD but also for encouraging and supporting me throughout the entire time I've been at Lancaster and helping me grow into a (fairly) independent and (slightly more) confident scientist.

I need to take a step back in time and thank all of those people during my undergraduate studies at Aberystwyth, without whom I definitely would never have had the most amazing time and actually enjoyed doing coursework and exam revision and getting to the point at which I could start a PhD. So in alphabetical order I'd like to thank: Ben, Clarissa, Elliot, Ffion, James A, James H, Jess, Kirsty, Les, Liam, Nathan, Matt, Meg, Morgan and Tim for being the best 'team' a girl could ask for. I'd also like to thank Rose for riding the highs and lows of completing a PhD with me.

I'd like to thank Dan, who at the time of writing is my fiancé but at the time of submission will be my husband. He has supported me throughout our joint journey into further education and without his love and support I would have a fraction of the confidence in my own work and my life would have a lot less laughter in it.

Finally, I'd like to thank my Mum and Dad, for their unwavering love and support throughout my education. My Grandma Pat, who showed me a love for astronomy through books as a child. My Grandparents, Ken and Betty, who told me that a grade or number means nothing as long as I always do my best and that they will always be proud of me. I did my best, and I hope you are all proud.

Additionally, without the years of dedicated hard work of thousands of people who took part in the Cassini-Huygens mission, this thesis would definitely not be a possibility. So I'd like to thank them for being the giant shoulders we could stand on, it was amazing to be even the smallest part of such a worldwide collaboration of human endeavour.

Contents

List of Figures

List of Tables

Abbreviations

AU - Astronomical Unit

CA - Closest Approach

CAPS - Cassini Plasma Spectrometer

FF - Force-Free

FTE - Flux Transfer Event

HICD - Height Integrated Current Density

ICME - Interplanetary Coronal Mass Ejection

IMF - Interplanetary Magnetic Field

KRTP - Kronocentric Radial Theta Phi coordinates

KSM - Kronocentric Solar Magnetospheric coordinates

MAG - Cassini MAGnetometer instrument

MHD - Magnetohydrodynamics

MSE - Mean Squared Error

NFF - Non-Force-Free

PPO - Planetary Period Oscillations

Rev/s - Orbit/s of Cassini around Saturn

R_J - Jupiter Radii

R_S - Saturn Radii

SLT - Saturn Local Time

TSY98 - Tsyganenko (1998)

Physical Constants

Astronomical Unit	AU	$=$	1.49598×10^{11} m
Boltzmann Constant	k_B	$=$	$1.38065 \times 10^{23} \mathrm{JK}^{-1}$
Electron Volt	eV	$=$	1.60218×10^{-19} J
Earth radius (mean)	R_E	$=$	6.371×10^{6} m
Saturn radius (1 bar pressure level)	R_S	$=$	6.0268×10^{7} m
Jupiter radius (1 bar pressure level)	R_J	$=$	7.1492×10^{7} m
Solar mass	$M_\odot$	$=$	1.98855×10^{30} kg
Solar radius	$R_\odot$	$=$	6.995×10^{8} m
Speed of Light	c	$=$	$2.99792 \times 10^{8} \mathrm{~ms}^{-\mathrm{s}}$
Vacuum Permittivity	ϵ_0	$=$	$8.85419 \times 10^{-12} \mathrm{~Fm}^{-1}$
Vacuum Permeability	μ_0	$=$	$4\pi \times 10^{-7} \mathrm{~Hm}^{-1}$

Chapter 1

Introduction

Saturn is the second largest planet in the solar system and is classed, with Jupiter, as a gas giant planet due to its thick hydrogen- and helium-rich atmosphere and interior. Saturn is visible by-eye in the night sky, however was not viewed through a telescope until Galileo first observed the planet in 1610. The fuzzy shape of the rings through his telescope led him to believe that Saturn had two large moons, or even arms. Galileo did however, view the seasons (unknowingly) of Saturn, where 2 years after his first observations the apparent *large moons* disappeared and returned again 2 years later.

Almost 50 years later, the Dutch astronomer Christiaan Huygens improved the optics in telescopes and correctly found that the *arms* were actually rings, and discovered Saturn's largest moon, Titan. Soon after, in 1675, the Italian mathematician and astronomer Giovanni Domenico Cassini discovered the large gap in the rings (*the Cassini division*) along with another four of Saturn's moons. The first orbiting space mission to Saturn was named for these pioneers.

The Cassini-Huygens mission was the fourth spacecraft to visit Saturn, and the first to enter orbit around the body. Discussed in more detail later, Cassini entered orbit in 2004, and after two mission extensions, the mission came to an end in 2017 with a controlled crash into Saturn's atmosphere. Before Cassini, the planet was visited by Pioneer 11, along with Voyagers 1 and 2, all of which took unprecedented new data during flybys. The data of these flybys led to the belief that Saturn was a mid-point between a rotation dominated magnetosphere, such as that of Jupiter, and the solar wind driven system of Earth's magnetosphere (Bagenal, 1992).

Saturn's largest moon, Titan, is another unique planetary body which is host to an unexpectedly thick atmosphere (Kuiper, 1944) and is larger than Earth's Moon and the planet Mercury. Titan has no measured intrinsic magnetic field, but retains an ionosphere formed from the ionisation of the thick atmosphere. One of the most extraordinary features of Titan is the moon's methane cycle, a methane based cycle that mimics Earth's hydrological cycle. Titan's surface is home to water-ice mountains, carved with liquid methane rivers, lakes and seas. Titan is tidally locked (like our moon) to Saturn with an orbital period of 16 days.

In this first chapter, we will explore the fundamental concepts of plasma physics that are crucial in the understanding of the dynamics and configurations of planetary magnetospheres. The various controls of the different magnetospheres within the Solar system will be outlined and the basic physics of magnetodiscs of the giant planets will be explored with specific emphasis on the Saturnian system and what current literature informs is the established understanding of this system. Additionally, the current understanding of the interaction of Titan, Saturn's largest moon, with Saturn's magnetic field is discussed. We will then conclude with an overview of the contents of this thesis and their contribution to the overall understanding of the Saturnian and Titanian system.

1.1 Plasma Physics

Plasma is the fourth state of matter, after solid, liquid and gas, which makes up over 99% of visible mass in the universe. Physically, plasma is described as a ionised gas where an atom or molecule has sufficient energy that its electrons are no longer bound to the nucleus. When the electrons are no longer bound, the ionised gas is an electrically conducting medium (Crookes, 1879). In the solar system, plasma is found in the magnetospheres and ionospheres of the planets, in the solar corona, and solar wind.

Here on Earth we live our entire lives mainly surrounded by the remaining <1% of mass. However, plasma and its effects influence our daily lives. From human-made technology like televisions and fluorescent lights to natural effects such as lightning and the aurora borealis and australis, plasma surrounds us every day. Kristian Birkeland stated in 1913 on his theory of a plasma filled universe: '*It seems to be a natural consequence of our points of view to assume that the whole of space is filled with electrons and flying electric ions of all kinds. We have assumed that each stellar system through its evolution throws off electric corpuscles* (early idea of photons or energetic particles) *into space. It is not unreasonable therefore, to think that the greater part of the material masses in the universe is found not in the solar systems or nebulae, but in 'empty' space*' (Birkeland, 1908), describing the first idea that the majority of the universe's mass is in a plasma state.

A natural progression in thought, is to infer that due to a large presence of an electrically conducting medium, a pervasive magnetic field is inherent in the universe. Although the presence of this 'galactic magnetic field' is still debated, the pioneer and maverick Hannes Alfvén, argued this idea to develop the foundations of magnetohydrodynamics (MHD). This concept introduces the constraint of a magnetic field on an electrically conducting fluid, and will be one of our discussion points in this introduction. However, it is important to first understand the dynamics of a single particle in a magnetic field, and the forces acting upon it.

1.1.1 Single Particle Motion

Much of plasma dynamics can be described as the motion of a single particle or collection of particles. In a uniform magnetic field, Lorentz law:

$$\boldsymbol{F} = q(\boldsymbol{E} + \boldsymbol{V} \times \boldsymbol{B}) \tag{1.1}$$

states that the electromagnetic force on a test charge is a function of its charge (q), velocity ($\boldsymbol{V} = \boldsymbol{V}_\perp + \frac{\boldsymbol{B}V_\parallel}{|\boldsymbol{B}|}$) and the external electric and magnetic fields ($\boldsymbol{E}$ & $\boldsymbol{B}$) and to a first approximation, a test charge will form a circular motion (when $\boldsymbol{E} = 0$ and $\boldsymbol{B}$ is constant on the time and length scales of the gyration) around the magnetic field with a radius of:

$$r_g = \frac{mV_\perp}{|q|B}, \tag{1.2}$$

which is called the *gyro-radius* of the single particle. Here m is mass, and $V_\perp$ is the velocity perpendicular to the magnetic field. Hence, we find that electrons have a smaller gyro-radius than ions due to a smaller mass. If velocity parallel, $V_\|$, to the magnetic field remains constant, the particles follow a helical trajectory (figure 1.1, where the magnetic field in the diagram also traces the *guiding centre* of the particle motion). The frequency at which a particle gyrates around its guiding centre is given by $\omega_g = \frac{q|B|}{m}$ (*gyro-frequency*) which has a *gyro-period* of $T_g = \frac{2\pi r_g}{v\perp}$. When including a $V_\|$, the particle has a *pitch angle* of:

$$\alpha = \arctan\left(\frac{V_\perp}{V_\|}\right) \tag{1.3}$$

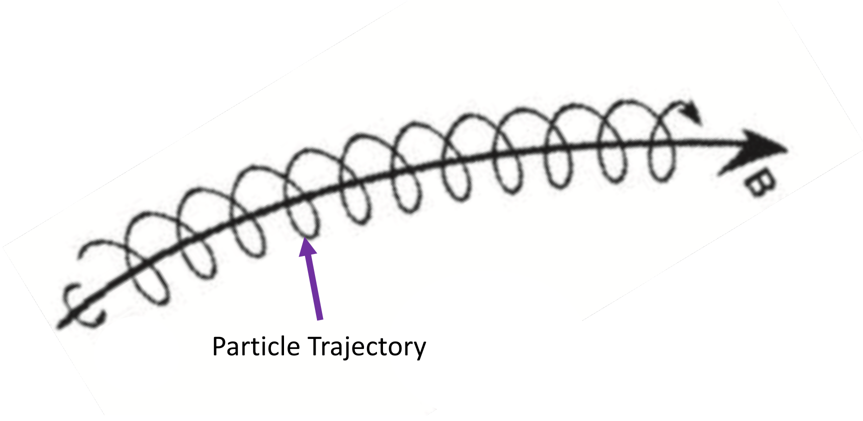

Figure 1.1: Diagram of a helical particle trajectory along a magnetic field line, modified from Kivelson and Russell (1995)

As this approach describes a charged particle moving in a circular orbit, it can be shown that this forms a current loop and hence a magnetic moment

$$\mu = iA, \tag{1.4}$$

where i is charge per second (current) and can be shown as:

$$\mu = \frac{|q|V_\perp}{2\pi r_g}\pi r_g^2 = \frac{|q|V_\perp r_g}{2} = \frac{|q|V_\perp}{2}\frac{mV_\perp}{|q|B} = \frac{\frac{1}{2}mV_\perp^2}{B} \tag{1.5}$$

where the area A is πr_g^2 and current i is $\frac{|q|V_\perp}{2\pi r_g}$. In the characteristic time scale and length scale of a system (τ & L) the magnetic moment can be considered invariant, i.e. when $\tau > T_g$.

We now discuss the motion of a single charged particle in a converging or diverging magnetic field. If the magnetic moment is constant:

$$\frac{\frac{1}{2}mV_\perp^2}{B} = \frac{\frac{1}{2}mV^2 sin^2(\alpha)}{B} = constant \tag{1.6}$$

We also know that total energy is conserved, hence:

$$\frac{sin^2(\alpha)}{B} = constant, \tag{1.7}$$

as B increases or decreases, so must α. Hence in a converging magnetic field, the pitch angle decreases until $sin^2(\alpha) = 1$ and the particle is moving only perpendicular to the magnetic field in this instance. The particle then reverses and begins to travel in to negative direction and α begins to decrease so the particle resumes its helical trajectory. This particle has been magnetically mirrored. If the magnetic field converges at either end the particle will *bounce* from one end to the other if the magnetic field is sufficient enough to trap the particle.

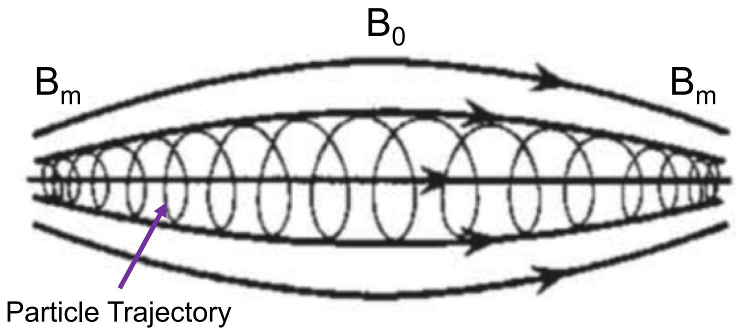

FIGURE 1.2: Diagram of a particle trajectory which mirrors in a diverging and converging magnetic field, modified from Kivelson and Russell (1995)

Again, using the invariance of μ it is shown that:

$$\frac{\frac{1}{2}mV_{\perp 0}^2}{B_0} = \frac{\frac{1}{2}mV_{\perp m}^2}{B_m}, \tag{1.8}$$

where the subscript *0* denotes the mid-point (in this example) and the subscript m denotes the point of maximum magnetic field in the plasma, shown in figure 1.2.

Using the conservation of energy we can show that the maximum field required for a particle to mirror is:

$$B_m = \frac{B_0}{sin^2(\alpha_0)}, \tag{1.9}$$

where α_0 is the pitch angle at the mid-plane. And $sin^2(\alpha_{0min}) = \frac{B_0}{B_m}$ where $\frac{B_m}{B_0}$ is the mirror ratio R_m. Hence, particles with a small pitch angle can pass through the magnetic mirror and are lost. Particles with these small pitch angles come from the *loss cone* area of velocity space. This leads to an anisotropic distribution of velocities. This process is highly important in planetary magnetospheres, where a converging magnetic field is found as the dipole field reaches higher latitudes and particles can become trapped and bounce from one hemisphere to the other.

We now consider an inhomogeneous magnetic field where the gradient in magnetic field strength is perpendicular to the direction of the magnetic field. As the particle gyrates into a region of higher magnetic field strength, its gyro-radius decreases, then as it continues moving into a region of lower field strength the radius increases again. This is illustrated in figure 1.4b.

The particle's perpendicular velocity can be described by:

$$\boldsymbol{V}_{\nabla \boldsymbol{B}} = \frac{1}{2}mV_{\perp}^2 \frac{\boldsymbol{B} \times \nabla \boldsymbol{B}}{qB^3} \tag{1.10}$$

The particle *drifts* perpendicular to the magnetic field direction and the gradient of magnetic field strength. As the direction of gyro-motion, or the guiding centre, is controlled by the sign of the charge, this process causes the electrons and ions to move differentially (*charge separation*) and forms a current (shown in figure 1.3b). This process is important in Earth's magnetosphere and contributes to the *ring current* and is commonly called the grad-B drift. This ring current is at Earth is not sufficient to stretch the magnetic

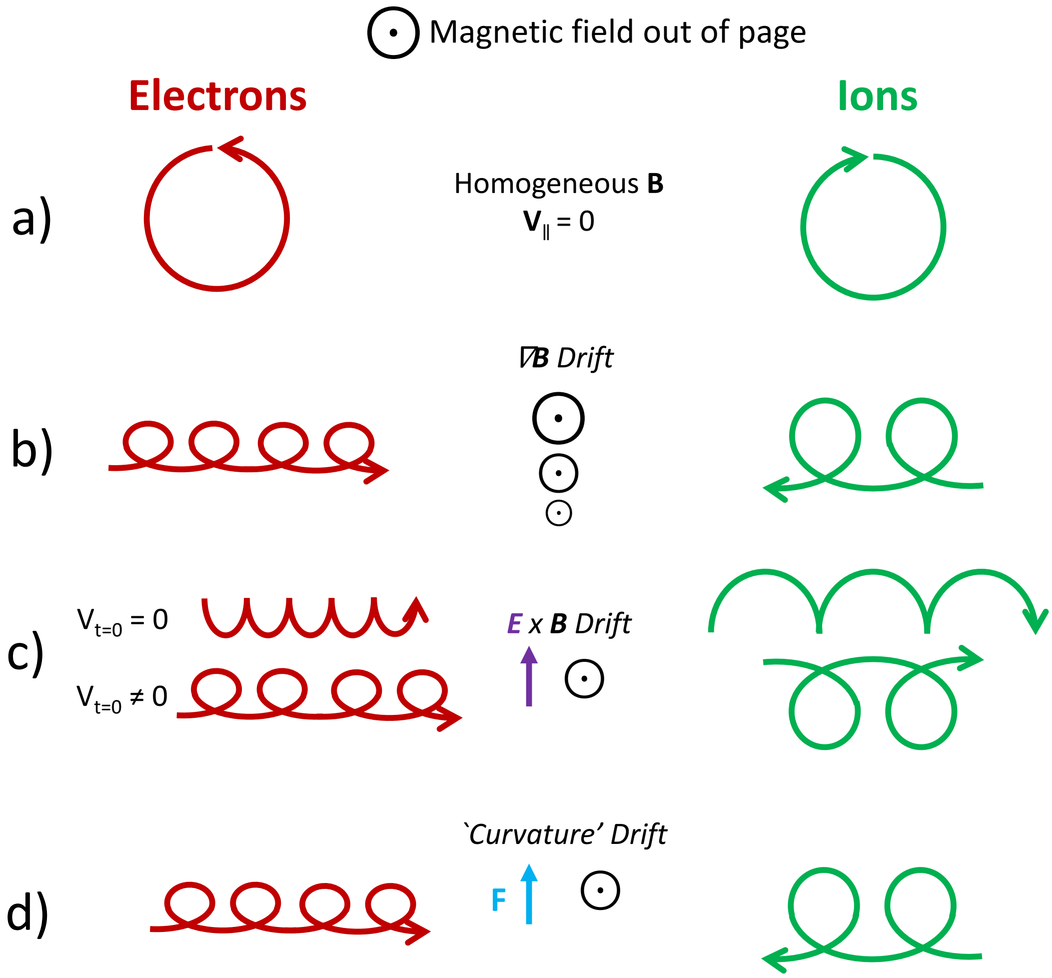

FIGURE 1.3: Diagram of an electron (red) and ion (green) trajectory in a) a homogenous magnetic field, b) a magnetic field with a perpendicular gradient, c) an additional electric field and d) an additional force (in this case curvature drift is due to apparent centrifugal forces.

field to form a magnetodisc, however a stronger current in this area could form a sheet of current and stretch the dipole like field outwards - which is what is found at the giant planets. Although, there may not be a magnetodisc at Earth, there is a tail plasma sheet with a distended field described in section 1.2.2.

However, if the Lorentz law is applied to a curved magnetic field with no electric field (like a dipole or giant planet magnetodisc) the apparent force is a centrifugal force, there is a charge dependence and a current is induced (fig 1.4d). The so-called *curvature* *drift* is given by:

$$\boldsymbol{V}_{CF} = \frac{\boldsymbol{F} \times \boldsymbol{B}}{qB^2} = \frac{mV_{\|}^2}{qB^2} \frac{\boldsymbol{R}_{CF} \times \boldsymbol{B}}{R_{CF}^2}, \tag{1.11}$$

where $\boldsymbol{R}_{CF}$ is the radius of curvature of the magnetic field. The current produced superposes with the grad-$\boldsymbol{B}$-drift-induced current to contribute to the ring current.

Addition of an electric field perpendicular to the magnetic field will also cause a drift of particles, however this drift does not cause differential motion of charges and as such does not generate a current; this is called $\boldsymbol{E} \times \boldsymbol{B}$ *drift* and is described by equation 1.12. A perpendicular electric field moves the test particle perpendicular to the magnetic field, as the particle accelerates, it experiences an increasing Lorentz force perpendicular to $\boldsymbol{E}$ and $\boldsymbol{B}$. Eventually this force causes the particle to move opposite to the $q\boldsymbol{E}$ force from the electric field and is now decelerated by the electric field. Hence, the particle effectively bounces, or moves in a cycloid trajectory, along perpendicular to both $\boldsymbol{E}$ and $\boldsymbol{B}$ due to the Lorentz law (shown in figure 1.3c).

$$\boldsymbol{V}_{\boldsymbol{E}\times\boldsymbol{B}} = \frac{\boldsymbol{E} \times \boldsymbol{B}}{B^2} \tag{1.12}$$

We have described one of three theoretical frameworks describing the motion of plasma and magnetic field, single particle motion. However, in some scenarios single particle motion is not appropriate, for example, simulating a large number of particles in small time steps for a large system will not be possible with current computing power. However, the second theoretical framework we will discuss was developed to solve this problem, and that is kinetic theory.

Kinetic theory is a progression of the single particle motion in that a collection of particles is now described by a velocity distribution $f(\boldsymbol{r}, \boldsymbol{V}, t)$, where $\boldsymbol{r}$ is position, and $\boldsymbol{V}$ is velocity in three dimensions and t is time. The dynamics of the distribution are controlled by kinetic equations or *Vlasov equations* which are equations of charge, current density in single particle distribution functions, and Maxwell's equations (where Ampére's Law includes the displacement current, equation 1.13).

$$\nabla \times \boldsymbol{B} = \mu_0 \left(\boldsymbol{J} + \epsilon_0 \frac{\partial \boldsymbol{E}}{\partial t} \right) \tag{1.13}$$

In these equations each particle species can be represented as any function, however, a Boltzmann energy distribution, corresponding to thermal equilibrium, is commonly used. We can find the number of particles in the distribution by integrating over velocity space:

$$n = \int_{-\infty}^{\infty} f(\boldsymbol{r}, \boldsymbol{V}, t) d\boldsymbol{V} \tag{1.14}$$

Further integrals can be used to find the particle flux, momentum flux and energy flux density of the plasma. To even further simplify this theory, one may track the progression of these moments in time and space, leading to a fluid description of plasma: magnetohydrodynamics, the third framework for describing particle motion in plasmas.

1.1.2 Magnetohydrodynamics and Maxwell's Equations

MHD, as it states, is the understanding of the dynamics and properties of an electrically conducting *fluid* in the presence of electric and magnetic fields, along with the forces they exert on the fluid. Essentially, it is the mathematical and physical framework of the behaviour of plasma when described as a fluid, and the behaviour of plasma is an essential concept in this thesis. As MHD is based on a series of assumptions there are some constraints on when MHD is applicable and a kinetic approach may be a more physically-accurate way to model the behaviour of some regions in a magnetosphere (e.g. Titan's interaction where gyro-radius is greater than Titan radius). The constraints are:

- Ion and electron gyro-period are larger than the characteristic time scale of the system (τ)
- Ion and electron gyro-radius are smaller than the characteristic length scale of the system (L)

In addition, we also assume plasma to be quasi-neutral within the characteristic time and length scales, so that n_e (number of electrons) $\sim n_i$ (number of ions). We will discuss the following parameters of a plasma, ρ_m mass density, ρ_C charge density, $\boldsymbol{B}$ magnetic field, $\boldsymbol{E}$ electric field, $\boldsymbol{u}$ velocity, P pressure, $\boldsymbol{j}$ current density, γ specific heat ratio, V specific volume and t time. To begin, fluids in general can be described by the conservation of mass, momentum and the adiabatic process equation:

$$\frac{\partial \rho_m}{\partial t} + \nabla \cdot (\rho_m \boldsymbol{u}) = 0 \qquad \text{Conservation of Mass Law} \tag{1.15a}$$

$$\rho_m \left[\frac{\partial \boldsymbol{u}}{\partial t} + (\boldsymbol{u} \cdot \nabla)\boldsymbol{u} \right] = -\rho_m \nabla \Phi - \nabla \cdot \boldsymbol{P} + \nabla \cdot \boldsymbol{T} \qquad \text{Conservation of Momentum} \tag{1.15b}$$

$$PV^{\gamma} = constant \qquad \text{Adiabatic Process Equation} \tag{1.15c}$$

The stress tensor $\boldsymbol{T}$ incorporates other forces in a system, and in the case of MHD this includes a magnetic field for which we need Maxwell's equations:

$$\nabla \times \boldsymbol{B} = \mu_0 \boldsymbol{j} \qquad \text{Ampère's Law for MHD} \tag{1.16a}$$

$$\nabla \times \boldsymbol{E} = -\frac{\partial \boldsymbol{B}}{\partial t} \qquad \text{Faraday's Law} \tag{1.16b}$$

$$\nabla \cdot \boldsymbol{B} = 0 \qquad \text{Gauss' Law for Magnetism} \tag{1.16c}$$

$$\nabla \cdot \boldsymbol{E} = \frac{\rho_C}{\epsilon_0} \qquad \text{Gauss' Law} \tag{1.16d}$$

ϵ_0 and μ_0 are the permittivity and permeability of free space.

The continuity equation (1.15a) expresses the conservation of mass, where the rate of change of mass inside a volume is equal to the mass flowing in/out of the volume. The conservation of momentum equation (equation 1.15b) states the various forces acting on the plasma, i.e. gravity (via a scalar potential Φ), pressure tensor $\boldsymbol{P}$ and stress tensor $\boldsymbol{T}$ which includes stresses due to the magnetic field and current density of a system ($\boldsymbol{j} \times \boldsymbol{B}$).

Ampère's law describes the idea that for any line current a perpendicular magnetic field is set up. The version presented above is a version of Ampère's law within the MHD limit (equation 1.16a) where the displacement current in equation 1.13 is neglected due to the low-frequency assumption ($\omega << \omega_p$, where ω_p is the plasma frequency and is given by $\sqrt{\frac{ne^2}{m\epsilon}}$). Faraday's law (equation 1.16b) states that a changing magnetic field with time gives rise to an induced current which is due to a force (voltage) in a circuit system. Conversely, a magnetic field that changes in time can be generated by an electric field which is changing in space, this law is the foundation of transformers, electric motors and generators which are at the basis of modern technology. Gauss' law for magnetism (equation 1.16c) states that the magnetic field is divergence-less, or for any closed surface, the amount of magnetic flux entering is exactly equal to the flux leaving. Gauss's electric field law (equation 1.16d) states that the net flux of electric field through a surface is proportional to the electric charge enclosed by said surface. Gauss's law is also commonly replaced by the *plasma approximation*, which states that $n_i >> n_e$ due to the aforementioned low frequency assumption.

The conservation of momentum equation (1.15b) shown above is for an individual species, however within a plasma one has both electrons and ions. By adding both species a relationship between electric field and current density can be derived called *Ohm's law*:

$$\boldsymbol{j} = \sigma(\boldsymbol{E} + \boldsymbol{u} \times \boldsymbol{B}), \tag{1.17}$$

where σ is the conductivity of a medium. Ohm's law is particularly instructive, as when in a collisionless plasma $\sigma \to \infty$ and $\boldsymbol{E} = -\boldsymbol{u} \times \boldsymbol{B}$. Substituted into Faraday's law (equation 1.3b) this concept represents the *frozen-in flux theorem* discussed in the following section.

1.1.2.1 Frozen-in Flux Approximation

A fundamental concept in space and planetary physics is the frozen-in flux approximation or Alfvén's theorem. Alfvén stated that '*In view of the infinite conductivity, every motion (perpendicular to the field) of the liquid in relation to the lines of force is forbidden because it would give infinite eddy currents. Thus the matter of the liquid is "fastened" to the lines of force*' (Alfvén, 1942) meaning that the plasma and magnetic field will move together.

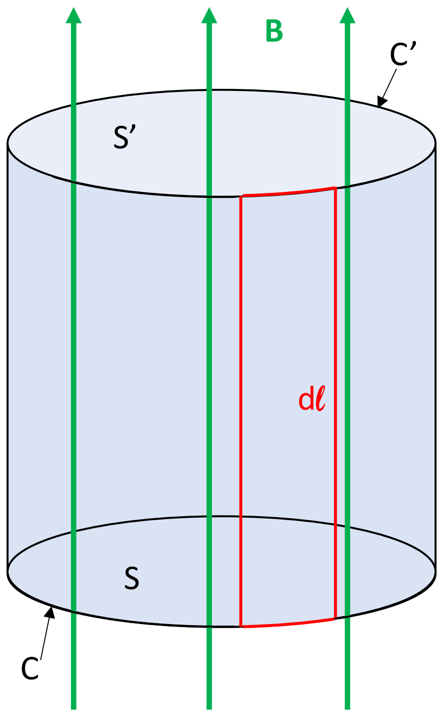

FIGURE 1.4: Diagram of a cylinder threaded by magnetic flux, showing the set-up for deriving frozen-in flux approximation.

To show this mathematically, we embark on a thought experiment: we know, through Gauss' law, that magnetic flux must be conserved,

$$\int\int \boldsymbol{B}.d\boldsymbol{s} = 0, \tag{1.18}$$

We then consider a surface S bounded by curve C, move with velocity $\boldsymbol{u}$ along a length $\boldsymbol{dl}$ to become surface S' bounded by curve C'. Flux entering the surface S must either exit at surface S' or via the side of the presumed cylinder (shown in figure 1.4). Hence, Gauss' law becomes:

$$-\int_S \boldsymbol{B}(t+\Delta t).\boldsymbol{n}dS + \int_{S'} \boldsymbol{B}(t+\Delta t).\boldsymbol{n}dS' + \oint \boldsymbol{B}(t+\Delta t).\boldsymbol{dl} \times \boldsymbol{u}\Delta t = 0, \tag{1.19}$$

where the first term is flux threading the bottom of the cylinder, the second term is flux threading the top of the cylinder and the third term is flux threading through the walls of the cylinder. $\boldsymbol{n}$ is the normal to the surface. Hence we find:

$$\int \boldsymbol{B}(t+\Delta t).\boldsymbol{n}dS' = \int \boldsymbol{B}(t+\Delta t).\boldsymbol{n}dS - \oint_{C'} \boldsymbol{B}(t+\Delta t).d\boldsymbol{l} \times \boldsymbol{u}\Delta t = 0 \tag{1.20}$$

We now consider the change of flux in the cylinder over time which can be represented as:

$$\frac{d\phi}{dt} = \lim_{\Delta t \to 0} \frac{\phi_{C'}(t+\Delta t) - \phi_C(t)}{\Delta t} \tag{1.21}$$

We substitute in $\phi = \int \boldsymbol{B}.d\boldsymbol{S}$:

$$\frac{d\phi}{dt} = \frac{\int \boldsymbol{B}(t+\Delta t).\boldsymbol{n}dS' + \int \boldsymbol{B}(t).\boldsymbol{n}dS}{\Delta t} \tag{1.22}$$

Substituting equation 1.20 into 1.22 returns:

$$\frac{d\phi}{dt} = \frac{\int(\boldsymbol{B}(t+\Delta t) - \boldsymbol{B}(t)).\boldsymbol{n}dS}{\Delta t} - \oint_{C'} \boldsymbol{B}(t+\Delta t).d\boldsymbol{l} \times \boldsymbol{u} \tag{1.23}$$

$$= \int \frac{d\boldsymbol{B}}{dt}.\boldsymbol{n}dS - \oint_{C'} (\boldsymbol{u} \times \boldsymbol{B}).d\boldsymbol{l} \tag{1.24}$$

as $\boldsymbol{B}.(d\boldsymbol{l} \times \boldsymbol{u}) = d\boldsymbol{l}(\boldsymbol{u} \times \boldsymbol{B})$ and using Stokes' theorem we can convert the second term to a surface integral to combine into one integral:

$$\frac{d\phi}{dt} = \int \left[\frac{d\boldsymbol{B}}{dt} - \nabla \times (\boldsymbol{u} \times \boldsymbol{B})\right] \boldsymbol{n}.dS \tag{1.25}$$

Hence, if $\frac{d\boldsymbol{B}}{dt} = \nabla \times (\boldsymbol{u} \times \boldsymbol{B})$ then $\frac{d\phi}{dt} = 0$. This equation states that the magnetic field and the plasma must move together - hence the magnetic field is 'frozen-in' to the plasma. To generalise this equation to form the induction equation we must substitute Ohm's law into Ampere's law:

$$\nabla \times \boldsymbol{B} = \mu_0 \boldsymbol{j} = \mu_0 \sigma(\boldsymbol{E} - \boldsymbol{u} \times \boldsymbol{B}), \tag{1.26}$$

take a cross product of both sides, rearrange to make the time differential the subject and simplify to return:

$$\frac{\partial \boldsymbol{B}}{\partial t} = \nabla \times (\boldsymbol{u} \times \boldsymbol{B}) + \frac{1}{\mu_0 \sigma} \nabla^2 \boldsymbol{B}, \tag{1.27}$$

where the first term on the right hand side is the advective term or frozen-in term which controls how the plasma and field are frozen together, and the second term is the diffusive term, which describes how much the plasma diffuses through the magnetic field. In the frozen in approximation the second term is considered negligible. The ratio of the two terms is called the magnetic Reynolds number which can determine if the frozen-in approximation is correct and MHD is appropriate. A large Reynolds number confirms the frozen-in approximation, but a Reynolds number of less than one shows that the plasma can diffuse from the magnetic field.

For a collisionless plasma in space with a magnetic Reynolds number of > 1, such as the magnetospheric plasma at Earth (discussed further in a following section), the frozen-in flux theorem is held. However, in some areas of the magnetosphere, a phenomenon called *magnetic reconnection* occurs where the field lines effectively break and reconnect with oppositely directed field lines, in which plasma which is *frozen-in* to one field line, becomes frozen-in to another. As such, the criteria for the frozen-in theorem and MHD must be invalid.

This process occurs in areas of plasma and field regime changes (i.e. current sheets) where the scale length becomes small and a local breakdown of MHD occurs. These areas are commonly called *x-type neutral lines* where the two field regimes are pushed together with a plasma velocity inflow (U_i), which is converted to a plasma outflow (U_o) along

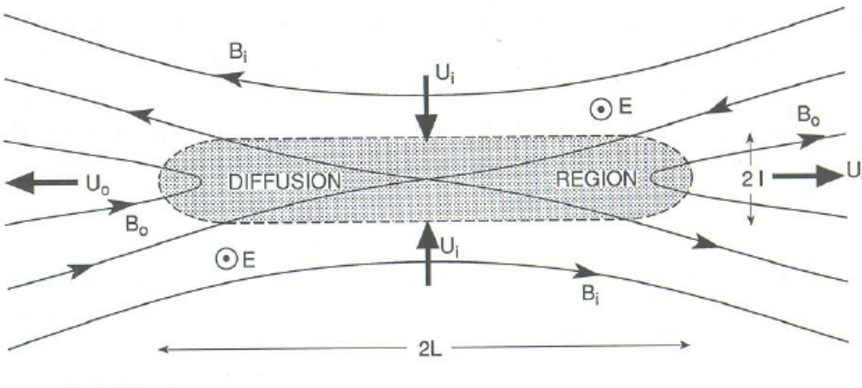

Figure 1.5: Illustration of a reconnection site with Sweet-Parker geometry from Kivelson and Russell (1995). U_i denotes the inflow velocity, U_o is the outflow velocity, B_i is the inflow magnetic field, B_o is the outflow magnetic field, E is the electric field and L is the length scale of the diffusion region which is shaded.

the boundary via a diffusion region at the centre with a magnetic Reynolds number is less than 1. The magnetic field also reduces to zero at the centre. This is illustrated in figure 1.5, which shows the Sweet-Parker reconnection geometry (Parker, 1957) which is one of several theoretical geometries.

1.1.2.2 Ideal MHD

In an infinitely conducting fluid (perfect electric conductor), where the magnetic Reynolds number is infinite and viscosity is ignored, ideal magnetohydrodynamics can be assumed. This is where equations 1.15 and 1.16 are reduced to:

$$\nabla \times \boldsymbol{B} = \mu_0 \boldsymbol{j} \tag{1.28a}$$

$$\frac{\partial \rho}{\partial t} + \nabla \cdot (\rho \boldsymbol{V}) = 0 \tag{1.28b}$$

$$\rho \left[\frac{\partial \boldsymbol{V}}{\partial t} + (\boldsymbol{V} \cdot \nabla) \boldsymbol{V} \right] = -\nabla \cdot \boldsymbol{P} + \boldsymbol{j} \times \boldsymbol{B} \tag{1.28c}$$

$$\frac{\partial \boldsymbol{B}}{\partial t} - \nabla \times (\boldsymbol{V} \times \boldsymbol{B}) = 0 \tag{1.28d}$$

Pressure here is evaluated as a tensor, however it is also common to approximate pressure as isotropic and as such may be represented as ∇P. We can evaluate the force density $\boldsymbol{j} \times \boldsymbol{B}$ by substituting Ampere's law to get:

$$\boldsymbol{j} \times \boldsymbol{B} = \frac{1}{\mu_0} (\nabla \times \boldsymbol{B}) \times \boldsymbol{B} = \frac{1}{\mu_0} (\boldsymbol{B} \cdot \nabla) \boldsymbol{B} - \frac{1}{\mu_0} (\boldsymbol{B} \cdot \boldsymbol{B}) \nabla_{\boldsymbol{B}} = \frac{1}{\mu_0} (\boldsymbol{B} \cdot \nabla) \boldsymbol{B} - \nabla \frac{B^2}{2\mu_0} \tag{1.29}$$

The first term on the right side is the *magnetic tension* term - or the force that acts to straighten curved magnetic field lines. The second term is the *magnetic pressure* term. The total pressure of a system is an addition of the plasma pressure and the magnetic pressure. The ratio of the two pressures is called *plasma beta*, $\beta = \frac{p}{B^2/2\mu_0}$. This factor shows if the plasma pressure or magnetic field controls the dynamics of the system.

1.1.2.3 Force-Free or Force-Balanced Systems

When describing magnetohydrostatic equilibrium in plasma, we are describing that the $\boldsymbol{J} \times \boldsymbol{B}$ force density is either balanced with the pressure gradients (balanced), or equal to zero (free) from the conservation of momentum equation (equation 1.30b): $\boldsymbol{J} \times \boldsymbol{B} = \nabla P$. Force-free solutions of $\boldsymbol{J} \times \boldsymbol{B} = 0$ include magnetic field-aligned current density, or a zero value for current density.

1.2 Magnetospheres of the Solar System

A magnetosphere is a volume around a body in which all plasma is controlled by the magnetic field of that body. A magnetosphere can be considered intrinsic, where the planet or moon itself is producing a magnetic field such as at Mercury, Earth, Jupiter, Ganymede, Saturn, Uranus, and Neptune. Here, the magnetic field of the planet forms an obstacle to the incoming solar wind. A magnetosphere may be considered induced where the draping effect on the incoming magnetic field of the Sun or parent planet induces a magnetic field at the body. This happens at Venus and Titan, where the ionosphere is the obstacle to the incoming magnetic field, and other unmagnetised moons where conducting layers in the interior are the obstacle. In this section we consider the former and discuss the specifics of the Sun, Earth and Jupiter systems. A following section outlines the Saturnian system, and the induced magnetosphere of Titan is discussed further in section 1.4.

Bodies with intrinsic magnetic fields generally have all the basic components described below. If the magnetosphere is placed in a super-sonic plasma flow a bow shock will form where the plasma is shocked to a sub-sonic speed before encountering the body. The bow shock is aptly named as a comparison to the surface water shock at the head of a ship's bow. All planets in the solar system, regardless of intrinsic or induced magnetic fields, form a bow shock upstream when the incoming solar wind is super-sonic (discussed further in the next section).

The next boundary is the magnetopause, which is the boundary between the plasma controlled by the body of interest and the external controller. The position of the magnetopause can be highly variable owing to its dependence on the balance of dynamic pressure of the outside medium, the magnetic pressure of the planetary body and magnetospheric current systems (Russell, 2007). The incoming plasma is sub-sonic and so the magnetopause is the current-layer which acts to divert the incoming plasma around the body. One current system is named the Chapman-Ferraro current and it confines the internal magnetic field and plasma (Chapman and Ferraro, 1929) by use of the Lorentz force. A particle from the solar wind that encounters a magnetic field (at a boundary like the magnetopause) will sense a $\boldsymbol{u} \times \boldsymbol{B}$ force and will partially gyrate before exiting the boundary. The different gyration directions of electrons and ions cause a charge separation where electrons are deflected in the opposite direction to ions. Between the bow shock and magnetopause lies a turbulent layer named the magnetosheath, this volume is occupied by shocked plasma and magnetic field that is now sub-sonic but of external origin to the planetary body.

Inside the magnetopause is the magnetosphere, where all plasma is controlled by the planetary body of interest. The magnetospheres of the solar system vary widely and we will discuss the main attributes and characteristics of the Sun's, Earth's and Jupiter's magnetospheres to give a background for the main topic of this thesis: Saturn's magnetosphere.

1.2.1 The Sun and Solar Wind

The solar wind is a stream of electrically charged particles that originate from the Sun's upper atmosphere (*corona*). The solar wind is highly variable temporally, and spatially is often observed to be faster over the poles of the Sun than at the equator (McComas et al., 2003).

The Sun's magnetic field carves out a bubble in the interstellar medium where all plasma and magnetic field is dominated by the Sun, hence it has its own magnetosphere named the heliosphere. Similar to the planetary magnetospheres it has a heliopause, which is analogous to the magnetopauses of the planets, and heliosheath (magnetosheath). Thus the Sun's magnetic field can be described as a very large magnetosphere.

Frozen-in to the solar wind is the interplanetary magnetic field (IMF) which is the internal field of the Sun, formed by a dynamo action in the Sun's interior convective zone, that is dragged outwards by particles ejected from the Sun (Parker, 1970). The Sun also rotates with a differential rate of 24.5 days at the equator and up to 38 days near the poles (Snodgrass and Ulrich, 1990). This rotation with the addition of outward flows of particles wraps the magnetic field into a spiral shape. This field system is named the Parker spiral (Parker, 1958). The flapping nature of the heliospheric current sheet is attributed to differences in the angle of the magnetic dipole axis and the Sun's rotational axis (Owens and Forsyth, 2013) and produces a flapping of the heliospheric current sheet, formed at the point where the field reverses direction about the magnetic equator.

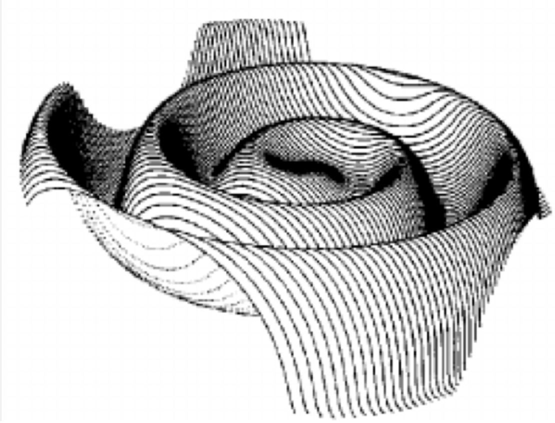

FIGURE 1.6: Diagram of the Sun's Parker spiral current sheet, modified from Dryer (1998) where the Sun is found at the centre.

The solar cycle is an ∼11 year cycle where solar activity increases to a maximum (solar maximum) and decreases to a minimum (solar minimum). This cycle describes magnetic activity such as sun spots and flares on the Sun's surface (photosphere), and hence the amount of electromagnetic radiation and particles ejected. The solar cycle can be easily tracked by the number of sunspots that appear in the photosphere and by the electromagnetic radiation that arrives at Earth due to the increased activity on the solar surface (i.e. flares, coronal mass ejections) during solar maximum. This also means that magnetospheric processes at Earth are also affected by the solar cycle due to the strong solar wind control of Earth's magnetosphere. It has been shown that auroral activity increases during solar maximum and a correlation between low activity and reduced global surface temperatures has been presented (e.g. Lassen and Friis-Christensen, 1995; Rind et al., 2008).

The main focus of this thesis is the magnetosphere of Saturn, however as the magnetospheres of the solar system are, to some degree, affected by the the solar wind an interplanetary magnetic field (IMF) it is important to understand the nature of the solar wind at Saturn's distant orbit. The solar wind exhibits periodic compression regions (regions of denser and higher magnetic field strength) due to rotating features on the surface, where the magnetic field can reach ∼0.5 - 2.0 nT at 10 AU. In a region of rarefaction it is commonly ∼0.1 nT.(Jackman et al., 2004). Additionally, there are transients and disordered periods where a periodic compression/rarefaction pattern is not apparent (e.g Moldwin et al., 2000). The Parker spiral angle (the angle between the tangential and radial velocities of the solar wind) increases from ∼ 45° at Earth to ∼ 90° at Saturn, along with the steepening of shocks present in the solar wind between 1-10 AU.

1.2.2 Earth

The field produced by the Earth's magnetic field is similar to that of a bar magnet, where the south pole of the magnet lies around 11° from the northern geographic pole and the north pole of the magnet lies near the southern geographic pole at the time of writing. In reality, however, Earth's magnetosphere does not resemble a perfect sphere. There are a number of external and internal processes that act to deform and warp the magnetosphere. The main process is the aforementioned solar wind, which acts to squash the front of the Earth's magnetic field and elongate and stretch the night side which is named the magnetotail. Figure 1.7 shows these regions.

Circulation of magnetic flux at Earth is dominated by the Dungey cycle (Dungey, 1961, 1963)]. The Dungey cycle describes the convection of plasma and magnetic flux over the polar cap driven by magnetic reconnection on the dayside and nightside of Earth. Figure 1.8 shows that when the interplanetary magnetic field (IMF) is oriented

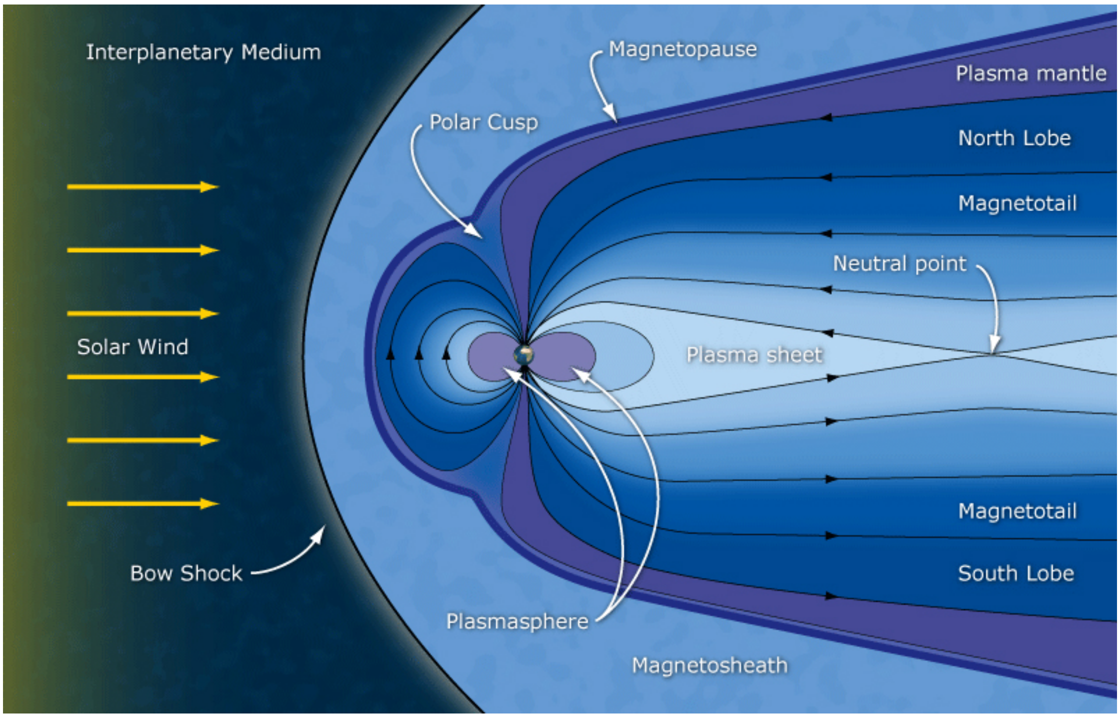

FIGURE 1.7: Diagram of Earth's magnetosphere. Image credit: ESA/C. T. Russell

opposite to Earth's magnetic field, we have the conditions for reconnection at site 1 in the diagram. These newly reconnected field lines contract due to tension and the solar wind ends are dragged backwards (2 and 3) to form the tail lobes, which then sink into the tail where once again the fields are opposing and conditions for reconnection occur (4). Magnetic field and plasma is then ejected from the tail via a plasmoid (5), and the magnetic field lines that are still connected to Earth snap back into a dipolar arrangement (6). Magnetic flux then travels around the sides of Earth, to begin the process again. This process occurs on the time scale of a few hours (Cowley, 1982).

Earth's tail is a dynamic region of the magnetosphere, where as we described previously, reconnection can occur between the two lobes, as well as plasmoid formation and release, and dipolarisation of the magnetic field. Figure 1.7 shows a region named the *plasma sheet*, this region is home to a current which is set up due to the opposing magnetic field within each lobe. The position and movement of the current sheet at Earth is controlled by a number of external and internal drivers. We know that the magnetosphere is affected largely by the IMF and the average position of the plasma sheet is controlled by the incoming solar wind flow angle and changes in the components

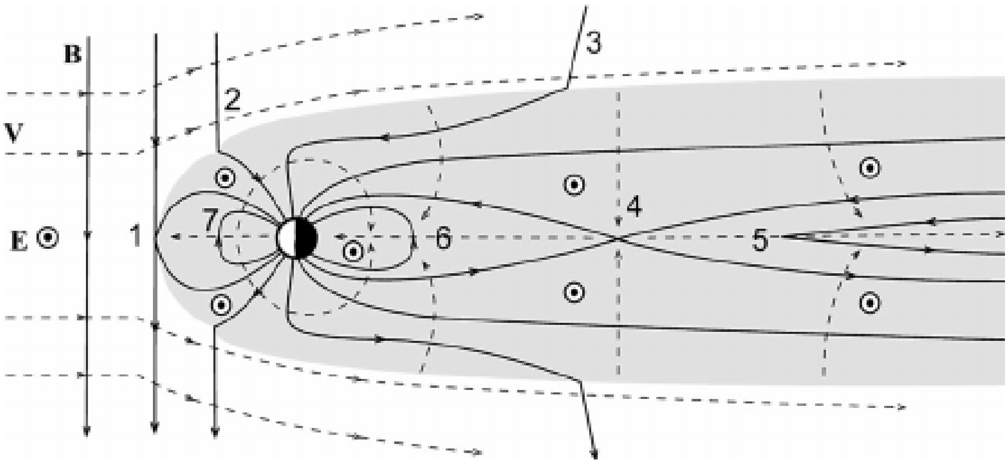

FIGURE 1.8: Diagram of the Dungey cycle at Earth, [Seki et al. (2015), (courtesy of Steve Milan). The solid black lines are magnetic field lines, the dotted lines show the direction of velocity of the field lines and circled dots show the electric field. Processes numbered are described in the text.]

of IMF will cause a twisting of the neutral sheet (e.g. Tsyganenko and Fairfield, 2004). The plasma sheet will always reside between the two magnetotail lobes and these flap in the IMF like a flag flaps in the wind. Larger twisting and waving of the plasma sheet can be caused by orientation and direction changes of the IMF (e.g. Case et al., 2018). Small scale waves and disturbances are also reported (e.g. Sergeev et al., 2004).

1.2.3 Jupiter

Jupiter's magnetosphere is the largest object within the solar system, and has vast differences to the magnetosphere of Earth. Jupiter's magnetosphere is 10 times larger than Earth's in terms of field strength and is nearly 100 times larger (Brice and Ioannidis, 1970) in volume. Jupiter's magnetosphere is rotationally driven, this means that as Jupiter rotates every 9 hours and 55 minutes, part of the magnetosphere is also attempting to rotate with the planet. Additionally, Jupiter's volcanic moon Io acts to load ~1000's kg s^{-1} of plasma into the magnetosphere (Brown, 1994). This process combined with a short rotation period means that Jupiter's magnetosphere is stretched at the equator by the centrifugal force into a large washer-shaped disk (Piddington, 1969; Smith et al., 1974) (Figure 1.9).

Mass loading of the magnetosphere, due to the large amount of internal plasma sources, acts to set up a current system in the magnetosphere that attempts to 'speed' the plasma up to co-rotation. The continuous addition of mass means the field becomes *swept backwards* so that it may transmit stress from the ionosphere to the newly created plasma, and as such a current is pulled from the ionosphere along the field lines to the point at which the magnetic field is starting to sub-corotate. The current then moves radially outwards along the current sheet, acting to enforce corotation of the plasma and magnetic field, and is theorised to return along the magnetic field to a higher latitude in the ionosphere, which is then closed through the conducting ionosphere (e.g. Hill, 1979; Southwood and Kivelson, 2001; Cowley and Bunce, 2001; Khurana et al., 2004, and references therein).

Jupiter's equatorial current sheet is present in all local time areas of Jupiter's magnetic field, as it exists between the two oppositely directed *lobes* of the magnetosphere. As Jupiter's magnetic dipole is offset by 10° from the rotational axis, this means the

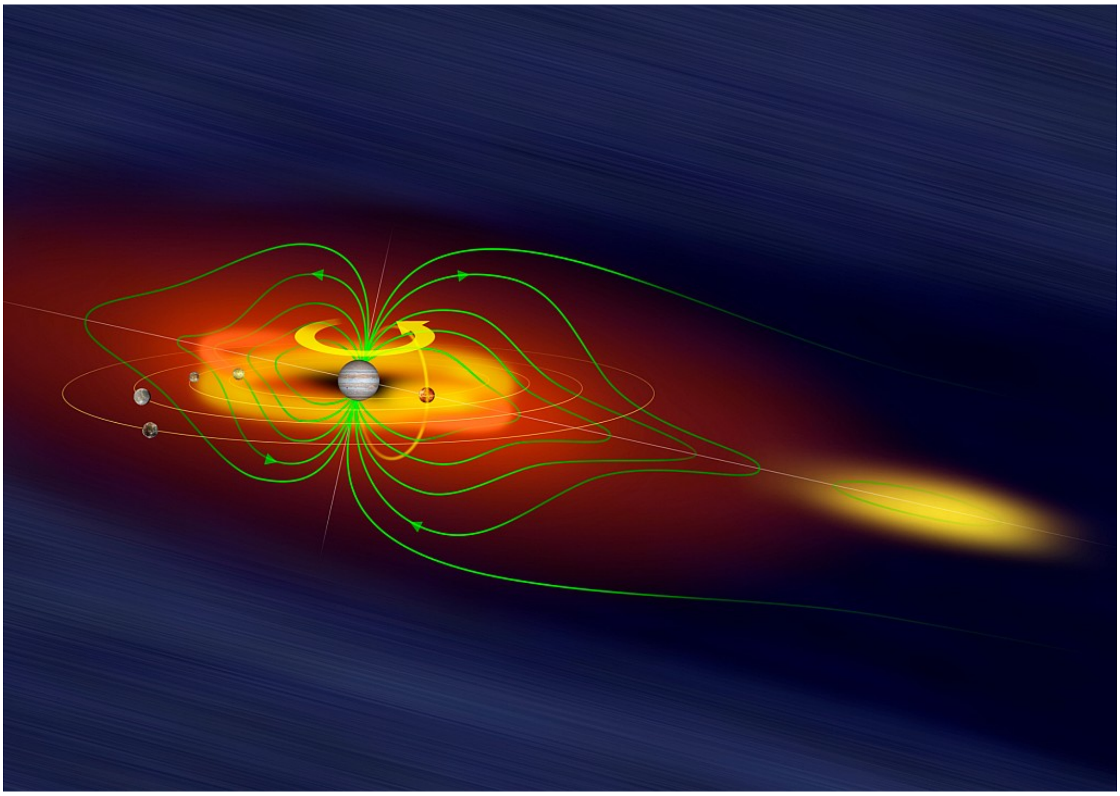

FIGURE 1.9: Diagram of Jupiter's magnetosphere from the side, Image credit: Max Plank Inst.

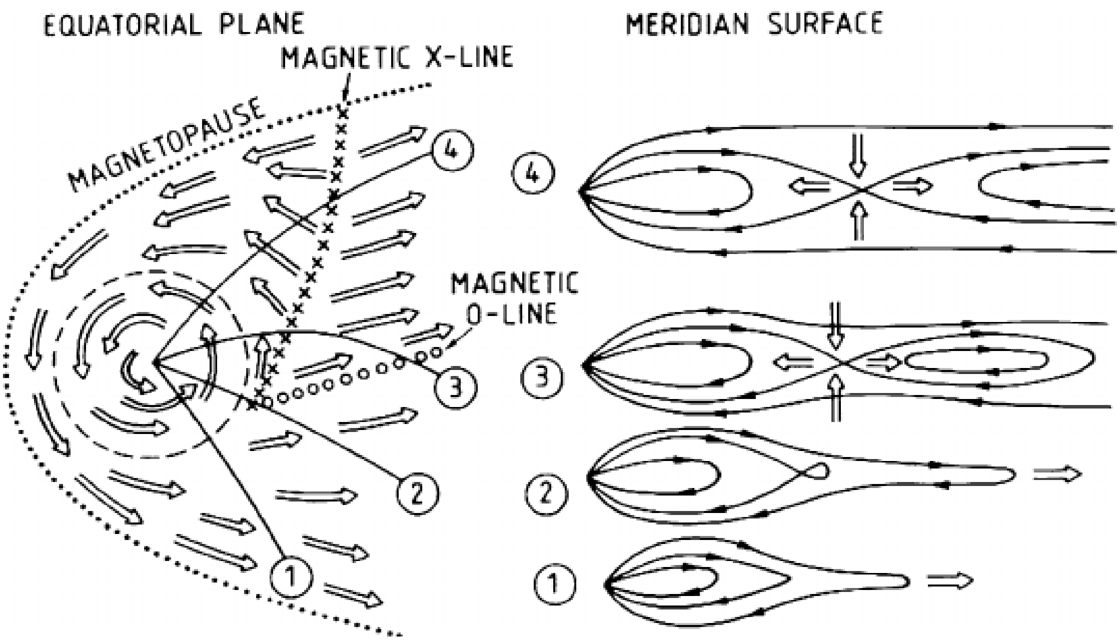

FIGURE 1.10: Diagram of the Vasyliunas cycle at Jupiter looking down on the equatorial plane from above (left) and from the side (right) (Vasyliunas, 1983)

current sheet moves above and below the rotational equator every 9.9 hours in a flapping motion [e.g Smith et al. (1974)]. Additionally, smaller scale movements of the current sheet have been seen in magnetometer data by Russell et al. (1999) as the current sheet was moving over the Galileo space craft.

Circulation of plasma and flux in Jupiter's magnetosphere is controlled by a process named the Vasyliunas cycle (Vasyliunas, 1983). Figure 1.10 describes this cycle where plasma is attempting to rotate with the planetary rotation period, is funnelled around the dayside of the magnetosphere and stretches the magnetic field by the frozen-in effect into a washer shaped disc (1). As the plasma travels around, the washer shape breaks down due to reconnection at the x-line and plasmoid formation at the o-line (denoted by a line of 'x' and 'o' on the left plot). Finally at (4) we see a release of the plasmoid down the tail with plasma being lost. The remaining plasma is funnelled back around the dayside by the magnetic field to begin the process again. In addition to this ideal theoretical cycle, Kivelson and Southwood (2005) show the importance of instabilities on the reconnection and plasma flow in the tail region of the magnetosphere. A streaming outflow of plasma resulting from an extreme instability is expected between (1) and (2) in figure 1.10, which then causes disconnection of plasmoids and depletion of plasma on the closed field lines as the cycle moves around to (3). The reconnected flux tubes then slowly flow sunward in the dawn flank.

1.3 The Saturnian System

1.3.1 Overview of Saturn's Magnetosphere

The magnetosphere of Saturn was first detected in-situ in 1979 during the first fly-by of Saturn by the Pioneer 11 spacecraft and is the second largest in our solar system, after Jupiter. Saturn's magnetosphere is, for the most part, rotationally driven like Jupiter's (Southwood and Kivelson, 2001). Saturn rotates roughly once per 10.7 hours and internal plasma sources, such as Enceladus and the other satellites, the rings and the planet itself (e.g. Jurac et al., 2002; Tokar et al., 2005; Pontius and Hill, 2006; Felici et al., 2016) operate to stretch the field radially to produce the magnetodisc.

The main internal source, Enceladus at 4 R_S, ejects up to 1000 kg of water vapour per second into the magnetosphere (e.g. Jurac et al., 2002; Ingersoll and Ewald, 2011; Fleshman et al., 2010a,b, 2013), some of which, up to 100 kgs^{-1} (Jurac et al., 2002), is then ionised and picked up by the magnetic field to corotate with the planet. The magnetodisc forms from the point where centrifugal stresses, caused by the mass loading of these internally sourced plasmas, balance gravitational force and magnetic tension (Arridge et al., 2007). This occurs at $\sim$ 15 R_S and continues to the magnetopause causing the field to become increasingly azimuthal (e.g. Went et al., 2011a).

Field structure in the azimuthal direction is additionally affected by the rotation of Saturn and solar wind conditions. In the distant magnetosphere, the magnetic field lines are *swept-back* due to subcorotation of plasma causing an increasingly azimuthal field with radial distance. *Swept-forward* field is also shown on the dusk-side magnetosphere where confinement by the solar wind causes the plasma to be pushed forward into the corotation direction (e.g. Delamere et al., 2015). The dynamic pressure of the solar wind also affects the azimuthal field structure in the day-side region. High dynamic pressure causes the dayside magnetosphere to compress, which is then closer to the corotation breakdown region which leads to a increasingly corotating dayside plasma with fewer swept-back and swept-forward field lines on the dawn and dusk flanks respectively due to the effects of the Chapman-Ferraro currents. The noon-sector may also experience super-corotating plasma, and hence swept-forward fields, during times of transient solar wind compressions along with the disappearance of the current sheet during times of high solar wind pressure (Southwood and Kivelson, 2001; Kivelson et al., 2002; Hanlon et al., 2004; Arridge et al., 2008a; Davies et al., 2017).

Inside of $\sim 6\ R_S$ the internal field of Saturn is dominant and yields a dipole-like field (Connerney et al., 1981; Bunce et al., 2007; Kellett et al., 2009). Saturn's internal field is aligned to within 0.01° of the rotational spin axis (Dougherty et al., 2018), and the magnetic north pole is the Kronographic north pole, opposite to Earth's configuration (Russell and Dougherty, 2010). Saturn's magnetic field has quadropole and higher components, however they are much weaker than the dipole and do not affect the analysis presented further in this thesis. The magnetic field is slightly shifted towards the north pole by 2808.5 ± 12 km (Dougherty et al., 2018).

Saturn's magnetic field is also compressed on the day-side by the solar wind and extended to form a magnetotail, similar to Earth's, on the night-side. The position of the magnetopause has been shown to have a bimodal distribution with peaks at 16 and 27 R_S with an average of 22 R_S (Slavin et al., 1985; Arridge et al., 2006; Achilleos et al., 2008; Pilkington et al., 2015*b*) at the sub-solar point, where in the time frame of study, the bimodal distribution was not related to the solar wind dynamic pressure, and as such must be a consequence of internal processes. Additionally, the magnetopause was shown to extend further on the dusk flank than the dawn flank as well as exhibit polar flattening (Pilkington et al., 2015*b*). Further to this the bow shock is situated at an average distance of 28 R_S (Went et al., 2011b).

We have previously discussed the Dungey and Vasyliunas cycles, the circulation patterns in Earth's and Jupiter's magnetospheres. Saturn is often thought of as a mid-point between both Earth and Jupiter, and as such a combination of both processes occur in the magnetosphere. Badman and Cowley (2007) theoretically suggest in the outer

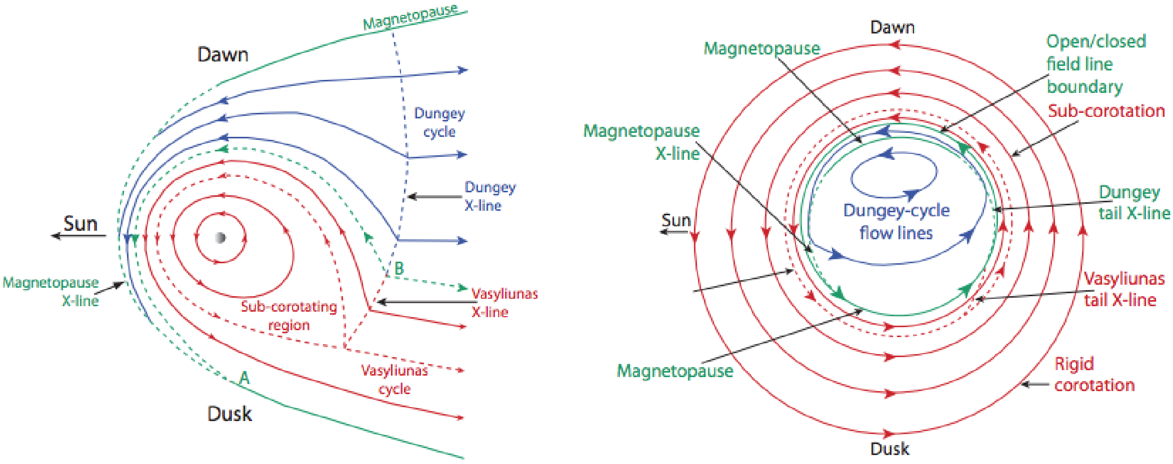

FIGURE 1.11: Diagram of the circulation pattern in Saturn's magnetosphere (left) and how that maps to the ionosphere (right) from Gombosi et al. (2009) modified from Cowley et al. (2004). Left shows the system from above Saturn from a distance, and right shows the same system mapped into the northern ionosphere of Saturn. Red lines shows a Vasyliunas-type circulation, blue shows a Dungey-type circulation and green shows the magnetopause. Solid lines are plasma streamlines, dashed lines are boundary streamlines.

magnetosphere both circulation patterns are important under compressed solar wind conditions. This can be shown where a region dominated by the Vasyliunas cycle (inner magnetosphere) will have heavier ions associated with the internal sources, whereas the area dominated by the Dungey cycle will have lighter, hotter externally sourced ions.

Figure 1.11 shows three regions of plasma circulation. As described the Vasyliunas cycle (red) is dominant in the inner corotating magnetosphere, and the Dungey cycle occurs generally under northward IMF (i.e. opposite sense to Earth), so that reconnection at the magnetopause can occur and flux is opened to the solar wind. This occurs only in the outer magnetosphere as the open flux is convected with the solar wind, however the ionospheric end of the flux tubes are being convected anti-sunward in a single circular convection pattern. A Dungey style x-line is then formed in the nightside (blue dotted) where the open field lines are closed via reconnection and flux is returned via the dawn magnetosphere.

In addition to the plasma circulation pattern described above, Saturn and Jupiter also show evidence of the importance of solar wind-magnetosphere coupling via intermittent small-scale reconnection and viscous interactions (e.g. McComas and Bagenal, 2007; Delamere and Bagenal, 2010; Delamere et al., 2015) such as Kelvin-Helmholtz instabilities (Desroche et al., 2013; Masters, 2018). Delamere and Bagenal (2013) suggest that the magnetotail structure is significantly affected by the viscous interactions at both Jupiter and Saturn.

1.3.2 Saturn's Magnetodisc and Current Sheet

A planetary magnetodisc is formed when the centrifugal force acting on the plasma sourced from Enceladus (at Saturn) is balanced with the gravitational force of the planet and the tension force of magnetic field. Hence, if the tension force cannot sustain a dipole-like arrangement, then the field stretches into a magnetodisc. This arrangement of magnetic field and centrifugal force confines the plasma at the equator to form the magnetodisc current sheet. As centrifugal potential scales with radius, a more stretched field line will find that the particles are more closely confined to the equator than on a more dipolar field line if they had the same kinetic energy and as more mass is added to the current sheet the magnetic field will become increasingly stretched.

The dayside magnetosphere at Saturn has been found to be quasi-dipolar like Earth, and early observations by Voyager and Pioneer concluded that a magnetodisc was not present (Smith et al., 1980; Connerney et al., 1983). However, after the arrival of Cassini, Arridge et al. (2007, 2008a) show that a magnetodisc, similar to Jupiter's, was present in the dusk flank and dayside of Saturn's magnetosphere and that the dayside magnetodisc is suppressed at times of high solar wind dynamic pressure when the magnetopause was inside of 23 R_S, which was the case during the Voyager and Pioneer flybys.

Figure 1.12 shows the distinctive bowl shape of the current sheet. Arridge et al. (2008b) showed that during the first part of Cassini's mission at Saturn, the current sheet was displaced northward from the rotational equator, where the current sheet and magnetodisc become parallel with the solar wind flow only in the outer magnetosphere. This displacement was shown to be a seasonal effect where, after solstice in 2009, the current sheet was displaced to the south of the rotational equator. The bowl shape is a feature of the middle and outer magnetosphere, where the *hinging distance* is the

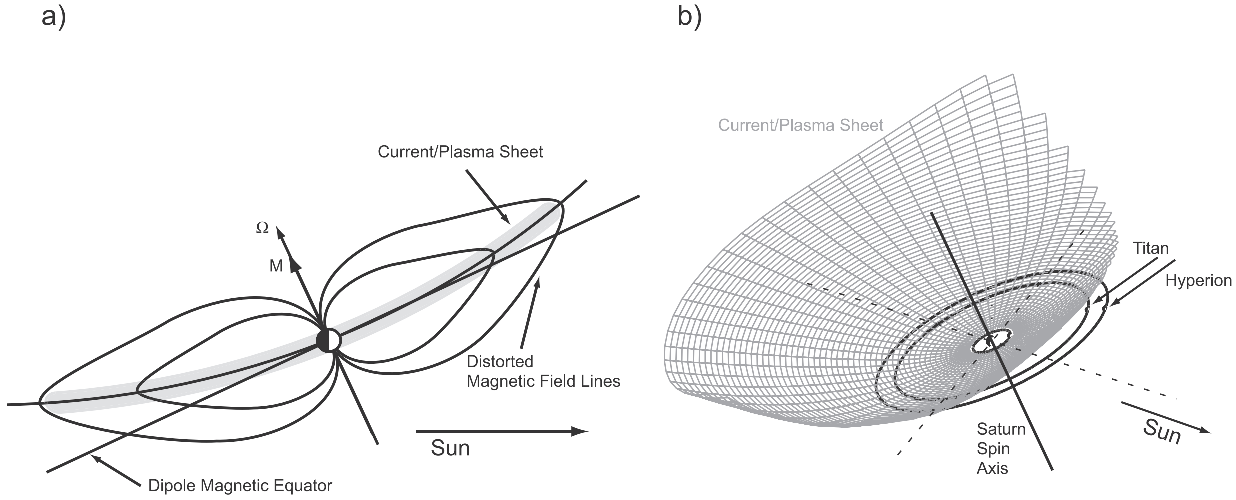

FIGURE 1.12: Figure showing a graphic of the bowl shape of Saturn's equatorial current sheet. a) shows a slice through the Sun-Saturn meridian and b) shows the system from above in 3 dimensions Arridge et al. (2008b).

characteristic distance over which the current sheet deviates away from the rotational equator. Arridge et al. (2008b) estimated this to be 15-30 R_S. Thus, if an observer were to be stationary in Saturn's magnetosphere for a Saturnian year, the observer would detect one full period of the bowl-shape wave in the magnetic field measurements. Seasonal differences are also present in the current sheet thickness. Sergis et al. (2011) shows that the thickness of the current sheet is highly variable between seasons (and even between Cassini revolutions (see also Kellett et al., 2009)) and exhibits a north-south asymmetry in the plasma sheet thickness.

Other periodicities in the current sheet are present, such as the near rotation rate *flapping* at around 10.7 hours which causes the current sheet to move up and down from a central position (Arridge et al., 2011; Provan et al., 2012). The flapping motion is thought to originate from two rotating magnetic perturbations in each hemisphere (e.g. Andrews et al., 2010; Southwood and Cowley, 2014). The periodicities in Saturn's magnetosphere are also though to act to thicken and thin the current sheet at a *beat* period as the two rotational perturbations do not have the same period (Thomsen et al., 2017). Also present are non-flapping and non-bowl dynamics which were explored by Arridge et al. (2007) as a tool to measure the stress balance in the magnetodisc, however, a statistical study of this pervasive phenomena (analogous to the small-scale movements presented in Russell et al. (1999)) and its sources has not been attempted.

Current density has been mapped by Sergis et al. (2017) from 5 - 16 R_S using stress balance in the magnetosphere showing that the thermal pressure outside of 12 R_S is dominated by the hot plasma pressure (hot ions) with some local time differences. The azimuthal current density calculated from this study was shown to be enhanced from post-noon to midnight compared to the post-midnight to noon sector inside of 13 R_S. Outside the azimuthal current is found to be strongest in the night and dawn sectors with a peak of 100 - 115 pA/m^2. In this same radial range, Kellett et al. (2011) showed that the strongest currents were found in the dusk-midnight sector with an increase in the morning sector at the radial extent of the study. The authors also show a temporal variability of a factor of 2-3 with increasing variability with radial distance. The current density between 2005 and 2006 was found to be $\sim$ 90 pA/m^2 at 9 R_S which reduced to $\sim$ 20 pA/m^2 at 20 R_S. Carbary et al. (2012) showed, through the use of pertubation magnetic fields, a peak of current density at 10 R_S of $\sim$ 75 pA/m^2. The authors study the radial distances between 3 and 20 R_S and calculate a total ring current in this area of 9.3 ± 1.0 MA. Current density in Saturn's magnetosphere has yet to be mapped outside of $\sim$ 20 R_S in all local times for the magnetodisc, along with the vertical structure of current density in the middle and outer magnetosphere.

1.4 Titan

Titan orbits Saturn at a mean distance of 1,221,850 km ($\sim$20 R_S). The moon is in a synchronous rotation with Saturn and so rotates at the same rate as it orbits, which is 15.94 Earth days. Titan is generally found within Saturn's magnetosphere, however when Titan is near the sub-solar point of Saturn's magnetosphere, the moon can be found in Saturn's magnetosheath or solar wind during a compression of Saturn's magnetic field caused by a higher solar wind dynamic pressure (figure 1.13b). During the Cassini mission, over 120 flybys of Titan were executed, they are named *T(number or letter corresponding to the flyby)*, e.g. TA is the first flyby, however after the release of Huygens the nomenclature turns to a numbered system - T3 is the first flyby after Huygens was released upon flyby TC.

Titan's interaction with Saturn's magnetosphere when the moon is inside the magnetopause is varied and unique in many ways. Firstly the corotation of Saturn's magnetosphere means that the ram side (hemisphere facing incoming corotating plasma) of Titan is generally found on the anti-orbital facing hemisphere, however, due to the orbital motion of Titan, this is also different to the hemisphere of the moon that is lit by the Sun. The overlap between the ram and sunlit hemispheres changes as Titan orbits Saturn. This makes Titan's ionosphere and atmosphere, and their interaction with the incident plasma a unique environment to study.

Titan is the only moon in the solar system known to harbour a dense atmosphere that includes cloud, haze layers and precipitation. The atmosphere of Titan is comprised of a similar layer system found in Earth's own atmosphere. The main constituent of Titan's atmosphere is molecular nitrogen (N_2), followed by methane (CH_4) and hydrogen (e.g. Coustenis et al., 1989; Coustenis and Bézard, 1995; Cravens et al., 2006). Molecular nitrogen is also the major constituent of Earth's atmosphere. However, as Titan is over 10 times further from the Sun than Earth the average temperature at the surface is ~ 90 K compared to a value of ~ 270 K at Earth (Mitchell and Lora, 2016). Additionally, due to the higher density of Titan's atmosphere and the lower gravity, Titan's atmosphere

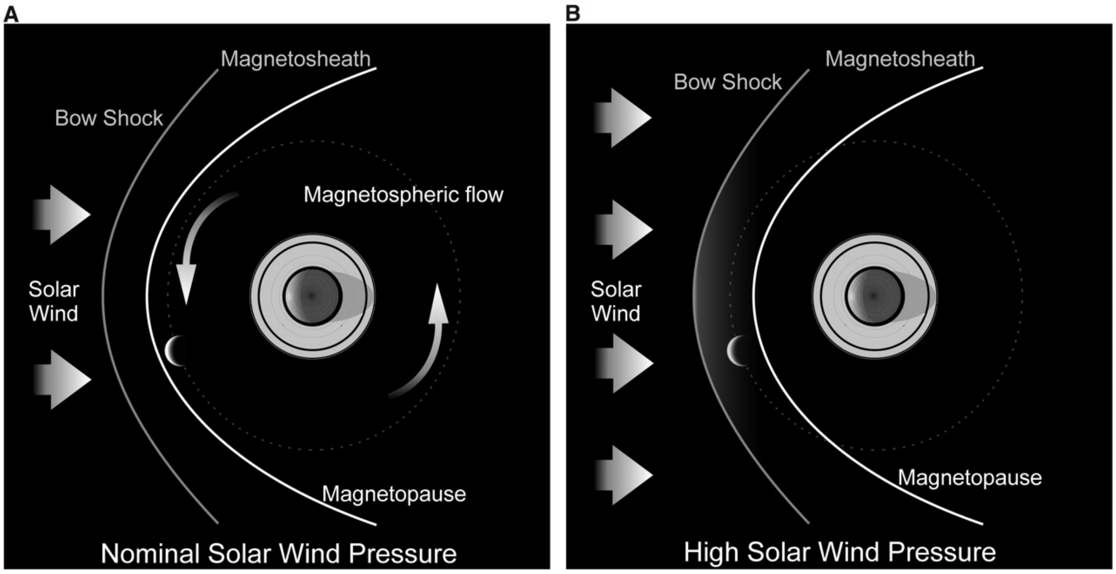

Figure 1.13: Figure showing Titan's orbit (white dotted), Saturn's bow shock (grey solid) and magnetopause (white solid) with Saturn and it's rings at the centre for a) nominal solar wind pressure and b) high solar wind pressure where Titan is in the magnetosheath. (Bertucci et al., 2008)

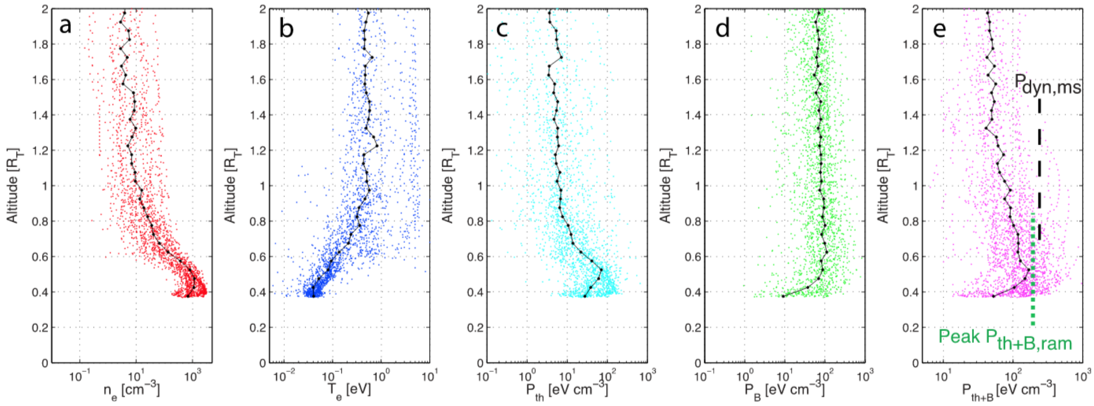

FIGURE 1.14: Figure 2 from Edberg et al. (2010) showing observed altitude profiles of (a) the electron density, (b) the electron temperature, (c) the thermal pressure, (d) the magnetic pressure and (e) thermal plus magnetic pressure. Black solid lines show median values. The black dashed line in e) shows the approximate magnetospheric ram pressure and the green dotted line shows the average peak pressure when only including ram side data. An altitude of 1000 km is $\sim 0.4\ R_T$

extends far further (exo-base found up to 1600 km (Cui et al., 2008)) in altitude than Earth's.

Titan's ionosphere (conducting layer of Titan's atmosphere) is found within the thermosphere, at between 1000-2000 km altitude. The height of the maximum electron and ion production peak is found using a one-dimensional photochemical model at around 1100 km at zenith angles of around 60°, and at 1195 km at zenith angles of around 90° (Keller et al., 1992). Edberg et al. (2010) shows in figure 1.14 a statistical study of all ionospheric properties during Titan flybys up to publication in 2010. A median maximum electron production is found at between 0.4 and 0.6 R_T, which is 1030-1545 km. Figure 1.14(b) also shows an increase in electron temperature with altitude up to 1 R_T where temperature levels out to a value of 0.5 eV.

Sources of this ionisation peak are found using models such as Keller et al. (1992) and Ip (1990). Keller et al. (1992) showed that photoionisation is the main source on the dayside, however magnetospheric electron precipitation is also a significant producer in both the day and night sides. Both models predict that $HCNH^+$ is the main ion at the peak density as both N_2^+ and CH_4^+ react to give $HCNH^+$. However, reexamination by Fox and Yelle (1997) showed that $HCNH^+$ is not the main ion at the density peak, but hydrocarbon chains with 3 or more carbon atoms ($C_xH_y^+$) are the main constituent above 1000 km. Further examination by Keller et al. (1998) shows that $HCNH^+$ is the main ion below 1200 km but agrees that the peak density is made primarily from $C_xH_y^+$ ions. Minor production methods in Titan's ionosphere also include cosmic rays at low altitudes (Capone et al., 1976), and proton and ion precipitation (Cravens et al., 2008).

During the Cassini era, it was now possible to have a larger data set of plasma data in Titan's ionosphere. Cravens et al. (2006) showed that $HCNH^+$ and $C_2H_6^+$ are the major ions in the ionosphere, and Ågren et al. (2007, 2009) also show from data that magnetospheric impact ionisation is a significant production method, but solar EUV is the main production method for the dayside ionosphere. However, Cui et al. (2010) also shows that the nightside ionosphere may be populated by transport from the dayside. If impact ionisation from magnetospheric electrons is a major contributor to the ionosphere, the question that needs to be addressed is: how are the electrons in Saturn's magnetosphere reaching Titan's ionosphere? Gan et al. (1992) suggested that electrons could reach the ionosphere by travelling along draped magnetic field lines from the far wake region.

Altitude variations such as those discussed previously in smaller chain hydrocarbons and nitrogen ions are also present in heavier ions such as longer chain hydrocarbon ions. These long chain hydrocarbons formed from photon and electron impacts of methane and molecular nitrogen increases with altitude as the probability of the photons and electrons reaching lower in the atmosphere is reduced due to the opacity of the haze layers and clouds and increasing density (Sittler et al., 2009).

1.4.1 Titan's Magnetospheric Interaction

As previously mentioned, Titan's orbit (at 20 R_S) can be co-located with the magnetopause sub-solar position under high solar wind dynamic pressure, meaning that Titan is sometimes found in the magnetosheath or solar wind. This variable environment leads to the changing draped field around Titan (figure 1.15). Titan itself lacks an intrinsic magnetic field and as such it is the interaction of Titan's *induced* magnetic field that will be discussed. The induced magnetic field is controlled entirely by the surrounding magnetic field. Simon et al. (2010, 2013) classified all of Cassini's flybys of Titan from

TA to T85 with regards to their environment, specifically the ambient field outside of the interaction region, the state of the induced magnetosphere (how far it has deviated from a steady-state draping picture) and which part of the induced magnetosphere Cassini sampled, the following paragraphs discuss these various environments.

Titan has been observed once in the solar wind (Bertucci et al., 2015), where a well-defined bow shock and an induced magnetosphere of IMF origin field were identified. Subsequently, Feyerabend et al. (2016) applied a hybrid simulation code which reproduces the features seen in the magnetometer data well and shows that the interaction is due to a steady-state interaction of Titan with the solar wind. Additionally, Omidi et al. (2017) showed that when Titan exits the bow shock of Saturn, this results in a deformed bow shock around both obstacles, shown in figure 1.16.

Titan has been observed in the magnetosheath of Saturn on a handful of occasions. This interaction was again modelled by the hybrid simulation code by Simon et al. (2009), where the authors show that the code can accurately model the abrupt change in environment and a sharp increase in density in the ionosphere during flyby T32. The abrupt changes in the environment give rise to another phenomenon found at Titan - *fossil fields*. Fossil fields are remnants of a previous magnetic environment which has been frozen-into the ionosphere of Titan and carried through another magnetic environment

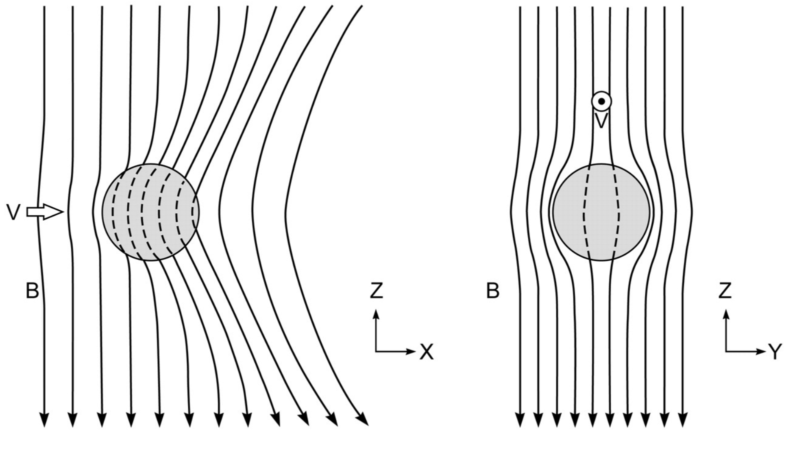

Figure 1.15: Figure from Dougherty et al. (2006) showing the draping of magnetic field lines in the vicinity of a conducting obstacle. Left shows the (X,Z) plane in TIIS co-ordinates at Titan where the plasma flow is along X. Right shows he (Y,Z) plane. The plasma is slowed down by the obstacle, and the field is draped around. Dash lines denote field lines that are moving through the conducting material.

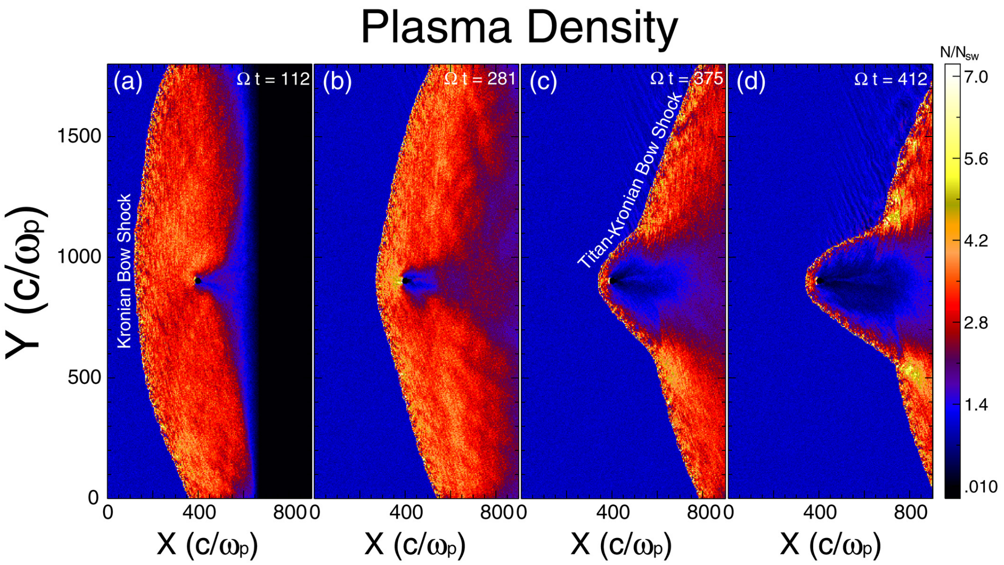

FIGURE 1.16: Figure from Omidi et al. (2017) which shows the single deformed bow shock in the simulation as Titan exits Saturn's magnetosphere.

to then be detected by Cassini at a later time. Bertucci et al. (2008) first noted this magnetic memory of Titan, and that reconnection could be the cause of the removal of fossil fields inside the induced magnetosphere. Feyerabend et al. (2016) shows in simulation that a bundle of differently oriented IMF is captured in Titan's ionosphere and remains there after the solar wind IMF rotates.

However, Titan mainly resides inside Saturn's magnetosphere though this does not mean Titan is in a static system either. As described in section 1.3, Saturn's magnetosphere is home to a current sheet and lobe structure which are both dynamic environments. Titan resides in the equatorial region, however we discussed earlier how the current sheet is pushed into a bowl shape, and as such will cause Titan to be mainly in the southern lobe of Saturn's magnetic field before equinox in 2009 and in the northern lobe post-equinox. The current sheet also flaps with a near planetary rotation rate which will then flap over Titan creating a highly dynamic interaction.

1.5 Flux Ropes

Flux ropes are ubiquitous throughout the solar system; they consist of bundles of magnetic field lines, where the field strength is strongest at the centre where the field is

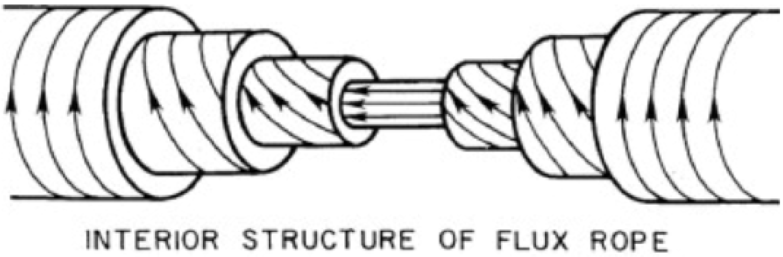

Figure 1.17: Figure from Wei et al. (2010) showing interior structure of a flux rope, modified from Russell and Elphic (1979).

aligned with the axis of the flux rope. As we move away from the centre of the rope the field becomes more helical or azimuthal around the axis of the rope. This design can be seen in figure 1.16, where each layer is cut away and the helical structure can be seen becoming more azimuthal with distance from the flux rope centre. They are common in the Sun's photosphere and corona, and can be attributed to active regions and the release of coronal mass ejections and other explosive solar activity. Additionally, large scale flux ropes are found in the solar wind, named 'magnetic clouds' where these magnetic clouds can interact with each planet's induced or intrinsic magnetosphere. (see Ishibashi and Marubashi, 2004; Romashets and Vandas, 2005; Vandas et al., 2005; Paissan et al., 2005)

Flux ropes are also found in planetary ionospheres such as those at Venus (Russell and Elphic, 1979; Elphic et al., 1980), Mars (Vignes et al., 2004; Briggs et al., 2011) and Titan, as well as on the magnetopauses of planets with intrinsic magnetic fields such as Saturn (e.g. Russell and Elphic, 1978; Jasinski et al., 2016). Mercury's magnetotail is also host to flux rope 'showers' which are a large number of flux ropes that were seen to pass the Messenger spacecraft very quickly and in quick succession, due to the intense and active interaction with the solar wind at such a small distance from the Sun (e.g. Slavin et al., 2009, 2010, 2012; DiBraccio et al., 2015). As flux ropes are found in most plasma environments in the solar system, they are certainly an important feature of the interaction between different plasma environments, different magnetic environments and even interactions with neutral particles, for example, in atmospheres and exospheres.

A number of different mechanisms have been postulated to describe the formation of flux ropes. At Mercury, a strong dependence on flux rope formation and IMF reversals is found, leading to the understanding that flux ropes in the dayside magnetosphere of Mercury are formed through reconnection and then move quickly down tail (e.g. Kidder et al., 2008; Slavin et al., 2009; Leyser et al., 2017). Reconnection is thought to be a possible formation mechanism at Mars also, where the crustal magnetic fields reconnect with the IMF to form flux ropes anchored to the surface fields Beharrell and Wild (2012). However, flux ropes at Mars were also found to be oriented perpendicular to the IMF (Briggs et al., 2011), which is opposed to the findings of random orientation found by Vignes et al. (2004). Additionally, (Briggs et al., 2011) find that there is very little correlation with the crustal fields and flux rope occurrence and occur more frequently when the solar wind has low dynamic pressure.

Other examples of flux ropes are found in the Venus ionosphere, where their formation is thought to be from processes originating from the planet, rather than the solar wind (e.g. Elphic et al., 1980) such as thermal plasma variations, atmospheric waves or velocity shears (Elphic et al., 1981; Luhmann and Elphic, 1985; Luhmann, 1990). Another proposed formation mechanism is discussed in Wei et al. (2010), where the flux ropes are formed at the ionopause and sink into the ionosphere, this also explains the helicity separation, where right-handed flux ropes are found on the dusk flank and left-handed ropes on the dawn flank (if Venus' rotation was not retrograde).

Flux ropes at Titan were first discussed by Wei et al. (2010), where two unusually-large spikes in magnetic field magnitude were found in Cassini magnetometer data. These spikes were found to adequately fit the force-free assumptions and so are considered flux ropes. Additionally, Wei et al. (2011) shows a highly unusual very strong magnetic field spike during the T42 flyby of Titan where the field strength exceeds all known values seen at Titan before. As yet, no statistical study of the flyby data for flux ropes has been attempted.

1.6 Content of This Thesis

In this chapter, a brief overview of the basic plasma concepts and how they help us to understand the different planetary magnetospheres in the solar system is presented.

We have specifically discussed the Saturnian system, with emphasis on the equatorial current sheet. Additionally, we discussed the interaction and environment of Titan in Saturn's magnetic field, and presented a short review of literature on flux ropes in Titan's ionosphere.

This thesis attempts to answer a number of open questions in the Saturn-Titan system, such as:

- What are the non-flapping and non-bowl related movements of the current sheet examined by Arridge et al. (2007)?
- Map the current density in the equatorial region of Saturn in the outer regions and determine the vertical structure of the current density of the current sheet - is the Harris current sheet model a fair assumption at Saturn?
- Does the magnetic environment at Titan hinder or encourage flux rope production and are the flux ropes accurately modelled by force-free assumptions?

There are however numerous open questions regarding the Saturn-Titan interaction and Saturn current sheet dynamics that are yet to be fully explored.

This thesis uses data from the Cassini magnetometer (presented in chapter 2) to form a statistical study of aperiodic waves on Saturn's equatorial current sheet (chapter 3) where both wave parameters and current sheet parameters are resolved by fitting a deformed current sheet model to magnetometer data. This is expanded in chapter 4 where the current sheet parameters are used to determine the current density in the current sheet. In addition, the vertical structure of current density during the aperiodic waves are also probed.

Chapter 5 shows a statistical study of flux ropes in the ionosphere of Titan. The location on Titan and the location of Titan in Saturn's magnetosphere is examined with emphasis on the different types of magnetic environment. In addition, the flux rope magnetometer signatures are fitted to various models of flux ropes and the models are then evaluated for a physical interpretation.

Chapter 2

Instrumentation & Methodologies

2.1 Instrumentation

2.1.1 The Cassini Spacecraft

Cassini launched from Cape Canaveral on 15th October 1997 and, after a number of flybys past Venus, Earth and Jupiter, finally arrived at Saturn and began orbiting on 1st July 2004. Even before orbit insertion, Cassini had tracked storms in the planet's atmosphere and discovered two new moons. The first image of Saturn from Cassini was taken on 21st October 2002 where Cassini was still over 280 million kilometers ($\sim$2 AU) away (Fig. 2.1). Cassini's initial mission was scheduled to end in 2008, but the mission received two extensions until the spacecraft's Grand Finale in 2017. This consisted of 20 ring grazing orbits, a final flyby of Titan and a plunge into the atmosphere of Saturn during which the spacecraft disintegrated. The 13 year long mission includes data from just after winter solstice in the northern hemisphere to equinox in August 2009, and ends on 15th September 2017, just after northern summer solstice. This large temporal range allows for seasonal changes to be tracked along with the diurnal differences and the 11 year solar cycle.

Unlike Galileo at Jupiter, Cassini was not restricted to the equatorial region (however that is the main focus of this thesis) and utilised a number of gravitational assists

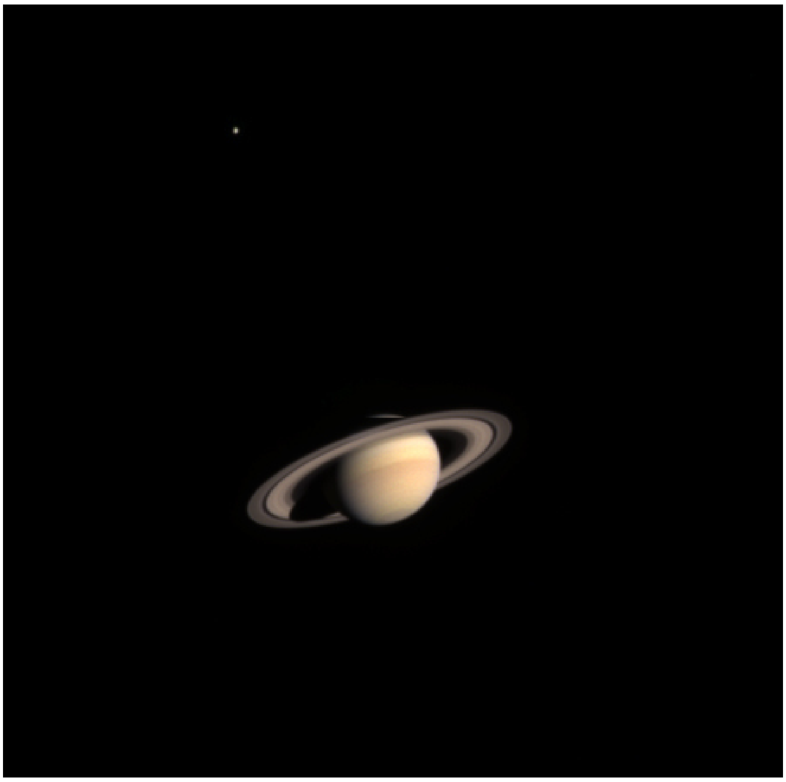

Figure 2.1: Cassini's first image of Saturn with Titan in the top left, Image credit: NASA/JPL/SSI

from Saturn's moons to reduce fuel consumption and allow Cassini to explore the higher latitudes. Figures 2.2 & 2.3 show the whole 13 years of Cassini orbits (called *revs*) split by colour into the three mission stages, Prime, Equinox and Solstice in green, orange and purple respectively. In this thesis, quasi-equatorial orbits are utilised, all of which occur between 2005 and 2012 and so data from all three mission stages is used.

The apoapsis of the equatorial revolutions (*revs*) of Cassini precessed in local time around Saturn during the mission. The dawn equatorial magnetosphere was sampled early in the mission, then, in 2006 Cassini sampled the equatorial magnetotail. Into 2007-2009 the inclination of Cassini's orbits increased to sample the higher latitudes with apokrone in the pre-midnight area. Cassini's apoapsis precessed around to the evening and noon equatorial region between 2010 and 2012. The higher latitudes were once again sampled from 2012 onwards until the final ring-grazing orbits of 2017 where Cassini ends its journey in the atmosphere of Saturn.

Figure 2.4 is a diagram of the Cassini spacecraft and its payload. The payload

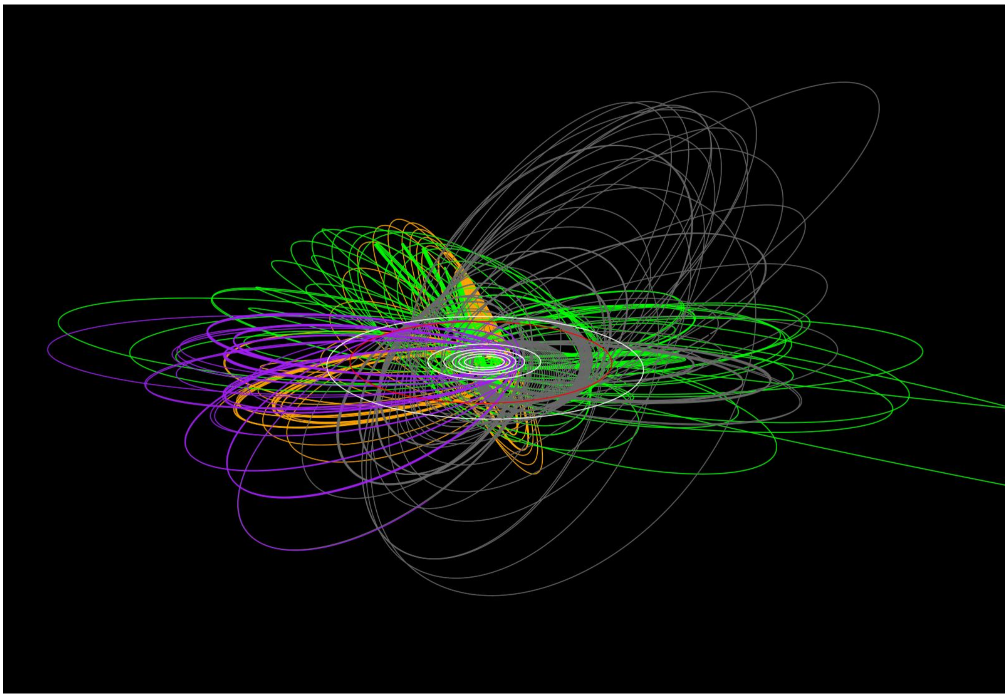

FIGURE 2.2: Diagram of all Cassini orbits seen from above. Green orbits are the Prime Mission (2004-2008), orange orbits are the Equinox Mission (2008-2010), purple orbits are the Solstice Mission (2010-2017). Image credit: NASA/Jet Propulsion Laboratory-Caltech-Erick Sturm.

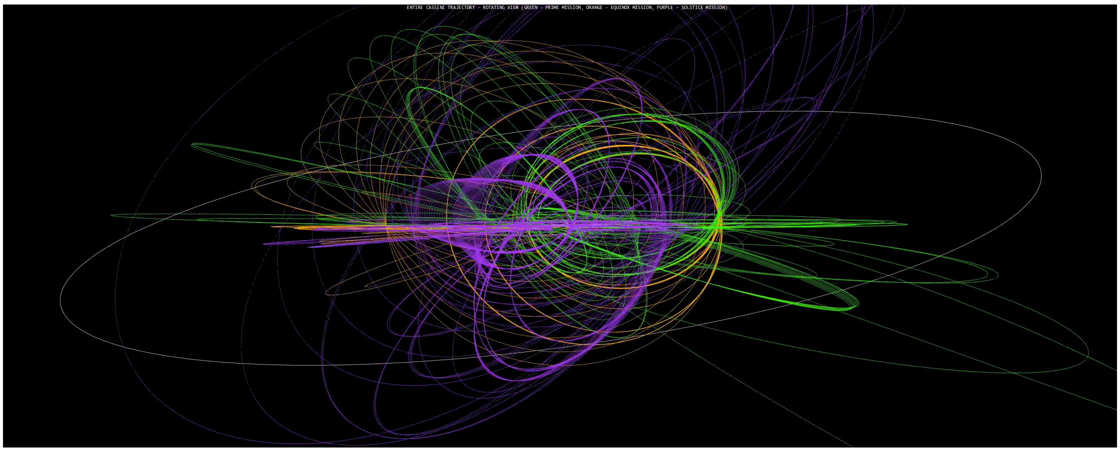

FIGURE 2.3: Diagram of all Cassini orbits seen from the side. Image credit: NASA/Jet Propulsion Laboratory-Caltech -Erick Sturm. Same colour scheme as figure 2.2 applies.

is separated into three categories: optical remote sensing; fields, particles and waves; and microwave remote sensing. The first included imaging science (**I**maging **S**cience **S**ubsystem), and spectrometers in infrared (**V**isible and **I**nfrared **M**apping **S**pectrometer, **C**omposite **I**nfra**R**ed **S**pectrometer), ultraviolet (**U**ltra**V**iolet **I**maging **S**pectrograph) which detailed the Saturn system in the electromagnetic spectrum. The second, and most utilised in this thesis, studied the plasma, dust and magnetic fields in the system. It contains the plasma spectrometer (**CA**ssini **P**lasma **S**pectrometer), cosmic dust analyser (CDA), ion and neutral mass spectrometer (INMS), magnetometer (MAG), magnetospheric imaging instrument (MIMI), and the wave science instrument (**R**adio and **P**lasma **W**ave **S**cience). The final category uses radio waves to probe moons and rings and contains the radar and radio science subsystem (RSS).

Additionally, Cassini also ferried a probe to Titan - the Huygens probe. The Huygens probe was released during an early flyby of Titan and landed on 14th January 2005 and returned, among much data, a photograph of the surface of the furthest planetary body ever to be landed on.

With regards to the magnetosphere, Cassini had a number of initial science objectives (summarised from Russell, 2013) that the mission hoped to achieve, these included but are not limited to:

1. Determining, through neutral and plasma monitoring in the magnetosphere, the global configuration and dynamics of the plasma population - including study of the ring current, neutral clouds and radiation belts.
2. Studying sources of plasmas.
3. Determining if Saturn, like Earth, experiences substorm magnetic activity.
4. Understanding how the moons interact with the magnetosphere.
5. Understanding how this magnetospheric interaction alters the moons' atmospheres and surfaces including absorption of energetic ions and electrons.
6. Describing the interaction of the rings, specifically the possibility of a plasma sink.
7. Describing the coupling of the magnetosphere and ionosphere through study of the aurora and remote sensing.

This thesis focusses on points 1, 4 and 5 using the magnetometer data, however the majority of points come into play and are linked when describing the system as a whole.

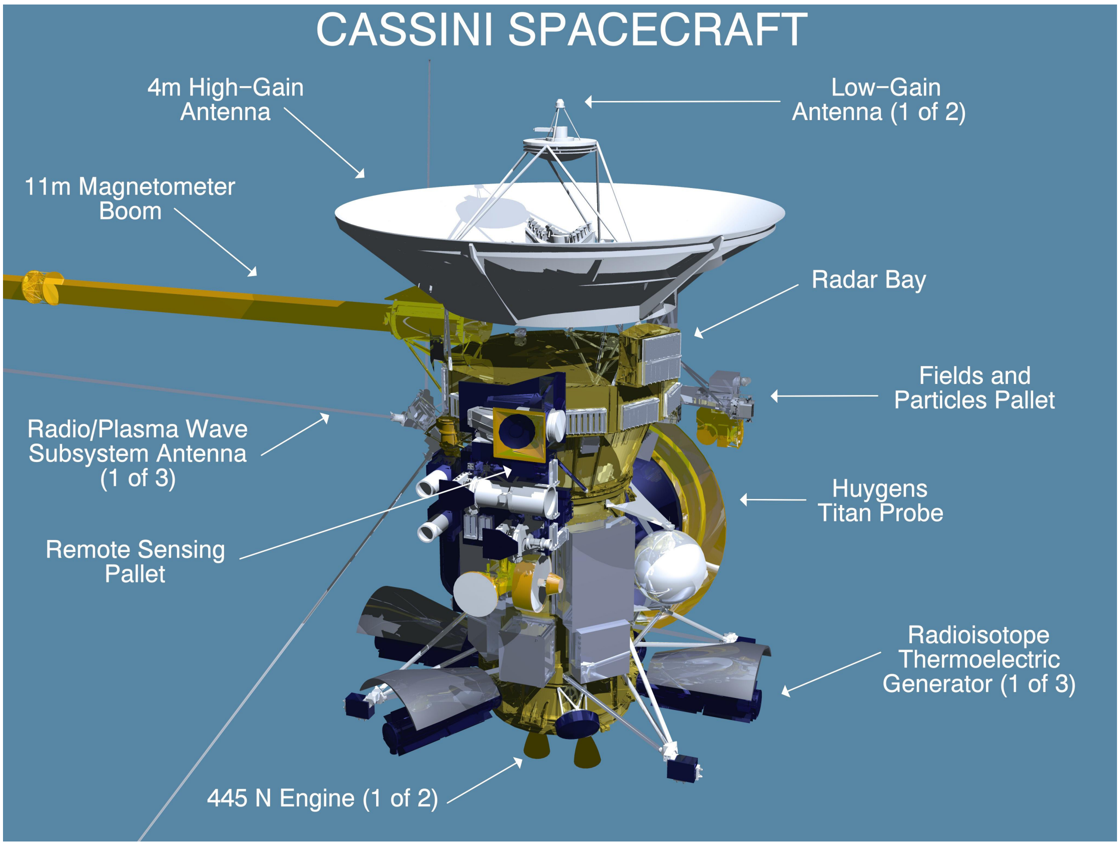

Figure 2.4: Diagram of Cassini's payload, Image credit: NASA/JPL

2.1.2 Magnetometer

Cassini's magnetometer initially began as a dual-technique magnetometer with a vector helium magnetometer and a fluxgate magnetometer, placed at different distances along the magnetometer boom. This dual system would allow for inter-sensor calibration, be able to characterise the space-craft's own magnetic field, and improve reliability. However, the vector helium magnetometer failed early in the mission so the focus here will be on the fluxgate magnetometer and its workings.

Fluxgate magnetometers were originally invented to detect submerged submarines prior to World War Two [Aschenbrenner and Goubau (1936), Geyger (1964) & Primdahl (1979)], and is so named in that the sensor itself 'gates' the magnetic flux. This style of magnetometer is commonly used in space-based magnetometry as it is a low-power, reliable and is operable in a large temperature range as well as radiation environments

(Acuna, 2002). Specifically useful for giant planet magnetospheres, fluxgate magnetometers can operate over a very large dynamic range of magnetic field and as such have been used for the Voyager and Pioneer missions along with a number of Earth-based spacecraft to describe Earth's magnetosphere [e.g. Acuna and Ness (1973), Behannon et al. (1977), Kivelson et al. (1992), & Balogh et al. (1997)].

The flux-gate magnetometer on Cassini was situated in the middle of the 11 meter boom shown in figure 2.4. The magnetometer itself is three single-axis ring core fluxgate sensors arranged orthogonally to characterise the three-dimensional field. Each ring core is made of a highly permeable material and around each ring core are wound two coils. The first is a drive coil which generates a magnetic field that saturates the core. This magnetic field is modulated by a square wave to saturate the ring core, then the polarity changes and the drive coil saturates the core in the opposite direction, this happens at 15 kHz.

The second coil is a sensor coil that senses changes in the symmetry of the saturation of the ring core as an increased/decreased voltage. An asymmetry in the saturation will be proportional to the ambient magnetic field that is parallel to the core. Hence having three orthogonal set-ups, a three-dimensional magnetic field can be resolved [Acuna (2002) & Dougherty et al. (2004)]. Figure 2.5 shows the flux gate magnetometer (white) with it's cover (silver) taken off and corresponding electronics board.

The initial science objectives of Cassini's magnetometer (Dougherty et al., 2004) were to study:

1. The internal magnetic field of Saturn.
2. Saturn's magnetosphere in three-dimensions.
3. Titan's magnetic state and environment.
4. Ring and dust interactions.
5. Icy satellite interactions.
6. Structure and dynamics of the magnetotail.

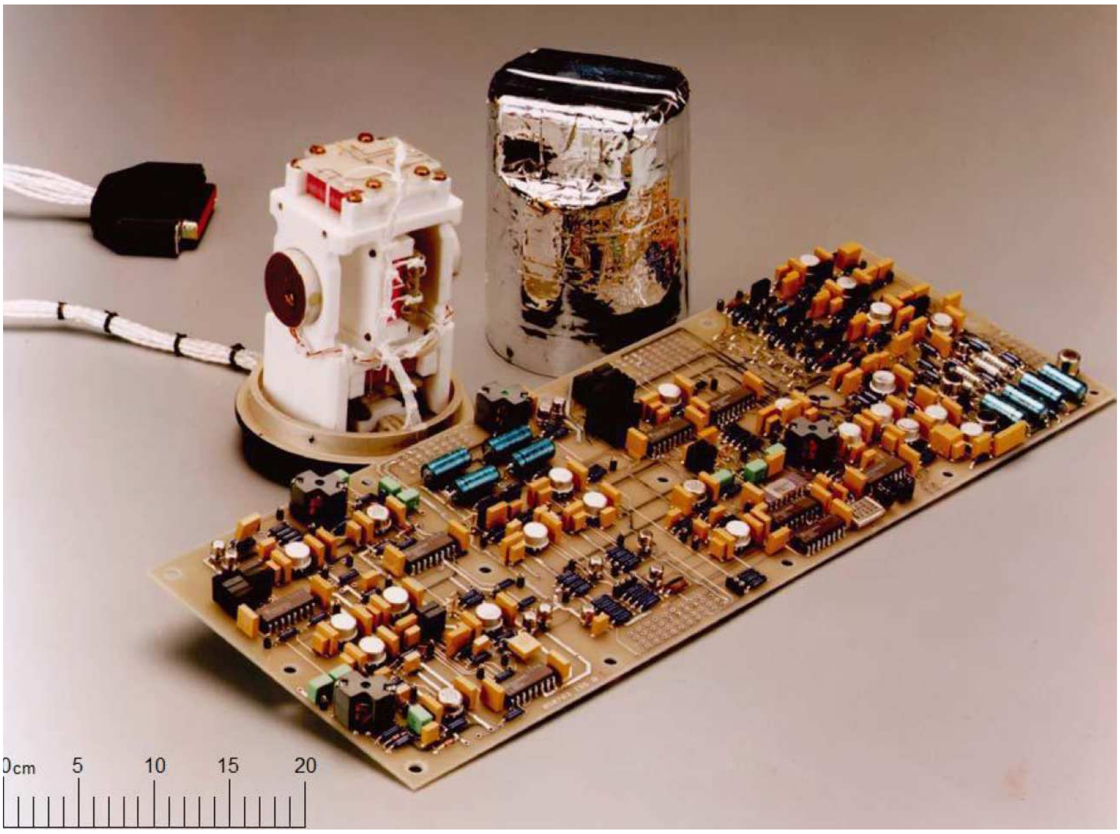

FIGURE 2.5: Photograph of Cassini's magnetometer, (Dougherty et al., 2004)

In this thesis we address points 2,3 and 6.

2.2 Methodologies

A number of methods are utilised in more than one chapter and hence will be described in general terms below. Specific uses and modifications are described within each chapter.

2.2.1 General Deformation Method for Magnetic Fields

This section follows the method laid out in Tsyganenko (1998), hereby referred to as TSY98, and is based on Euler potentials and was initially used to model Earth's dipole tilt (Stern, 1987). Outlined in this section is a general method of deformation for any orthogonal coordinate system, which will be applied in chapters 3 & 5.

The general method of deforming a magnetic field model is based on the idea that the magnetic field $\boldsymbol{B}(f,g,h)$ is represented by two Euler potentials, α and β. The coordinates f, g and h are coordinates in an orthogonal system; $\boldsymbol{e}_f$, $\boldsymbol{e}_g$ and $\boldsymbol{e}_h$ are the unit vectors and S_f, S_g, and S_h are the scale factors for the chosen coordinate system. This method of deforming a magnetic field is preferably used as the Euler potentials required for the transformation do not need to be known, and the field found after the deformation remains divergence free.

$$\boldsymbol{B}(f,g,h) = \bigtriangledown\alpha(f,g,h) \times \bigtriangledown\beta(f,g,h) \tag{2.1}$$

The gradient of the two Euler potentials can be expressed as follows:

$$\bigtriangledown\,\alpha = \frac{1}{S_f}\frac{\partial\alpha}{\partial f}\boldsymbol{e}_f + \frac{1}{S_g}\frac{\partial\alpha}{\partial g}\boldsymbol{e}_g + \frac{1}{S_h}\frac{\partial\alpha}{\partial h}\boldsymbol{e}_h \tag{2.2}$$

$$\bigtriangledown\,\beta = \frac{1}{S_f}\frac{\partial\beta}{\partial f}\boldsymbol{e}_f + \frac{1}{S_g}\frac{\partial\beta}{\partial g}\boldsymbol{e}_g + \frac{1}{S_h}\frac{\partial\beta}{\partial h}\boldsymbol{e}_h \tag{2.3}$$

The undistorted field components are then given by:

$$B_f = \frac{1}{S_g S_h}\left(\frac{\partial\alpha}{\partial g}\frac{\partial\beta}{\partial h} - \frac{\partial\beta}{\partial g}\frac{\partial\alpha}{\partial h}\right) \tag{2.4}$$

$$B_g = \frac{1}{S_f S_h}\left(\frac{\partial\alpha}{\partial h}\frac{\partial\beta}{\partial f} - \frac{\partial\beta}{\partial h}\frac{\partial\alpha}{\partial f}\right) \tag{2.5}$$

$$B_h = \frac{1}{S_f S_g}\left(\frac{\partial\alpha}{\partial f}\frac{\partial\beta}{\partial g} - \frac{\partial\beta}{\partial f}\frac{\partial\alpha}{\partial g}\right) \tag{2.6}$$

A new coordinate system is defined where the original coordinates described above are deformed and replaced with the coordinates (i,j,k) where it is known that each coordinate is a function of the old coordinates. The new deformed magnetic field reads as:

$$\boldsymbol{B}'(f,g,h) = \bigtriangledown\alpha(i,j,k) \times \bigtriangledown\beta(i,j,k) \tag{2.7}$$

To find the components of magnetic field in the original coordinate system (f,g,h), the partial derivatives in equations 2.4 - 2.6 can be expanded with the new coordinates using the differential chain rule. For example, the first partial differential reads:

$$\frac{\partial \alpha}{\partial f} = \frac{\partial \alpha}{\partial i}\frac{\partial i}{\partial f} + \frac{\partial \alpha}{\partial j}\frac{\partial j}{\partial f} + \frac{\partial \alpha}{\partial k}\frac{\partial k}{\partial f} \tag{2.8}$$

Written in matrix form for simplicity, the expansions from the partial derivatives can be condensed into:

$$\boldsymbol{B}' = \hat{\boldsymbol{T}}\boldsymbol{B}^{*}, \tag{2.9}$$

where the asterisk denotes the undeformed magnetic field evaluated in the deformed coordinate system. $\boldsymbol{B}'$ is the desired magnetic field in the new coordinate system. The elements of $\hat{\boldsymbol{T}}$ read as follows:

$$T_{ff} = \frac{S_g^* S_h^*}{S_g S_h}\left(\frac{\partial j}{\partial g}\frac{\partial k}{\partial h} - \frac{\partial j}{\partial h}\frac{\partial k}{\partial g}\right), \tag{2.10}$$

$$T_{fg} = \frac{S_f^* S_h^*}{S_g S_h}\left(\frac{\partial i}{\partial h}\frac{\partial k}{\partial g} - \frac{\partial i}{\partial g}\frac{\partial k}{\partial h}\right), \tag{2.11}$$

$$T_{fh} = \frac{S_f^* S_g^*}{S_g S_h}\left(\frac{\partial i}{\partial g}\frac{\partial j}{\partial h} - \frac{\partial i}{\partial h}\frac{\partial j}{\partial g}\right), \tag{2.12}$$

$$T_{gf} = \frac{S_g^* S_h^*}{S_f S_h}\left(\frac{\partial j}{\partial h}\frac{\partial k}{\partial f} - \frac{\partial j}{\partial f}\frac{\partial k}{\partial h}\right), \tag{2.13}$$

$$T_{gg} = \frac{S_f^* S_h^*}{S_f S_h}\left(\frac{\partial i}{\partial f}\frac{\partial k}{\partial h} - \frac{\partial i}{\partial h}\frac{\partial k}{\partial f}\right), \tag{2.14}$$

$$T_{gh} = \frac{S_f^* S_g^*}{S_f S_h}\left(\frac{\partial i}{\partial h}\frac{\partial j}{\partial f} - \frac{\partial i}{\partial f}\frac{\partial j}{\partial h}\right), \tag{2.15}$$

$$T_{hf} = \frac{S_g^* S_h^*}{S_f S_g}\left(\frac{\partial j}{\partial f}\frac{\partial k}{\partial g} - \frac{\partial j}{\partial g}\frac{\partial k}{\partial f}\right), \tag{2.16}$$

$$T_{hg} = \frac{S_f^* S_h^*}{S_f S_g}\left(\frac{\partial i}{\partial g}\frac{\partial k}{\partial f} - \frac{\partial i}{\partial f}\frac{\partial k}{\partial g}\right), \tag{2.17}$$

$$T_{hh} = \frac{S_f^* S_g^*}{S_f S_g}\left(\frac{\partial i}{\partial f}\frac{\partial j}{\partial g} - \frac{\partial i}{\partial g}\frac{\partial j}{\partial f}\right), \tag{2.18}$$

where the asterisk denotes that the scale factor is found in the deformed coordinate system (i, j, k).

2.2.2 Minimum Variance Analysis

In minimum variance analysis (MVA), the normal of a boundary layer can be found from the direction in which the magnetic field varies the least. This method was first employed by Sonnerup and Cahill (1967) to find the normal to a current sheet layer using a single spacecraft. When calculating the minimum variance direction, the intermediate and maximum variance direction are also calculated as eigenvectors $\boldsymbol{x_3}$, $\boldsymbol{x_2}$ and $\boldsymbol{x_1}$ respectively. This method assumes that the orientation of the boundary layer does not change during the encounter.

Minimum variance analysis in this section is used on the magnetic field measurements during an encounter with the current sheet. This means many magnetic field vectors measured can be used in the analysis. To find the minimum or maximum variance direction, the magnetic variance matrix must be constructed.

$$\boldsymbol{M}^B_{\mu\nu} = \langle B_\mu B_\nu \rangle - \langle B_\mu \rangle \langle B_\nu \rangle, \tag{2.19}$$

where μ and ν are the coordinate components (i.e. X,Y and Z in Cartesian). The eigenvectors for each of the variance directions, $\boldsymbol{x_1}$, $\boldsymbol{x_2}$ and $\boldsymbol{x_3}$, corresponding to the maximum, intermediate and minimum variance directions respectively are found by solving $\boldsymbol{Mx} = \lambda \boldsymbol{x}$. The matrix is symmetric so the eigenvalues are real numbers, λ_1, λ_2 and λ_3. These values represent the variance in the field in the corresponding vector direction and can be used to determine the validity of the analysis.

For example, the three eigenvalues and eigenvectors form an ellipsoid in variance space, shown in figure 2.6a. When this ellipsoid is 'sausage' shaped, this can mean that two eigenvalues (λ_2 and λ_3) are much smaller than the maximum direction λ_1, and as such the minimum direction cannot be determined. This means $\lambda_1 \gg \lambda_2 \approx \lambda_3$ and so the maximum variance direction is well defined, but the intermediate and minimum directions are not (figure 2.6b). Other cases include: when $\lambda_1 \approx \lambda_2 \approx \lambda_3$ meaning that none of the variance directions are well defined, the ellipsoid is a sphere and the variance matrix is degenerate (figure 2.6c); where $\lambda_1 \approx \lambda_2 \gg \lambda_3$, this shows that the minimum variance direction is well defined but the maximum and intermediate are not, this is a pancake shape (figure 2.6d).

Uncertainties in the minimum variance analysis are estimated by the process of bootstrapping. Bootstrapping with MVA is a method where a large number or samples are taken from the original magnetic field data at random with replacement. Each of these samples is then run through the MVA function, and this gives a distribution of the directions of the different variances. The statistics of this distribution can describe the uncertainties expected for MVA. Commonly, the standard deviation is used as an estimate for the uncertainty of using this method.

2.2.3 Least Squares Fitting Methods

References to a least squares fitting procedure in this thesis refer to the mathematical procedure of fitting a model curve/line to a set of data by reducing the sum of the squares of the offsets of the data to the model curve. In non-linear models, such as those described further in following chapters, this process is extended to solving a number of unknown parameters n with a known function f(x) and a set of equations which number $n + 1$. A non-linear function is defined as a model that is nonlinear in the coefficients (or a combination of linear and nonlinear). As a nonlinear fitting requires more than a simple matrix solution, like a linear fit does, an iterative fitting procedure with initial estimates is required to solve the fitting.

There are a number of optimised iterative algorithms for this process, all based from the original Newton algorithm which is a method of finding the roots or minimum of a function that is twice differentiable. The Gauss-Newton algorithm is an advance on this to minimise the sum of squares. The Gauss-Newton algorithm uses the assumption that the function is locally a quadratic equation and finds the χ^2 minimum. Another method, the gradient-descent method, calculates the steepest descent in the function to determine the best fit (Seber and Wild, 2003).

In this thesis, the Levenberg-Marquardt algorithm is used as it is a combination of the previous two and is considered the most robust, effective and efficient algorithm

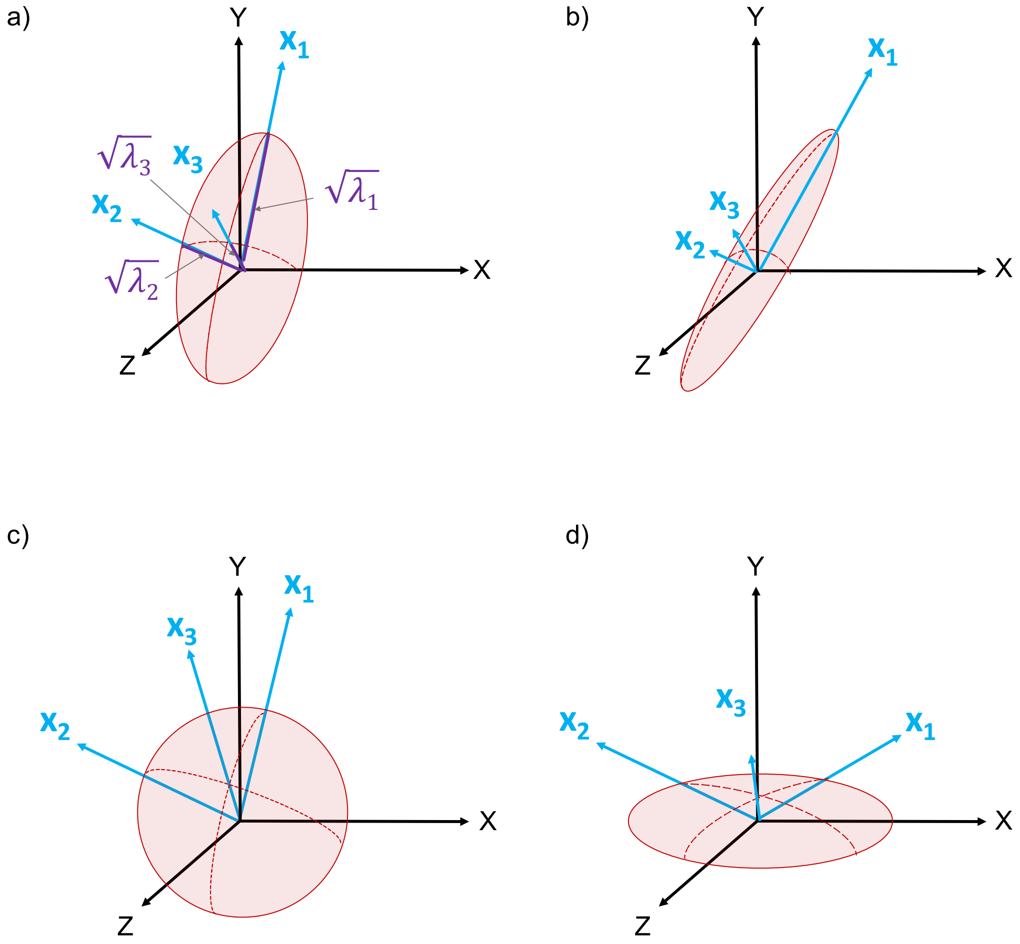

FIGURE 2.6: Figure showing the different set up for variance ellipsoids. a) a typical variance ellipsoid, b) a 'sausage' ellipsoid, c) a spherical ellipsoid and d) a 'pancake' ellipsoid. Modified from Sonnerup and Scheible (1998).

for nonlinear fitting in that it uses each previous method dependent on how close to the optimal value of parameters the algorithm is [Seber and Wild (2003), Levenberg (1944), Marquardt (1963), Press et al. (1989)]. Uncertainties of the optimal parameters using the Levenberg-Marquardt algorithm are determined by using the Jacobian matrix calculated in the fitting process, where the roots of the diagonal elements are the estimated uncertainties of the corresponding parameters. Alternatively, bootstrapping can be used to confirm or independently calculate the uncertainties as the Jacobian matrix gives only *estimated* uncertainty values [Press et al. (1989), Ridler and Salter (2002)].

The Jacobian matrix is calculated during the fitting procedure, and is formed of first order partial derivatives of the function with the updated parameters and hence gives the best linear approximation of the function near a point. In other words, the Jacobian describes the gradient of a function in multiple variable space, as this is calculated at each step of the fitting process it describes the local environment of the function.

Ultimately, this process returns the optimised parameters of the fit which are then used to gain further understanding of the science behind the data fitted (Kaplan, 1952). Non-linear least squares fitting can have a number of local minima which the fitting algorithms will converge to, depending on the initial estimates, therefore the best available estimates must be used to equip the algorithm with the best start. This is not always possible, however, a coarse view of the parameter space can be explored by selecting various initial parameters to make certain the global minimum of χ^2 is reached. Additionally, one can view the χ^2 parameter space by plotting the value of χ^2 for a range of values for two parameters (see figure 3.9 for example) which can also help determine if the global minimum is where the algorithm settles.

2.2.4 Bayesian Inference

The basis for Bayesian statistics is Bayes' theorem:

$$P(A|B) = \frac{P(B|A)P(A)}{P(B)}, \tag{2.20}$$

where $P(A|B)$ is a conditional probability of the likelihood of event A occurring given event B, as such $P(B|A)$ is the conditional probability of the likelihood of B occurring given A. $P(A)$ and $P(B)$ are the individual probabilities of observing events A or B independently. $P(A)$ is considered the *prior* probability, so what is already known about A. $P(B|A)$ is considered the *likelihood* function, which is the the probability given the observed data. $P(A|B)$ is therefore the *posterior* probability which is the unknown probability that is desired. $P(B)$ is a marginal likelihood which is the same value for any event and as such is considered a constant for the purposes of this thesis (Lee, 2012).

A simplified example of this is as follows, I want to know whether I should ride my bike into work today to write there, or write my thesis from home. This action is entirely dependent on the weather, event B is that it rains. The Met office gives me a *likelihood* of 80% that it will be dry for the day, so my $P(dry|correct)$ (probability that it is dry given the Met office is right) is 0.8. Hence, event A is the Met office being right about the rain. However, I live in Lancaster in the North-West of England and I know that the weather here is temperamental, especially going into storm season. I know the Met office is right only 60% of the time due to the changing winds. So my *prior* $P(correct)$ probability is 0.6. As both are already normalised there is no need to determine $P(dry)$. So, the *posterior* probability $P(correct|dry)$ (the Met office is right and it stays dry), is 0.8×0.6 which is 0.48, only 48% chance it will be dry. This means that it is 52% likely to rain, and that's enough to convince me to stay home and write today.

Using Bayesian inference as a fitting technique uses the same logic, but instead of events there are probability density functions for each fitted parameter. A posterior distribution is a superposition of a prior distribution and the distribution formed from a likelihood function. The prior distributions are set up with known factors, and can be any function but commonly are normal, uniform or bimodal distributions. A set number of samples are taken from the prior distributions and put into the model that is attempting to be fitted to the data. Each of these samples is then compared to the data to give a fit indication parameter, such as χ^2 or mean squared error (MSE). The likelihood function then works to reduce the fit parameter to give only the best fits, in this case the likelihood selects only the samples from the distribution that fall below an acceptable fit level, i.e. $\chi^2 < 5$. The parameters corresponding to the samples that give an acceptable level of fit are combined to give a posterior distribution (Box and Tiao, 2011).

Each posterior distribution corresponds to a parameter that was fitted. Ideally a normal-like posterior distribution is found and the peak of this distribution is equivalent to a best fit value for that parameter. Uncertainties can be estimated using a credible interval, which is where, for example, 30% - 60% of the data resides inside the credible interval, equivalent to standard deviation of a normal distribution and the value needed inside the credible interval is dependent on the user (Martz, 2014).

Bayesian inference is a powerful tool in fitting procedures as it allows a much deeper analysis of the posterior distribution and what it means for the data than a least squares fitting. However, this comes at a price of computational time and complexity and as such a mixture of the two fitting procedures are used in this thesis where appropriate. It is noted that the selection of prior distributions is similar to the selection of initial parameters used in least squares fitting, but the distributions used as priors in the Bayesian method are much more effective for locating local minima and will find all minima not just 'the nearest one' and as such gives much improved representations of the parameter space.

Chapter 3

Aperiodic Waves on Saturn's Current Sheet

3.1 Introduction

There are a number of dynamic processes that can cause Saturn's equatorial current sheet to be displaced from the rotational equator. The seasonal bowl shape (Arridge et al., 2008b) causes the sheet to flap with a period of 29.46 years into a upwards bowl shape during southern summer and a downwards bowl shape in northern summer due to the dynamic pressure of the solar wind. Additionally, the current sheet also flaps with a shorter $\sim$10.7 hour period due to planetary period oscillations (PPO) which cause the sheet to move up and down during one period [e.g. Arridge et al. (2011) & Provan et al. (2012)]. This effect also causes a thickening and thinning effect due to the independent PPO systems of the northern and southern hemispheres (Thomsen et al., 2017).

In addition to these periodic displacements, and the focus for this chapter, solitary waves of aperiodic nature are also observed. An aperiodic wave is defined as a single transverse waveform, where the motion of the wave is at right-angles to the propagation direction, upon the equatorial current sheet of Saturn that causes the current sheet to move up or down away from its original position as the wave travels along it. The waves are detected by their distinctive characteristics in Cassini MAG data. Aperiodic waves have a smaller duration than the global flapping waves (1-30 minutes), they do not repeat and show a magnetic field deflection of over 1 nT. Each event is found inside of the magnetopause position, which is determined by examination of magnetic field data. To detect these waves, they must have sufficient amplitude to move the current sheet to Cassini. This means Cassini travels through the current sheet twice during each event, hence these waves were originally coined current sheet encounters (Arridge et al., 2007).

First detected at Saturn by Smith et al. (1980) using Pioneer 11 magnetometer data, these waves are also found in Earths magnetotail [e.g., Sergeev et al. (2004)] and on Jupiter's magnetodisc [e.g., Russell et al. (1999)]. Cassini's varied spatial coverage and orbital trajectory give a unique opportunity for statistically studying these aperiodic waves in detail. Arridge et al. (2007) originally use these transient features to explore the stress balance in the magnetodisc of Saturn, but the origins and properties of the events remained unknown.

In the magnetodisc configuration, Saturn's magnetic field is stretched radially leading to the major contribution of the magnetic field being in the radial direction, hence the magnetic field components at Saturn are presented in KRTP coordinates, discussed fully in section A.1. Saturn's magnetospheric configuration was explored in chapter 1 where the swept back and swept forward regime is described.

Small-amplitude fluctuations and periodicities such as ion cyclotron waves (Leisner et al., 2006), mirror mode waves (Russell et al., 2006) and ultra-low frequency waves are also found at Saturn (Kleindienst et al., 2009) and in Jupiter's magnetosphere (Khurana and Kivelson, 1989*b*). Field aligned resonances are discussed by Mitchell et al. (2016), Palmaerts et al. (2016) & Yates et al. (2016) where quasi-periodic waves connect auroral observations with particle and magnetic field data. These waves have periodicities of around an hour and appear in magnetometer data with similar signatures to aperiodic waves, however this study solely focuses on singular and non-repeating waves.

Additionally, some aperiodic waves may also be included within the studies of von Papen et al. (2014) & von Papen and Saur (2016), where all fluctuations of the magnetic field are studied. The authors measure fluctuations within 10 minutes bins in Saturn's inner and middle magnetosphere, where the spatial range overlaps with the

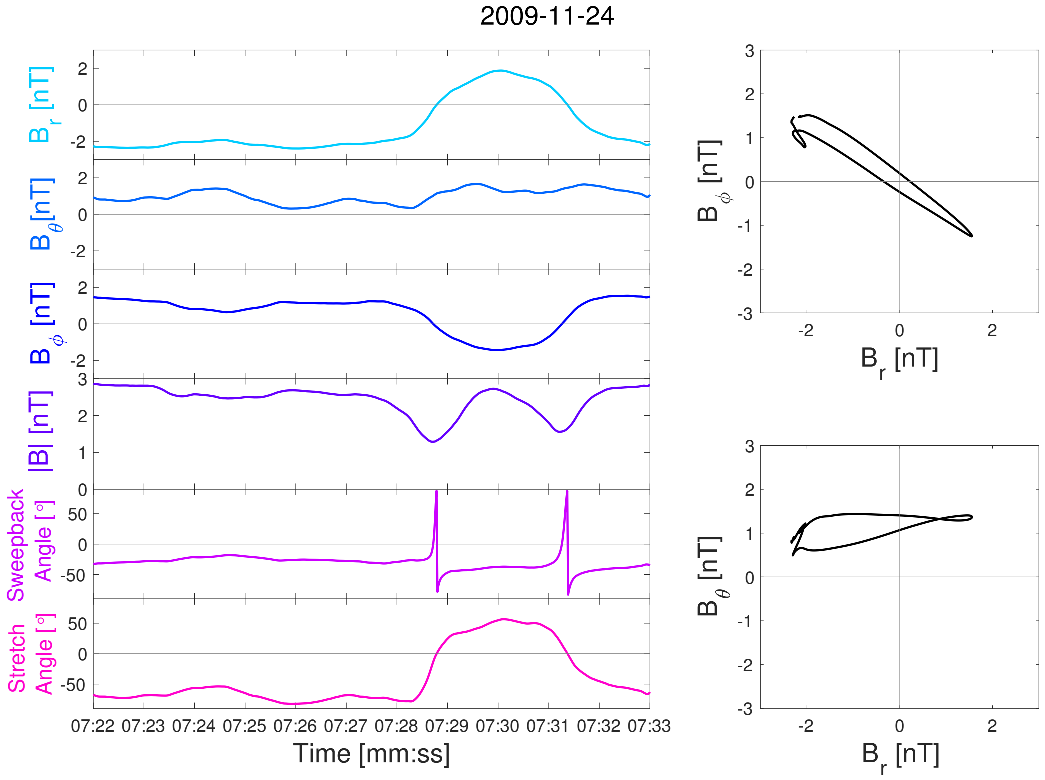

FIGURE 3.1: Figure showing an example of 1 Hz magnetometer data during the passage of an aperiodic wave when Cassini was at 18 SLT and 28 R_S. KRTP components are shown with the total magnetic field, the sweepback angle ($\tan^{-1}\left(\frac{B_\phi}{B_r}\right)$), stretch angle ($\tan^{-1}\left(\frac{B_r}{B_\theta}\right)$) as well as two hodograms showing the common relationships between the components.

spatial range of this study, it is possible that these studies includes the aperiodic waves in their analysis.

With this in consideration, traversing the current sheet during the passage of an aperiodic wave means leaving one lobe regime and entering the other. An example of an aperiodic wave is shown in figure 3.1, Cassini is initially located in the southern lobe of Saturn at 28 R_S and 18 SLT, where the magnetic field of Saturn is pointing radially towards the planet. A negative B_r component and a positive B_ϕ due to the swept back feature of magnetic field is shown, this feature was described previously in section 1. The magnitude then drops as B_r and B_ϕ decrease towards zero as Cassini reaches the current sheet's centre.

Cassini then continues on to the northern lobe where the opposite regime occurs, the magnitude increases as B_r becomes positive and B_ϕ now becomes negative. Throughout the entire encounter, B_ϕ varies in anti-phase with B_r this relationship can be seen in the hodogram of B_r and B_ϕ where a quasi-linear relationship between the two components is seen.

Additionally, the sweepback and stretch angles are included in the bottom two plots, sweepback angle is calculated using $\tan^{-1}\left(\frac{B_\phi}{B_r}\right)$ and shows the direction and magnitude of how swept forward or swept backwards the field is. In the example, the sweepback angle is negative, showing a swept backwards arrangements. The stretch angle is given by $\tan^{-1}\left(\frac{B_r}{B_\theta}\right)$ and describes how stretched the magnetic field is along the radial direction, if the stretch angle is near zero, this means the field has a mainly dipolar appearance, whereas if, like in the example, the stretch angle is large in magnitude, the field is stretched out into the 'washer' shape.

3.2 Distribution of Aperiodic Waves

During Cassini's tour, equatorial orbits where Cassini is less than 10 R_S from the rotational equator are used to show the distribution of aperiodic waves, these revolutions are shown in figure 3.2 and span the years 2005-2012. The figure shows that all local times are sampled. The position of all aperiodic waves found are shown in figure 3.3.

Dwell time of Cassini is calculated for each hour of SLT and each 1 R_S. Figures 3.4 & 3.5 show the distribution of current sheet encounters in SLT and R_S normalised to the dwell time of Cassini in each bin. The histograms show that the majority of encounters occur from $15R_S$ to $50R_S$ with a peak at $20R_S$, near the orbit of Titan. Very few encounters occur below $15R_S$, this is due to the magnetic field of Saturn being more dipolar, so a clear current sheet may not form. The distribution of current sheet encounters in SLT seems to be fairly even. The SLT bin of 5-6 SLT appears to have a large number of encounters, these encounters all occur within 5 Rs of Titan's orbit. The large number of encounters from 1-2SLT are due to a sampling inconsistency in one orbit of the tail, where one leg of the orbit occurs entirely within one SLT bin.

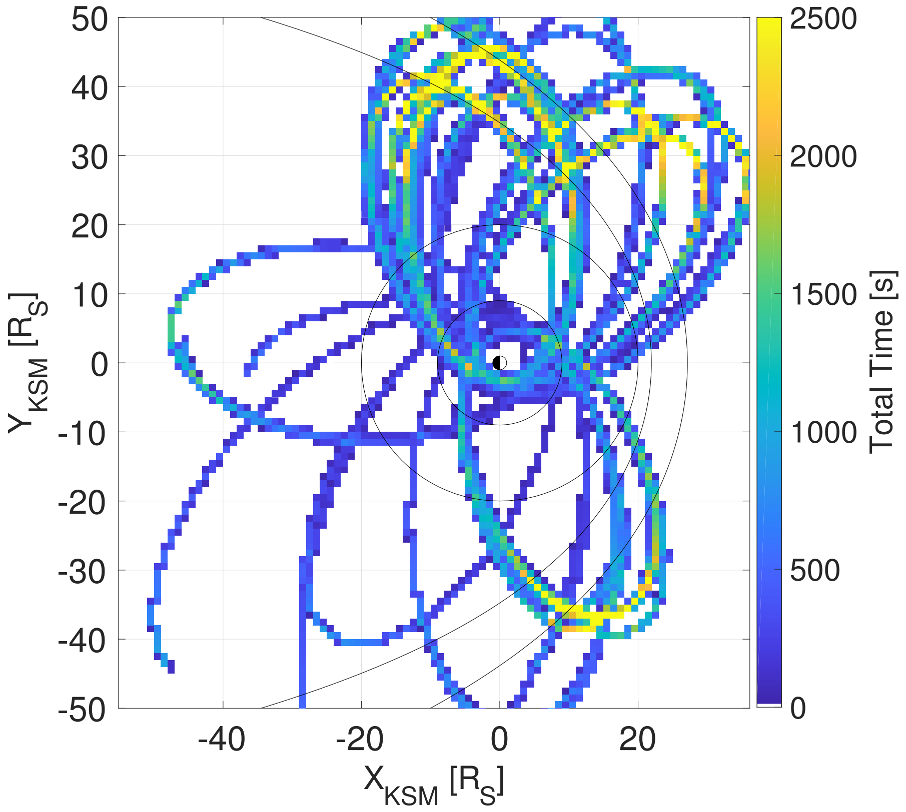

FIGURE 3.2: Trajectories of Cassini's equatorial revolutions around Saturn between 2005-2012, coloured by time spent in each bin, of size 1 R_S by 1 R_S, in seconds, projected onto the X-Y KSM plane. Overlaid are the orbits of Rhea (9 R_S) and Titan (20 R_S) along with a range of magnetopause positions calculated from Arridge et al. (2006) which reflect a dynamic pressure range of 0.0012-0.0300 nPa.

Some sampling biases still persist after normalisation, but meaningful conclusions on the spatial distributions of current sheet encounters are still possible. It is also important to recognise that this analysis occurred over many years of Cassini orbits and so temporal as well as spatial differences are visible.

The bowl shaped current sheet (Arridge et al., 2008b), also acts to move the current sheet away from the equator, and so if Cassini is at the equator, but the planet is tilted as in Northern summer the current sheet can be pushed down by a distance of a few Saturn radii, meaning that even though Cassini's orbit was near-equatorial, there may not be any encounters of the current sheet as it was located too far away.

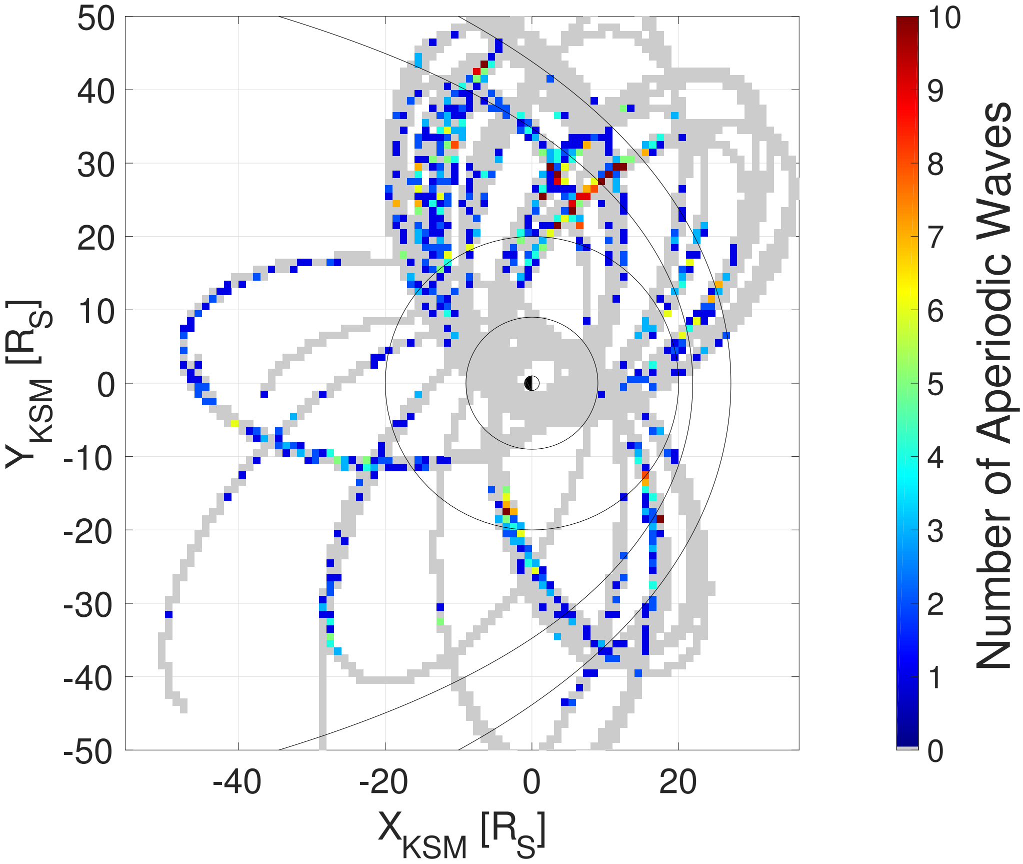

Figure 3.3: Number of events found in each $1R_S$ by $1R_S$ sized bin projected onto the X-Y KSM plane. Grey are areas visited by Cassini that had no aperiodic wave signatures. Overlaid are the orbits of Rhea (9 R_S) and Titan (20 R_S) along with a range of magnetopause positions calculated from Arridge et al. (2006) which reflect a dynamic pressure range of 0.0012-0.0300 nPa.

3.3 Modelling the Current Sheet

3.3.1 Harris Current Sheet

To model the magnetic field of a thin current sheet, a Harris current sheet model is utilised in the radial component to model the different magnetic field regimes above and below the current sheet (Harris, 1962). In the azimuthal direction, the swept backwards field can also be modelled using a Harris current sheet, however to model the direction of the swept field lines a positive hyperbolic tangent can be used for the swept forward fields and a negative one for the swept backwards fields where the sign is included within

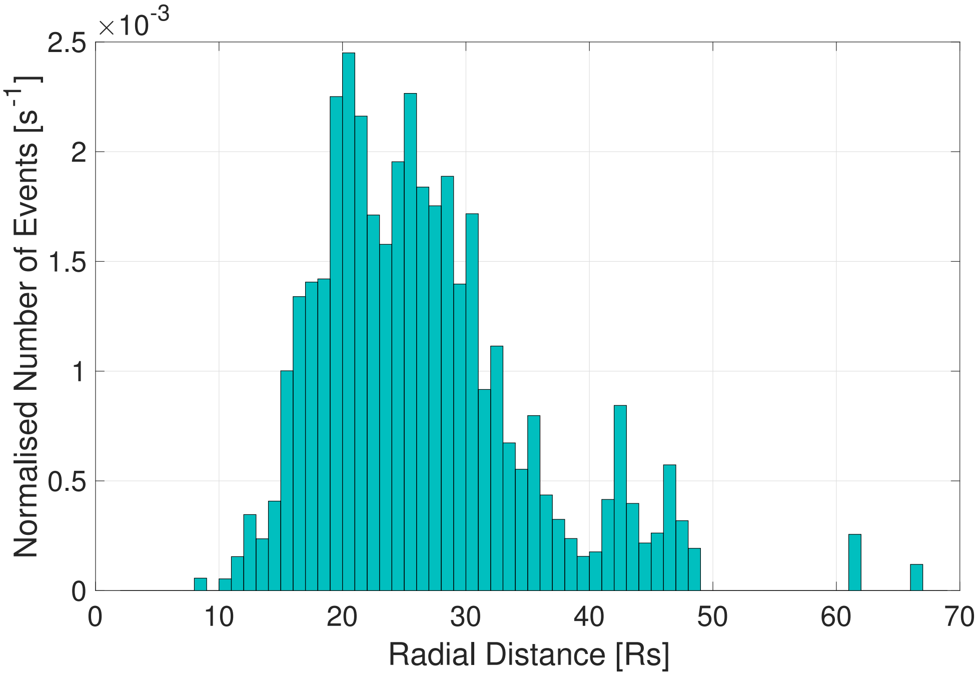

FIGURE 3.4: Radial distribution of current sheet encounters normalised to the number of seconds spent in each 1 R_S bin by Cassini.

the B_{y0} constant. To complete a three dimensional model of the local magnetic field at the current sheet, the third dimension, $\hat{\boldsymbol{z}}$, is modelled at a constant value. As this is a local model, a Cartesian co-ordinate system relative to the directions of the cylindrical system is used in the Harris current sheet model. $\hat{\boldsymbol{x}}$ is in the radial direction, $\hat{\boldsymbol{y}}$ is in the

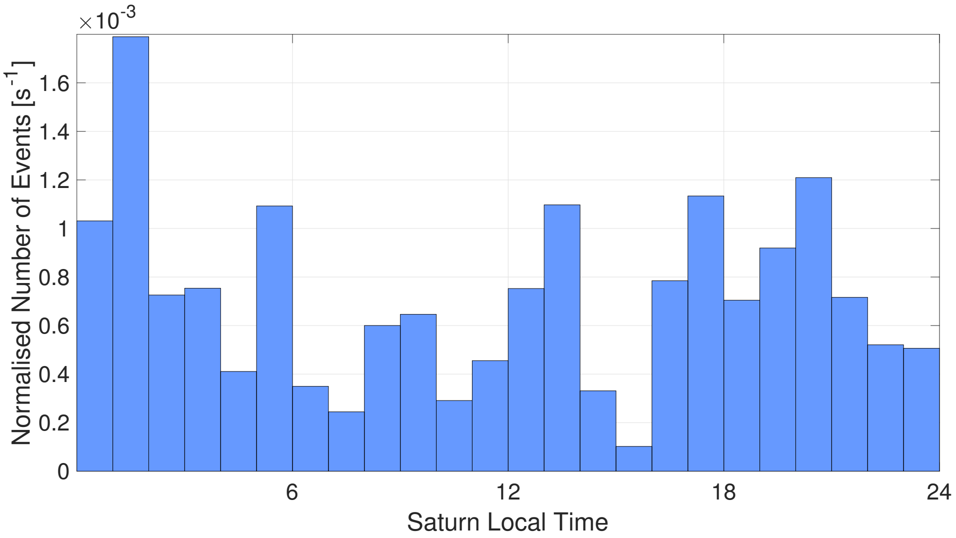

FIGURE 3.5: Local time at Saturn distribution of current sheet encounters normalised by the number of seconds spent in each 1 SLT bin by Cassini.

azimuthal direction locally and $\hat{\boldsymbol{z}}$ remains unchanged from the cylindrical coordinate.

$$B_x = B_{x0} \tanh\left(\frac{z - z_0}{H_x}\right), \tag{3.1}$$

$$B_y = B_{y0} \tanh\left(\frac{z - z_0}{H_y}\right), \tag{3.2}$$

$$B_z = B_{z0}, \tag{3.3}$$

where B_{x0} and B_{y0} are magnetic field values within the lobes away from the current sheet. This value is what the magnetic field component will asymptotically approach as z increases away from the current sheet. B_{z0} is the value that B_z is assumed to have throughout the current sheet and local area and is close to or at zero value. z_0 is the distance from $z = 0$ that the current sheet has moved due to other processes such as the near planetary period oscillating of the current sheet, viewed as a ~10.7 hour wave in the magnetometer data. Another phenomena leading to the current sheet being away from $z = 0$ is the bowl-shaped current sheet (Arridge et al., 2008b) that causes the whole sheet to be situated above the equator in northern winter and below in northern summer. Scale heights of the magnetic field in $\hat{\boldsymbol{x}}$ and $\hat{\boldsymbol{y}}$ are also included in the Harris current sheet model as H_x and H_y. These values control how quickly the hyperbolic tangent function approaches the saturation (lobe) values.

3.3.2 Deforming Harris Current Sheet with a Gaussian

The general deformation method is laid out in chapter 2, here a specific deformation is described. The undeformed magnetic field that is in the original coordinate system is the Harris current sheet model laid out in section 3.3.1. The following method is a specific implementation of the general deformation method of TSY98 using a Gaussian wave pulse to deform a Harris current sheet using Cartesian coordinates (x, y, z). The geometry of the current sheet will be deformed by the equation for a Gaussian wave pulse:

$$z = Ae^{-(\boldsymbol{k}\cdot\boldsymbol{r}+\boldsymbol{k}\cdot\boldsymbol{u}t-\omega t-\Phi_0)^2}, \tag{3.4}$$

where A is the amplitude, $\boldsymbol{k}$ is the wave vector, ω is the angular frequency and Φ_0 is the phase of the wave. Also included is a doppler shift using $\boldsymbol{k} \cdot \boldsymbol{u}t$.

Firstly, the deformed coordinate system needed must be found for the gaussian pulse used. A normal vector, X-vector and Y-vector (normal to the current sheet, new x-direction and new y-direction in old coordinates respectively) are needed to find the deformed coordinate system. The normal vector is calculated by the differentials of equation 3.4.

$$n_x = \frac{\partial z}{\partial x} = -2k_x \gamma A e^{-(\boldsymbol{k}\cdot\boldsymbol{r}+\boldsymbol{k}\cdot\boldsymbol{u}t-\omega t-\Phi_0)^2} \tag{3.5}$$

$$n_y = \frac{\partial z}{\partial y} = -2k_y \gamma A e^{-(\boldsymbol{k}\cdot\boldsymbol{r}+\boldsymbol{k}\cdot\boldsymbol{u}t-\omega t-\Phi_0)^2} \tag{3.6}$$

$$n_z = -1 \tag{3.7}$$

Where,

$$\gamma = \boldsymbol{k} \cdot \boldsymbol{r} + \boldsymbol{k} \cdot \boldsymbol{u}t - \omega t - \Phi_0 \tag{3.8}$$

The Y-vector (Y) is given by the cross product of the normal and the undeformed y-axis, and the X-vector (X) is given by the cross product of the Y-vector and the normal vector. The normal vector is equivalent to the 'Z-vector' in this system and is used to calculate the new z*-direction. From this, the new coordinate system and positions can be found.

$$x^* = xX_x + yX_y + (z + z0)X_z \tag{3.9}$$

$$y^* = xY_x + yY_y + (z + z0)Y_z \tag{3.10}$$

$$z^* = xn_x + yn_y + (z + z0)n_z \tag{3.11}$$

These new positions are then used to find the new magnetic field values using the Harris current sheet model in both $\hat{\boldsymbol{x}}$ and $\hat{\boldsymbol{y}}$ as outlined in section 3.3.1.

$$B_x = B_{x0} \tanh\left(-\frac{z^*}{H_x}\right)' \tag{3.12}$$

$$B_y = B_{y0}\tanh\left(-\frac{z^*}{H_y}\right)' \tag{3.13}$$

$$B_z = B'_{z0} \tag{3.14}$$

where H_x and H_y are the scale heights of the magnetic field as you approach and recede from the current sheet. Finally, TSY98 is used to deform the magnetic field using equation 2.9 where $\mathbf{T}$ is given by the following equations:

$$T_{xx} = \left(\frac{\partial y^*}{\partial y}\frac{\partial z^*}{\partial z} - \frac{\partial y^*}{\partial z}\frac{\partial z^*}{\partial y}\right) \tag{3.15}$$

$$T_{xy} = \left(\frac{\partial x^*}{\partial z}\frac{\partial z^*}{\partial y} - \frac{\partial x^*}{\partial y}\frac{\partial z^*}{\partial z}\right) \tag{3.16}$$

$$T_{xz} = \left(\frac{\partial x^*}{\partial y}\frac{\partial y^*}{\partial z} - \frac{\partial x^*}{\partial z}\frac{\partial y^*}{\partial y}\right) \tag{3.17}$$

$$T_{yx} = \left(\frac{\partial y^*}{\partial z}\frac{\partial z^*}{\partial x} - \frac{\partial y^*}{\partial x}\frac{\partial z^*}{\partial z}\right) \tag{3.18}$$

$$T_{yy} = \left(\frac{\partial x^*}{\partial x}\frac{\partial z^*}{\partial z} - \frac{\partial x^*}{\partial z}\frac{\partial z^*}{\partial x}\right) \tag{3.19}$$

$$T_{yz} = \left(\frac{\partial x^*}{\partial z}\frac{\partial y^*}{\partial x} - \frac{\partial x^*}{\partial x}\frac{\partial y^*}{\partial z}\right) \tag{3.20}$$

$$T_{zx} = \left(\frac{\partial y^*}{\partial x}\frac{\partial z^*}{\partial y} - \frac{\partial y^*}{\partial y}\frac{\partial z^*}{\partial x}\right) \tag{3.21}$$

$$T_{zy} = \left(\frac{\partial x^*}{\partial y}\frac{\partial z^*}{\partial x} - \frac{\partial x^*}{\partial x}\frac{\partial z^*}{\partial y}\right) \tag{3.22}$$

$$T_{zz} = \left(\frac{\partial x^*}{\partial x}\frac{\partial y^*}{\partial y} - \frac{\partial x^*}{\partial y}\frac{\partial y^*}{\partial x}\right) \tag{3.23}$$

And so, to get the final deformed magnetic field components the matrix $\hat{T}$ is multiplied with the magnetic field components found in equations 3.12 - 3.14 to get:

$$B'_x = T_{xx}B_x + T_{xy}B_y + T_{xz}B_z \tag{3.24}$$

$$B'_y = T_{yx}B_x + T_{yy}B_y + T_{yz}B_z \tag{3.25}$$

$$B'_z = T_{zx}B_x + T_{zy}B_y + T_{zz}B_z \tag{3.26}$$

3.4 Fitting Model to Magnetometer Data

To find a suitable fitting of all encounters in the Cassini magnetometer data of 1 second resolution, within the time period 2005-2012, an iterative method of finding the wave values is used. All variables within the method are fitted using a Levenberg-Marquardt non-linear least squares fitting algorithm. The variables that are fitted are as follows: scale heights H_x and H_y; wave vectors k_x and k_y; angular frequency ω; phase Φ_0; lobe magnetic field values B_{x0}, B_{y0} and B_{z0}; the amplitude of the wave A; and the z-axis offset $z0$.

Initially, a 'first guess' array of the variables is entered into the iterative fitting function that consists of likely values. The first fitting keeps half the variables (B_{x0}, B_{y0},B_{z0},A,z_0) constant and allows for a fitting of the other six variables. A second fitting is used where the fitted values of the first fitting are kept constant and the variables kept constant in the first fitting are now available to be fitted. This method is then repeated with the new fitted values as the constants for the first fitting until the mean squared error of the fitting is less than 0.1 nT^2. This arbitrary number is used as preliminary tests showed that anything below this MSE is sufficiently fitted and anything above is either not fitted, or fitted to non-physical values. A common example of a non-physical value is a fitted value of more than 100 R_S for a scale height.

The separation of the variables into two fittings allows for certain variables that are coupled to be determined separately. An example of this is that a fitting of a CSE may give a very large scale height far away from the current sheet centre, whereas the same or a similar fitting could give a more reasonable smaller scale height, i.e. scale height and z_0 are coupled in the argument of tanh. Additionally, to reduce bias in the fitting, the whole process is run with opposing signs for values that physically allow positive and negative values to occur. For example, this process is run for wave numbers (k_x, k_y) with differing sign combinations. The fitting with the lowest MSE value is taken as the most accurate fit for each current sheet encounter.

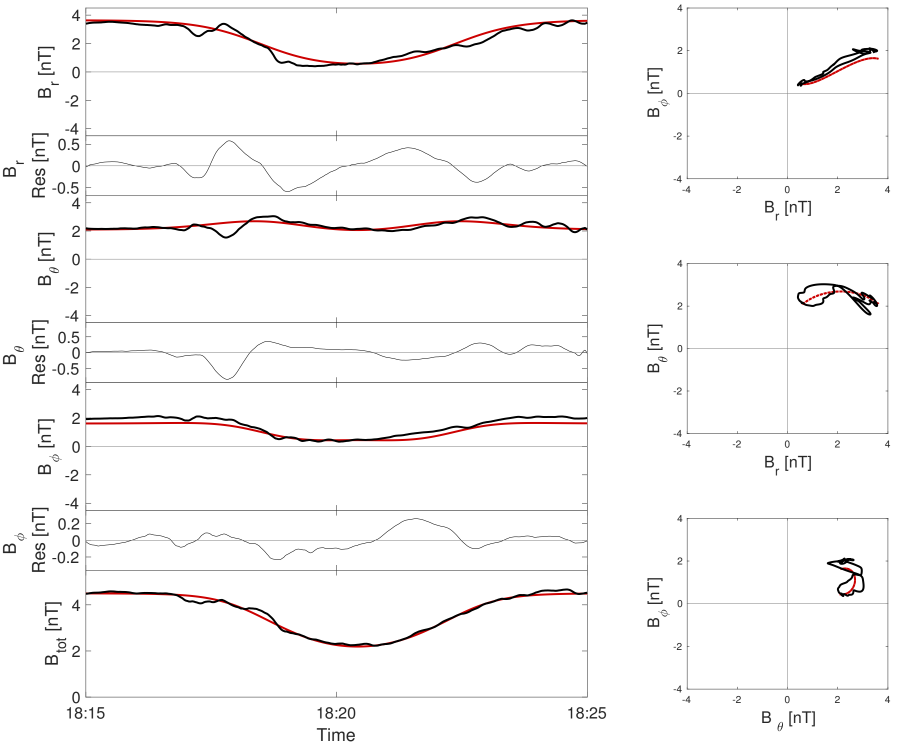

FIGURE 3.6: Figure showing 1 Hz magnetometer data of a passage of an aperiodic wave fitted with the local model. KRTP components are shown with the total magnetic field as well as three hodograms showing the relationships between the components. Residuals from the data and model for each component are shown directly below the component plot. This example takes place on 10th September 2011, at 28.7 R_S and 16.7 SLT

TABLE 3.1: Table of wave variables corresponding to figure 3.6

Variable	Value	Variable	Value
B_{x0}	$3.53 \pm 0.60 nT$	k_x	$0.06 \pm 0.10 \times 10^{-3}\ R_S^{-1}$
B_{y0}	$2.03 \pm 0.11 nT$	k_y	$0.02 \pm 0.10 \times 10^{-4}\ R_S^{-1}$
B_{z0}	$2.10 \pm 0.005\ nT$	Φ_0	-5.83 ± 0.17 Rad
H_x	$2.48 \pm 0.27\ Rs$	A	$3.77 \pm 0.04 Rs$
H_y	$1.15 \pm 0.12 Rs$	ω	$0.01 \pm 0.3 \times 10^{-4} s^{-1}$
z_0	$3.79 \pm 0.22 Rs$	MSE	$0.12\ nT^2$

As the fitting is done in Cartesian coordinates, it is important to remember to convert from and to spherical when plotting. An example of a fitting is shown in figure 3.6 where the variables of the fit with given errors can be found in table 3.1. This example shows a swept forward field in B_r and B_ϕ along with the subtle changes in B_θ described by the following section.

A second example, shown in figure 3.7 shows a more generic example of an aperiodic wave where a swept backward field in B_r and B_ϕ and very little variation in B_θ is shown. This method of fitting a local current sheet model that is deformed by a Gaussian wave pulse, allows for the resolution of variables associated with the current sheet and magnetic

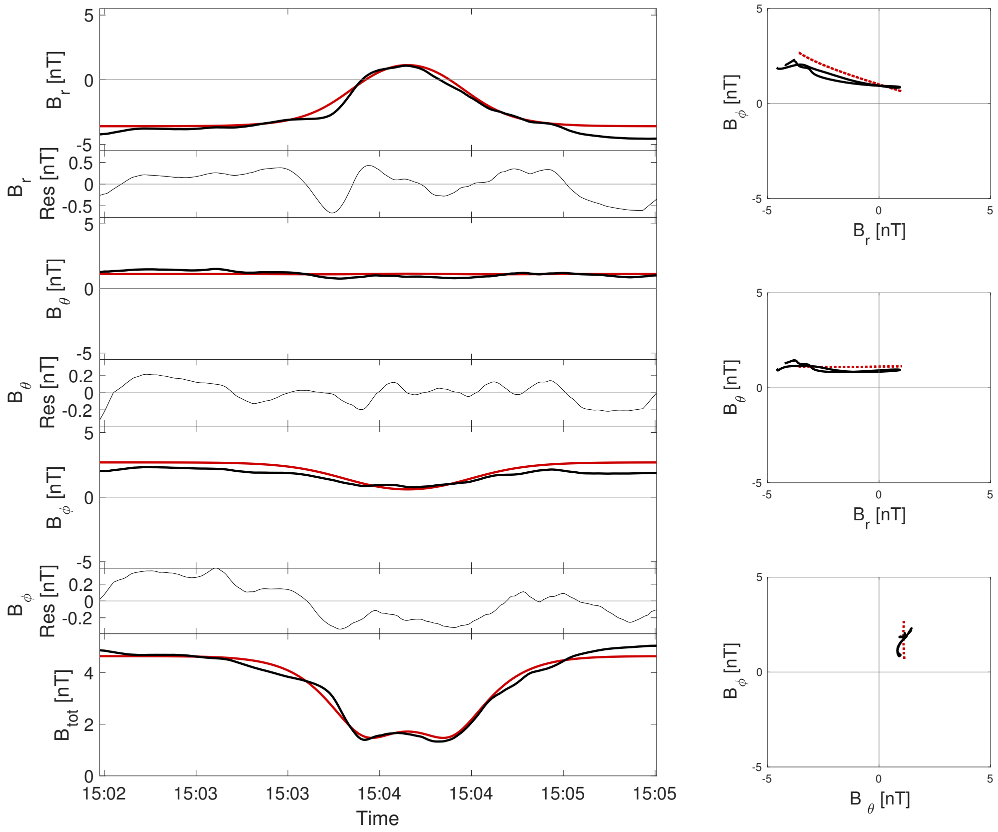

FIGURE 3.7: Figure showing magnetometer data of a passage of an aperiodic wave fitted with the local model. KRTP components are shown with the total magnetic field as well as three hodograms showing the relationships between the components. Residuals from the data and model for each component are shown directly below the component plot. This example takes place on 18th February 2005, at 18.7 R_S and 5.3 SLT

field during the passage of an aperiodic wave, and parameters relating to the wave itself. Each fitted parameter has an associated uncertainty explored in section 3.4.2.

3.4.1 Radial and Azimuthal Propagation

Resolution of accurate wave numbers are key to deciphering the propagation direction of the wave that encounters Cassini. It is possible to fit these parameters to the magnetometer data as the propagation direction affects the B_θ component. Figure 3.8 shows that as a radial wave passes the θ component dips slightly just before the passage through the current sheet and just after the second passage through the current sheet. However, a purely azimuthal wave dips during the first passage through the current sheet and increases during the second passage through the current sheet and hence the magnetic signatures can determine the propagation direction of the wave.

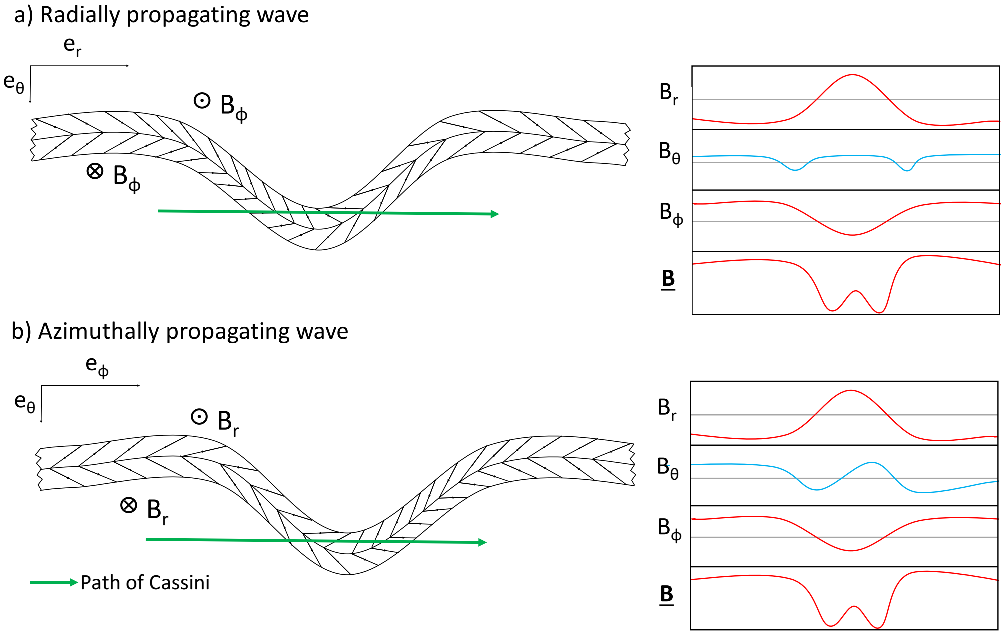

FIGURE 3.8: Figure shows two extreme examples of the traversal of Cassini through a purely radial wave (a) and a purely azimuthal wave (b). The magnetic field signature created from the passing of either wave is show to the right where the difference is seen in the θ component in blue. From Martin and Arridge (2017).

3.4.2 Uncertainty Calculation

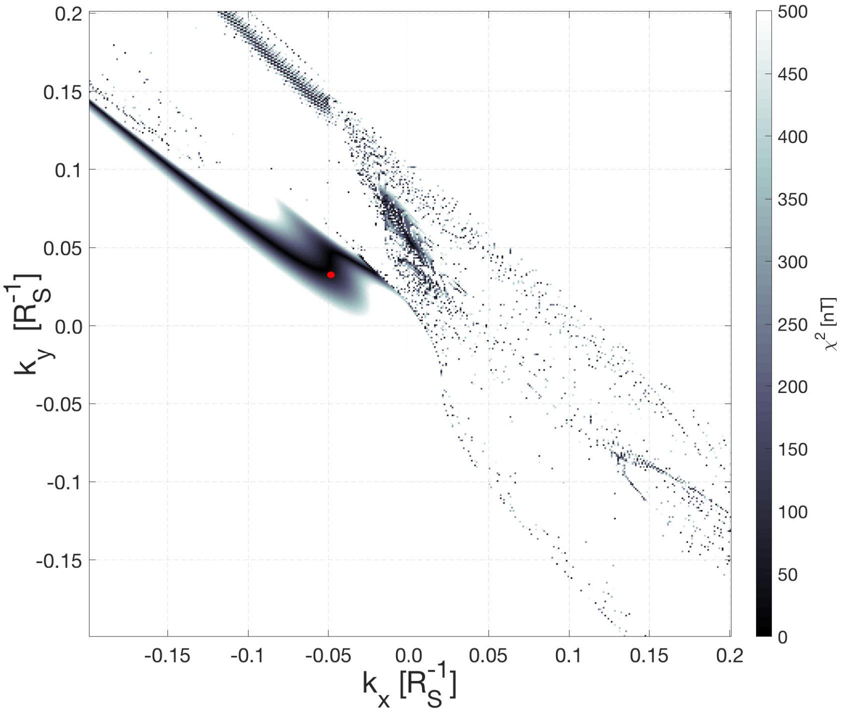

FIGURE 3.9: Figure shows a restricted χ^2 space for wave numbers given for an example fitting, the red circle is the values given by the fitting algorithm. This is a representation of a 2D slice through a multi-dimensional (11-D) χ^2 parameter space. Modified from Martin and Arridge (2017).

Each parameter has an associated uncertainty related to the fitting. This uncertainty is calculated from the square root of the diagonals of the Jacobian (estimated covariance) matrix, constructed using finite differences during the fitting algorithm. Uncertainties of a successful fit lie at around 1-5% for current sheet parameters and 1-10% for wave parameters. Example uncertainties can be found with parameter values in table 3.1. These uncertainties are related to the position of the fitted value and the χ^2 space minimum that it falls in. If the minimum (black area) is wide and shallow, this will increase the uncertainty of the parameter, and if the minimum of χ^2 is sharp and steep the uncertainty will be small. As the wave numbers form a large part of the discussion section, the example in figure 3.9 shows the χ^2 space for values of k_x and k_y, it can be concluded that the uncertainty in k_y will be much larger than the uncertainty in k_x. The lower values of χ^2 show a better fit, and the red circle is the fitted values of k_x and k_y. These values are also affected by the 9 other parameters that are fitted so an ideal fit for the wave numbers may not be an ideal fit for another parameter.

3.5 Results

This section is split into two with current sheet variables being explored first from the use of a Harris current sheet, and secondly, parameters from the travelling aperiodic waves are explored. All results are displayed as an overall picture of the magnetosphere where each coloured square represents the weighted average of that parameter found inside the bin of size $1R_S$. The weighting used is the inverse of the mean squared error for the original fitting of the model to the magnetometer data. Shown on each figure are the orbits of Titan ($20R_S$) and Rhea ($9R_S$), as well as a range of magnetopause positions calculated from Arridge et al. (2006). Below the overall view, the parameters are shown with radial distance in different SLT sectors, 'Morning' is defined as $0300 - 0900$ SLT, 'Noon' as $0900 - 1500$ SLT, 'Evening' as $1500 - 2100$ SLT and 'Night' as $2100 - 0300$SLT.

The sector plots are coloured with the revolution number, that is the number associated with each orbit that Cassini makes around Saturn. This allows for temporal differences to be easily identifiable. Clearly shown are that the 'Noon' and 'Evening' sectors are made up from a number of revolutions with large temporal differences, whereas 'Morning' and 'Night' are both similar times and revolution numbers, and so there are clearer relationships within these sectors. Where a variable has a statistically significant trend in a local time sector a line will be fitted with dotted confidence intervals using the uncertainty of the fitting parameters of the linear function with weighting on each event of 1/MSE of the original fitting to magnetometer data. A statistically significant trend means that the correlation between the variable and radial distance is above a correlation coefficient absolute value of 0.25 (absolute values of 0.20-0.30 are generally considered a weak but positively identified correlation) and has a probability of accepting a null hypothesis, H_0, is $\leq 5\%$.

3.5.1 Current Sheet Variables

3.5.1.1 Magnetic Field

Due to the nature of the hyperbolic tangent function in the modified Harris current sheet equations (3.1, 3.2 &, 3.3), B_{x0} will always be positive as B_x will always go from negative below to positive above the current sheet centre. The same is true for B_{y0} however, the direction of the change of magnetic field depends on the swept-backwards or forwards nature of the field. Therefore, B_{y0} can be either positive and negative.

Figure 3.10 shows how the radial component of lobe magnetic field changes spatially. It is observed that with radial distance B_{x0} decreases. The local time differences in B_{x0}, again being careful in considering temporal changes that are most apparent in the noon and evening sectors, show that the morning and night sectors have on average larger values of B_{x0}. However, the 'noon' sector shows that blue events (early revolutions) have, on average, a larger value than the yellow events (later revolutions).

Figure 3.11 shows the spatial distribution of the B_{y0} variable. A general decrease in B_{y0} is shown with radial distance associated with a decrease in the field magnitude as a whole. The 'evening' and 'Noon' sectors both show some positive values of B_{y0}, which is where one would expect more swept forward fields, which is described by a positive hyperbolic tangent relationship with z.

The final magnetic field component, B_{z0}, is shown in figure 3.12 where again a general decrease in magnitude with increasing radial distance is shown. A better fitting may be found for the decrease in field using a polynomial fit, however the large spread of data in the sectors fits similarly well to a line and a polynomial fit is described in the analysis in the following chapter.

3.5.1.2 Scale Height

Magnetic scale height is found using the Harris current sheet where scale height regulates how quickly the magnetic field approaches zero at the centre of the current sheet. This value describes the scale height of the magnetic field and is not directly associated

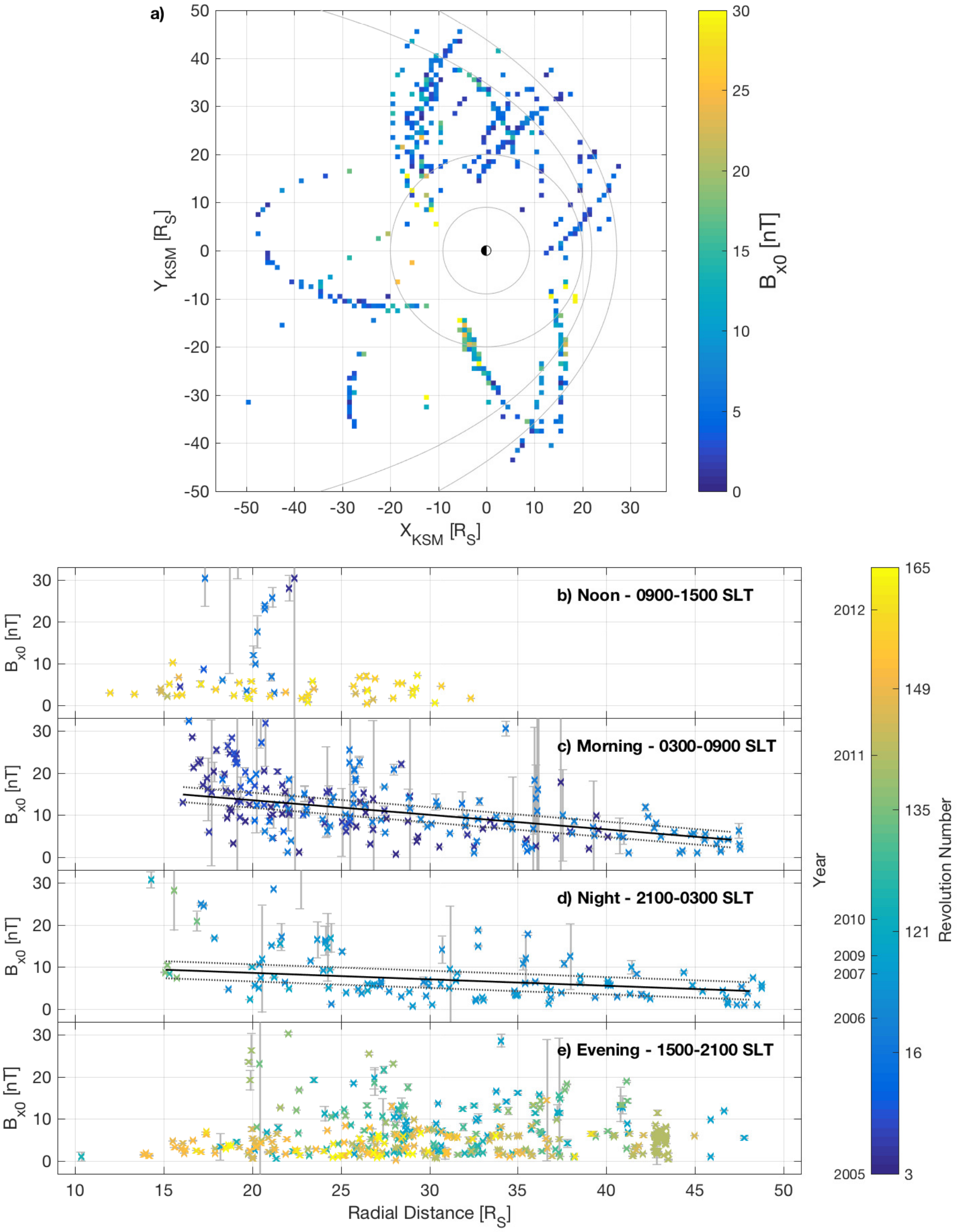

FIGURE 3.10: Figure showing spacial distribution of lobe radial magnetic field component during the passing of an aperiodic wave. Layout is described at the beginning of section 3.5.

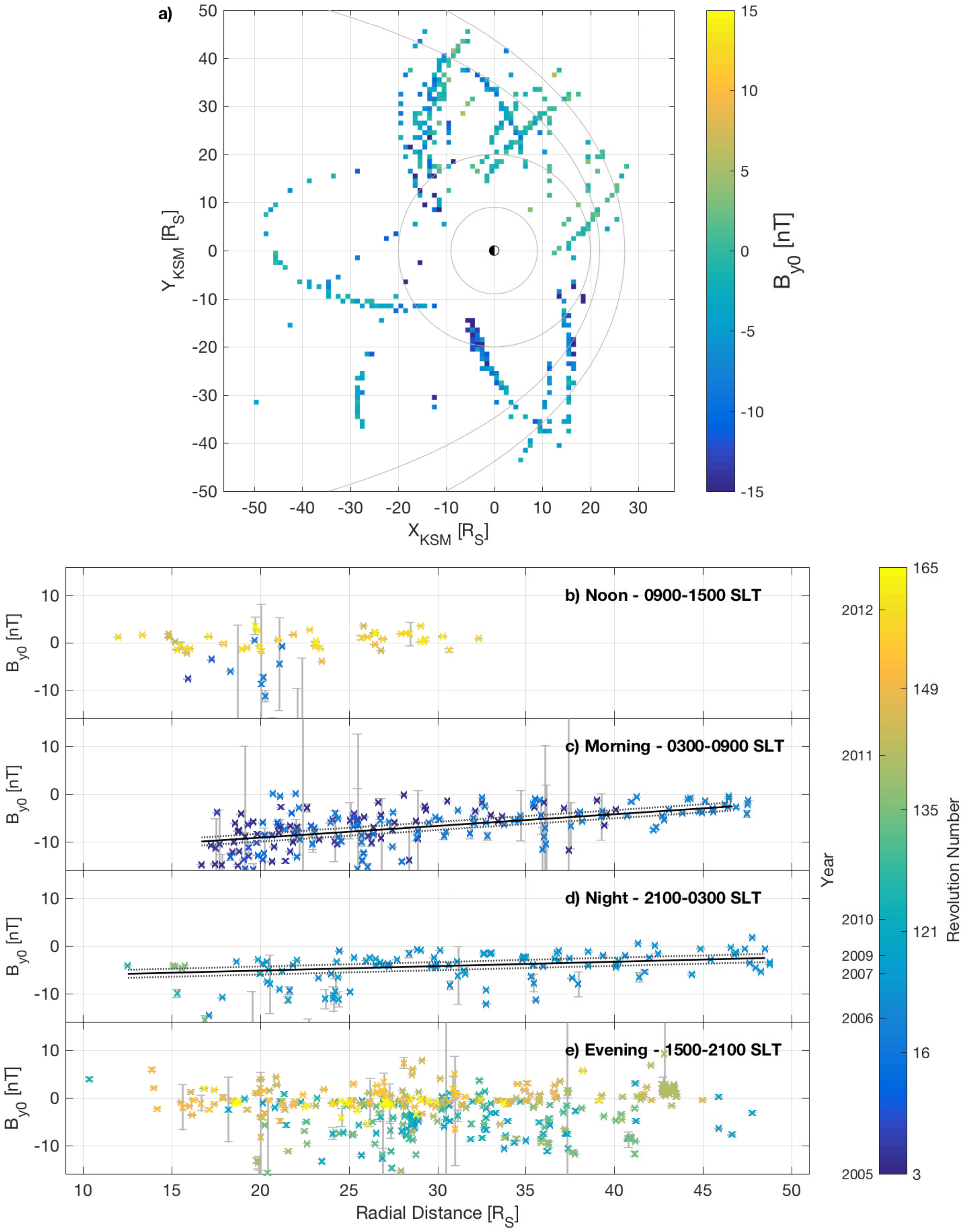

FIGURE 3.11: Figure showing spatial distribution of lobe azimuthal magnetic field component during the passing of an aperiodic wave. Layout is described at the beginning of section 3.5.

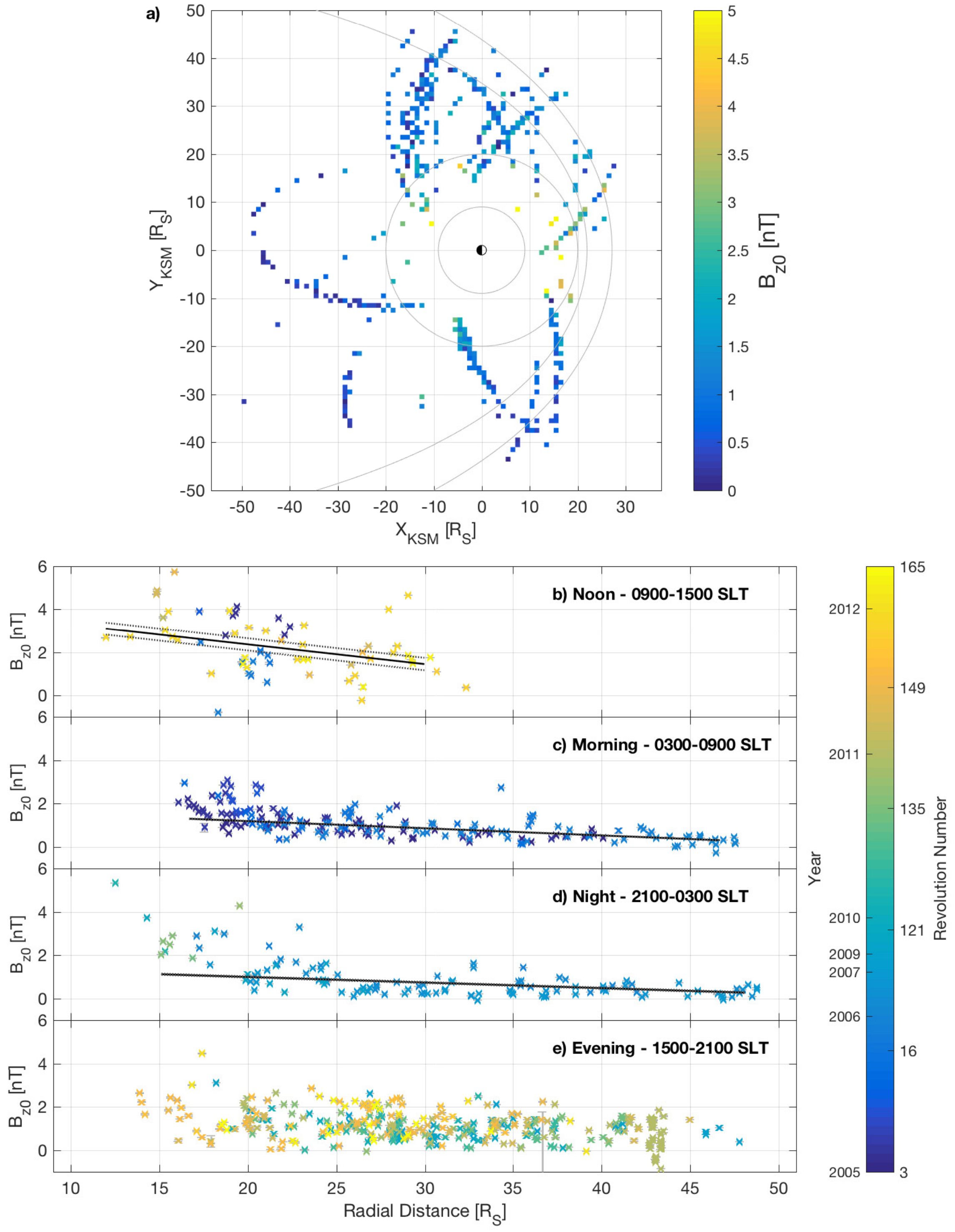

FIGURE 3.12: Figure showing spatial distribution of B_z component during the passing of an aperiodic wave. Layout is described at the beginning of section 3.5.

with the scale height of the plasma density of the current sheet, but is expected to be correlated with the plasma scale height. Using Harris in two magnetic field components means that a scale height for both radial magnetic field and azimuthal magnetic field can be retrieved. Both of the scale heights are calculated using distance along the z-axis, and so a geometric mean of the values is used to estimate the overall scale height of the magnetic field as the geometric mean is less sensitive to large outliers and is a more effective averaging method for variables with a large range.

Figure 3.13 shows an increase in scale height with radial distance in general, with statistically significant increases in the 'noon', 'morning' and 'night' sectors.

$$H_{MF} = \sqrt{H_r H_\phi} \tag{3.27}$$

3.5.1.3 Z-axis offset and Hinging Distance

The final current sheet parameter originating from the use of the Harris current sheet is the z-axis offset. This offset includes all processes that will cause the centre of the current sheet to be displaced from the $z = 0$ plane except the aperiodic waves. As this includes the seasonal bowl shape, temporal changes will be apparent in the overall data set as the span 2005-2012 spans equinox. Therefore, the value of the z-axis offset will first be displayed, along with the z-axis offset with the expected bowl shape removed.

Figure 3.14 shows the value of the distance of the centre of the current sheet from $z = 0$. The figure shows an increase of z_0 with radial distance, as expected with a bowl shaped current sheet. It is expected that larger offsets will be found in 2005 and 2012, as the equinox of Saturn was in 2009, a much smaller offset would be expected during this time.

When the expected bowl shape is removed, the remaining z_0 should reflect only processes that displace the current sheet at a large frequency (flapping at planetary period) or aperiodic wave, that are already being modelled. In theory, after the bowl displacement is removed from values and assuming that the flapping has symmetrical

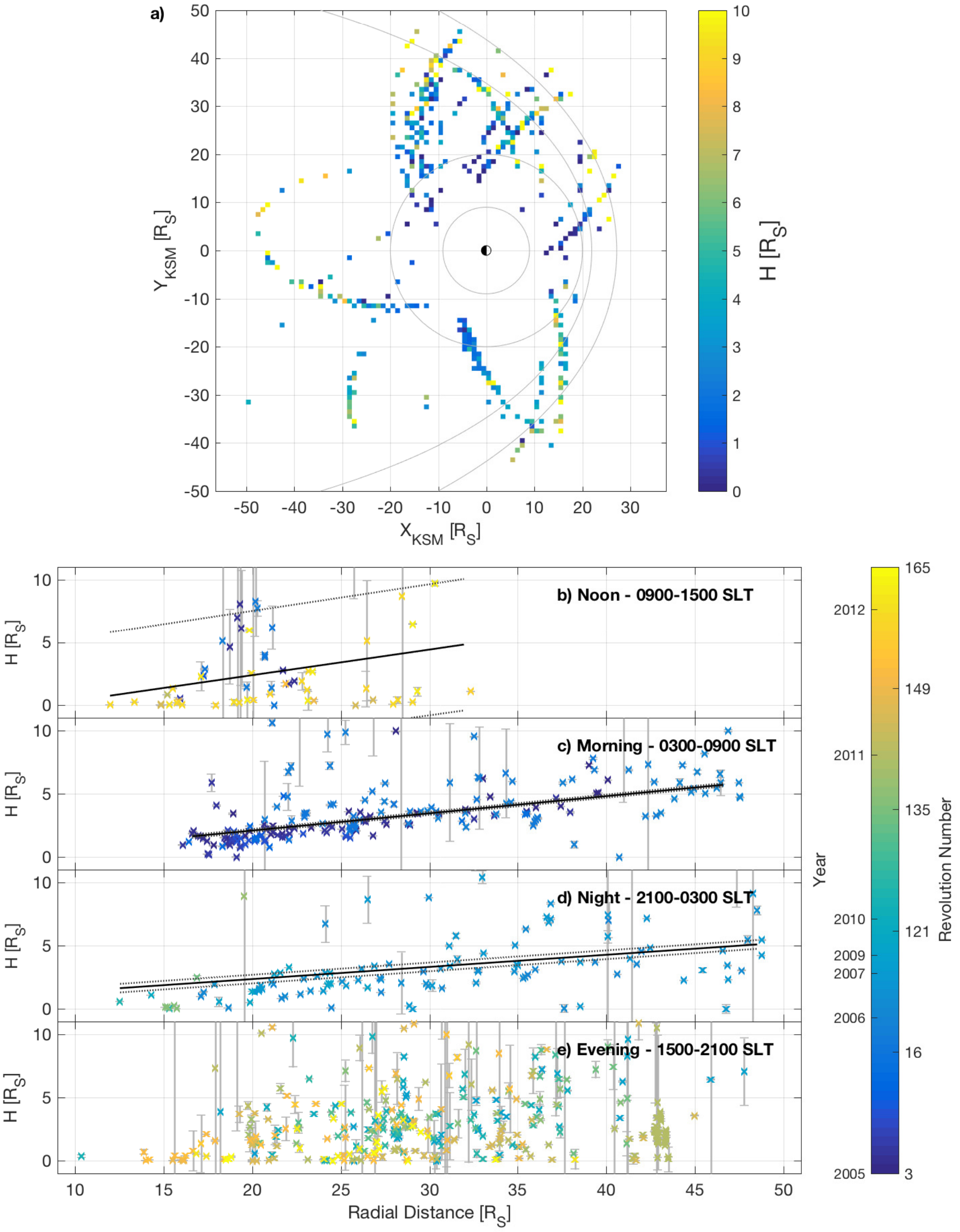

FIGURE 3.13: Figure showing spatial distribution of geometric scale height using H_x and H_y. Layout is described at the beginning of section 3.5.

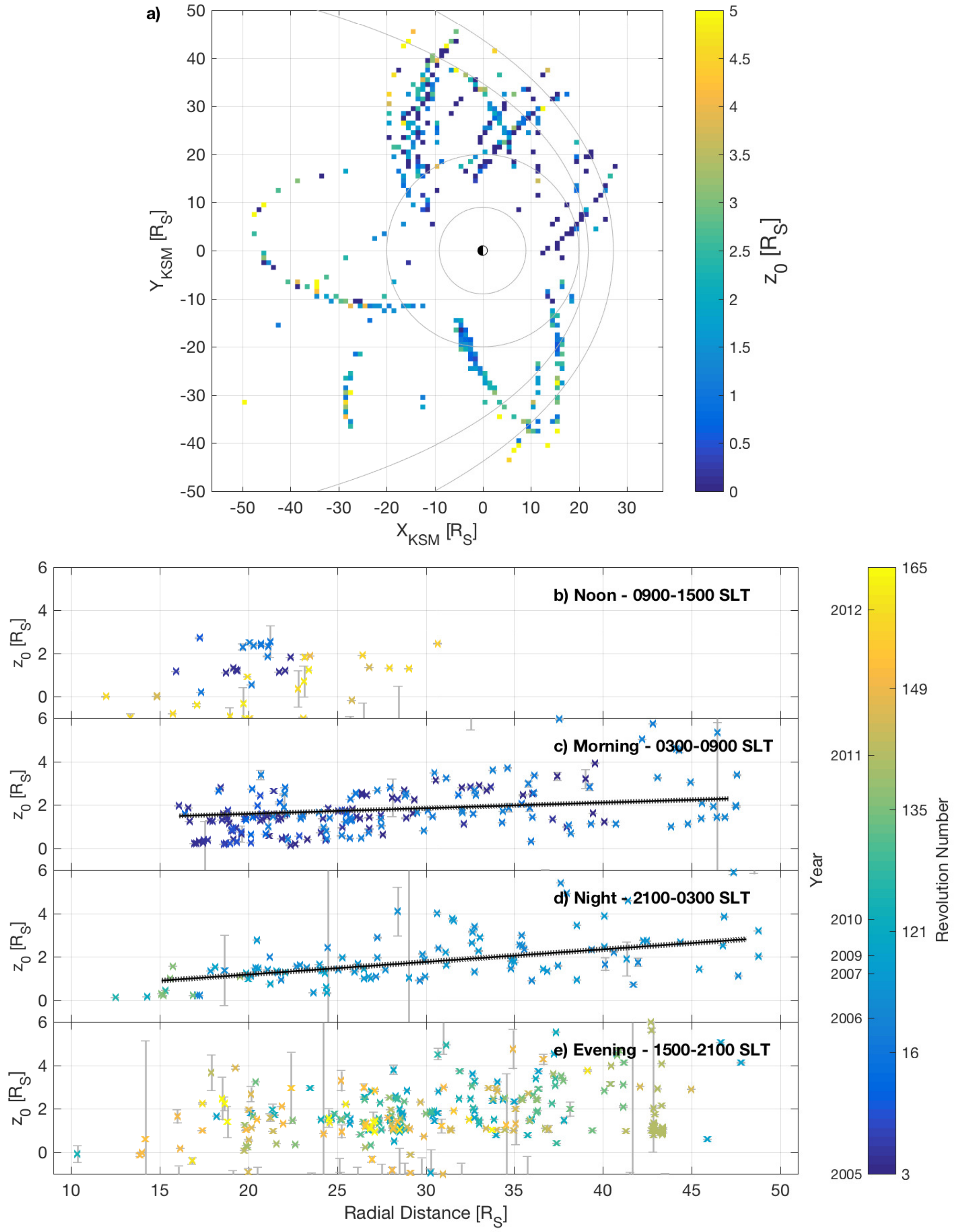

FIGURE 3.14: Figure showing spatial distribution of distance of current sheet from $z = 0$. Layout is described at the beginning of section 3.5.

movement, there should be an equal number of positive and negative values of B_{z0} as this displacement is caused by a periodic wave, this relies on an estimate of the hinging distance that is global and constant, this is however not true and the hinging distance of the sheet changes with mass of the plasma sheet and solar wind dynamic pressure. The hinging distance comes from the equation from Arridge et al. (2008b) where the displacement of the current sheet due to the bowl shape is as follows, where r is radial distance, R_H is hinging distance and θ_{SUN} is the latitude of the Sun from the rotational equator.:

$$z = \left[r - R_H \tanh\left(\frac{r}{R_H}\right) \right] \tan(\theta_{SUN}) \tag{3.28}$$

Figure 3.15 shows the z-axis offset assuming a 50.0 R_S hinging distance. A value of averaged hinging distance for the entire data set can be estimated by removing the bowl shape from z_0 and then testing for which distance of hinging causes the resultant B_{z0} values to be closest to zero using a MSE from the zero-line. The average hinging distance is found to be 52±30 R_S. This large uncertainty stems from the large time scale of the data set where the hinging distance will change considerably between 2005 and 2012.

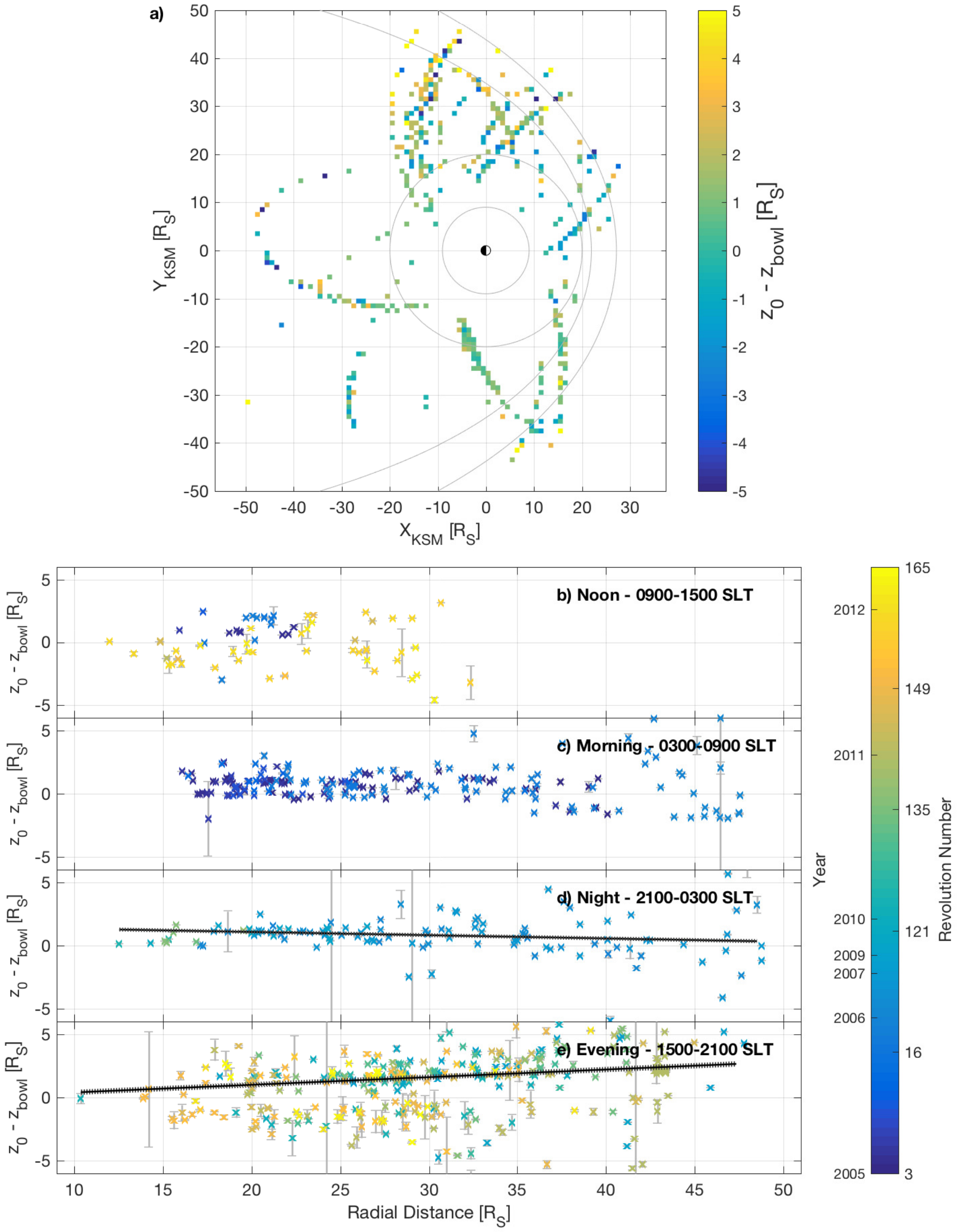

FIGURE 3.15: Figure showing spatial distribution of distance of current sheet from $z = 0$ with z-axis offset due to bowl shape removed with a hinging distance of 50 R_S. Layout is described at the beginning of section 3.5.

3.5.2 Wave Parameters

Wave parameters in this section are all resultant from the use of a Gaussian wave pulse to model a travelling aperiodic wave upon the current sheet. Equation 3.4 gives the function for an aperiodic wave with a Gaussian profile, and from this a number of wave parameters are available for analysis. Phase is included in the equation, however it corresponds to the position of the wave in the time period and has no physical interpretation other than to aid fitting, therefore it is not presented here as a wave parameter.

3.5.2.1 Amplitude

Figure 3.16 shows the spatial distribution of the amplitude of aperiodic waves. The amplitude is seen to increase with radial distance, with a statistically significant increase in the 'morning' and 'night' sectors.

Additionally, it is observed that the majority of aperiodic waves have a negative amplitude, which in the method of fitting the waves means that the Gaussian pulse moves the current sheet in the negative $\hat{z}$-direction. Apparent when taking the temporal changes into consideration is that, the yellow/orange values that occur in the later revolutions have a mixture of positive and negative amplitudes and the earlier revolutions have mainly negative amplitudes. This is also an indicator of whether Cassini was above or below the average position of the current sheet, Cassini cannot detect positive amplitude waves if it is situated beneath the current sheet. A statistical increase is seen only in the 'morning', 'night' and 'evening' sectors.

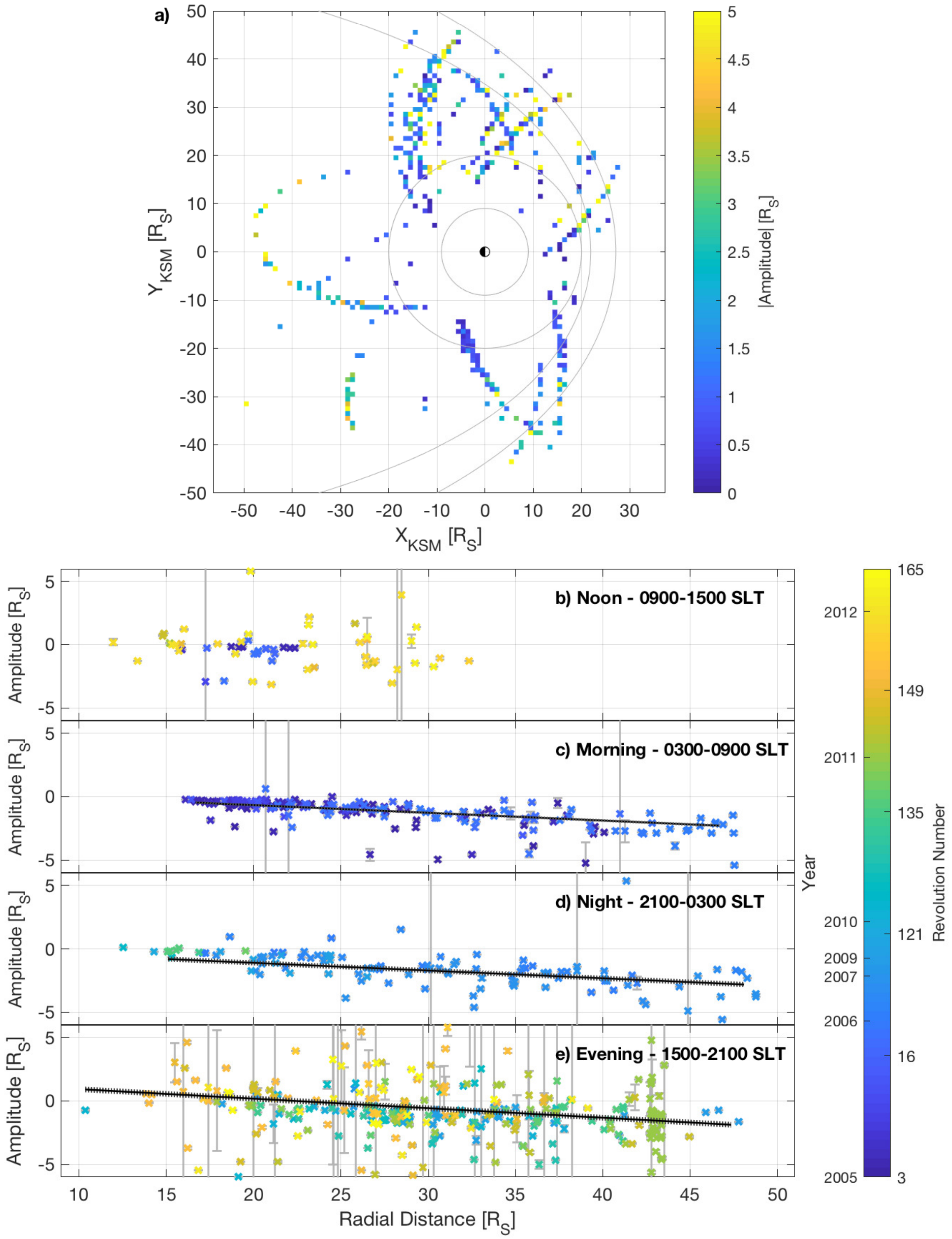

FIGURE 3.16: Figure showing spatial distribution of amplitude of aperiodic waves. Layout is described at the beginning of section 3.5. a) shows the magnitude of amplitude, whereas b-e) show the sign of the amplitude.

3.5.2.2 Wave Number and Propagation Direction

Wave numbers k_x and k_y are found using the Gaussian wave pulse. As the wave is assumed to be travelling on a 2-D plane, these wave numbers are used to form the wave vector $\boldsymbol{k}$, and the direction that the wave is travelling can be found. To find the trend in propagation direction, the components are converted to k_{xKSM} and k_{yKSM} in the KSM co-ordinate system and plotted on polar axes to display the direction. Figure 3.17 shows these directions for each local time sector, used previously, but with additional binning in radial distance. Each plot is constructed using an angle between k_{xKSM} and k_{yKSM}, and the uncertainty in the angle for each event. This means that each event forms a Gaussian profile with the centre on the angle as the mean of the Gaussian distribution, and a standard deviation of the uncertainty in the angle. Each Gaussian profile is superposed on top of each other in each bin to form a probability distribution of the propagation direction of the wave. In figure 3.17, positive x_{KSM}-axis is directed to the right of the figure and represents the direction of the Sun with Saturn at the origin, and positive y_{KSM}-axis is directed to the top of the figure which represents the dusk-ward direction.

We see that the main propagation direction is radially outwards with a small positive azimuthal component in all sectors apart from ‘noon’.

3.5.2.3 Angular Frequency and Phase Velocity

The final parameter directly inferred from the wave pulse is the angular frequency of the wave. The angular frequency ranges from $0.0005 - 0.0750$ s^{-1} with a large majority occurring at 0.01 s^{-1}. These values correspond to time periods of a few minutes to half an hour, which is notably the criteria for detecting an aperiodic wave. There appears to be no SLT or radial distance preference for particular angular frequencies.

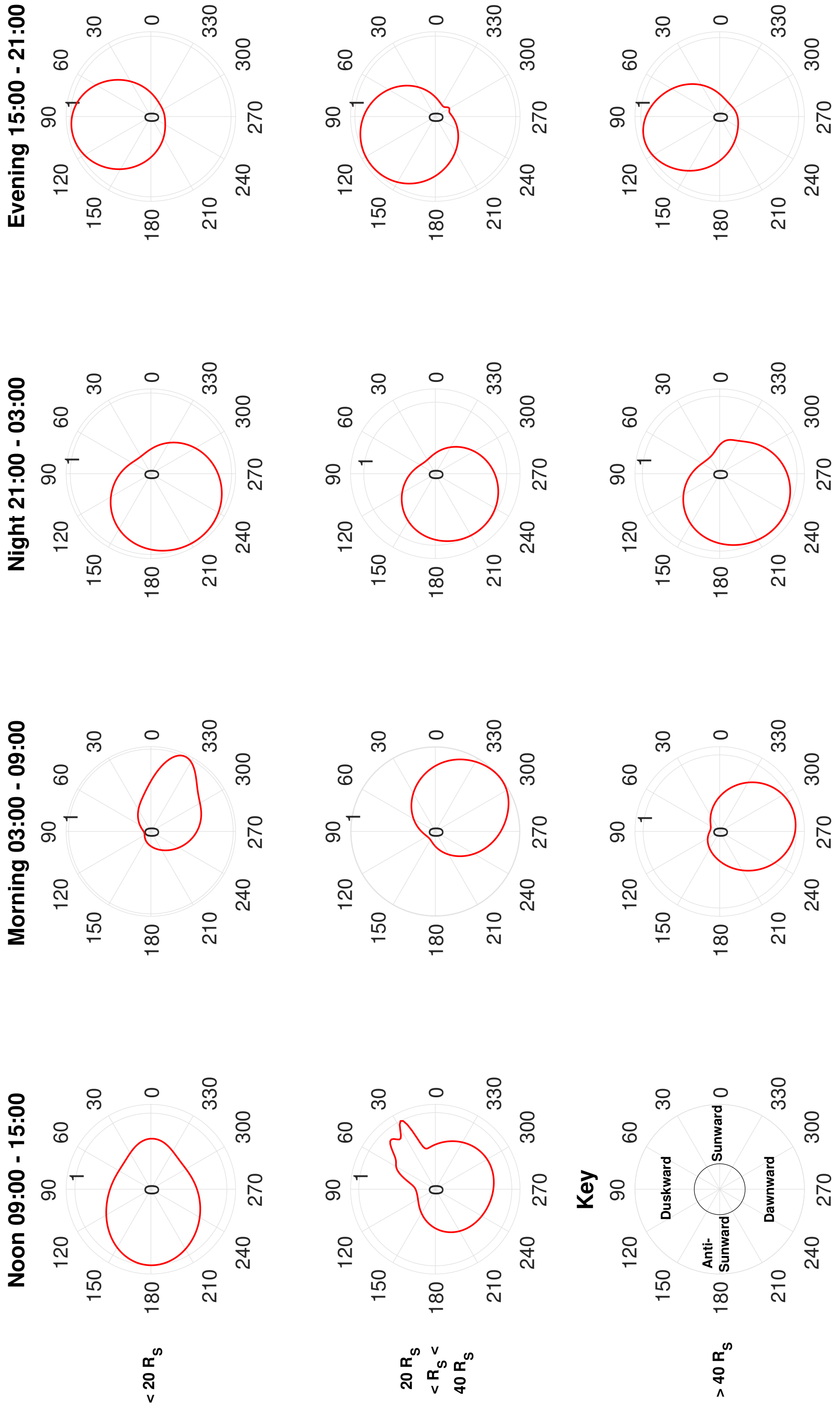

FIGURE 3.17: Figure showing the direction of propagation of waves as a probability distribution (red) in each local time and radial sector of Saturn's magnetosphere.

Phase velocity can be calculated from the angular frequency and the wave number mentioned earlier.

$$V_{ph} = \frac{\omega}{|\mathbf{k}|} \tag{3.29}$$

As angular frequency has no SLT or radial dependence, the profile of phase velocity follows that of the inverse of the magnitude of **k**. The median phase velocity is found to be 0.21 $R_S s^{-1}$ ($\sim$10000 kms^{-1}) with little variation in SLT and radial distance which is an order of magnitude comparison to the Alfvèn velocity in the middle magnetosphere.

3.6 Discussion

This method of fitting a model current sheet deformed by a Gaussian wave pulse allows for the extraction of variables associated with the current sheet, such as scale height, lobe magnetic field and distance of the current sheet centre from the equator. Additionally, when deforming the current sheet, the use of a Gaussian pulse wave allows the resolution of wave variables, such as amplitude, frequency and wave vector.

Through the extraction of these variables, various other quantities can be derived from them, for example, direction of propagation can be found when considering the wave numbers in $\hat{x}$ and $\hat{y}$. This section will begin with a discussion of the temporally broad local time sectors, the current sheet parameters, then the wave parameters. The section will end with a short discussion on the use of the Gaussian and possible sources of the aperiodic waves.

3.6.1 Noon and Evening Sectors

Evident in all figures of parameters separated by local time sectors is the fact that the evening and noon sectors rarely allow for a correlation with the parameter and radial distance. Whilst there may not be any correlation in the underlying data, the analysis method may introduce systematic errors that mask any real correlations. Firstly, it is important to view the differences in the current sheet between the morning/night area and the evening/noon sectors. It is known that the current sheet at Jupiter is seen to be thicker on the dusk sector than on the dawn sector (Krupp et al., 1999; Arridge et al., 2015) and the same may be true for Saturn. As the model relies on a thin current sheet approximation, the thicker current sheet will cause larger uncertainties in the parameters fitted in the evening or noon sectors.

Additionally, events in the noon sector are widely separated in time, where only the first few revolutions and final few revolutions of the survey are found in this sector. Changes of the seasons on Saturn can be seen in the data in this sector and this may account for that fact that in most parameters there is little or no correlation with radial distance, it is also evident in some parameters that the blue coloured data points (early 2005) show a different relationship with radial distance than the yellow coloured data points(late 2012).

3.6.2 Current Sheet Properties

3.6.2.1 Magnetic Field Components

Firstly, larger values of the radial magnetic field (figure 3.10) component (B_{x0}) are found closest to the planet. A dipolar planetary magnetic field is expected to reduce in strength with distance as r^{-3} and as such each component is expected to decrease in magnitude with distance, but as Saturn is not strictly a dipolar field, a decrease is expected but not with an exact r^{-3} relationship. It is observed that the inner morning sector has the highest radial magnetic field, however this may also be a temporal change as the 'noon' sector has two time periods (shown as yellow and blue) where blue is on average larger than yellow, and as the 'morning' sector is primarily blue this may be the case.

The second magnetic field component B_{y0} (figure 3.11) shows a similar relation to B_{x0} where the largest absolute values are found closer to the planet. However, B_{y0} can have positive and negative values relating to the direction of sweepback of the magnetic field. The 'morning', 'night' and parts of the 'noon' and 'evening' sectors show mainly negative B_{y0} where this corresponds to a swept backwards field, described by B_y being positive below the current sheet and negative above.

The third and final magnetic field component B_{z0} (figure 3.12) displays a similar relation with distance as the radial component. Saturn's magnetic field dipole has its magnetic north pole at the planets Kronographic North pole, with no external forces acting to change this, the magnetic field at the equator would be directed Southward, or negative in $\hat{z}$ in the model's Cartesian coordinates, or positive $\hat{\theta}$ in KRTP.

3.6.2.2 Scale Height

Figure 3.13 shows the distribution of scale height derived from the geometric mean of the magnetic scale height in the radial and azimuthal field components using a Harris equation to model the current sheet. An increase is observed in morning and night sectors of the scale height radially from 2 R_S to 6 R_S in the morning sector and from 2 R_S to 5 R_S in the night sector.

Previous studies [e.g. Khurana and Kivelson (1989*a*); Giampieri and Dougherty (2004); Kellett et al. (2009); Kidder et al. (2009)] using plasma data, models and magnetic field data show that an increase in scale height is expected with distance. The magnetopause currents encourage the magnetic field to become more dipolar and hence the current sheet will be less confined at the equator as the particles can more easily travel up the magnetic field lines. This means that the magnetic scale height will also increase.

It is important to note that this is the scale height of the magnetic field in the $\hat{\boldsymbol{z}}$ direction, and no plasma data had been included in the analysis. This means that the scale height described here is not directly related to the thickness of the current sheet determined by calculating the current density or inferred from stress balance, however further discussion on this topic can be found in Sergis et al. (2009) & Sergis et al. (2011), showing that the two may be correlated and show similar trends.

3.6.2.3 Z-axis offset and Hinging Distance

To account for processes that cause the current sheet to be displaced from the rotational equator, a z-axis offset is used within the Harris equation. This offset includes displacement from the seasonal bowl shape and flapping of the current sheet at near the rotational rate of the planet. Additionally, due to the seasonal nature of the bowl shaped current sheet, the bowl is expected to be above the equator for events occurring in 2005-2009 and below the equator for events that occur in late 2009-2012 (Arridge et al., 2008b). Figure 3.14 shows the distribution of this z-axis offset around Saturn. The morning and night sectors show an increase in absolute z-axis offset, where an increase is expected as the morning sector was explored in 2005-2006 which is before equinox and so the bowl shape is expected to push the current sheet above the z=0 axis.

3.6.3 Wave Properties

3.6.3.1 Wave Number, Propagation Direction and Wavelength

The azimuthal and radial wave numbers k_y and k_x determined by the model fitting can be used to determine the direction that the wave is propagating. Figure 3.17 shows the probability distribution built from 1-D kernel smoothing of the angle of propagation from the Sun-Saturn line and its uncertainty. An overwhelming majority of sectors display a positive radial skew with a small additional positive azimuthal component. This means that the majority of the waves in the bin are travelling radially away from the planet.

This probability distribution is tested against an isotropic distribution equal to the mean of each bin as null hypothesis. All sectors, except the noon sector, give a probability of less than 5% that the null hypothesis is correct. An additional check used is that the χ^2 value of the isotropic distribution compared with the probability distribution is much greater than the mean of the distribution plus two standard deviations, this process is a standard check for the reliability and evaluation of a χ^2 value. Below, table 3.2 shows these values to show that all sectors except noon reject the null hypothesis of isotropic propagation.

Waves in the noon sector are propagating in all directions, however the other sectors are all skewed towards a particular direction, that direction being radially outwards from Saturn. All radial bins of the evening sector give a peak of the distribution at around 10° - 130° showing a radially outwards propagations direction, with a small addition in the azimuthal direction with corotation. This is also true for the night sector where the global maximum of the distribution occurs at 210° (travelling down tail away from Saturn).

The morning sector has only one large global maximum in each radial bin, and outwards of 20 R_S that direction is again radially outwards with an addition in the azimuthal direction. However, inwards of 20 R_S the probability distribution peaks at 340°, which is again in the direction of corotation.

The final sector, noon, shows lower event numbers coupled with multiple possible wave sources. Hence, this sector shows a much larger spread in the probability distribution. Important to consider in this sector is that the magnetopause is generally seen between 21 and $26R_S$ (Pilkington et al., 2015*a*) thus the majority of events in the $> 20R_S$ bin are assumed to occur when the magnetopause is in an extremely expanded phase. This bin shows a large spread mainly across the $210 - 0°$ area. This bin is formed from events on the dusk side of the noon magnetosphere and hence this may show these events propagating perpendicular to the magnetopause. A small number of events are situated close to the morning sector, and these account for the two thinner peaks at 60° and 30° which also show propagation perpendicular to the magnetopause.

TABLE 3.2: Table of χ^2 values, probability of null hypothesis being correct and whether or not the null hypothesis was rejected for each section

Sector	Radial Distance $[R_S]$	χ^2	$\mu + 2\sigma$	Probability	Reject
Morning	$R \leq 20$	409	13	$< 1\%$	Yes
-	$20 < R \leq 40$	113	46	$< 1\%$	Yes
-	$R > 40$	549	10	$< 1\%$	Yes
Noon	$R \leq 20$	472	12	39%	No
-	$20 < R \leq 40$	347	14	9%	No
Evening	$R \leq 20$	329	11	$< 1\%$	Yes
-	$20 < R \leq 40$	440	96	$< 1\%$	Yes
-	$R > 40$	195	25	$< 1\%$	Yes
Night	$R \leq 20$	144	31	$< 1\%$	Yes
-	$20 < R \leq 40$	147	32	$< 1\%$	Yes
-	$R > 40$	160	29	$< 1\%$	Yes

Inwards of $20R_S$ a primarily bimodal distribution of inwards and outwards radially travelling waves is observed, however this bin is not statistically significantly different to an isotropic propagation distribution. These signatures suggest a possible magnetopause source for a percentage the waves found. However, the majority of all waves are propagating radially, concluding that a source of waves is found in the inner magnetosphere and propagate outwards, further discussed in section 3.6.5.

3.6.3.2 Amplitude

Figure 3.16 shows a radial dependence on the amplitude of waves in the morning and night sectors. The largest negative values of amplitude are found at large radial distances in the morning and night sectors, and the largest positive amplitudes are found in the evening sector. Initially, this may be due to the large scale bowl shape of the current sheet at the times the events are found. In the morning sector, the bowl is above the equator and so only negative values of amplitude may be seen, and conversely, the evening sector events are seen during 2010-2012 where the bowl is expected to be below the equator and hence a mixture of positive and negative amplitudes are seen as Cassini has a varied trajectory in $\hat{z}$.

This leads to the discussion of amplitude having a radial dependence due to the bowl shape, meaning that as the bowl shape causes the current sheet to become further from the equator, only increasingly larger amplitudes may be seen as the current sheet will need to be deformed more to be able to be seen at the equator, i.e. an observer bias is present. This seems likely due to the positive and negative dependence on the bowl position. However, during this time, Cassini is not constrained to the equator, but travels between $+10R_S$ and $-10R_S$ therefore smaller waves should still be sampled at larger radial distances. The only change will be that the bowl is more likely to be above or below Cassini, thus seeing more positive amplitudes in the evening sector (post-equinox, northern summer, downwards bowl), and more negative amplitudes in the morning and night sectors (pre-equinox, southern summer, upwards bowl). The conclusions here being that the radial dependence of the amplitude of the waves is not affected by the bowl shape, however the sign of the amplitude seen is. Additionally, this could mean that almost double the number of waves seen could actually have been propagating at the time as only one sign of amplitude can be viewed at a specific time.

Additionally, now having ruled out the observer bias of an increasing amplitude, a physical interpretation is examined. To understand conceptually why the amplitude is increasing with radial distance, the physical analogy of a wave on a string or a wave upon water is used. A comparison is drawn from the physics of water shoaling, where in a dispersive medium the energy of a wave must remain constant. This energy is related to the linear mass density, amplitude and frequency of the aperiodic wave. As the amplitude is increasing, then the linear mass density or the frequency must decrease. Frequency has been shown to have no radial distribution in this study, and Arridge et al. (2011) shows a decrease in linear mass density with radial distance, hence it is suggested that amplitude increase is due to a medium that is decreasing in density.

3.6.4 Gaussian Differential Testing

As discussed in the previous section, Cassini may have a sampling bias of sign of amplitude due to position with respect to the current sheet. A Gaussian derivative will be used to deform the current sheet model and fitted to the magnetometer data of the events to compare and contrast the fittings and physical properties. A Gaussian differential is chosen as it shows both positive and negative displacements in one pulse. The Gaussian differential (differential of equation 3.4) is as follows:

$$z = -2(\boldsymbol{k} \cdot \boldsymbol{r} - \omega t) A e^{-(\boldsymbol{k} \cdot \boldsymbol{r} - \omega t - \Phi_0)^2} \tag{3.30}$$

This equation was fitted to magnetometer data, noted is the removal of the Doppler shift signature, this was a simplification that improved the number of events that were able to be fitted. Overall, fewer events allowed fitting of a Gaussian differential profile. This included almost no events from the evening and noon sectors, with a total of 462 events being fitted compared to 742 events fitted using the Gaussian profile. Additionally, large uncertainties are common in the fitting process of the derivative, with the average uncertainty for some parameters, such as scale height and amplitude, reaching 40-50%.

However, events that managed to be adequately fitted with both methods show similar parameter values for both fitting methods there are just far fewer events fitted with the Gaussian derivative.

This concludes that the Gaussian profile was a suitable candidate for the shape of the current sheet deformation, and that it is preferable over the Gaussian derivative due to lower uncertainties and a larger number of fitted events. The fact that both Gaussian and derivative give similar values for parameters when both are well fitted shows that either is a suitable physical model for the shape of the waves. Also taken into account is the reduced computational time needed to fit the Gaussian, and hence more complex wave pulses are not explored.

3.6.5 Aperiodic Wave Sources

Aperiodic waves can originate from a number of processes, many of which can act together or occur simultaneously. The main mechanisms will be discussed and evaluated for likelihood in this section. The dayside magnetopause is subject to changing solar wind conditions that buffet the magnetosphere causing compressions and expansions of the magnetopause position. The current sheet extends all the way to the magnetopause on the dayside (Krupp et al., 2005) and hence any sudden changes in magnetopause position due to solar wind condition changes will be transmitted to the current sheet. Small scale changes in the magnetopause position could perturb the current sheet to form an inward travelling aperiodic wave. The propagation directions discussed in section 3.6.3.1 show that the dayside magnetosphere appears to show a bi-directional propagation where inward travelling waves are possibly caused by changes in magnetopause position.

Additionally, the magnetopause on the dayside is subject to reconnection in primed solar wind conditions (McAndrews et al., 2008). This reconnection can introduce perturbations in the magnetic field (Snekvik et al., 2017) and hence these perturbations can be transmitted to deform the current sheet. This mechanism could be the cause of the larger number of inward travelling waves in the dayside magnetosphere. Furthermore, the dayside magnetosphere is home to an, on average, thicker current sheet due to a more dipolar field arrangement, this however can still produce reconnection within the current sheet [e.g Guo et al. (2018) & Delamere et al. (2015)] which could also act to produce aperiodic waves on the current sheet in all local time sectors. However, as the x-line in the tail region of Saturn is expected to be inside the range of radial distances for this study [e.g. Vogt et al. (2010)], it is expected that more inward travelling waves are found closer to the planet and more outward travelling waves further in the magnetotail. This is in contrast to the number of events observed propagating in either direction and so the mechanism of reconnection may only be a minor source of aperiodic waves.

A small scale version of the centrifugal interchange instability [e.g. Gold (1959) & Burch et al. (2005)] may also be a method of producing aperiodic waves, where hot, rarefied plasma from the outer magnetosphere interchanges with cold, dense plasma of the inner magnetosphere. This localised change in plasma conditions may cause a local change in the position of the current sheet, the current sheet position is expected to hinge (Arridge et al., 2008b) due to changes in mass of the current sheet and solar wind conditions. If a local change in density arrives at Cassini it may appear as a sudden change in position of the current sheet. This may then propagate outwards from the inner magnetosphere where interchange is expected, thus appearing as outward travelling aperiodic waves.

Finally, planetary period oscillations (PPO) are known to effect the position and thickness of the current sheet [Arridge et al. (2011); Thomsen et al. (2017); Cowley et al. (2017)], however, detections of aperiodic waves are dependent on how close Cassini is to the current sheet, and this position is dependent on PPO. When this observation bias is removed from the data, no dependence on PPO within uncertainties is found for the occurrence of aperiodic waves. The observation bias is tested using synthetic data sets with dependence and with no dependence for the trajectories of Cassini, this is then compared to the measured dependence. An overview of this test can be seen in figure 3.18 where the null hypothesis is accepted for the measured occurrence (southern phase only displayed) (Arridge, C.S., private communication). The measured dependence on PPO values resembles the 'no dependence' plot in figure 3.18.

The majority of sources explored could possibly source the aperiodic waves, however it is most likely that the large distribution of wave parameters point to a combination of all the above mechanisms as sources.

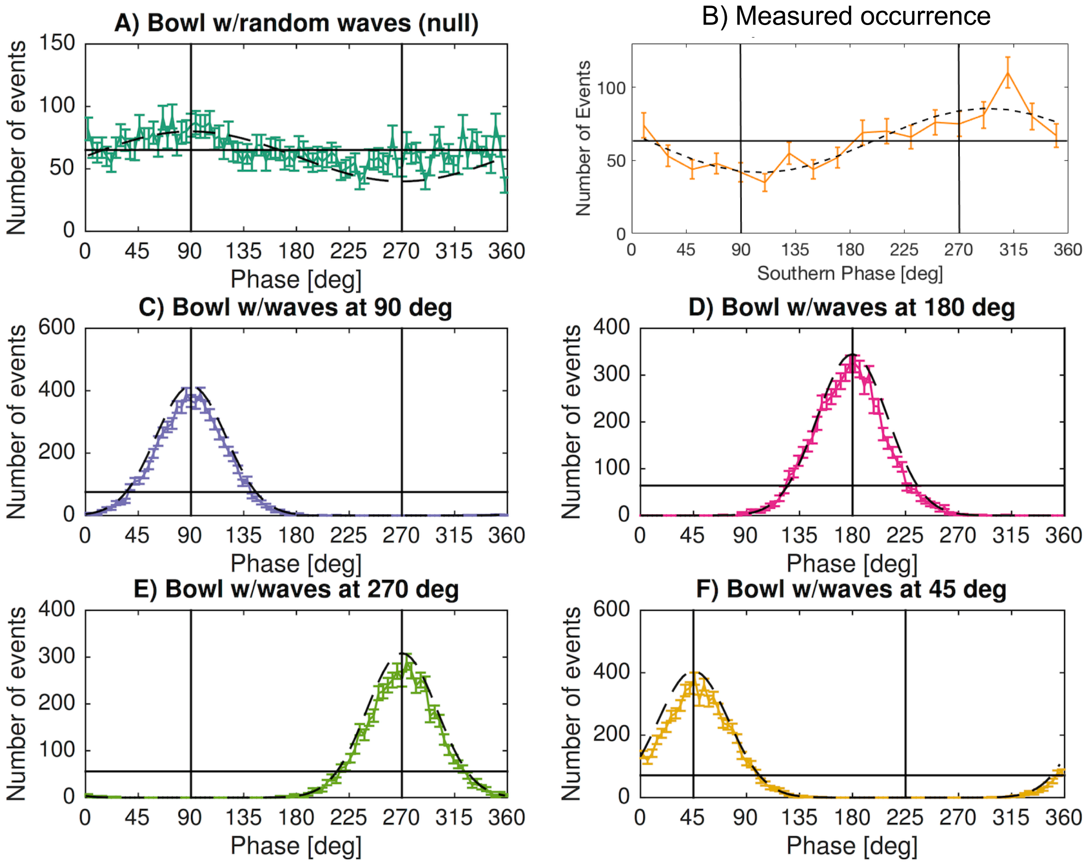

FIGURE 3.18: Figure shows a test for dependency of aperiodic waves on PPO. A) shows the null hypothesis of no PPO dependency, B) shows the measured distribution for southern phase. C) - F) show the distribution with dependencies on different phase angles and what one would expect if a dependency was shown (Arridge, C.S., private communication).

3.7 Conclusion

Saturn's current sheet has shown to be a dynamic and changing environment. Along with periodic waves such as the rotation rate flapping and the seasonal bowl shaped movement of the current sheet, frequent aperiodic waves also travel along the sheet. These waves last from 1 to 30 minutes, show a deflection of more than 1nT in the magnetic field magnitude and have a uniform occurrence where the current sheet exists in the magnetosphere.

A model of the passage of these waves is constructed by using a modified Harris current sheet model for the radial and azimuthal magnetic field components, and a constant value for the meridional component. This model of the localised current sheet is then deformed to the shape of a Gaussian wave function moving along the current sheet to simulate the passage of a wave using the general deformation method laid out in TSY98. The use of the Harris and Gaussian equations means that eleven variable parameters can be fitted to the magnetometer data including scale height and other current sheet properties, and amplitude along with other wave parameters.

After each event is fitted to the model, the statistical view of the current sheet and its properties in Saturn's magnetosphere is displayed and discussed. It is observed that the scale height increases with radial distance from $2R_S$ to around $5R_S$ with the morning sector increasing to a maximum of $6R_S$ at $40R_S$ which is in line with previous studies on the plasma scale height. It is also shown that the distance of the bowl shaped current sheet from the equator is as expected with the seasons, and the average hinging distance is found to be 52 ± 30 R_S over the whole data set.

The two wave numbers are used to find the direction of propagation of the waves in two dimensions. The distribution shows that the majority of waves are travelling in the positive radial direction, away from the planet. However, there is a second faction of waves that appear to be travelling inwards, specifically in the noon and evening sectors which is possibly attributed to the movement of the magnetopause causing the waves as the magnetosphere expands and contracts. A definitive source of the waves is still an unknown, however the source on the outward travelling waves must be located in the inner magnetosphere and a number of possibilities were explored and evaluated.

Additionally, the amplitude of the waves increases with radial distance.The orbit of Cassini would allow detection of small amplitude waves at large distance. Their absence when they could be present in the data, leads to the conclusion that amplitude grows with distance. This increase in amplitude can then be attributed to a decreasing density, if all parameters remain constant as a wave travels than if it is travelling in a decreasing density medium the amplitude will increase proportionally.

In conclusion, fitting magnetometer data with a model is an effective technique to extract wave and current sheet parameters from magnetometer data as an aperiodic wave travels past Cassini. The waves are travelling outwards from the planet radially with increasing amplitude, along a thickening current sheet. The model described also has further possible use at other planets with single spacecraft data.

Chapter 4

Current Density Structure of Saturn's Equatorial Current Sheet

4.1 Introduction

The previous chapter outlines the use of aperiodic waves, fitted with a model, to find properties of the current sheet and of the waves themselves. In addition, we use the magnetic field components and current sheet parameters from the fitting to estimate the height integrated current density flowing in Saturn's current sheet in the radial and azimuthal directions. As the model, defined in section 3.3, is fitted in a local Cartesian system, which at the equator is very similar to a cylindrical system, we assume that B_{x0} is equivalent to the radial magnetic field in the lobes, B_{y0} is equivalent to the azimuthal magnetic field in the lobes and B_{z0} is the magnetic field perpendicular to both and northwards. For ease of understanding, this chapter will use the cylindrical coordinate system unit directions where for each event, $\hat{\boldsymbol{r}}$ is equivalent to the radial direction, and $\hat{\boldsymbol{\phi}}$ is equivalent to the azimuthal direction, however the analysis itself is done in a Cartesian sense. Height integrated current density will be referred to by the acronym 'HICD'.

Khurana (2001) previously showed that the HICD in Jupiter's magnetosphere is asymmetric with local time. With a comparison to Earth and despite the radically different magnetospheric plasma flow drivers in each system, the authors argued for a solar wind influence on Jupiter's equatorial current sheet. Sergis et al. (2017) describe the current density in Saturn's ring current between 5 and 15 R_S using particle and magnetic field measurements from Cassini. The authors show that, between 12 R_S and the outer limit of the study, the particle pressure is dominated by hot plasma with some local time effects and additionally, the authors describe the local time and radial dependencies on the azimuthal current density. The azimuthal current density is shown to be asymmetric with an enhancement in the post-noon to midnight area around 10 R_S. The total current in Saturn's ring current has been calculated by Carbary et al. (2012) to be 9.2 ± 1.0 MA between $\sim 3-20$ R_S, with a peak strength of ~ 75 pA/m^2 at around 10 R_S, however Sergis et al. (2017) calculate a maximum current density of $100-115$ pA/m^2 between $7-13$ R_S.

In this chapter we discuss the current density of Saturn's equatorial current sheet from 10 - 50 R_S to extend the current knowledge of the current density which has been explored up to ~ 20 R_S by previous authors. The current density is calculated using Ampére's law and uses the method laid out by Khurana (2001) previously used at Jupiter for HICD. These calculations use the measured and fitted magnetic field from the previous chapter.

Additionally, this chapter explores the vertical structure of the current sheet during aperiodic wave traversals. Previous current sheet studies assume the smooth function of current density at the centre of the current sheet and that the magnetic field surrounding the current sheet behaves as a Harris current sheet. These assumptions are necessary for the analysis techniques presented by the authors, and so this section of the chapter will present the test of whether this assumption is restrictive or not in the Saturn system.

This chapter also investigates bifurcation of the current sheet, which describes the splitting of the current density into two maxima around the centre where a minimum occurs. Bifurcation is common in the Earth's current sheet: 25% of all current sheets sampled (Asano et al., 2005; Thompson et al., 2006). Bifurcation in Earth's cross-tail current sheet has been shown to be a precursor or a result of magnetic reconnection events [e.g Nakamura et al. (2002), Thompson et al. (2006) & Birn and Hesse (2014)] and more recently, a link to substorm onset and current density increases has been shown

(Saito, 2015). Perturbations in a model dipole field have also shown a bifurcated current sheet at Earth (Sitnov and Merkin, 2016). Current sheets that exhibit bifurcation in models have also been found to be stable against a number of instabilities [Ricci et al. (2004), Camporeale and Lapenta (2005), Génot et al. (2005), Matsui and Daughton (2008)]. At Earth these instabilities can also be associated with a flapping motion of the current sheet, which is also shown to be related to bifurcation [Sergeev et al. (2003a), Sitnov et al. (2004)] and also reconnection [Runov et al. (2003), Mok et al. (2006)].

Cluster mission observations of plasma and magnetic field at Earth and models of bifurcated current sheets have also been used to show that anisotropies in the ion temperature and pressure can form a bifurcated current sheet [Sitnov et al. (2003), Sitnov et al. (2004), Israelevich and Ershkovich (2008)]. Motion of particles around the centre of the current sheet have also been explored by Zelenyi et al. (2002), Zelenyi et al. (2003) & Delcourt et al. (2006), showing that a current maximum is found away from the magnetic null point, especially when considering the role of oxygen ions (Dalena et al., 2010; Greco et al., 2007).

4.2 Methodology

4.2.1 Height Integrated Current Density Calculations

Azimuthal current density in the local cartesian system is given by equation 4.1 where B_r and B_ϕ are the radial and azimuthal magnetic field components. This equation is the azimuthal component of Ampére's law.

$$J_\phi = \frac{1}{\mu_0}\left(\frac{\partial B_r}{\partial z} - \frac{\partial B_z}{\partial r}\right) \tag{4.1}$$

We must consider the 'differenced' magnetic field lobe values, where the value of the dipolar magnetic field of Saturn is already removed from the values calculated by the model in the previous chapter (section 3.3). Assuming a thin current sheet we can assume that the differenced radial magnetic field is a function of only z, and the north-south magnetic field is only a function of r. Therefore we may rewrite equation 4.1 as:

$$J_\phi = \frac{1}{\mu_0}\left(\frac{\partial \Delta B_r}{\partial z} - \frac{\partial \Delta B_z}{\partial r}\right), \tag{4.2}$$

where Δ denotes a 'differenced' field. We then integrate over the height of the current sheet - or the scale height, H, that we calculate in the previous chapter, to retrieve an estimate of the height integrated current density of the current sheet.

$$J'_\phi = \int J_\phi \, \mathrm{d}z = \frac{1}{\mu_0}\left(2B_{r0} - 2H\frac{\partial B_{z0}}{\partial r}\right) \tag{4.3}$$

We can obtain all of the values above from the model used in the previous chapter, apart from the differential in the second term on the right hand side of equation 4.3. This is found by fitting a polynomial of order three to the differenced magnetic field (where $\Delta B_z = B_{z0}$) value shown in equations 4.4 and 4.5.

$$B_{z0} = \frac{a}{r} + \frac{b}{r^2} + \frac{c}{r^3} \tag{4.4}$$

$$\frac{\partial B_{z0}}{\partial r} = \frac{a}{r^2} + \frac{2b}{r^3} + \frac{3c}{r^4} \tag{4.5}$$

Figure 4.1 shows the example of B_{z0} values (blue) from the study in the previous chapter as a function of radial distance. Values of B_{z0} are outputs of the model which is already a 'differenced' field component. A best-fit polynomial of the form given by equation 4.4 is shown with a solid red line. The values of a, b and c are then used in equation 4.5 to calculate the differential at each radial distance to be used within the analysis. In this example, a = 216.0 ± 38 $nT\ R_S$, b = 6364 ± 498 $nT\ R_S^2$ and c = 56410 ± 2911 $nT\ R_S^3$.

The radial height integrated current density is derived from the radial component of Ampére's law 4.6 using the differenced magnetic field values.

$$J_r = \frac{1}{\mu_0}\left(\frac{\partial \Delta B_z}{\partial \phi} - \frac{\partial \Delta B_\phi}{\partial z}\right) \tag{4.6}$$

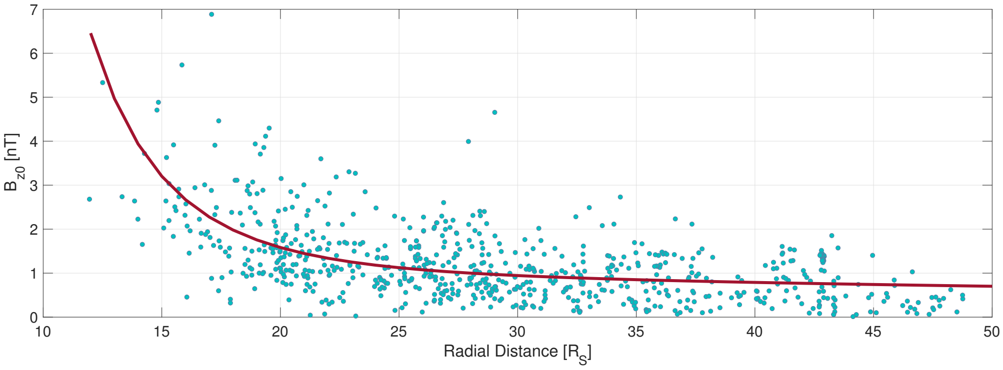

FIGURE 4.1: Figure showing measured values of B_{z0} against radial distance (blue dots) fitted with a polynomial (red line)

B_z is shown to be unvarying in local time, and so the first term is assumed to be 0. We then integrate over the scale height of the current sheet to get the radial height integrated current density.

$$J'_r = \int J_r \, \mathrm{d}z = -\frac{2B_{\phi 0}}{\mu_0} \tag{4.7}$$

4.3 Results

4.3.1 Local Time Structure of Height Integrated Current Density

Azimuthal HICD (J'_ϕ) is shown in figure 4.2 on a logarithmic scale of Am^{-1}. The top panel shows all events projected onto the X-Y KSM plane, where each bin is 1x1 R_S in size and values for each event are averaged inside each bin. All of the figures also show the orbits of Rhea (8 R_S) and Titan (20 R_S) along with a minimum and maximum magnetopause position using the Arridge et al. (2006) magnetopause model. Below the overview are four radial profiles, one for each specified local time sector. The radial profiles are colour-coded according to Cassini Rev and year.

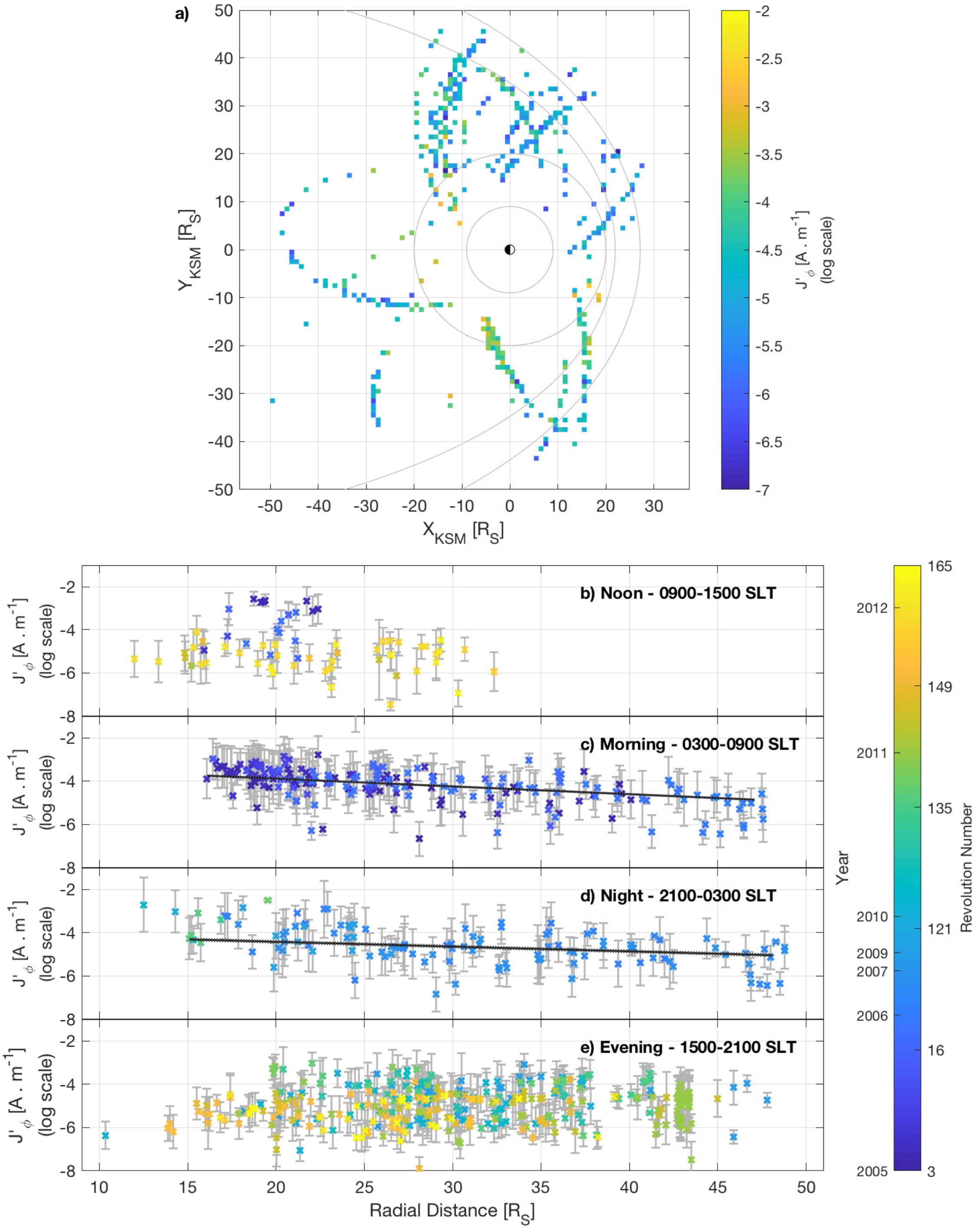

FIGURE 4.2: Azimuthal HICD in Saturn's magnetosphere. All plots are shown on a log scale. a) shows the overall view where each coloured box gives the average azimuthal HICD in the bin. The orbits of Titan and Rhea along with a minimum and maximum magnetopause position are shown. b-e) show local time and seasonal changes.

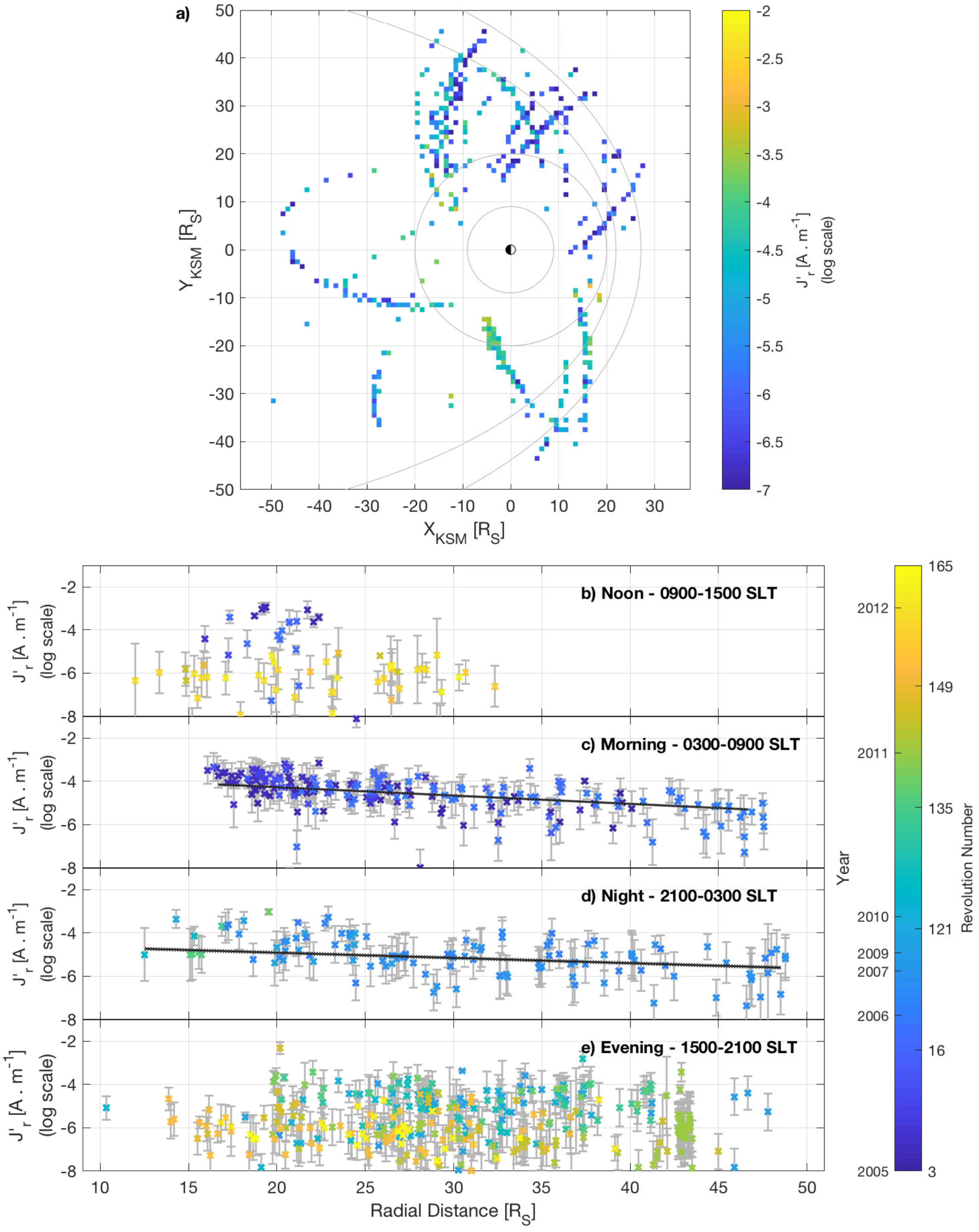

FIGURE 4.3: Radial HICD in Saturn's magnetosphere. All plots are shown on a log scale. a) shows the overall view where each coloured box gives the average radial HICD in the bin. The orbits of Titan and Rhea along with a minimum and maximum magnetopause position are shown. b-e) show local time and seasonal changes.

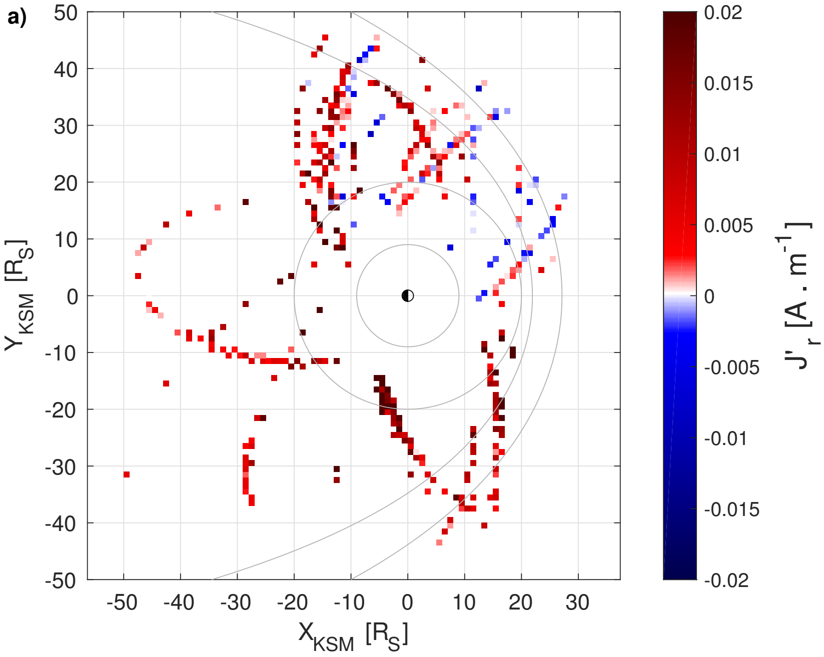

FIGURE 4.4: Radial HICD in Saturn's magnetosphere. Each coloured square represents the average value of radial height integrated current density, where the emphasis is given to positive (red) or negative (blue) values. The orbits of Titan and Rhea along with a minimum and maximum magnetopause position are shown.

The azimuthal HICD decreased with radial distance in both the morning and night sectors (figure 4.3). There are large temporal difference in the noon and evening sectors with little correlation with radial distance seen within them. We can however see a small decrease in the yellow (late 2011 and 2012) events in the noon sector with radial distance and hence an overall decrease is seen in the noon sector. The median value of azimuthal height integrated current density in the current sheet is $\sim 0.5\ MA/R_S$.

Radial height integrated current density (J'_r) is shown in figure 4.3; this plot has the same layout as figure 4.2. We see a decrease with radial distance in the morning and night sectors, and large temporal differences in the noon and evening sectors are seen. The majority of negative values of radial HICD are found in the evening/late noon sector. This can be seen in figure 4.4 where the values are presented on a linear scale with red as positive values of radial HICD, and blue as negative values. The median value of radial height integrated current density is $\sim 0.3\ MA/R_S$.

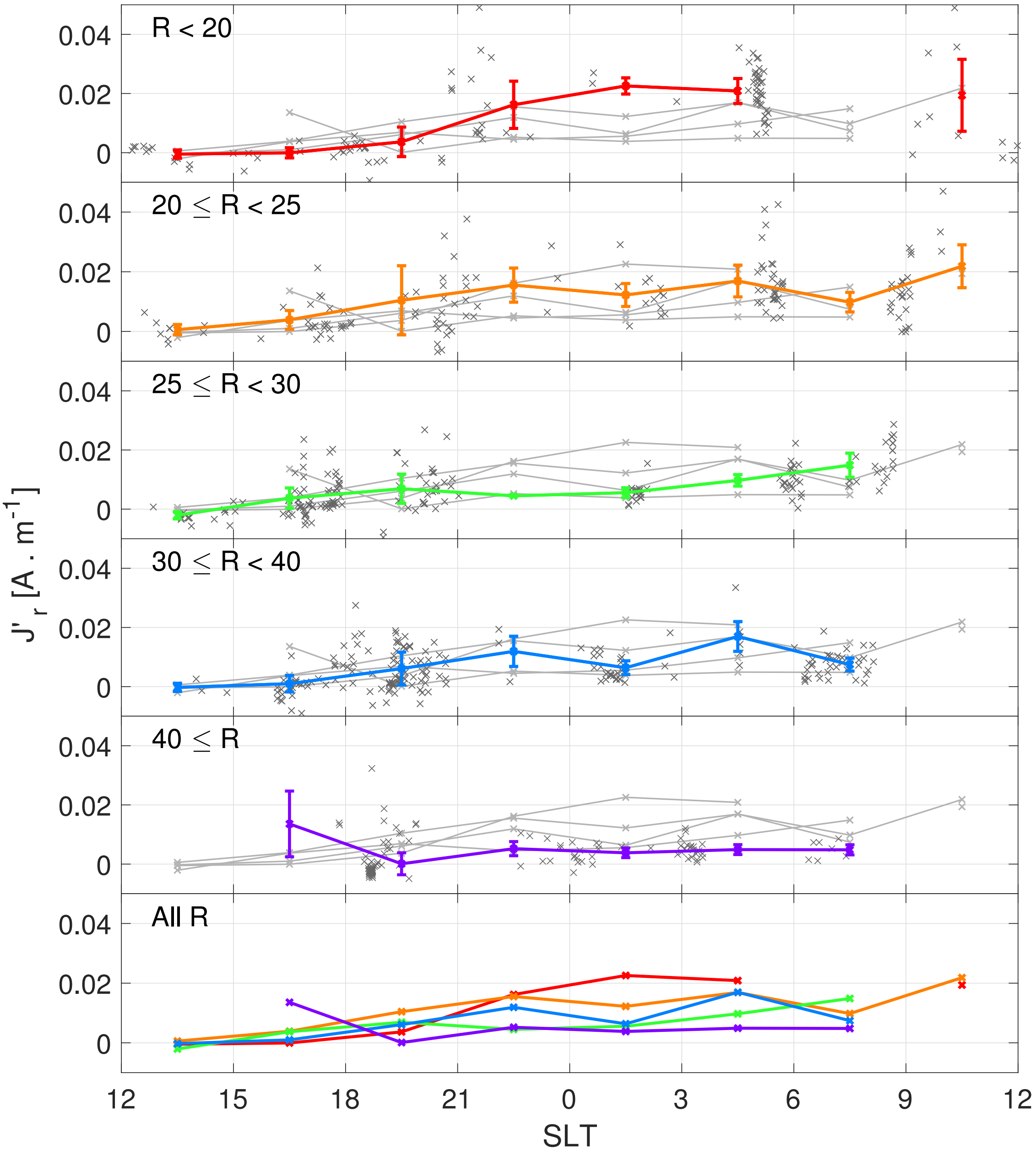

FIGURE 4.5: Radial HICD vs. local time at different radial distances. The mean of each 3hr local time bin is shown by the coloured lines.

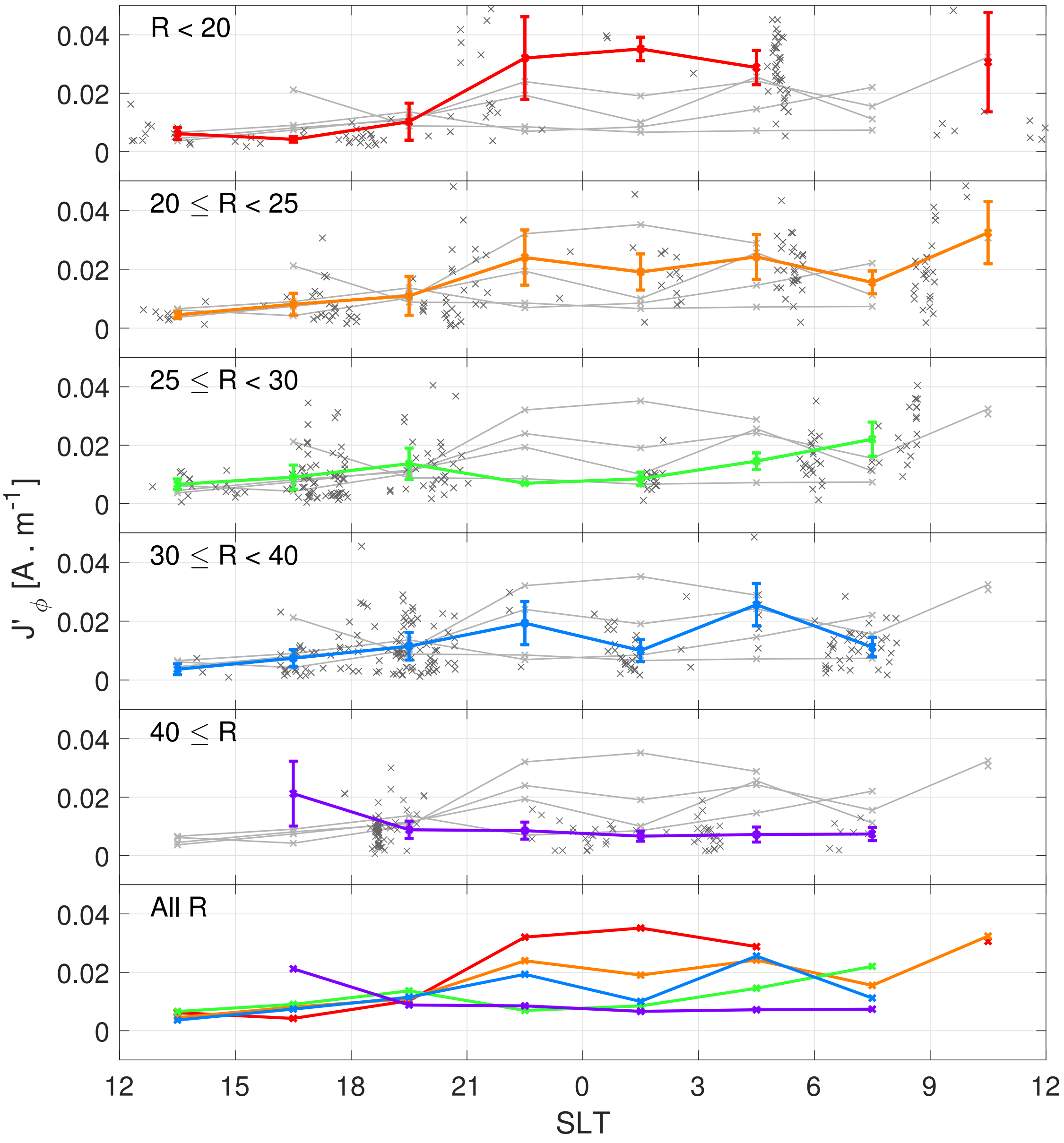

FIGURE 4.6: Azimuthal HICD vs. local time at different radial distances. The mean of each 3hr local time bin is shown by the coloured lines.

Figures 4.5 and 4.6 show local time structure of the HICD at different ranges in radial distances. Each plot shows the HICD in Am^{-1} vs. Saturn local time. The mean of 3hr local time bins is shown as a coloured marker with error bars relating to the standard deviation of values within each bin and the number of points in each bin (i.e. standard error). A trend line is shown between the mean values of each bin to better identify the local time structure. The bottom plot shows the comparison of the trend lines for each radial distance. Radial HICD (figure 4.5) shows a small local time change with larger positive values found in the post-midnight sector at smaller radial distances. All negative values are found between 12 and 21 SLT (evening sector) where swept forward fields are expected. At larger radial distances, the current density is constant across SLT. Azimuthal HICD (figure 4.6) again shows a similar SLT structure to the radial HICD in that a peak is seen post-midnight, however no negative values are found in azimuthal HICD as the field of Saturn is directed southward and will always cause a positive azimuthal current at the equator, if no larger perturbations affect the magnetosphere. A decrease in HICD is also seen with radial distance at all SLT.

Local Time		Radial Current [MA]	Azimuthal Current [MA]
All SLT		15.4 ± 4.4	32.8 ± 5.5
Morning	$3 \leq$ SLT < 9	23.3 ± 3.2	34.0 ± 4.8
Noon	$9 \leq$ SLT < 15	4.7 ± 1.5	13.7 ± 2.1
Evening	$15 \leq$ SLT < 21	7.7 ± 2.8	20.1 ± 2.7
Night	$21 \leq$ SLT < 3	20.3 ± 1.7	35.8 ± 2.7

Table 4.1: Mean total current for all local time sectors and total current for each individual 6 hour local time sector.

By integrating the HICD radial and azimuthal values radially, one can find the total current flowing in each local time sector and in the entire system. Uneven numbers of data points in each radial bin of 1 R_S width is solved by stratifying the data i.e. 20 events are sampled in each bin with replacement so that an event may be sampled multiple times, or not at all, in one bin. These 20 events are then averaged to give a value for that radial bin. This is repeated for radial distances of 10-61 R_S which are then summed to give a total current value. A mean and standard deviation are then found for each local time bin of 6-hours width by repeating this process 1000 times. The means and standard deviations are presented in table 4.1.

4.3.2 $\nabla \cdot \boldsymbol{J'}$: Divergence of Height Integrated Current Density

The divergence of the HICD in the radial and azimuthal direction can be used to infer the divergence of the perpendicular HICD, which in turn can be used to estimate the field-aligned currents using the continuity of currents equation (shown in full in appendix A.4):

$$\nabla \cdot \boldsymbol{J_{\perp}} = -B\frac{\partial}{\partial s}\left(\frac{J_{\parallel}}{B}\right), \tag{4.8}$$

where s is a length along the field which is positive towards North and $J_{\parallel}$ is the magnitude of field-aligned current. If equation 4.8 is integrated over the current sheet thickness, we find:

$$\nabla \cdot (\boldsymbol{J'_r} + \boldsymbol{J'_\phi}) = \nabla \cdot \boldsymbol{J'_r} + \nabla \cdot \boldsymbol{J'_\phi} = -2J_{\parallel}\frac{B_z}{B_{lobe}}, \tag{4.9}$$

where $\frac{B_z}{B_{lobe}}$ is the ratio of the perpendicular field in the current sheet and the field strength in the lobe just outside of the current sheet with the assumption that B_z is invariant over the current sheet thickness.

The divergence in each of the plots is calculated by finding the gradient in radius (for the radial HICD) and in azimuth (for the azimuthal HICD). This is done by finding the central differences, $\nabla \cdot J'_r \sim \frac{J_r^{i+1} - J_r^{i-1}}{2\Delta r}$. Perpendicular divergence is found by adding the divergence of the radial HICD to the divergence of the azimuthal HICD, as described in equation 4.9.

Khurana (2001) states that the individual divergence of the azimuthal and radial HICD's show the region 2 like field-aligned currents and the plasma acceleration field-aligned currents respectively. Figure 4.7 a, c and e show the radial, azimuthal and perpendicular HICD in Saturn's magnetosphere, respectively. Uncertainty plots can be found in figures 4.7 b, d and f. For reference, the number of events in each bin can be found in figure 4.7 g. A positive value of $\nabla \cdot \boldsymbol{J_{\perp}}$ requires field-aligned currents to flow into the equatorial current sheet from the lobes.

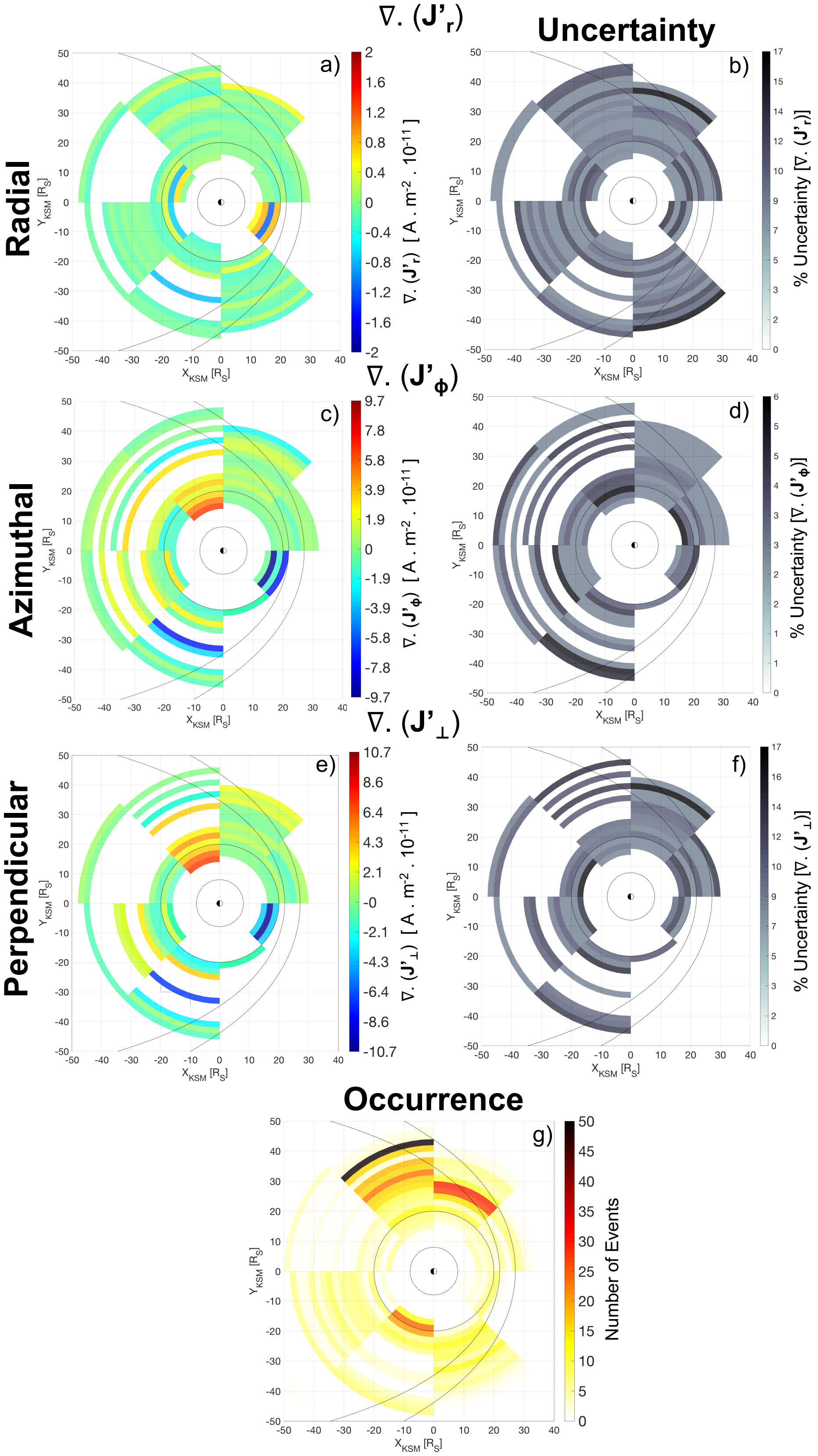

FIGURE 4.7: Divergence of the HICD. Coloured blocks show the average value of the divergence of the HICD projected onto the X-Y KSM plane. An approximate minimum and maximum magnetopause position calculated from Arridge et al. (2006) along with the orbits of Titan and Rhea at 20 R_S and 9 R_S are indicated by the grey lines.

4.4 Vertical Structure of the Current Sheet

Israelevich and Ershkovich (2006) developed a method of detecting bifurcated current sheets at Jupiter based on the method laid out by Hoshino et al. (1996) used for detecting bifurcated sheets at Earth. The updated method uses the full time derivative of the magnetic field that is perpendicular to the flow direction of the current. The component normal to the current sheet is used as a proxy for the distance from the current sheet 'centre'. The authors examine one bifurcated event, which is then expanded upon by several other examples in Israelevich et al. (2007) where an ion pressure anisotropy is described as the cause of the bifurcated sheets.

Bifurcated sheets make up a very small percentage of current sheets that were examined by these studies. Hence the authors conclude that the phenomenon is very rare at Jupiter and that the difference in bifurcated vs. Harris-like current sheet at Earth and Jupiter may be due to a difference in ion distribution functions, originating from the different transport processes of plasma in the magnetospheres that create the current sheets.

Investigating the vertical structure of Saturn's current sheet requires data that shows frequent encounters with the current sheet. Due to the offset of the magnetic axis and the rotational axis in Jupiter's magnetosphere, an equatorial orbiter (such as Galileo) would observe a regular flapping motion of the current sheet, frequently described as a 'square wave' in magnetometer data. This flapping at Jupiter allows for predictable and periodic sampling of the current sheet. However, this process (to the degree seen at Jupiter) is not present at Saturn due to a $< 1^\circ$ offset of the magnetic and rotational axes and, as such, a periodic sampling of the sheet is not possible. Also noted is that planetary period oscillations (PPO) do allow for a quasi-flapping process to occur [Arridge et al. (2011), Provan et al. (2012)]. However, this mainly acts to move the current sheet towards and away from Cassini which does not periodically sample both lobes. Therefore, the aperiodic wave structures outlined in chapter 3 and featured in Martin and Arridge (2017) are ideal candidates to investigate the vertical structure.

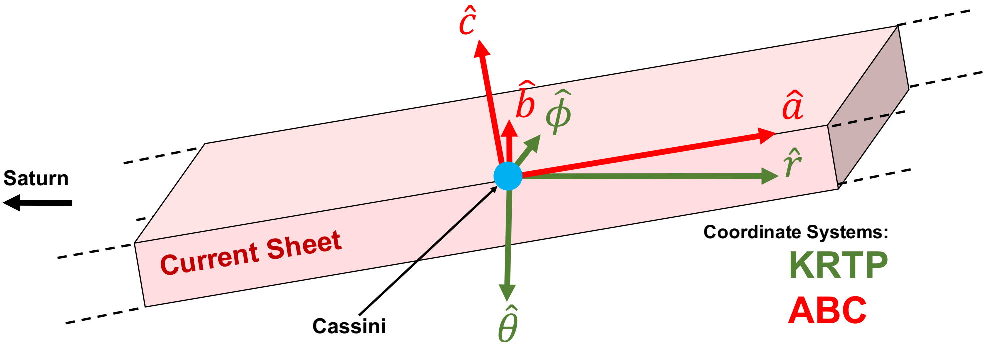

FIGURE 4.8: Figure showing the relation between the current sheet coordinate system (ABC) and the KRTP (Kronian, Radial, Theta, Phi) coordinates with respect to the current sheet and Saturn.

Firstly, the magnetic field must be rotated into a coordinate system relative to the current sheet (A, B, C), where $\hat{c}$ is normal to the current sheet, $\hat{b}$ is in the direction of the flow of current and $\hat{a}$ completes the right handed system and is positive roughly in the outward radial direction. Figure 4.8 describes the two coordinate systems (A, B, C) and KRTP with respect to Saturn and the current sheet. To rotate into the current sheet coordinate system, a normal to the current sheet must be found which is then used to calculate the angles needed to rotate the original system by. Two methods are utilised to estimate the normal direction, MVA (described in chapter 2), where the minimum variance direction is equivalent to the normal of the current sheet, and coplanarity, which are both discussed in the following sections.

In certain cases, MVA produces directions which are degenerate, when this occurs the uncertainty on the direction of the current sheet normal is large and, in most cases, unusable. Hence, a second method of determining the current sheet normal is used to calculate and check the direction of the normal. This method is named coplanarity, as the vectors to be discussed are coplanar. The difference between the northern lobe magnetic field and the southern lobe magnetic field ($\Delta \boldsymbol{B}$) and the cross product of those values ($\boldsymbol{B_N} \times \boldsymbol{B_S}$) are both in the plane of the current sheet and hence the cross product of these two vectors $\Delta \boldsymbol{B} \times (\boldsymbol{B_N} \times \boldsymbol{B_S})$ will be in the normal direction as shown in figure 4.9.

MVA is initially used to determine the normal direction as uncertainties obtained

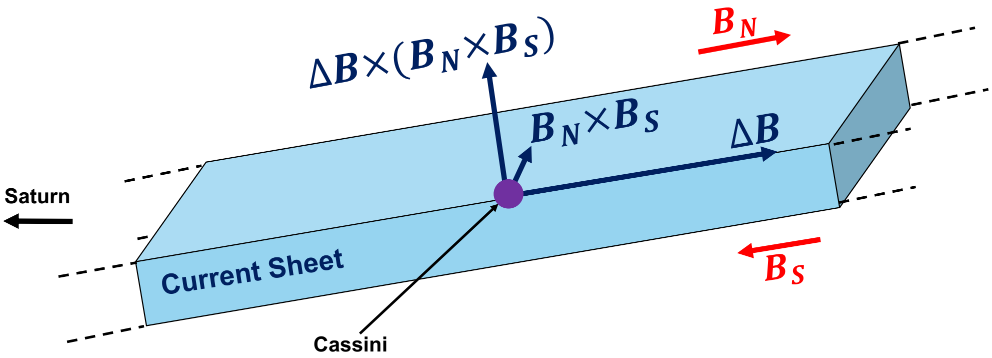

FIGURE 4.9: Figure showing the vectors involved with calculating the normal to the current sheet using coplanarity with respect to the current sheet and Saturn.

from a bootstrapping method are generally smaller than those found during coplanarity. However, this is under the assumption that the minimum and intermediate directions are not degenerate (i.e figure 2.6 b or c). When these directions are degenerate or uncertainties are large, the second method, coplanarity, is used. An additional aspect of the two methods is that the direction of maximum variance, which is usually well defined and not degenerate, is equivalent to the $\Delta \boldsymbol{B}$ direction in coplanarity. This can be used as a check for both methods, and when both methods are utilised give the same values within uncertainties.

Once a normal direction is established, the angles (α, β, γ) needed to rotate KRTP into ABC are defined from the three planes of the normal from the radial direction for α and β, and from the ϕ-direction for γ which follow the method of Euler angles for rotating a coordinate system.

Now the magnetic field is presented in a current sheet coordinate system, the focus now rests on the magnetic field in the direction of a (B_a). B_a is dependent on time and also the position of the current sheet relative to Cassini, and hence is expressed as $B_a(t) \approx B_a(c(t))$ where c is the position of the current sheet in $\hat{c}$. An expression for the full derivative reads:

$$\frac{dB_a}{dt} = \frac{\partial B_a}{\partial c}\frac{dc}{dt} \tag{4.10}$$

Over the course of one aperiodic wave, it is evident that $\left\langle \frac{dc}{dt} \right\rangle$ will equal zero, and hence $\left\langle \frac{dB_a}{dt} \right\rangle \approx 0$. $\frac{\partial B_a}{\partial c}$ is proportional to the current density in the current sheet, through Ampére's law, and by plotting $\left\langle \left|\frac{dB_a}{dt}\right| \right\rangle$ versus B_a the current density profile of the sheet that Cassini measures is displayed. A Harris-like current sheet produces a peak at $B_a = 0$ in $\left\langle \left|\frac{dB_a}{dt}\right| \right\rangle$ with a gradual decrease with increasing B_a (e.g. figure 4.10). A bifurcated sheet will show two off centre maxima and a minimum at $B_a = 0$ (e.g. figure 4.11). Additionally, anything outside of these specified profiles is classed as 'striated'. It is noted that a shift of a maximum or minimum from $B_a = 0$ can be caused by global motion of the current sheet during the time period of an aperiodic wave, such as flapping motions, so it is not uncommon to find a shift of the profile to slightly off $B_a = 0$. However, the binning of data, described later, is in larger bins than any expected offset and so removes such an effect.

Estimating the current density profile at Jupiter, Israelevich and Ershkovich (2006) calculate the differential value using larger windows of time over the 'square-wave' flapping motion of the current sheet to achieve $\left\langle \frac{dc}{dt} \right\rangle = 0$. This flapping motion is regular and predictable at Jupiter using Galileo data as Galileo is a strictly equatorial orbiter and the dipole offset of Jupiter allows a planetary period wave. However, at Saturn, Cassini has a much more varied orbit in the z-direction, covering a large range of latitudes and so it cannot be assumed that the flapping caused by PPO will achieve $\left\langle \frac{dc}{dt} \right\rangle = 0$. Using the aperiodic waves that sample both lobes equally this can be met on smaller time scales at Saturn.

To calculate $\frac{dB_a}{dt}$, the numerical differential is taken, $[B_a(t+\Delta t) - B_a(t-\Delta t)]/2\Delta t$, where Δt is 1 second. The values of the differential are then binned into bins of size 0.1-0.25 nT depending on the total number of data points for each event. This allows for a reasonable number of data points in each bin throughout the event. Hence, a plot of $\left\langle \left|\frac{dB_a}{dt}\right| \right\rangle$ versus B_a can be constructed showing a proxy for distance from the current sheet versus a proxy for the current density allowing a description of the vertical structure of the current density in the sheet.

Now, a test to determine if a bifurcated, Harris-like or striated profile of current density must be determined. For this task a model of three Gaussians is used. The first Gaussian, or central Gaussian, is positioned at a *centre* value of close to or at $B_a = 0$ called 'C'. The second and third Gaussians, or peripheral Gaussians, are centred on a value *offset* (Ω) from the centre value (C- Ω and C + Ω). Each Gaussian has the same *spread* (standard deviation, σ). The central Gaussian has an amplitude (A_{Harris}) independent of the peripheral Gaussians ($A_{Bifurcated}$). If a Harris current sheet is present the first amplitude will be considerably higher than the second, and vice versa for a bifurcated current sheet.

Bayesian regression analysis (described in full general terms in chapter 2) is used to fit the model to the $\langle|\frac{dB_a}{dt}|\rangle$ versus B_a binned plots, where prior knowledge of the system is used to give a probability distribution of the most likely final result and its uncertainty. The unknown values C, Ω, σ, $A_{Bifurcated}$ and A_{Harris} are given limiting 'prior' distributions. C is modelled as a normal distribution around $B_a = 0$, the remaining are given positive only normal distributions with decreasing probability of larger results. Both amplitude prior distributions are centred around the average value of $\langle|\frac{dB_a}{dt}|\rangle$. The likelihood function is determined by finding the samples that give the lowest χ^2 values, the total number of samples from the prior distributions is 100,000 which are randomly taken from each prior distribution. The posterior is then used to estimate the 'best fit' parameters with uncertainties. The best fit parameters are then used to algorithmically determine the profile of the current density. A number of criteria must be considered for either classification. A sheet is considered Harris if:

- $A_{Harris} > 1.5A_{Bifurcated}$
- $\sigma < 2\Omega$
- $C < \Omega$

A bifurcated sheet meets the following criteria:

- $A_{Bifurcated} > 1.5A_{Harris}$
- $\Omega > 2\sigma$
- $C < \Omega$

Striated current sheets are those that fit into neither category, these events are visually inspected along with any borderline classified events as a secondary check. Examples of a striated current sheet are found in appendix A.5.

4.4.1 Results

From a total of 1461 aperiodic events, 1018 events have a non-degenerate and singly valued normal direction. Of these, 807 events sample both lobes adequately enough to give a representation of the structure of current density. In total, 79 bifurcated signatures are identified, along with 632 Harris-like/single-peaked signatures. 96 events are striated or ambiguous profiles. Hence, 10% of the current sheets with adequate sampling have bifurcated current sheet signatures, 78% show a Harris-like profile and 12% are striated.

Figures 4.10 and 4.11 display respectively, a Harris-like example and a bifurcated example of a current sheet at Saturn. Grey error bars represent the standard deviation of $\langle|\frac{dB_a}{dt}|\rangle$ for each B_a bin, the means of each bin are connected by a dotted grey line. The model best fit is represented by a solid orange line.

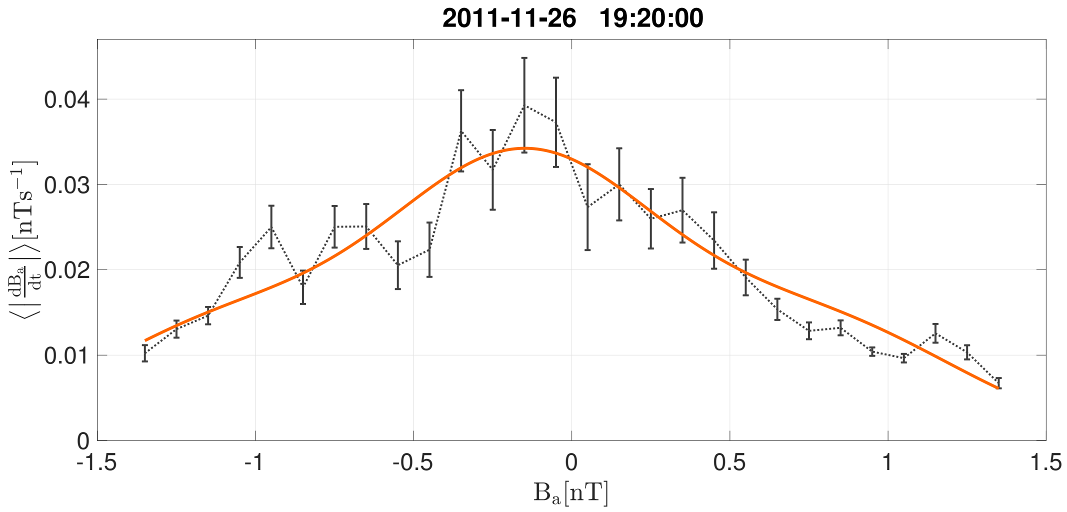

FIGURE 4.10: A current sheet with a Harris-like current density profile. The solid black lines show the spread in each B_a bin where the means of each bin are connected by the black dotted line. The solid orange line is the fitted model of three Gaussians, where the central Gaussian is dominant and hence this example is a Harris-like current sheet.

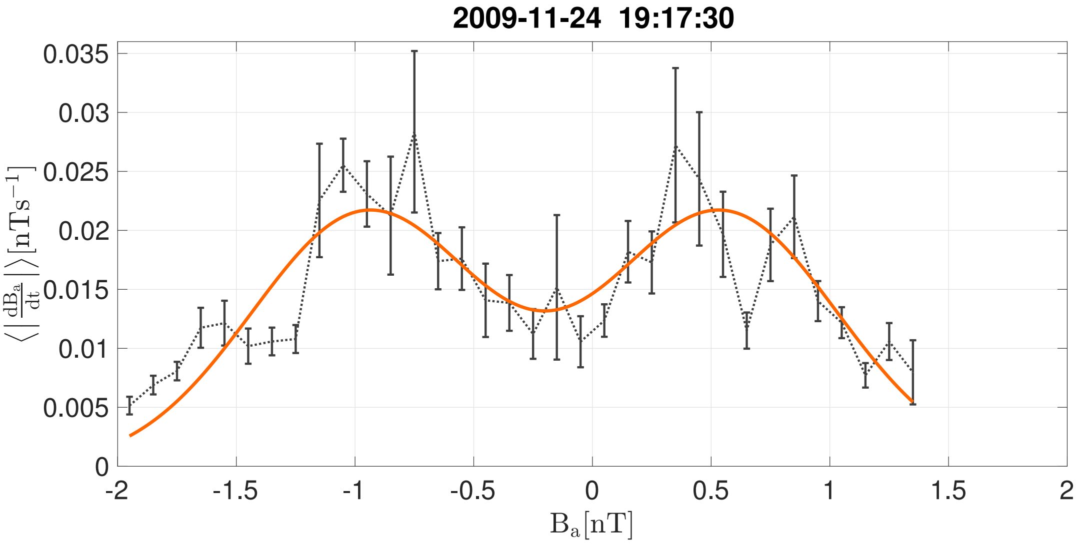

Figure 4.11: A current sheet with a bifurcated current density profile. The solid black lines show the spread in each B_a bin where the means of each bin are connected by the black dotted line. The solid orange line is the fitted model of three Gaussians, where the peripheral Gaussians are dominant and hence this example is a bifurcated current sheet.

Figure 4.12 shows spatially the distribution of Harris-like (a), bifurcated (b) and striated (c) along with diagnostic tools: the ratio of bifurcated to Harris sheets (d), number of aperiodic waves in each bin (e) and number of NED (not enough data) events (f). Each plot show the orbits of Rhea (8 R_S) and Titan (20 R_S) along with a minimum and maximum magnetopause position using the Arridge et al. (2006) magnetopause model. Spatially, there is no statistically significant overall correlation with radial distance, however an increase in bifurcated signatures is seen at dusk and inside of Titan's orbit in the morning sector. The remaining areas average at the mean value of occurence - 10%. The distributions in a, b and c are normalised by the number of aperiodic waves in each bin and converted to a percentage of total events. This is also a proxy for time spent in each bin as the number of aperiodic waves is correlated with the time spent in each spatial bin.

On average, around 50% of sheets are Harris-like sheets (a), which is expected due to around half of all events not having enough data (see 4.12 f). To compare the number of Harris-like sheet and bifurcated sheets, a normalised number of Harris-like to bifurcated signatures is shown, where 1 represents Harris dominated regions, and -1 represents bifurcated dominated regions. This is shown in (4.12 d) where as expected the

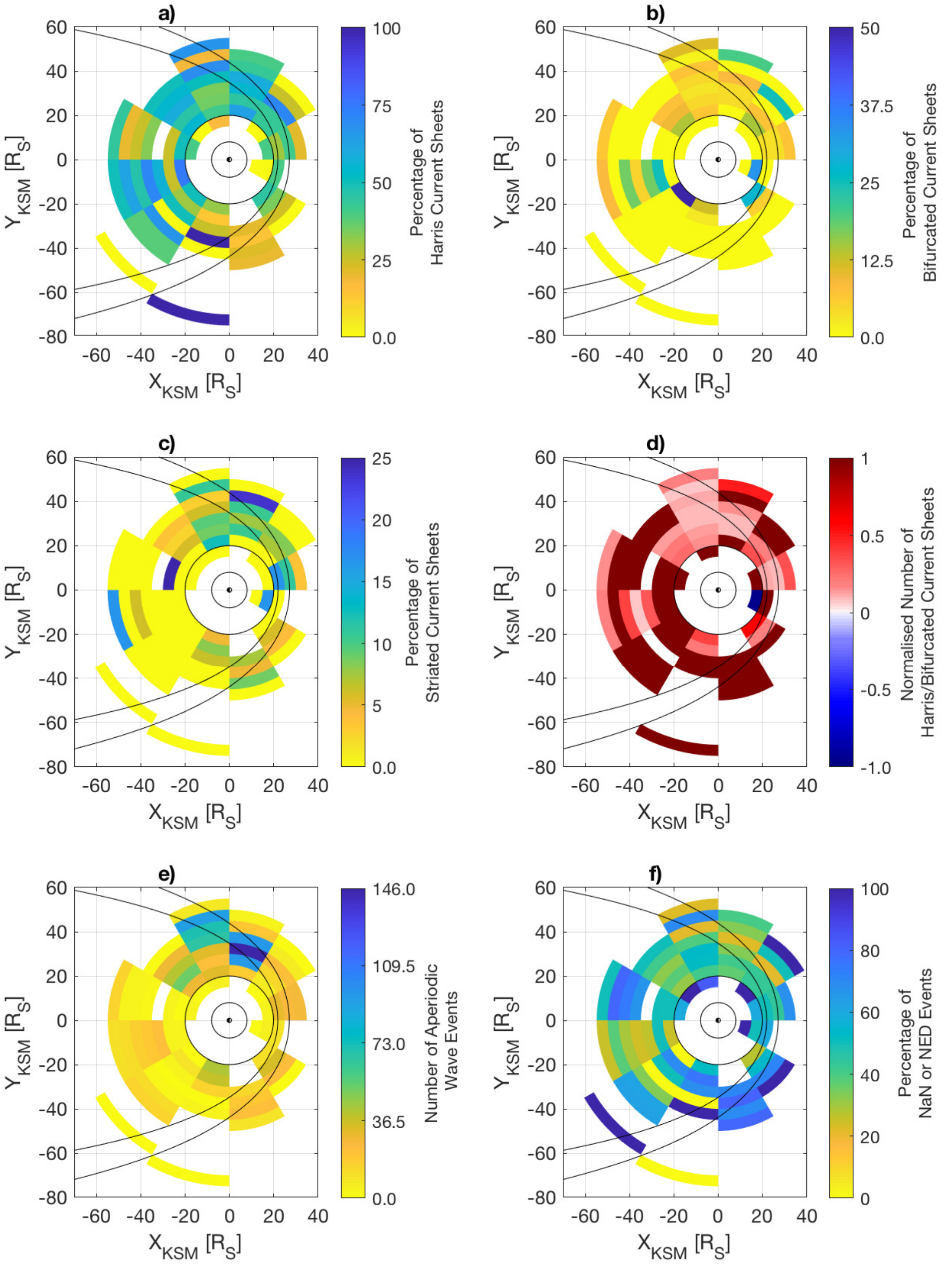

FIGURE 4.12: The position and number of Harris-like (a), bifurcated (b) striated (c) and NaN and NED (f) current sheets normalised by the total number of aperiodic wave events (e). d) shows the ratio of bifurcated to Harris-like current sheets. The figure also shows nominal magnetopause positions to guide the eye in black, Titan's orbit at 20 R_S and Rhea's orbit at 9 R_S.

majority shows Harris dominated (red) however the asymmetry in dawn-dusk occurence shown in bifurcated occurence is also present, i.e., where almost no bifurcation is seen outside of Titan's orbit in the morning sector. This lack of bifurcated signatures could be the result of a more stable and on average thinner current sheet in this area [e.g. Kellett et al. (2009), Kidder et al. (2009) & Giampieri and Dougherty (2004)].

4.5 Discussion

4.5.1 Height integrated current density

A general decrease in HICD is found in Saturn's magnetosphere with radial distance. Additionally, a peak in the post-midnight sector at smaller radial distances is seen in both components when. Negative and positive values of radial HICD are found in the late-noon and evening sectors where we sometimes expect swept forward field lines. A comparison is drawn with Khurana (2001) where the same study was applied to Jupiter's magnetosphere, in which traversals of the equatorial current sheet were used to measure the magnetic field as a function of distance from the centre of the current sheet in the z-direction to estimate the HICD using the same method outlined in section 4.2.

In figure 4.13 a comparison of radial and azimuthal HICD at Saturn with plots modified from Khurana (2001) at Jupiter using a similarly coloured colour bar are shown. We can see that at Jupiter the azimuthal HICD is stronger in the centre of the plots (noting that the azimuthal HICD is plotted as a log scale) near Jupiter than the radial HICD. This study on Saturn has a limiting factor in coverage compared to the study at Jupiter as it does not cover areas as close to Saturn because current sheet traversals due to aperiodic waves are only seen in magnetometer data outside of 10 R_S. However, we can see that on average at Saturn the azimuthal component of HICD is stronger in magnitude than the radial component.

Jupiter's radial HICD shows a large local time asymmetry in the morning and evening where the post-midnight - morning sector is enhanced compared to the night sector (figure 4.13 top right). A larger coverage of the post-noon sector of Saturn's magnetosphere allows the resolution of a similar pattern where we see the larger values of radial HICD in the morning sector and the lowest values in the post-noon to evening sector. Additionally, negative values in both studies are found in the post noon sector, relating the the occasional occurrence of field lines that are swept forwards into corotation.

To explore this local time asymmetry, plots of HICD with SLT for a number of radial distance bins are presented in figures 4.5 & 4.6. In this section, a comparison is drawn once again with the Khurana (2001) study at Jupiter and the Iijima et al. (1990) study at Earth. Figures 4.14 to 4.19 show the comparison of HICD of local time asymmetries at Earth (left), Jupiter (right) and Saturn's (middle) magnetospheres. Plots of Jupiter's local time differences are modified from Khurana (2001) and plots of Earth's local time differences are modified from Iijima et al. (1990). Figure 4.16 shows an asymmetry in Jupiter's HICD in the post mid-night section at all radial distances from 35 R_J outwards, as seen on the overall magnetosphere plots presented previously. However, at Saturn (figure 4.15) we see the largest absolute asymmetry at inwards of 20 R_S, with smaller asymmetries where the post-midnight sector is slightly enhanced out to 40 R_S. At Earth (figure 4.14) a highly sinusoidal relationship with a similar magnitude is seen for all L-shell distances due to the strong solar wind control over the magnetosphere. Unlike Jupiter's signature, the radial HICD at Saturn also shows a quasi-sinusoidal signature, similar to Earth, but shifted so it peaks at post-midnight.

The majority of negative radial HICD in the outer radial distances at Jupiter are in the evening and post-noon sector, whereas at Saturn, the mean of the bins does not drop below zero, but a large number of negative values can be seen in the data (grey crosses) at all radial distances for the evening and post-noon sectors. Therefore, Saturn's magnetosphere is similar to Jupiter's in regards to radial HICD, but has some similarities to Earth's HICD.

It is also important to note that in relation to the top two panels of figure 4.13 , the measurements of HICD in the far dusk sector are taken from the Ulysses spacecraft on its flyby of Jupiter. The spacecraft entered the system near noon at the equator but

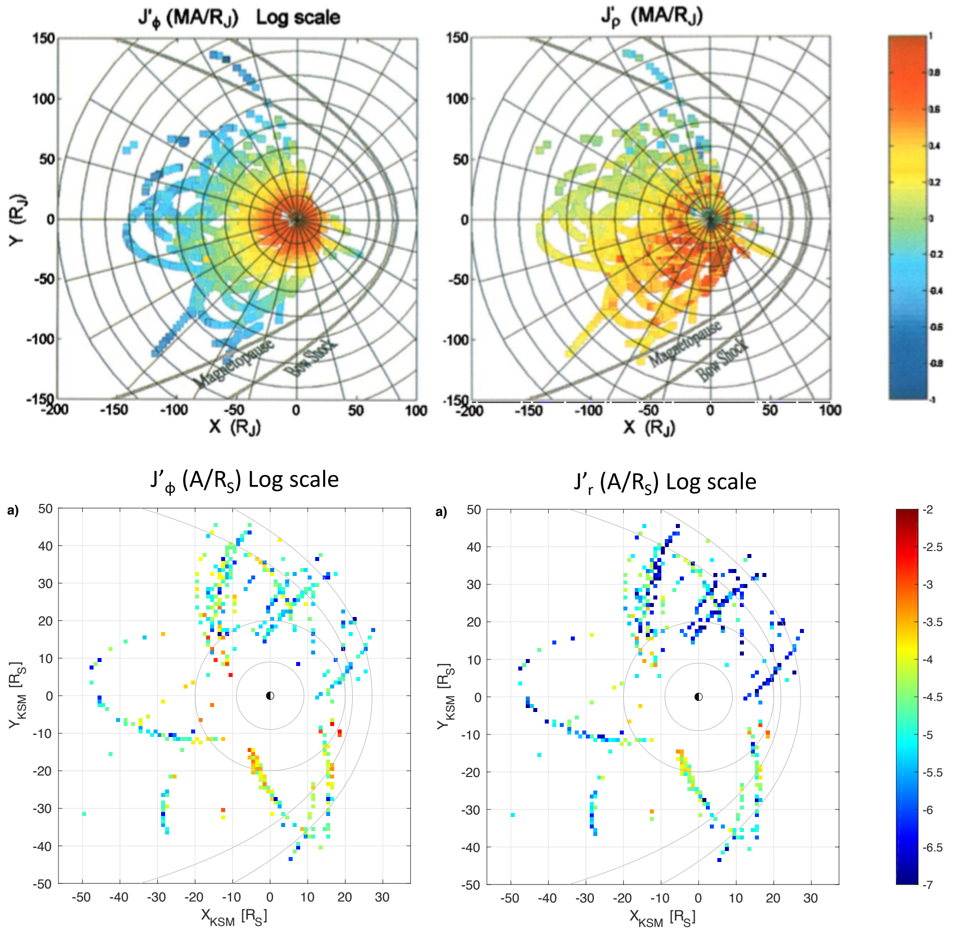

FIGURE 4.13: Figure showing the comparison of HICD in Jupiter and Saturn's magnetospheres. The top two panels are plots of azimuthal and radial HICD with Jupiter at the centre and a range of magnetopause positions from Khurana (2001). The bottom two panels are plots of azimuthal and radial HICD with Saturn at the centre, orbits of Rhea and Titan and a range of magnetopause positions.

on the outbound trajectory, Ulysses was pushed to a polar orbit around the Sun, this outbound pass constitutes some of the data in the dusk sector, which is where Ulysses was found at higher latitudes. Kivelson et al. (2002) showed that swept forward field is more likely in the higher latitudes of the magnetosphere due to magnetopause currents, but not as likely at the equator and so this is an important feature to bear this in mind when looking at different spacecraft as the data may be atypical. Cassini's trajectory is much more varied in latitude than Galileo at Jupiter, however due to the nature of the measurements (only using traversals of the current sheet in the form of aperiodic waves) we can assume that Cassini at the time of each event is inside, or very close to, the current sheet and so did not venture into the high latitude regions where swept forward fields may be more likely to occur.

The solar wind may affect the direction of the magnetic field in the post-noon sector making it sweep forward into the corotation direction, the radial HICD will be reversed compared to the majority of the magnetosphere that exhibits a swept backwards configuration due to the frozen-in effect and an attempt to accelerate mass up to the corotation rate of Saturn. Hence negative values of radial HICD in the post-noon sector are produced. Additionally, the increase of radial HICD magnitude in the post-midnight sector is interpreted as the swept backwards field of Saturn due to corotation being enhanced by the Chapman-Ferrero magnetopause currents, showing a strong coupling between HICD in Saturn and Jupiter's magnetic field and the solar wind. A decrease in the magnitude of the magnetic field with radial distance is interpreted as the reason for the decrease in HICD overall with radial distance.

Figures 4.17, 4.18 and 4.19 compare the azimuthal HICD results from Khurana (2001) at Jupiter, azimuthal current at Earth (Iijima et al., 1990), and azimuthal HICD results from this study. In the inner magnetosphere, the azimuthal currents are much larger than in the outer magnetosphere of Jupiter, where again a subtle asymmetry with an enhanced azimuthal HICD is seen in the post-midnight sector, where the absolute asymmetry is reduced with radial distance. A similar relationship occurs in Saturn's current sheet where an enhancement is seen in the post-midnight sector for the inner radial distances. The enhancement is then reduced as Cassini samples the magnetic field further out in the magnetosphere. The decrease of azimuthal HICD with radial distance is attributed to the decrease in magnetic field magnitude with radial distance.

A local time asymmetry in azimuthal HICD, where an enhancement is seen around the post-midnight sector of Saturn's magnetosphere, has a number of interpretations. A similar enhancement is seen in Jupiter's magnetosphere (Khurana, 2001) which is interpreted as a consequence of a field-aligned current system comparable to Earth's Region 2 current system which closes Earth's partial ring current (which can also be seen in figure 4.17) (Iijima et al., 1990). At Jupiter this azimuthal enhancement is described as a partial ring current closing in a similar manner (see figure 4.20), and this can be applied to observations of this small enhancement at Saturn that decays with radial distance similarly to Jupiter. However, a decay in magnitude of the peak not seen at Earth with radial distance (figure 4.17).

Additionally, Sergis et al. (2017) showed an increase in current due to pressure gradients with radial distance in the morning sector, where hot plasma injections may occur due to reconnection in the tail region. This increase in plasma pressure and hot plasma density being funnelled around to the dayside of Saturn could enhance the azimuthal current in the post-midnight to morning sector.

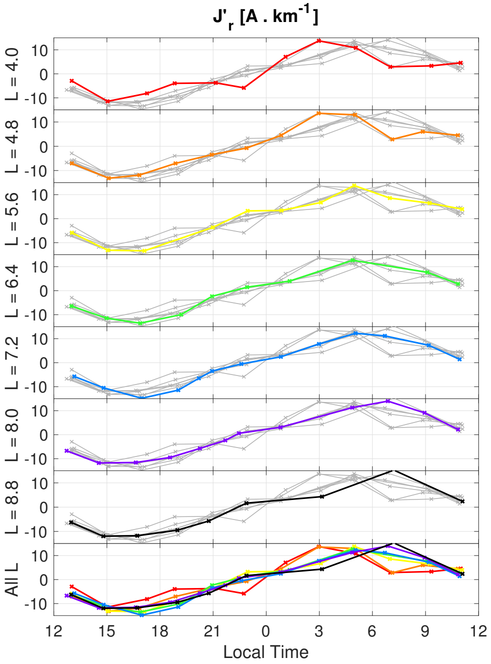

FIGURE 4.14: Radial HICD for various L-shells at Earth. Modified from Iijima et al. (1990)

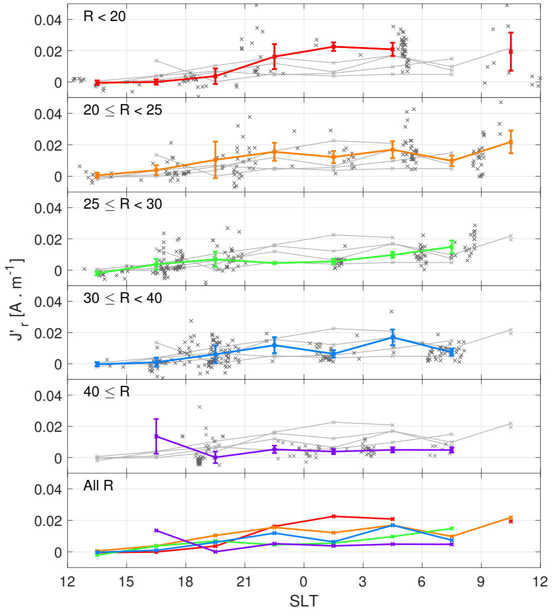

FIGURE 4.15: Radial HICD at Saturn for a range of radial distances

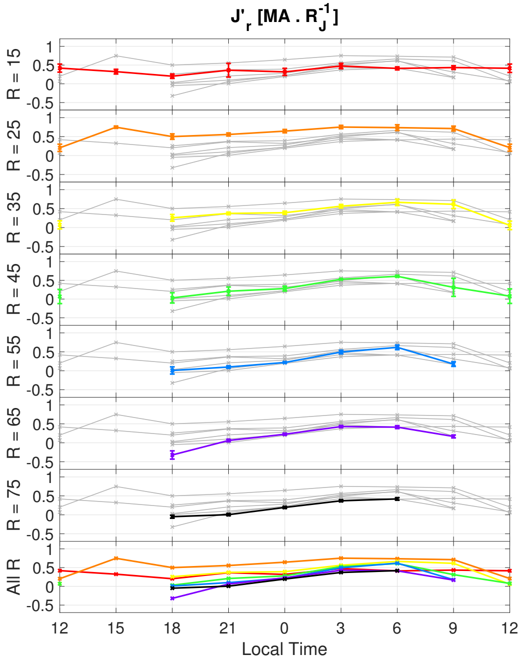

FIGURE 4.16: Radial HICD at Jupiter for a range of radial distances. Modified from Khurana (2001)

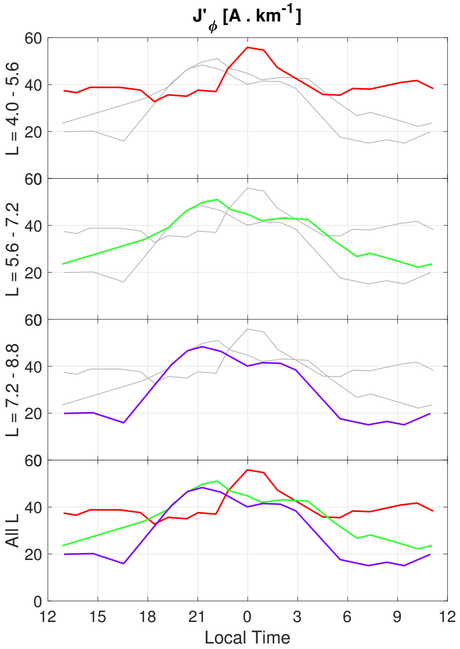

FIGURE 4.17: Azimuthal HICD for various L-shells at Earth. Modified from Iijima et al. (1990)

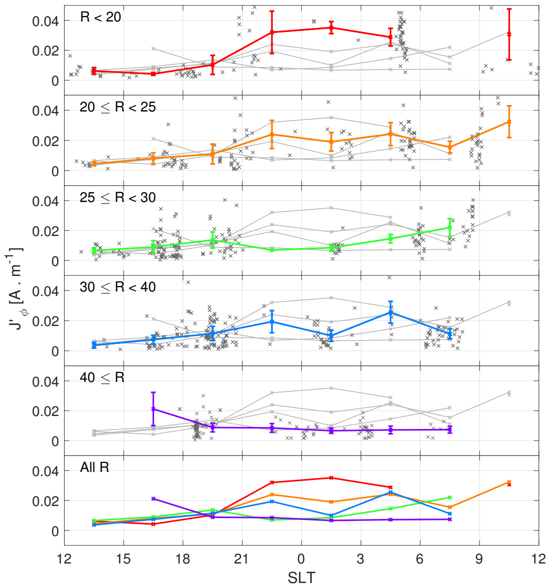

FIGURE 4.18: Azimuthal HICD at Saturn for a range of radial distances

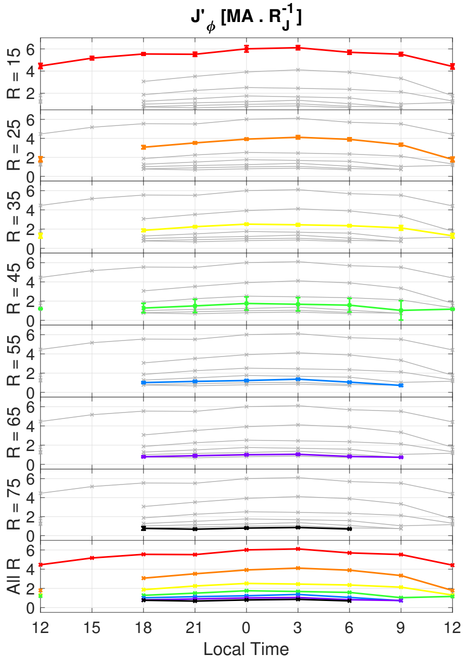

FIGURE 4.19: Azimuthal HICD at Jupiter for a range of radial distances. Modified from Khurana (2001)

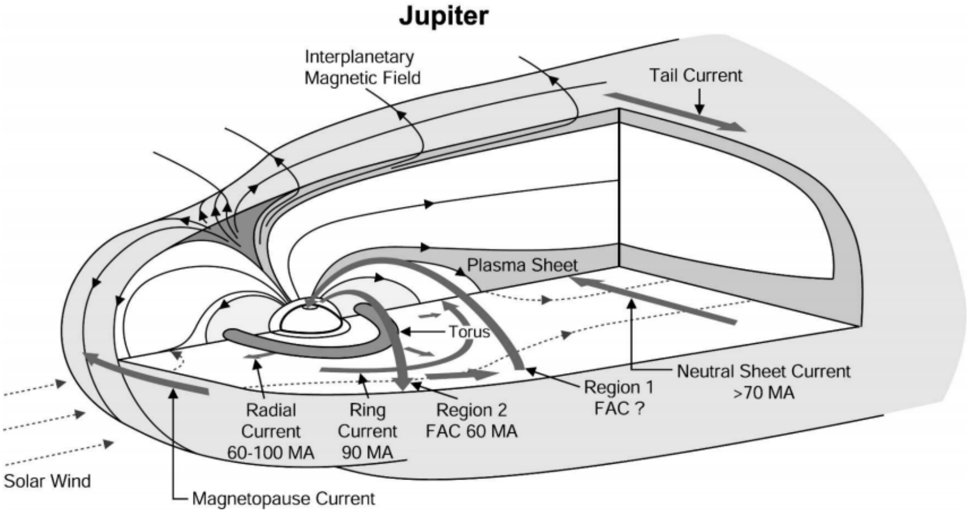

FIGURE 4.20: Diagram showing the different current systems within Jupiter's magnetosphere from Khurana et al. (2004), originally modified from Khurana (2001).

The temporal changes in Saturn's magnetosphere over the Cassini mission must be considered when surveying the magnetosphere as a whole. The equatorial Cassini revolutions used in this study range from 2005 to 2012 where at the beginning Saturn was experiencing a northern summer, and a declining solar cycle. At the end of this time period Saturn was tilting towards southern summer and was experiencing increasing solar activity. All of these changing factors could have an impact on the current density and HICD in Saturn's equatorial current sheet.

For example, figure 4.2b) shows the temporal changes in the magnetosphere, where dark blue events are from early 2005 and yellow events are from 2012. Noticeably, the yellow events have a larger radial coverage, however, their values of azimuthal HICD are on average smaller than the early 2005 values (blue). The same is true for figure 4.2e), where a gradient from yellow (2012) at the bottom to green/blue (2009) at higher values of HICD, the same is also true of the radial HICD. With this in mind, the 'bend-back' and 'bend-forward' of the magnetic field can be measured using the quantity $\frac{B_{y0}}{RB_{x0}}$, where R is the radial distance and B_{x0} and B_{y0} are the magnetic field components for each event in the lobe.

A figure containing an overview of this parameter can be found in figure 4.21. The figure shows the temporal changes in the parameter in parts b) - e) where yellow and

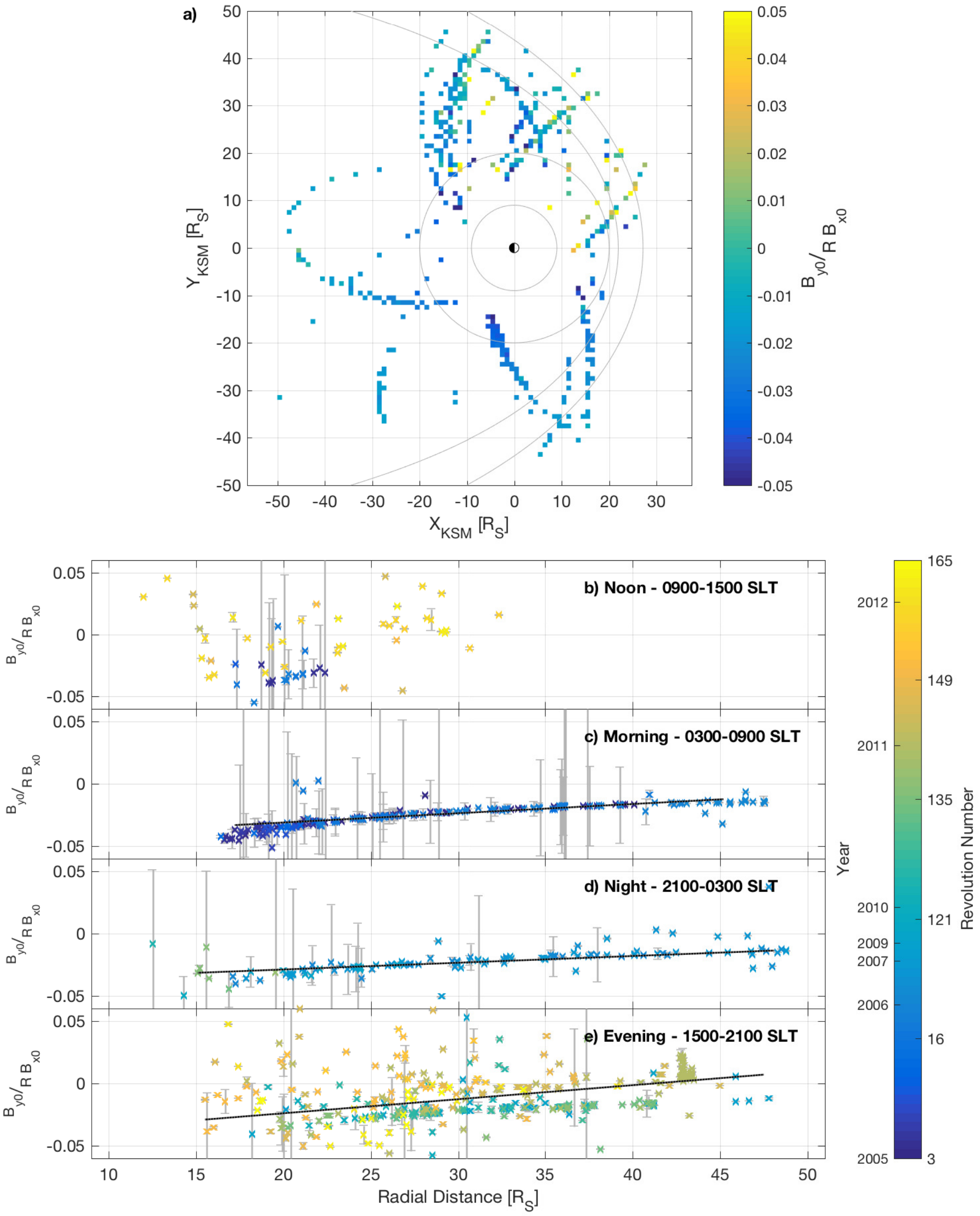

FIGURE 4.21: Figure showing the value of $\frac{B_{y0}}{RB_{x0}}$ throughout the magnetosphere.

orange events (or events that occur post 2011) are on average positive and the earlier revolutions (blue) are on average negative. Hence, there was a temporal difference in sweep-back and sweep-forward fields in the noon and evening sectors. The events that occur on swept forward fields are the events which exhibit a smaller magnitude of HICD for the current sheet, which could be related to magnetopause currents (Kivelson et al.,

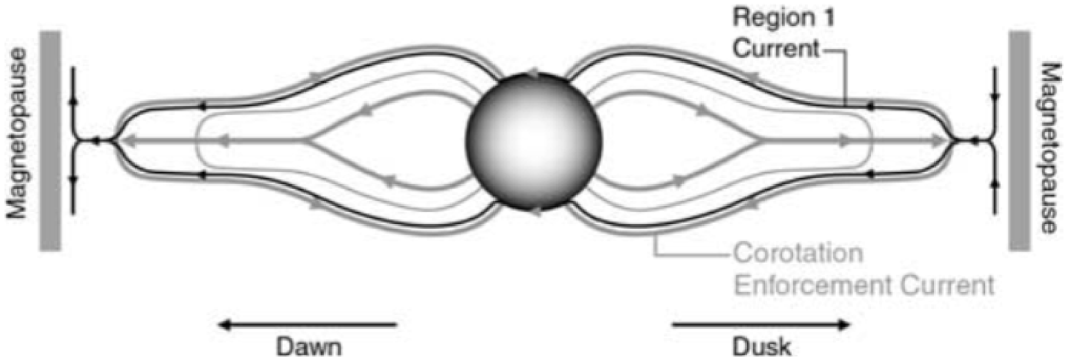

FIGURE 4.22: The magnetopause currents that may be the cause of swept-forward field lines in the dusk sector, reproduced from figure 7 in (Kivelson et al., 2002).

2002) causing a swept-forward field in the dusk sector at high latitudes, see figure 4.22. It therefore stands to reason, that these values would be smaller as they are the results of a superposition of two current systems, where the corotation enforcement currents will always be positive radially and the magnetopause current system will enhance the Region-1 type current at the higher latitudes in the dusk sector.

As the higher latitude current system is enhanced, the magnetic tension force would act upon the equatorial field and hence a large current density in the CEC (corotation enforcement current) would not be necessary, and in some cases is reversed due to super-corotation. Hence, yellow values of HICD (predominantly found at dusk) will be lower than blue values (predominantly found at dawn). However, this theory does not rule out a temporal (either Saturn season or solar wind) dependence of swept-back fields in Saturn's dusk magnetosphere, as a temporal dependence of the magnetopause currents could be occurring also. It is also important to note that to date, neither the region-1 or return CEC currents have been directly sampled by spacecraft, so future work in modelling these currents will be a useful addition to physics of the high latitude giant planet magnetospheres. For now, the evidence points to a temporal dependence, but with no direct evidence for its causation.

Solar activity is at a minimum in 2009 and near maximum in 2012, and this may help in discovering the temporal changes along with the seasonal changes in Saturn's magnetosphere. However, Vogt et al. (2017) find a weak correlation at Jupiter between current density and internal (e.g moons) or external (e.g. solar wind) drivers, hence the cause of current density changes in giant planet magnetospheres is still an open and very interesting question.

Figure 4.7 shows the divergence of the HICD in the equatorial region of Saturn along with the uncertainties of each plot and a plot of occurence for each spatial bin. The divergence of the radial HICD (figure 4.7a) is, in general, below 1 pAm^{-2} in magnitude with an average uncertainty (figure 4.7b) of 1 fAm^{-2}. There is very little evidence for spatial, and hence temporal, changes in the radial HICD. The divergence of the azimuthal HICD, however, does have some local time differences. Evident in figure 4.7c is an area of positive divergence pre-midnight in the inner magnetosphere meaning that current is being added to the current sheet inside 30 R_S and between 18 and 21 SLT. A negative divergence is found inside 30 R_S and between 09 and 12 SLT meaning that in this area current is being taken from the current sheet and supposedly being deposited in the ionosphere, which may also be driving the addition of current in the pre-midnight sector with a current system that closes in the ionosphere, like the so-called Region 2 currents in Earth's magnetosphere. The remaining areas, in general, have a much lower values of 2 pAm^{-2} and an uncertainty of 2 fAm^{-2} which can be considered the noise floor for this analysis.

This pattern of addition and subtraction of current in the dawn and dusk sectors is analogous to a partial ring current found in Earth's magnetosphere which is driven by an enhanced particle pressure in the tail fed by continual convection of magnetic flux into the area. As Saturn is a rotationally driven magnetosphere, this continual addition of flux may be where the similarity of the two planets ends. However, Sergis et al. (2017) show a pressure gradient strengthening from around 10 R_S in the midnight-dusk sector which may be a contributing factor to the the source of the region 2-type currents seen in Saturn's magnetosphere, shifted by a strongly rotating system. A direct comparison of Earth and Saturn, however, is not physically meaningful due to the vastly different magnetospheric drivers.

The divergence of radial and azimuthal HICD can be combined to give an indicator of the field aligned currents flowing from and into the ionosphere. This is seen in figure

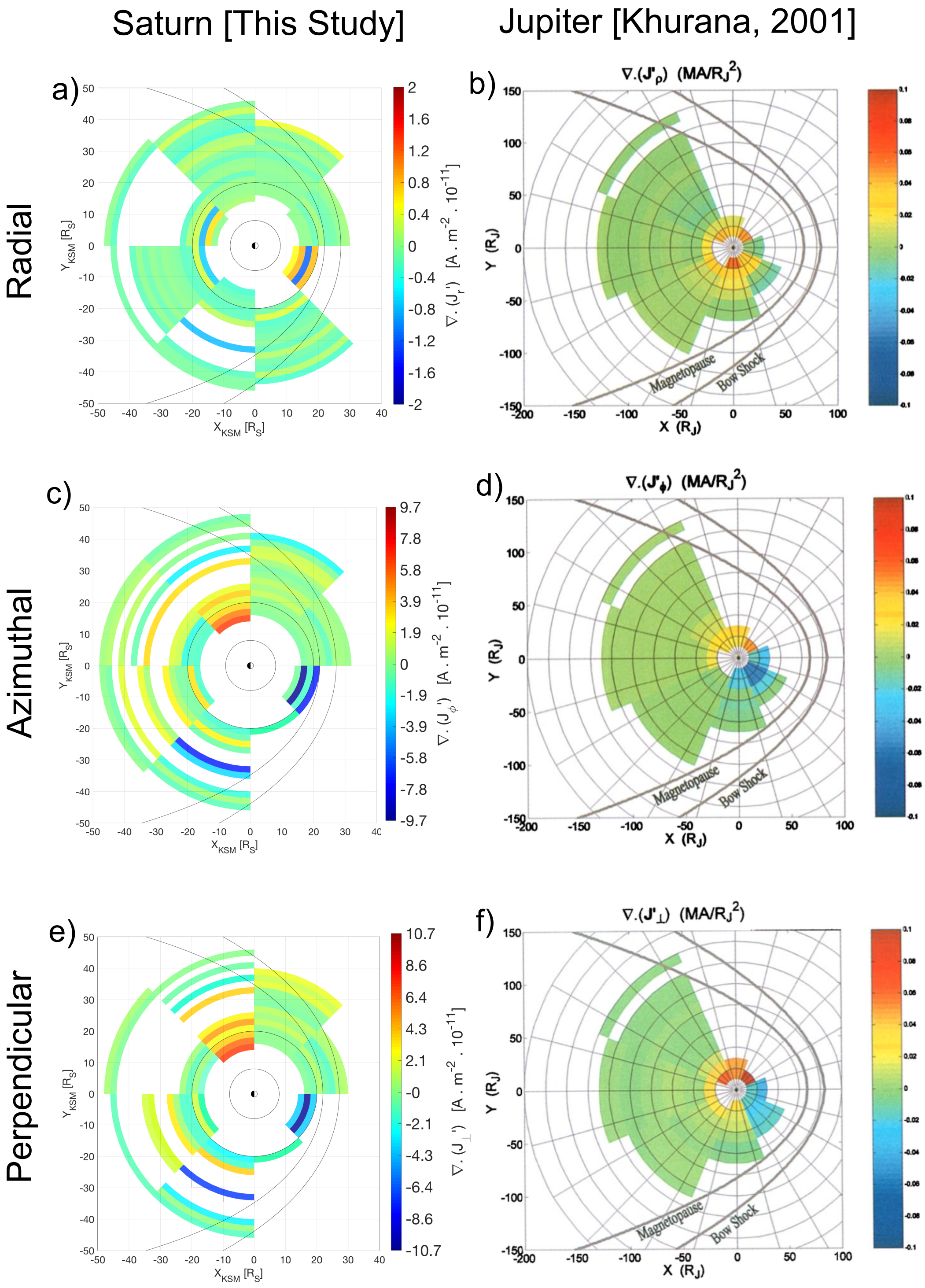

FIGURE 4.23: The comparison of divergence of HICD at Saturn and Jupiter (Khurana, 2001).

4.7e, where due to the small values of the radial divergence, the spatial distribution of field aligned currents is governed by the azimuthal divergence in the equatorial plane. A direct comparison may not be achievable with Earth, but a comparison with divergence of HICD found in Khurana (2001) at Jupiter is valuable.

Figure 4.23 shows a comparison of the divergence of HICD with a similar study at Jupiter (Khurana, 2001). The largest difference between the two systems is found in the radial components: at Jupiter there is a divergence into the current sheet (red blocks) in the inner magnetosphere and a slight negative turn outside around 20 R_J. Some areas of negative divergence in Saturn's magnetosphere are seen, but coverage of the inner magnetosphere is limited and so a conclusion of similarity cannot be reached.

The azimuthal component, however, shows a similar pattern to pre-noon negative divergence and pre-midnight positive divergence. The main difference is that at Saturn the negative and positive areas seem to be confined to just one 3-hour local time bin whereas at Jupiter they appear spread over 3-4 bins; again, this could be due to the different spatial coverage, or the fact that the current systems are found in slightly different areas or have temporal differences. The same can be said for the divergence of the perpendicular HICD.

4.5.2 Auroral Intensity

In terms of auroral intensity, an upward current in the pre-midnight sector should be associated with downward precipitation of electrons into the ionosphere. Parallel current density along the field lines connected to Saturn can be estimated using equation 4.9, where $J_{||}$ depends on the divergence of the perpendicular current density and the ratio between the magnetic field in the lobes and B_z in the current sheet. The divergence of current density in the pre-midnight sector averages to 0.04 nAm^{-2}, which, using equation 4.9, gives a value of 0.02 nAm^{-2} for parallel current density near the current sheet in the magnetosphere ($J_{||CS}$). To relate this to the current density in the ionosphere, this value must be scaled by the mirror ratio in Saturn's magnetosphere, hence the ionospheric parallel current density is calculated as 200 nAm^{-2} for a mirror ratio of 10000.

Field-aligned acceleration is required if this current is larger than the maximum current density that can be carried without acceleration by magnetospheric thermal electrons along the field lines. This is given as (from equation 10 in Cowley et al. (2004)):

$$J_{th} = eN\left(\frac{W_{th}}{2\pi m_e}\right)^{\frac{1}{2}}, \tag{4.11}$$

where e is the charge on an electron, W_{th} is the thermal energy equivalent to kT, N is the number density and m_e is the mass of an electron. Values of $N =\sim 0.2\ cm^{-3}$ and a temperature of $\sim 150\ eV$ are used for the central magnetosphere and $N =\sim 0.01\ cm^{-3}$ and a temperature of $\sim 1\ keV$ for the outer magnetosphere given by Cowley et al. (2004) are used to find the range of values for J_{th} of 66 to 8.5 nAm^{-2}. The average parallel current density ($J_{\|I}$) across the whole current sheet is $\sim 20\ nAm^{-2}$ which means that it is unlikely that this population will result in auroral emission, however the peak values of $\sim 200\ nAm^{-2}$ in the pre-midnight area (which is current away from the ionosphere) and an average in the pre-noon area reaches $\sim 100\ nAm^{-2}$ (current into the ionosphere).

$$E_{f0} = 2NW_{th}\left(\frac{W_{th}}{2\pi m_e}\right)^{\frac{1}{2}} \tag{4.12}$$

$$E_f = \frac{E_{f0}}{2}\left[\left(\frac{J_{\|I}}{J_{th}}\right)^2 + 1\right] \tag{4.13}$$

The electron energy flux for thermal electrons is given by equation 4.12 (equation 11 of Cowley et al. (2004)). For the average values given above, the electron energy flux is found to be between ~ 0.004 and $\sim 0.02\ mWm^{-2}$. The enhanced electron energy flux for precipitating electrons (Knight, 1973; Lundin and Sandahl, 1978) is given by equation 4.13 assuming that the ratio of the energy acquired by the electrons precipitating to their original energy is less than the mirror ratio between the planet and the acceleration region. I.e. the acceleration region is far from the planet so that the electron population in the magnetosphere can be considered an infinite source of particles.

However, evidence for acceleration regions at Jupiter and Saturn that occur at high magnetic latitudes due to gravitational forces at the ionosphere and centrifugal forces in the magnetosphere which confine the plasma population, and as such the full current-voltage, energy flux- current density relation (Lundin and Sandahl, 1978) must be considered for these systems (Ray et al., 2009, 2013). However, in the middle magnetosphere at Saturn Ray et al. (2013) showed that a linear approximation to the current-voltage relation is adequate because of the small acceleration potentials relative to the thermal electron energy and the small ambipolar potentials. Hence, this study outlines only the Cowley et al. (2004) formulation to give an estimate of auroral intensity in the ionosphere.

E_f can range from $\sim 0.1 - 1.1\ mWm^{-2}$ using the above values in the upward current region pre-midnight. Hence, the auroral intensity can be obtained using the common relation of source brightness in far ultra-violet emission (FUV) of $\sim 10\ kR$ to an electron energy flux of $1\ mWm^{-2}$ where an energy efficiency of $\sim 15\%$ can be assumed (Waite et al., 1983; Rego et al., 1994; Grodent et al., 2001). The auroral intensity addition expected from this current system is therefore $1 - 11\ kR$.

In the magnetosphere, the region of positive divergence of the equatorial current sheet from the equator is seen around 18-21 R_S, which can be related to an area in Saturn's ionosphere of between 12° and 15° colatitude in the northern hemisphere using coefficients from Burton et al. (2010) and the Bunce et al. (2008) magnetic mapping model using a typical magnetopause position. Lamy et al. (2009); Bader et al. (2018) show an enhancement of around 2 kR at 18-20 LT in the southern hemisphere which is also seen in infrared northern data (Badman et al., 2012). The peak, however, is not seen in ultraviolet northern observations from 2011-2013 (Nichols et al., 2016). The pre-noon downward current density maps to the region which is typically the brightest (e.g Lamy et al., 2009; Nichols et al., 2016; Bader et al., 2018). The change in the auroral intensity of the downward current region could measure $0.1 - 1.1\ kR$, this is very small compared to the other contributions and hence a trough in the auroral intensity is not expected in this area.

4.5.3 Vertical Structure of the Current Sheet

Vertical structure is examined using magnetometer data during the passage of aperiodic waves that pass fully through the current sheet. This is done by calculating the full time derivative of the magnetic field in the direction of a in the current sheet coordinate system. This coordinate system is calculated by determining the normal to the current sheet using either MVA or coplanarity of vectors which is then used to rotate magnetic field in KRTP to current sheet coordinates (a,b,c).

On average, $\sim 10\%$ of current sheets examined at Saturn displayed a bifurcated signature, with around 78% of the total number of suitable events exhibiting a Harris-like structure and the remaining 12% were striated. At Earth, Thompson et al. (2006) showed that around 25% of examined current sheet encounters were bifurcated, a much larger percentage than at Saturn. However, figure 4 in Asano et al. (2005) (figure 4.24) shows that this percentage of bifurcated sheets is dependent on plasma velocity at Earth: at higher velocities the number of bifurcated sheets could reach 50% of all sheets but at smaller velocities the numbers compare to the values given for Saturn in this study at around 10% for bifurcated sheets and 90% Harris-like.

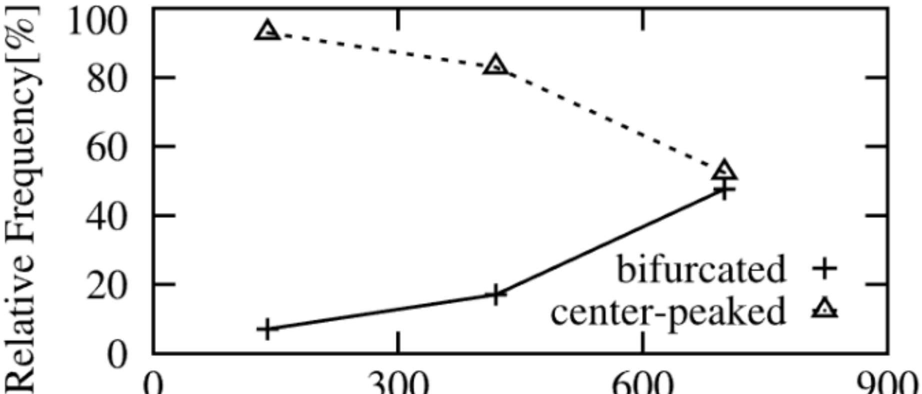

Figure 4.24: Relative occurence frequency of bifurcated current sheets (solid line) and Harris-like (centre-peaked) current sheet (dashed line) plotted against $|V_x|$, the component of velocity along the Earth-Sun line. Asano et al. (2005)

Explored earlier (section 4.4) were theories on what causes bifurcation of the tail current sheet at Earth. A reasonable conclusion from the explored sources is that a perturbation or instability of the current sheet is linked to the sheet itself bifurcating, such as during reconnection [e.g. Hoshino et al. (1996), Nakamura et al. (2002), Thompson et al. (2006) & Birn and Hesse (2014)], hence there is a link to substorms at Earth (Saito, 2015).

Reconnection at Earth is generally confined to the dayside magnetopause and tail current sheet, however at Saturn with an equatorial current sheet in all local times, reconnection in the current sheet could occur at any local time (Guo et al., 2018). As bifurcated sheets are found in most local time sectors reconnection could be associated with bifurcation of the current sheet, especially where an increase in bifurcated sheet numbers in the post-midnight area is in the same region as an expected x-line for the Vasyliunas cycle. However, the aperiodic waves do not occur at the same time as plasmoids, travelling compression regions or dipolarisation, so a connection to increased reconnection would be unlikely. As previously stated, the relation to plasma velocity could also be a relation to reconnection occurring in the tail.

Additionally, a number of authors show a relation to plasma and wave instabilities on the tail current sheet. Instabilities are more prevalent on thin current sheets, which at Earth is where it is soon expected to reconnect [Sanny et al. (1994), Sergeev et al. (1993)], however at Saturn, we find that on the dawn side where a thinner sheet is expected there are much fewer bifurcated examples. However as both instabilities and reconnection are part of the same process of substorms at Earth, it is noted that the sources explored are all part of the same cycle of plasma transport in Earth's magnetosphere.

The final possible source of bifurcated current sheets considered here, is pressure or temperature anisotropy at the current sheet that sets up a ambipolar electric field and allows ions to be pulled from the centre of the current sheet creating two peaks of current density. This is a phenomenon known to occur at Saturn and Earth, and attempting to remove the velocity dependence bias on bifurcation could show that both Saturn and Earth could have similar rates of bifurcation, and hence a similar source. At Jupiter, however, Israelevich et al. (2007) explained that the number of bifurcated sheets at Jupiter is very small and so we can see that the mechanism for bifurcation is much less common than at Earth or Saturn.

4.6 Conclusions

A model was developed to fit aperiodic waves on Saturn's current sheet, using a modified Harris current sheet to fit lobe values of magnetic field. The HICD in the equatorial current sheet can be estimated using the method laid out in Khurana (2001) using the fitted magnetic field values from the Harris current sheet equations and the estimated dipole field. Results show that Saturn's radial and azimuthal HICD signatures are similar to Jupiter in that there is a large local time asymmetry in the radial HICD interpreted as solar wind interaction causing enhancements and decreases in HICD all in agreement with asymmetries seen in Khurana (2001) at Jupiter, and Carbary et al. (2012); Sergis et al. (2017) at Saturn.

Both giant planet magnetospheres exhibit negative values of radial HICD in the post-noon to evening sector caused by swept forward field lines caused by interaction with the solar wind. Additionally, an overall decrease in current density is found with radial distance. The current density at the centre of the current sheet can be estimated using Ampére's law and the fitted values of magnetic field and scale height of the current sheet from the previous chapter. The central current density has a similar relationship with radial distance as the HICD, and there is also a region of negative radial current density where swept forwards magnetic field lines are expected in the post-noon sector. These results can be compared to ring current results from Sergis et al. (2017) where the values are split into local time sectors. Where both studies overlap, an agreement within uncertainties of both measurements is found. Overall, in each sector there is a decrease in total current density as expected with a decrease in magnetic field magnitude with radial distance.

Additionally, the vertical structure of the current density is also explored by calculating the full time differential of the magnetic field in the a direction (roughly radial) of a current sheet coordinate system. It is concluded that around 10% of sheets showed bifurcation and 78% of sheets were Harris-like, where the remaining 12% were striated. Spatially we find no statistically significant deviation except in the dawn sector where outside of Titan's orbit almost no bifurcated signatures are found. Bifurcation at Earth is related to reconnection, instabilities and pressure anisotropies and the source for bifurcation at Saturn is likely to be similar.

Chapter 5

Study of Flux ropes in Titan's ionosphere

5.1 Introduction

Titan has a unique and active environment, from its ever changing surroundings in Saturn's magnetosphere, to its thick atmosphere and dynamic ionosphere. Titan is the only moon within the solar system to have a thick atmosphere, composed of mainly nitrogen, methane and hydrogen with trace amounts of heavier hydrocarbons [e.g. Coustenis et al. (1989), Coustenis and Bézard (1995) & Cravens et al. (2006)].

In this chapter, the detection of flux ropes is discussed and two models of flux ropes are fitted to magnetometer data. Through use of force-free and non-force-free models we can extract parameters related to each flux rope and build a statistical picture of what flux ropes at Titan look like. We also discuss the location of the flux ropes, and what deformations to the flux rope can improve the fit of the flux rope models.

5.2 Detection of Flux Ropes

Cassini MAG data is utilised to detect flux ropes. As there are only 126 flybys, and only around half of these reach a low enough altitude to sample the ionosphere, the sampling process was not automated. Elphic and Russell (1983*a*) & Elphic and Russell (1983*b*) define a flux rope as a discrete individual 'excursion' in the magnetic field, where a peak in the total magnetic field is seen to be larger than the surrounding, usually with a lower limit (at Venus this is commonly around 10 nT, but this value is much lower at Titan).

Flux ropes are seen as an unexpected peak in the total magnetic field when plotted versus altitude. In the example shown in figure 5.1, a flux rope is visible at around 1200 km and the magnetic barrier is seen at around 1500 km (time series data for T30 can be found in appendix A.6). The magnetic barrier is defined as the barrier where the dynamic

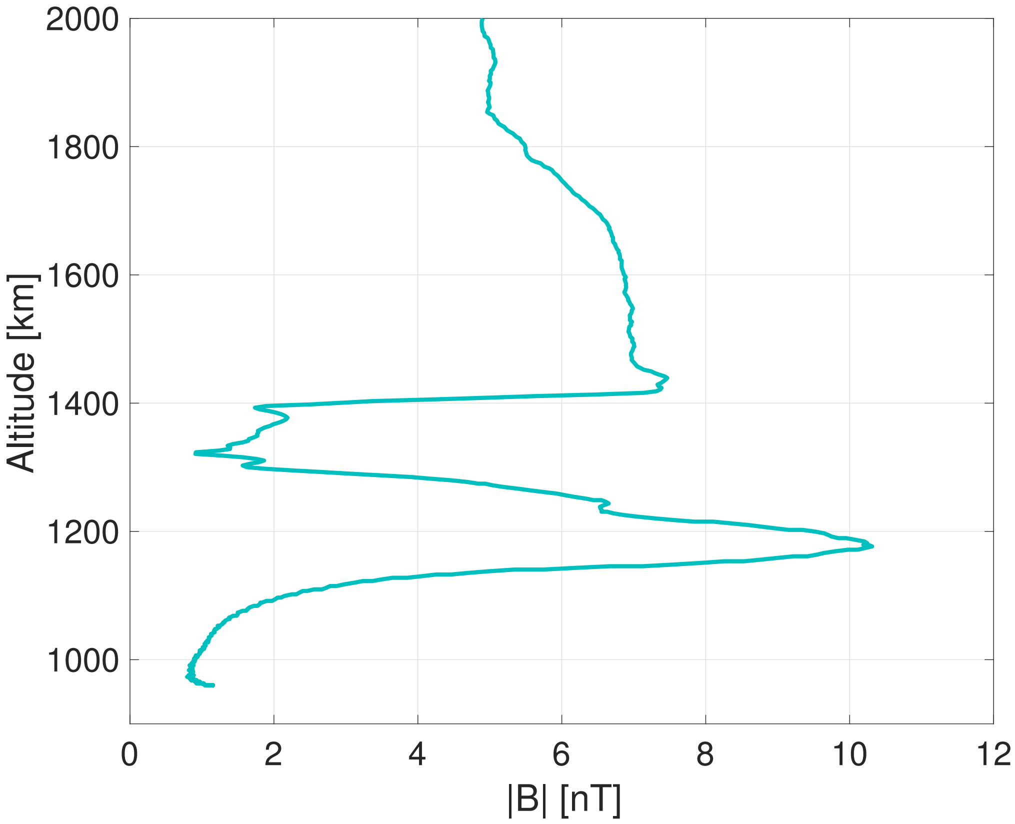

FIGURE 5.1: Figure of the inbound pass of Cassini during Titan flyby T30. Visible is the magnetic barrier at around 1500km in altitude. A large peak in magnetic field attributed to a flux rope is shown around 1200 km.

pressure of the solar wind equals the magnetic pressure in an induced magnetosphere. Minimum variance analysis (section 2.2.2) is then used on this smaller time series of the three magnetic field components to determine a 'flux-rope coordinate system'. The signature of a flux rope in the flux rope coordinate system should then appear similar to the example in figure 5.2, where the intermediate field direction should appear as a broad peak (B_z), the maximum field direction should appear similar in shape to a 3rd order polynomial (B_θ), either positive or negative depending on the *handedness* of the flux rope, for examples.

Handedness of the rope corresponds to the direction of the twist of the magnetic field around the central field. A right-handed rope will twist to the anti-clockwise direction if the central field is perpendicular from the clock face, and a left-handed rope will twist in the clockwise direction, similar to polarisation of circular or elliptical waves. The final component, the minimum variance component (B_r), should be a near-zero constant value. In a number of cases, the maximum and intermediate field structures are switched, this may be a consequence of the flux rope not complying with the physical conditions that will be discussed in section 5.4.

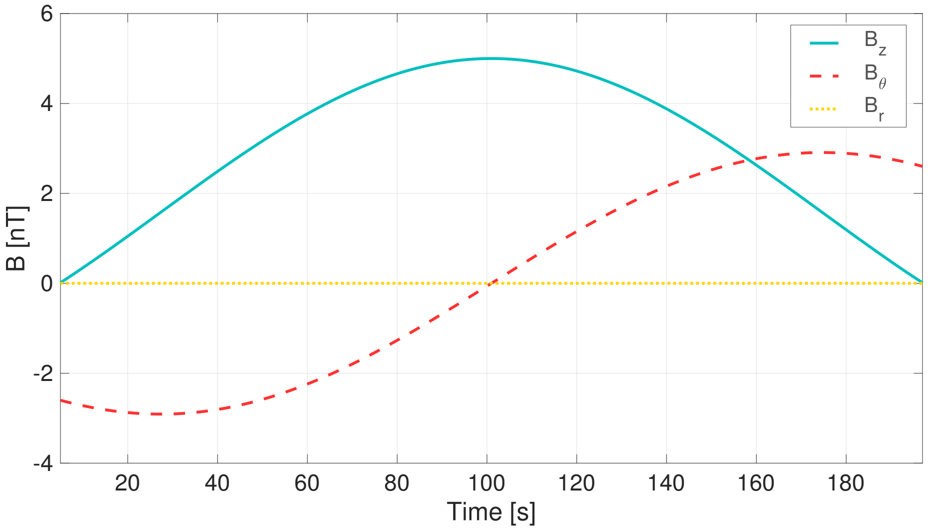

FIGURE 5.2: Figure of an ideal flux rope signature after MVA in cylindrical coordinates. The cylindrical coordinates are found using the Cartesian flux rope coordinate system, where B_z is the intermediate direction component and B_θ is a summation of the maximum and minimum directions. B_r is a constant zero value.

An alternative method for finding the axial direction is to explore cylindrical symmetry of the flux rope (Li et al., 2016). The method calculates a plane within the flux rope coordinates using the velocity and the magnetic field vector at closest approach. The axial direction is confined to this plane, and using the location of the closest approach projected on to this plane the axial direction can be inferred. However, the cylindrical symmetry will be questioned in a later section and as such this method is not utilised.

5.3 Location of Flux Ropes

In total, 85 flux ropes are detected over all Titan flybys of Cassini between 2004 and 2017 with value of magnetic field excursion of over 1 nT in magnitude from the background field. These flux ropes appear more common in the noon sector of Saturn's magnetosphere, as indicated by the distribution of flux ropes by Saturn local time, normalised to the number of flybys that reach an altitude of 2400 km shown in figure 5.3. The cut-off value of 2400 km is determined from an altitude analysis of flux rope occurrence shown in figure 5.4.

Flux ropes at Venus are generally found on the day side hemisphere of the planet and may travel around past the terminator on occasion (Luhmann, 1986). However, on

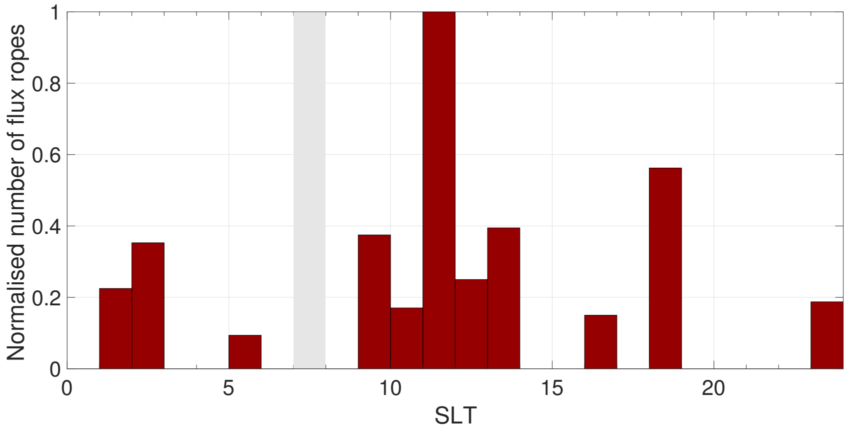

FIGURE 5.3: Figure of flux rope occurence for each SLT bin, normalised to the number of Titan flybys in each bin that reach an altitude of lower than 2400 km. Grey shaded areas show SLT ranges where Cassini did not sample below 2400 km.

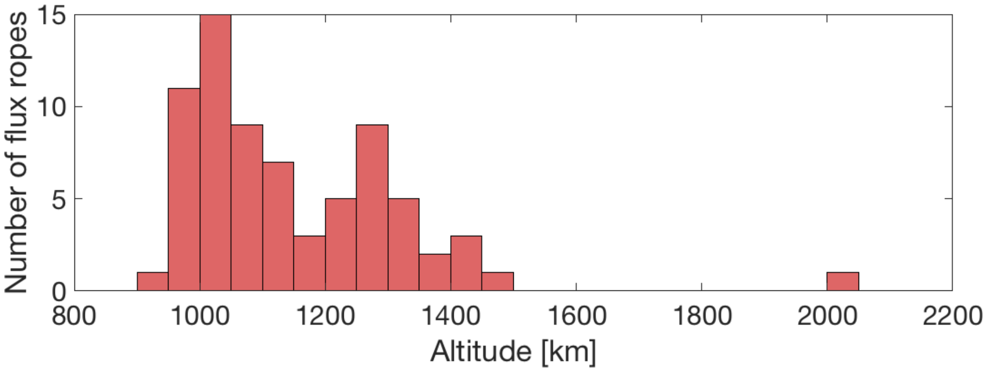

FIGURE 5.4: Figure of flux rope occurrence with altitude above Titan's surface. The lower limit is limited by the closest approach of Cassini.

Mercury flux ropes are most common travelling down tail in the night side hemisphere of its magnetosphere. Differences in how they are produced in the ionosphere and magnetosphere, as well as the surrounding environment such as the solar wind, give rise to flux ropes that occur with a range of life spans and locations. The aim of this section is to decipher where flux ropes are most commonly observed in Titan's ionosphere and why they occur there. Titan itself is a unique flux rope environment in that the dayside ionosphere is not always the hemisphere that is facing the oncoming plasma.

Within Saturn's magnetosphere, Titan interacts with a number of different magnetic field regimes and the plasma flow is roughly in the direction of co-rotation with Saturn. For simplicity, we state that 'ram-side' is in reference to the hemisphere of Titan that is facing the oncoming corotating plasma, and 'sunlit-side' is in reference to the hemisphere which is illuminated by the Sun.

To determine if there is a bias in flux rope location, in relation to the sun direction and ram-direction, we first must rotate the observations of flux ropes into a 'Titan-Centric Sun facing coordinate system' (TiCS). Where the x-axis in this system is a vector from Titan to the Sun. The z-axis is positive northward and the y-axis completes the right-handed system. This co-ordinate system facilitates analysis of flux ropes with respect to the sunlit-side of Titan. Figure 5.5 shows the position of flux ropes around Titan with respect to the Sun position, where the Sun is in the direction of the positive x-axis on the plots by definition. Additionally the range of corotation plasma direction is given by the red arrows. All trajectories for flybys that reach an altitude of 2 R_T

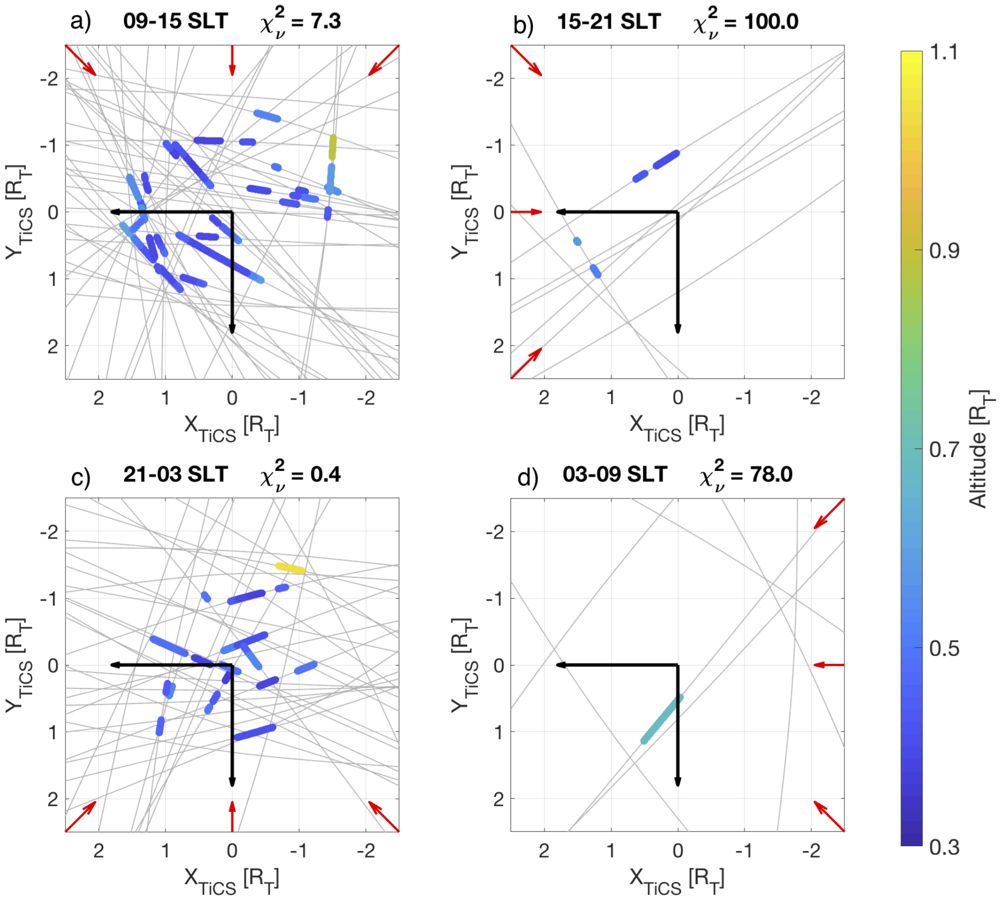

FIGURE 5.5: Figure showing flux ropes around Titan when Titan is in a) the noon sector (0900 - 1500 SLT), b) the evening sector (1500 - 2100 SLT), c) the night sector (2100 - 0300 SLT), d) the morning sector (0300 - 0900 SLT) of Saturn's magnetosphere. Red arrows show the range of direction of corotating plasma in each sector. The trajectories of all flybys that occur in each SLT area are shown in grey. The flux ropes are also coloured by altitude of detection in Titan radii. χ^2 values represent the agreement with the null hypothesis of equal detection in each spacial bin.

(determined from figure 5.4) or lower are shown in grey. Each subfigure shows a different sector of Saturn's magnetosphere where a) is noon, b) evening, c) night and d) morning.

SLT Sector	Bin Number	Bin description	Percentage of Flux Ropes
21-03 (Night)	1	Sunlit, anti-ramside	29.1
	2	Anti-Sunlit, anti-ramside	24.9
	3	Sunlit, ramside	25.1
	4	Anti-Sunlit, ramside	20.9
03-09 (Morning)	1	Sunlit, anti-ramside	0.0
	2	Anti-sunlit, ramside	0.0
	3	Sunlit, anti-ramside	100.0
	4	Anti-sunlit,ramside	0.0
09-15 (Noon)	1	Sunlit, ramside	21.3
	2	Anti-sunlit, ramside	36.9
	3	Sunlit, anti-ramside	34.2
	4	Anti-sunlit, anti-ramside	7.6
15-21 (Evening)	1	Sunlit, ramside	90.9
	2	Anti-sunlit, anti-ramside	0.0
	3	Sunlit, ramside	9.1
	4	Anti-sunlit, anti-ramside	0.0

Table 5.1: Table showing the percentage of flux ropes in each bin for each local time sector. There is also a description of which hemisphere the bin lies in.

5.3.1 Statistical Analysis

To show an asymmetry in detection of flux ropes, we apply a significance test on each SLT sector plot to show that flux ropes are detected more in certain areas and conditions than others. We begin by separating flybys into the SLT sectors shown in the previous section. These sectors are then further split into four bins of sun-lit/dark (positive/negative X_{TiCS}) and positive/negative Y_{TiCS}. The bin limit $X_{TiCS} = -0.25$ R_T is used as we are statistically testing whether illumination from the Sun or ram pressure from the corotation direction are correlated to an increased number of flux ropes detected. Hence, as the flux ropes are occurring above the surface, we know that the ionosphere will still be illuminated up to 0.5 R_T at $X_{TiCS} = -1$ R_T. Hence we use $X_{TiCS} = -0.25$ R_T as a conservative estimate of 'sun-lit' area behind the terminator and this is included in the 'sun-lit' bins.

Equal number of flux ropes in each bin, normalised to the time Cassini spent within each bin is expected under a null hypothesis H_0. Hence, the null hypothesis is that 25% of total flux ropes in each sector of Saturn's magnetosphere will occur in each bin. The reduced χ^2 values for the comparison of the percentage of flux ropes (normalised) to the null hypothesis is shown in the title of each sector plot. A value of one means that the null hypothesis is an excellent hypothesis, and a value of above five is commonly used as a cut-off for a 'good' fit.

The null hypothesis is rejected for the morning and evening sectors, and a bias towards positive X_{TiCS} areas is present. This probability is calculated from the χ^2 probability distribution function. The P-value is tested against a 5% level. The noon sector has a probability of 2.9%, which is lower than 5% and as such H_0 rejected and a bias is statistically present in this sector. However, the night sector has a probability of 21.3, hence, the null hypothesis is accepted. This analysis, however, only states that the distribution of flux ropes is not equal in all areas. Table 5.1 shows the percentage of flux ropes, normalised by time spend in each bin for each SLT sector along with the environment of each bin.

5.3.2 Zenith Angle and Corotation Direction

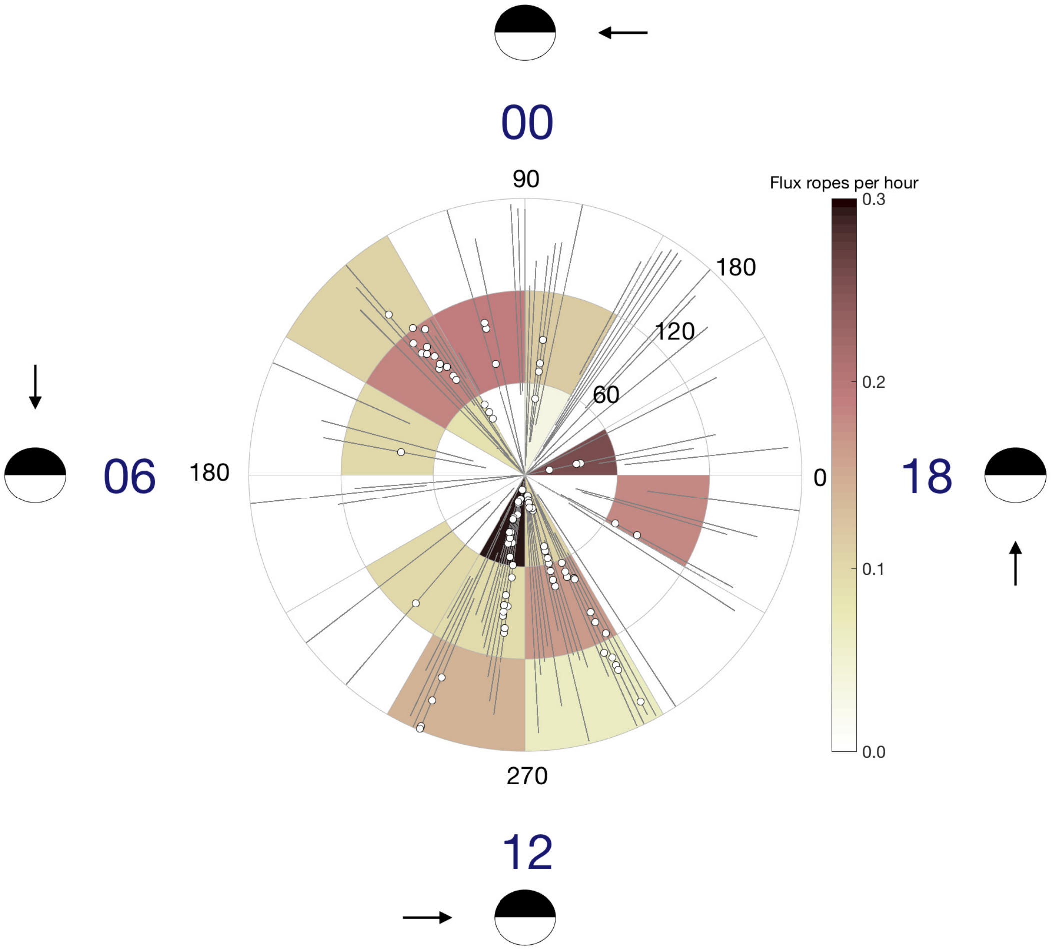

FIGURE 5.6: Figure showing the position of flux ropes at Titan with regards to the zenith angle of the detected fluxrope, and the angle between the corotation direction and the solar radiation direction. Grey lines are trajectories of Cassini in the parameter space, white dots are the flux ropes detected, sectors are coloured by number of flux ropes in each zenith angle, corotation and solar radiation angle sector bin. The angle between the corotation direction and solar radiation direction can be used as a proxy for SLT which is also shown along with a diagram of Titan's illuminated hemisphere and corotation direction (black arrow) for each main sector.

The position of flux ropes with regards to sun-lit hemisphere and co-rotation direction can be summarised into figure 5.6, where the zenith angle is measured from the sub-solar point on Titan (0°), to the anti-sub-solar point (180°) which is the side of Titan facing away from the Sun. The terminator on Titan is therefore 90°. Furthermore, the 'interaction angle' is defined anti-clockwise as the angle from the direction of incoming solar radiation to the direction of incoming plasma moving with corotation.

In general, more flux ropes are found in the inner circle of the figure (figure 5.6) which relates to the hemisphere of Titan that is illuminated by the Sun. Only when corotation direction and Sun-direction are anti-parallel are a statistically significant number of flux ropes present in the non-illuminated hemisphere. Additionally, also visible in the diagram is the much larger number of flux ropes within the vicinity of 12 SLT i.e. interaction angle of $\sim 270°$. A secondary peak at pre-midnight is also found where the x-line from Vasyliunas cycle reconnection is expected. The only other positions that flux ropes are found, are when the current sheet is close to, and passing over Cassini frequently, i.e. for events found around 18 SLT. Trajectories of Cassini during all encounters below 2000 km above Titan's surface are also plotted in the parameter space in grey, showing that every sector of this parameter space is sampled by at least 2 flybys.

5.4 Force-Free Flux Rope Model

To extract variables parameterising each flux rope, a force-free model is initially utilised. In a force-free model the magnetic pressure force $\left(\frac{B^2}{2\mu_0}\right)$ is balanced with the magnetic tension force $\left(\frac{B^2}{2\mu_0 R_c}\right)$, where B is the magnetic field magnitude, μ_0 is the permeability of free space and R_c is the radius of curvature of the field. A force-free flux rope is assumed to be the final configuration of a flux rope as it is considered the lowest energy state (Osherovich et al., 1993). Wei et al. (2010) discusses that a developing flux rope appears to not be force-free and the success of a fitting with a force-free model will depend on the maturity of a flux rope.

Minimum variance analysis is used to orient the magnetic field components into a 'flux rope coordinate system' where the intermediate variance direction should appear as axial field direction and shows a peak at closest approach to the centre of the flux rope. The two remaining field components, maximum and minimum should combine to give the tangental field of the flux rope (in a Cartesian system being converted to cylindrical) which is at maximum on the edge of the flux rope and at a minimum at the closest approach of the centre of the flux rope. The last magnetic field component in the local cylindrical coordinate system is the radial field component which in a force-free situation is assumed to be constant zero as the field is contained either in the tangental or axial direction. Figure 5.7 shows an example trajectory of Cassini through a circular cross-section flux rope, and shows the local cylindrical coordinate system at a specific point along the trajectory. The equations for the three magnetic field components are shown in equations 5.1, 5.2 and 5.3,

$$B_{\text{Axial}} = B_0 J_0(\alpha R) + b_0, \tag{5.1}$$

$$B_{\text{Tangential}} = H B_0 J_1(\alpha R), \tag{5.2}$$

$$B_{\text{Radial}} = 0, \tag{5.3}$$

where B_0 is the maximum magnetic field of the flux rope; J_0 and J_1 are the zeroth and first order Bessel functions of the first kind; α is a constant of 2.40 (appendix A.2); R is

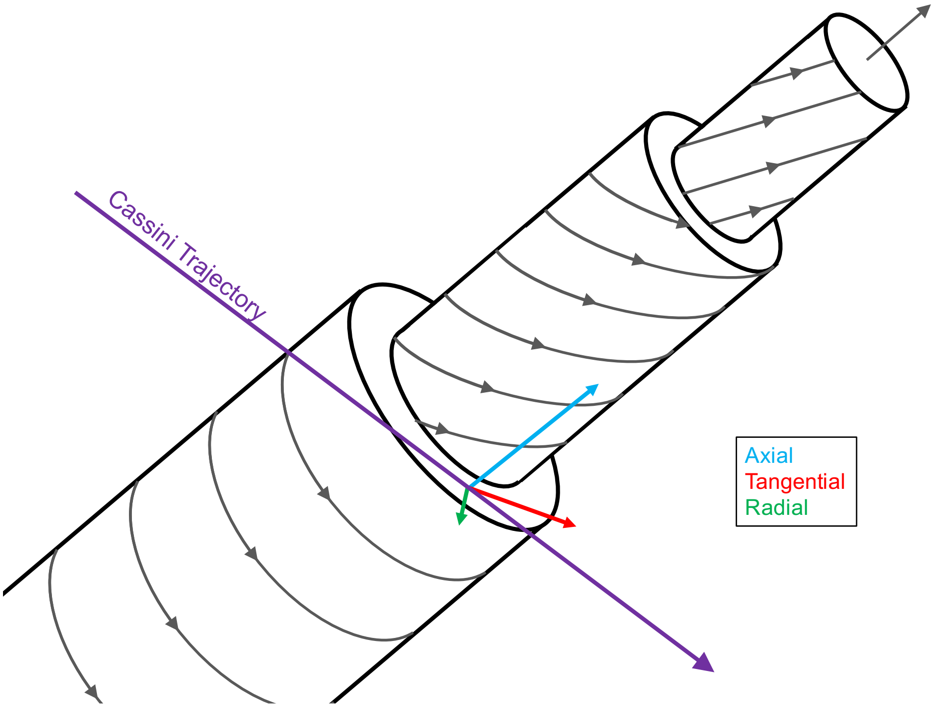

Figure 5.7: Figure showing example trajectory of Cassini through a flux rope

the radial distance from the centre of the flux rope; b_0 is an offset in the axial direction and H is the handedness of the flux rope which takes values of 1 or -1 depending on which way the rope is twisted.

As R is an input vector of values for each of these equations, and we do not directly know R yet because we do not know the position of the centre of the flux rope, we must use a proxy for the distance to the flux rope centre. The vector u is used as a proxy for distance to the centre of the flux rope. u ranges from -1 at the start of the traversal to 1 at the end of the traversal. In figure 5.8 we can see that $u = \frac{Z}{Z_0}$, where Z is the distance of the spacecraft through the flux rope and Z_0 is the distance at which the trajectory of the spacecraft and the flux rope edge coincide, both measured along the z-axis shown in figure 5.8.

We can use this vector u as a proxy for αR using the following equation,

$$\alpha R = 2.40\left(\sqrt{\left(\frac{Y_0}{R_0}\right)^2 + u^2\left(1 - \left(\frac{Y_0}{R_0}\right)^2\right)}\right), \tag{5.4}$$

where Y_0 is the distance (in km) of closest approach to the centre of the flux rope seen in

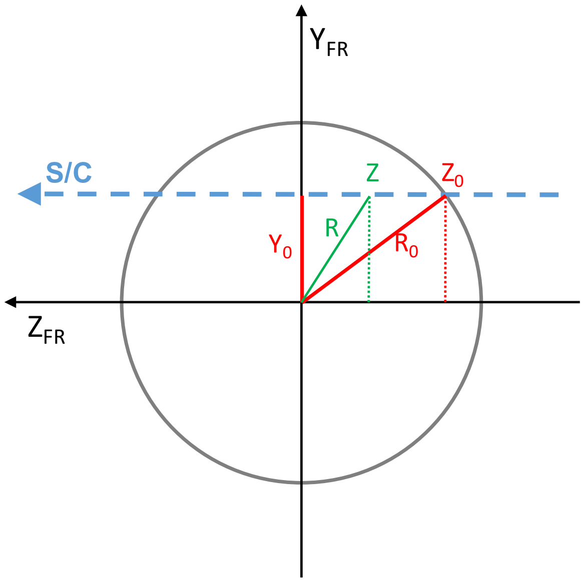

FIGURE 5.8: Figure showing flux rope geometry - adapted from figure 1 of Lepping et al. (2017)

figure 5.8 and R_0 is the flux rope radius in the cross-section geometry, $\frac{Y_0}{R_0}$ is the impact factor or closest approach value where 1 is the edge of the flux rope and 0 is directly through the centre. The actual radius of the flux rope is calculated using geometry and the known velocity of the spacecraft:

$$R_0 = \frac{0.5Vt\cos(\phi)}{\sin((CA))}, \tag{5.5}$$

where ϕ is the angle between the axis of the flux rope (recovered using MVA) and the trajectory subtracted from 90° (see figure 5.9), V is the speed of the spacecraft, t is the

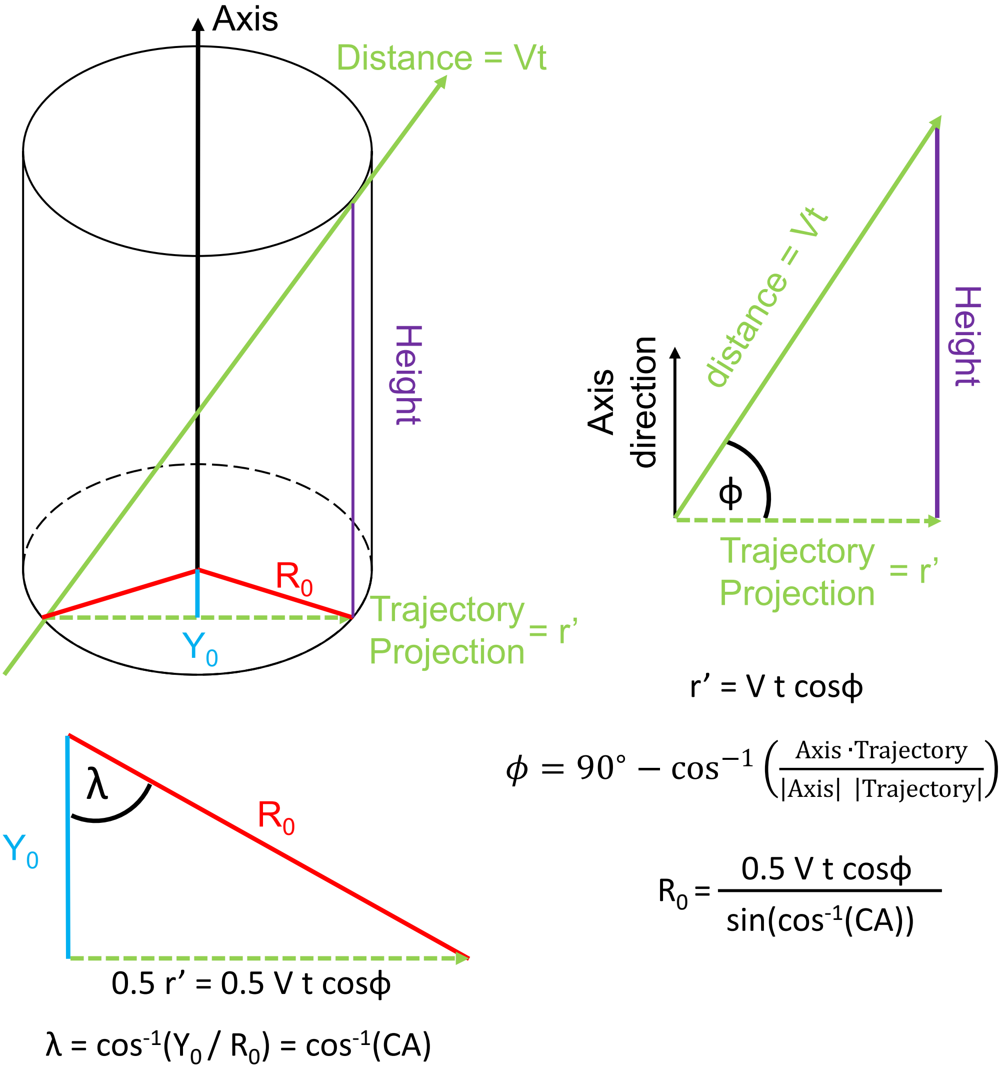

Figure 5.9: Figure showing flux rope geometry, equations and parameters for deriving the radius of the flux rope.

time taken to traverse the flux rope, CA is the closest approach distance (retrieved from fitting the force-free model). The geometry of the system with corresponding equations is shown in figure 5.9.

The maximum magnetic field and the radius are then used, via Faraday's law, to estimate the characteristic parameter, flux content of a flux rope, using the following equation:

$$\Phi = \frac{2\pi}{\alpha} B_0 R_0^2 J_1(\alpha) \tag{5.6}$$

The model described by equations 5.1-5.4 is fitted to magnetometer data using a Levenberg-Marquardt nonlinear least squared fitting algorithm where χ^2 is automatically reduced in the fitting (further discussed in chapter 2).

5.4.1 Force-Free Model Results

The force-free flux rope model, described in the previous section, fitted 49 out of the 85 detected flux ropes to a satisfactory degree, i.e. the mean squared error (MSE) statistic

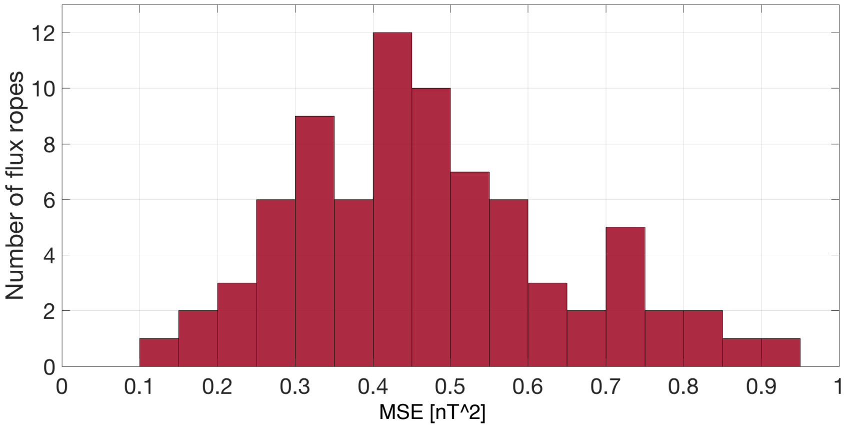

FIGURE 5.10: Figure showing the distribution of MSE values for each flux rope fitting.

was equal to or below 0.5 nT^2 and probability of returning the χ^2 value by chance was 5% or less. These conditions were designed so that the fitting procedure would have room to attempt to fit flux ropes that may not fit completely the assumptions of a force free flux rope. The MSE of each fit is then related to how well the observed flux rope fits the force free category, where a lower value of MSE implies a near force-free flux rope. Figure 5.10 shows the distribution of the MSE values for the 78 flux ropes where the fitting algorithm converges, regardless of goodness of fit. 7 flux ropes were unable to be fitted at all (the algorithm does not converge) by the force-free model. Figure 5.11 shows an example of a flux rope fitted with the FF model, where χ_v^2 is 3.5182 nT.

Figure 5.12 shows the main results of the statistical properties of Titan's flux ropes. Panel a) shows a histogram of flux rope radius of the 49 flux ropes that have an adequate fitting. Each histogram has different bin sizes to best display the data. Each bin size is chosen so that the uncertainties of each value in the bins are encapsulated within the bins. The maximum field strength bins are 1 nT wide from 0-10 nT, 2 nT wide from 10-40 nT. Flux rope radius bins are 50 km from 0-500 km, and 100 km from 500 - 1500 km. Finally, the flux content bins are 5 Wb from 0-20 Wb, 20 Wb from 20-200 Wb and 100 Wb bins from 200-400 Wb.

In the maximum field strength distribution (panel a) we find the majority of flux ropes (90%) have a maximum magnetic field of 1-15 nT, with one much larger value. A majority of flux ropes with radii of $150 - 500$ km, with six larger flux ropes ranging from just over 500 km to nearly 1000 km. The final panel (c) shows the distribution of flux content derived by equation 5.6 which considers the radius and maximum field of each flux rope. We see a maximum of frequency density for flux content of around 5 Wb with a long tail up to 400 Wb.

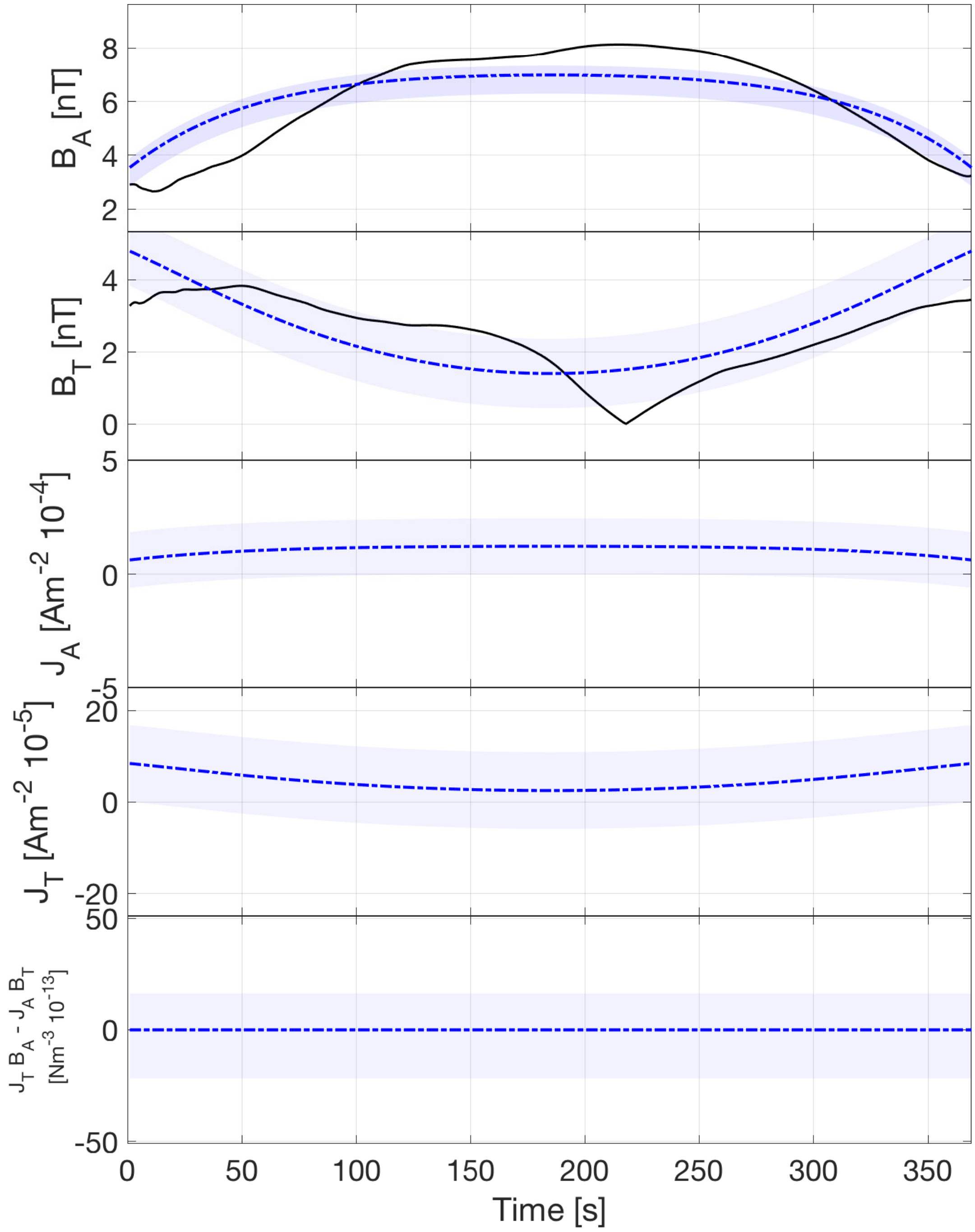

Figure 5.11: Example of flux rope signature (black) fitted to a force-free flux rope model detected during T5. The figure shows axial magnetic field, tangential magnetic field, axial current density, tangential current density and force density where data is in black and FF model is in blue with a blue shaded area representing the uncertainties in the model. This example occurred at 5.3 SLT on 16th April 2005 at 19:05 space craft time during titan flyby T5.

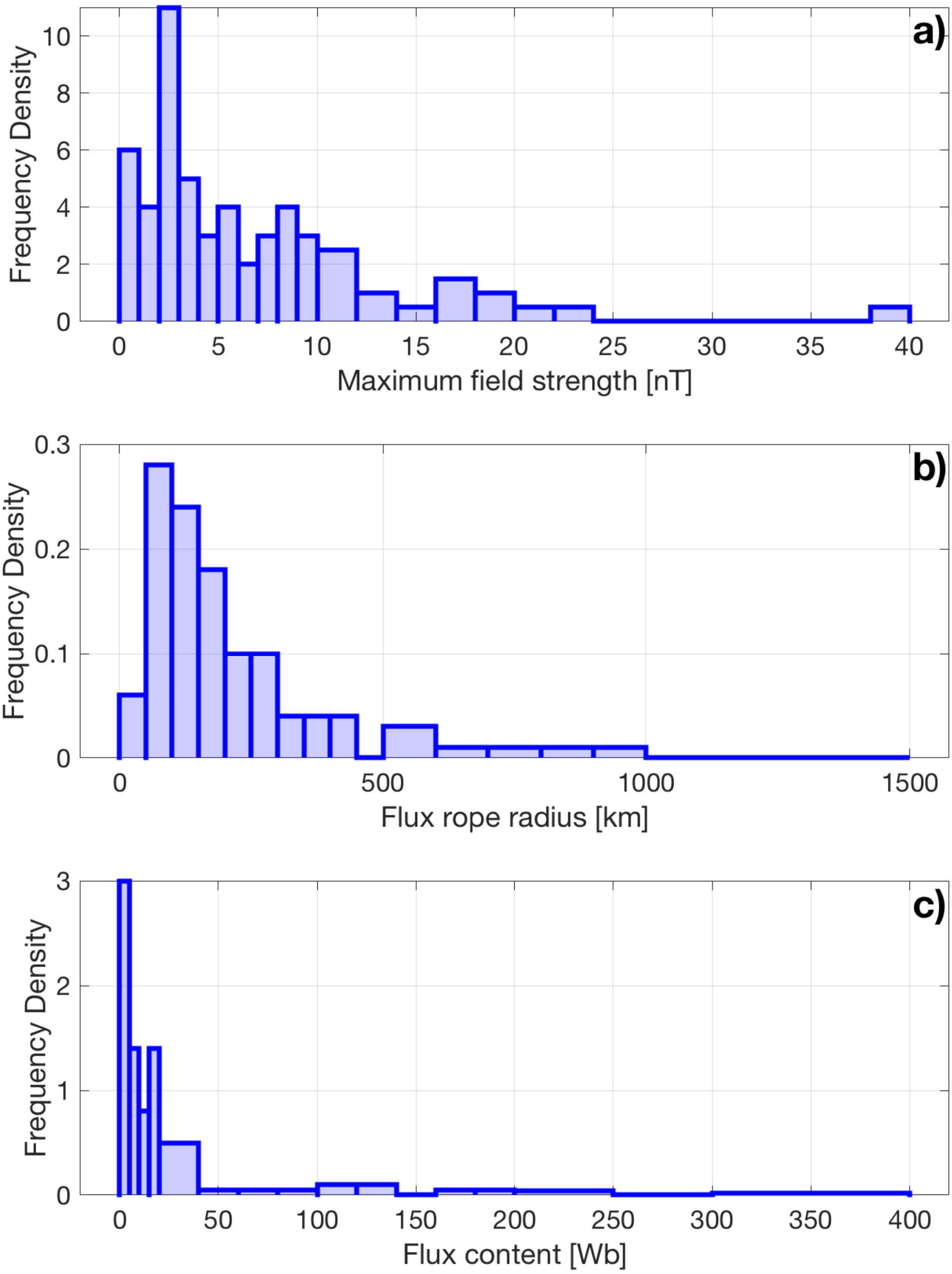

FIGURE 5.12: Histogram of a) maximum flux rope magnetic field b) flux rope radius and c) flux content

37 flux ropes out of 49 fitted have a right-handed twist around the axial field (anticlockwise) and the remaining 12 have a left-handed twist (clockwise). Previous studies at Venus and Mars have found that the handedness of the flux rope is related to which hemisphere (e.g. dawn/dusk) that the flux rope is formed on. At Venus it was found that left-handed flux ropes are typically found on the orbital facing direction and right-handed ropes on the anti-orbital facing hemisphere (see figure 3d of Wei et al. (2010)). This helicity bias is formed from the velocity shear at the magnetic barrier where the flux ropes are thought to be formed (Russell, 1990). It is unclear whether this process is occurring at Titan as there is no statistical significance detected in the position of right- or left-handed flux ropes.

5.4.2 Orientation of Flux Ropes

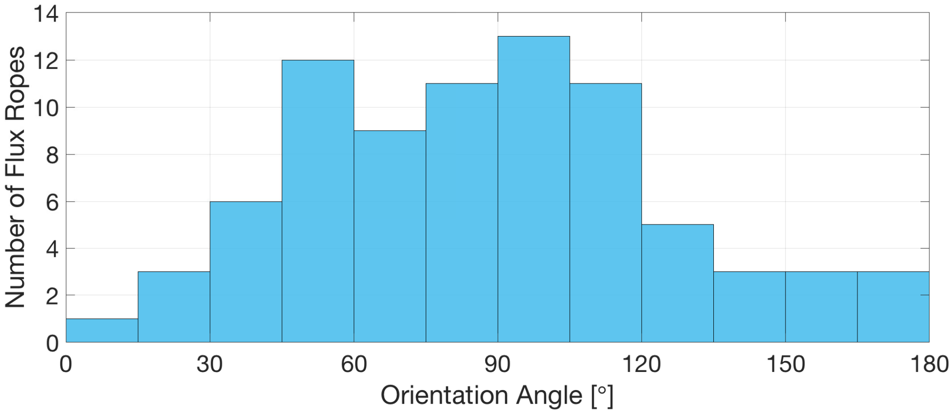

Figure 5.13: Histogram of the occurrence of orientation angles for flux ropes in Titan's ionosphere. Where the orientation angle is the angle between the flux rope axis determined by MVA, and the normal to Titan's surface.

The orientation of flux ropes in Titan's ionosphere can also be determined using MVA. Where the maximum variance direction is assumed to be along the flux rope axis, as described in the previous section. Figure 5.13 shows the distribution of orientations of flux ropes. The angle of orientation is described as the angle between the flux rope axis and the normal to Titan's surface. The figure shows a broad peak at 90°, which is describing that the majority of flux ropes are lying broadly near-parallel to Titan's surface.

5.5 Non-Force-Free Flux Rope Model

The significant number of flux ropes not fitted by the force-free model suggests that its assumptions are not valid, thus requiring a non-force-free model. Hidalgo et al. (2002) presented a non-force-free model to understand magnetic clouds in the solar wind, in which the model also uses the geometry of spacecraft and incoming magnetic clouds so that it can fit for the angles of rotation of the magnetic cloud, thus not needing to use MVA i.e. the orientation of the flux rope is a free parameter. Nieves-Chinchilla et al. (2016) improved further upon this method to return the following model:

$$B_{\text{Radial}} = 0, \tag{5.7}$$

$$B_{\text{Axial}}(r) = B_A^0 + \mu_0 \int_0^r j_T(r)dr, \tag{5.8}$$

$$B_{\text{Tangential}}(r) = -\frac{\mu_0}{r} \int_0^r r j_A(r)dr, \tag{5.9}$$

where r is radius, j_T and j_A are the tangential and axial current densities and B_A^0 is a boundary condition of the flux rope that can be imposed. The current densities are further modelled as polynomial expansions $\boldsymbol{j} = \sum_{m=0}^{\infty} \beta_m r^m \boldsymbol{e}_A - \sum_{n=1}^{\infty} \alpha_n r^n \boldsymbol{e}_T$ where α_n and β_m are the polynomial coefficients. The model now reads:

$$B_{\text{Radial}} = 0 \tag{5.10}$$

$$B_{\text{Axial}} = B_A^0 + \mu_0 \sum_{n=1}^{\infty} \alpha_n \frac{1}{n+1} r^{n+1} \tag{5.11}$$

$$B_{\text{Tangential}} = -\mu_0 \sum_{m=0}^{\infty} \beta_m \frac{r^{m+1}}{m+2} \tag{5.12}$$

The degree of the polynomial was set at order three for axial field and four for tangential field after preliminary tests that showed an increased order past three and four did not improve the fitting substantially. The boundary condition $B_A^0 = \mu_0 \sum_{n=1}^{\infty} \alpha_n \frac{1}{n+1} R^{n+1}$ where R is the flux rope radius is used to ensure that the field is tangential at the edge of the flux rope. This assumption can be relaxed to give an ambient magnetic field outside of the flux rope, but for simplicity and ease of fitting the flux rope radius the assumption is held for this study, the effects of relaxing this assumption are described in Nieves-Chinchilla et al. (2016). Axial flux content can be calculated using the following equation:

$$\Phi_A = \pi R^2 \left(B_A^0 + 2\mu_0 \sum_1^{\infty} \alpha_n \frac{1}{(n+1)(n+3)} R^{n+1} \right) \tag{5.13}$$

Maximum field strength is determined by calculating the axial field B_A when the radius $r = 0$ using fitted values for each flux rope. The order of the polynomial expansion to the current density and its effects on results are described in the following section. It is important to note that a large difference between the FF and NFF is that the NFF model will present a radial force. The handedness of the flux rope is included with the sign of j_A, where a positive value gives a right-handed flux rope and a negative value gives a left-handed flux rope.

5.5.1 Non-Force-Free Results

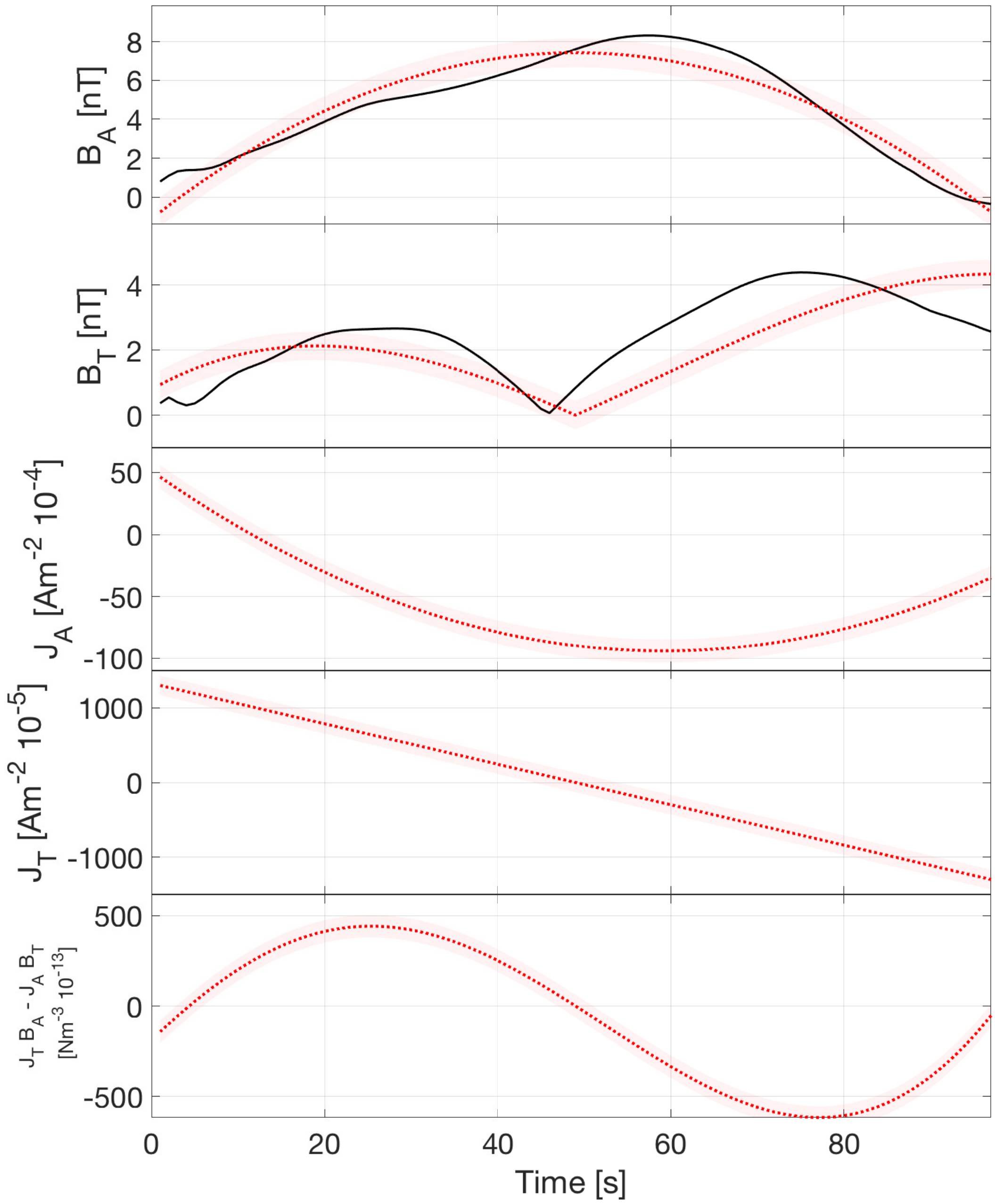

FIGURE 5.14: An example fit for a flux rope at Titan, the figure shows axial magnetic field, tangential magnetic field, axial current density, tangential current density and force density where data is in black and NFF model is in red with a red shaded area representing the uncertainties in the model.

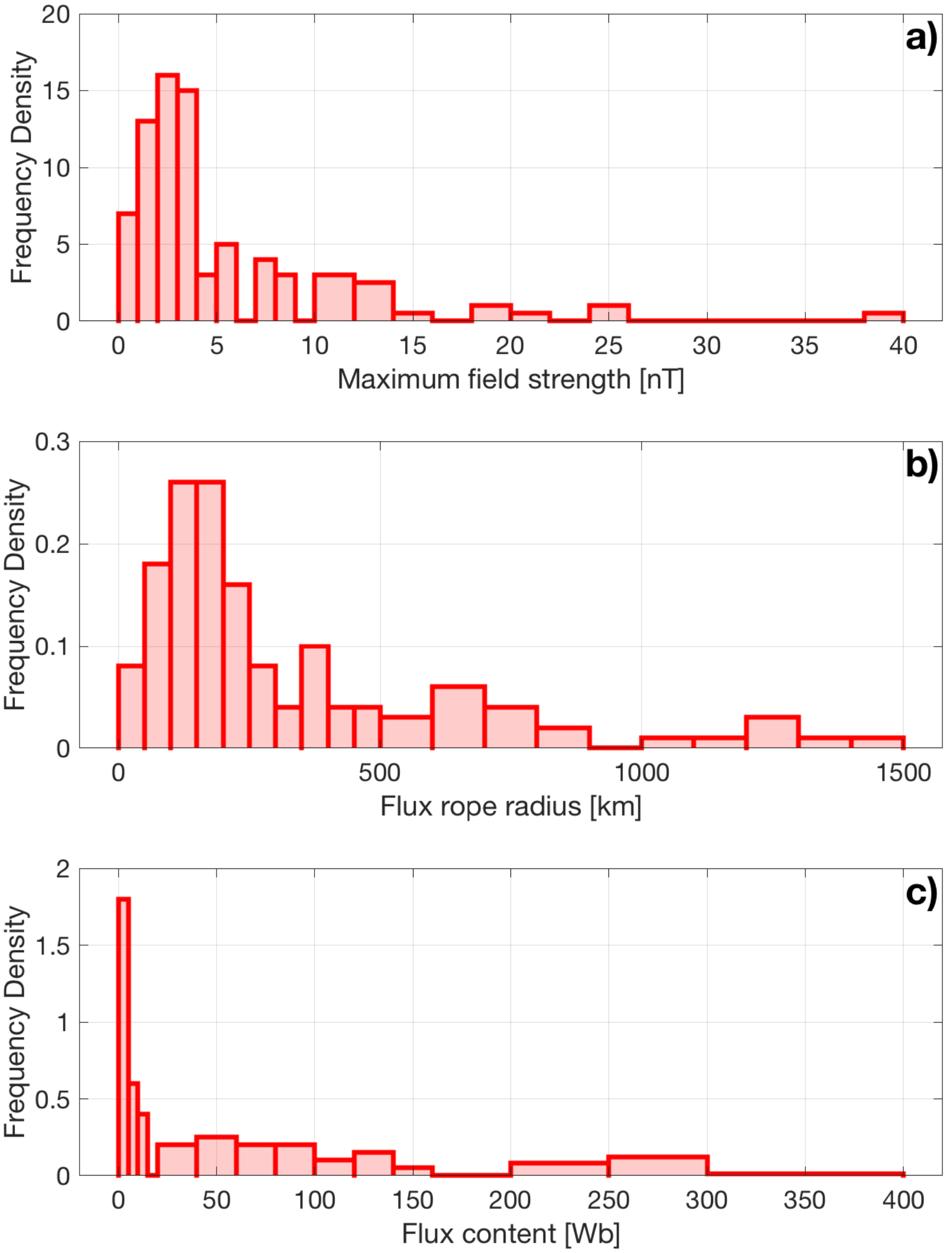

FIGURE 5.15: Histogram of a) maximum magnetic field b) flux rope radius and c) flux content

The non-force-free (NFF) model fitted 84 out of 85 flux ropes with a probability of returning the χ^2 value by chance was 5% or less, and the statistical results, shown in figure 5.15, are comparable to the force-free model. However, there are slight differences in the radii which are on average larger than for the force-free fits, and have a wider range to larger sizes (50 - 750 km). The maximum magnetic field is comparable to the force-free model (1 - 15 nT). However, there is a great improvement in the percentage of flux ropes that are able to be fitted with the NFF model along with the reduction of uncertainties through use of the NFF model. Figure 5.14 shows an example of a flux rope fitted (black) with the NFF model (red) along with the derived current densities and $\boldsymbol{J} \times \boldsymbol{B}$ force density. Model uncertainties are shown as a shaded red area.

Uncertainties in the fit of the model are calculated using the Jacobian matrix that the non-linear fitting procedure produces. The square roots of the diagonal elements of the Jacobian matrix correspond to the standard deviation of the corresponding parameter. In general, these uncertainties are below 10% for successful fits. Figure 5.15 presents the statistical analysis results of the fitted flux ropes discussed above, the binning described in section 5.4.1 incorporates the uncertainties on each value.

The handedness of flux ropes is controlled by the sign of j_A and the NFF and FF models each find the same handedness in the 61 corresponding flux ropes that both models fit to. In total, 56 flux ropes are right handed, 28 flux rope are left-handed and the remaining flux rope does not fit to either the FF or NFF model with a $P(\chi^2) < 0.05$. Again, no significant spatial relationship is resolved in these data.

5.6 Discussion

5.6.1 Flux Rope Location

Titan is a unique environment where the incoming plasma is not always in the same direction as the solar radiation direction. We see in the cartoons in figure 5.6 that in the different SLT sectors of Saturn's magnetosphere that Titan has various different ram-directions due to Saturn's corotating plasma population. This figure shows a large bias towards 12 SLT where the majority of flux ropes are found between 10 and 14 SLT. Additionally, the position of each flux rope is plotted with zenith angle of Cassini, where the inner circle of the plot is sunlit, and the outer circle is in shadow. 56 flux ropes out of 85 are found in the sunlit hemisphere of Titan, showing that production of flux ropes is induced primarily in the illuminated hemisphere. However, 29 flux ropes are found in the shadowed hemisphere of Titan. Taking into consideration the ram direction of Saturn's corotating plasma population, the flux ropes are generally only occurring in SLT sectors where the ram direction is not aligned with the direction of incoming solar radiation.

Additionally, plots of trajectories and flux ropes in each SLT sector are presented in figure 5.5 where the position of flux ropes in Titan's ionosphere can be seen. The diagrams show that flux ropes are detected on the ram-side and sunlit-side of Titan, but are not detected on the anti-ram side and night side in the majority of local time sectors. However, we find that in the night sector (21-03 SLT) it is equally likely to find flux ropes in any hemisphere of Titan. This sector corresponds to the increased number of flux ropes seen in the 00 - 04 SLT area in figure 5.6 where we can assume that another process is causing the formation of flux ropes, or the conditions in the sector

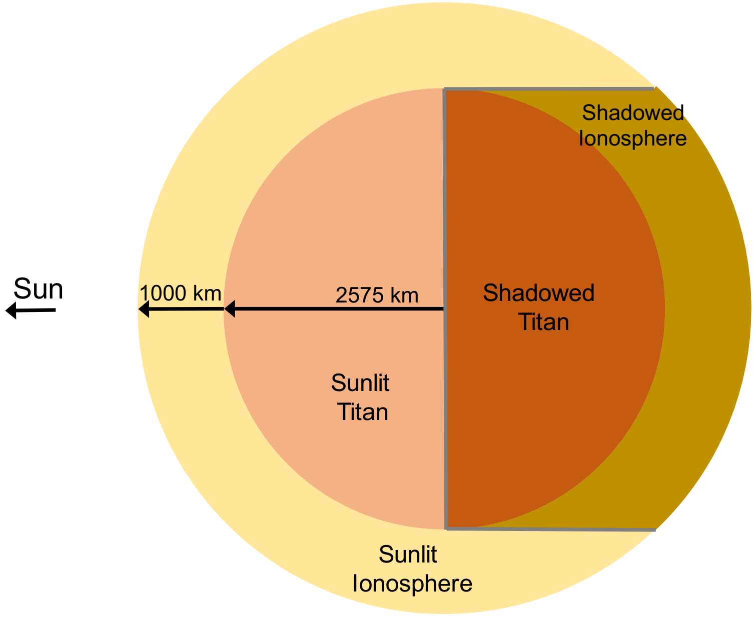

FIGURE 5.16: Figure of cartoon showing a non-disturbed ionosphere of Titan with the Sun to the left. A sunlit area of ionosphere past the terminator on the planet is visible in higher latitudes.

allow flux ropes to be preserved for a longer period of time and hence are more likely to be detected.

Figure 5.5 d) suffers from lack of data, with only one flux rope detected along seven flybys, however this sector could hold the key to finding which driver influences the production of flux ropes most strongly as the corotating plasma and solar radiation directions are anti-parallel. Alternatively, it may be that the flux rope to flyby ratio is low for another reason in this sector, e.g. that flux ropes are initiated most easily with a combination of a sunlit ionosphere and dynamic pressure from an incident plasma.

Furthermore, these sectors and spatial bins are statistically tested against a null hypothesis of equal likeliness of detection of a flux rope in each spatial bin. The spatial bins are shifted slightly to $-0.25\ R_S$ in X_{TiCS} as flux ropes are detected in the ionosphere at above 900 km in altitude where the ionosphere will still be sunlit. $-0.25\ R_S$ is shown to be a conservative average of the sunlit extent of the ionosphere at above 900km, shown in figure 5.16. Results of the statistical testing shows that the null hypothesis is rejected in all but the night SLT sector with a probability of the null hypothesis being correct below the 5% level.

5.6.2 Flux Rope Models

5.6.2.1 Force-Free

A force-free flux rope model was implemented to extract radii and the central magnetic field strength of each flux rope. These two parameters can be used to estimate the flux content of each flux rope using equation 5.6. In total, 49 flux ropes fit the force-free model with a MSE of less than 0.5. 5 flux ropes were unable to be fitted, where the remaining 31 do not fit adequately to the force-free model; this shows that the majority of flux ropes at Titan do not adhere to the force-free assumptions completely.

To accurately statistically evaluate all flux ropes at Titan, an improved, or different model must be implemented to allow fitting of all flux ropes in the future. However, a small statistical study can be made using the 49 fitted flux ropes. We therefore only evaluate the force-free flux ropes of Titan. We find a mean flux rope radius of 220 ± 260 km and a mean central magnetic field of 6 ± 8 nT. The individual flux rope values for radii and magnetic field, along with equation 5.6, estimate a mean flux content of around 5 ± 54 Wb. As can be seen via the large standard deviations of the mean values, there is a large spread of flux rope sizes and content and hence the large uncertainties in these values represents the large spread of values and not an uncertainty in their sizes.

5.6.2.2 Non-Force-Free

In total 84 out of 85 flux ropes are fitted with a χ^2 probability of less than 5% and an MSE of less than 0.5 (comparable with the restriction on the force-free model). The algorithm does not converge for one flux rope, this flux rope is also unable to be fitted with the force-free model, however, this flux rope signature will remain in the total list.

The NFF model gives a mean flux rope radius of 210 ± 310 km, a mean maximum magnetic field of 3 ± 10 nT and a mean flux content of 5 ± 48 Wb calculated using equation 5.13 and the individual flux rope parameters. Similar to the force-free results, the uncertainty value on these mean values does not represent the error in calculation but the spread of the different flux rope parameters. These values are all within the values presented by the force-free model on a statistical basis, however singular examples are not always in accordance, as described in the following section.

5.6.2.3 Comparison of FF and NFF Models

A comparison overview of the spatial distributions, sizes and core field strength from the two models is given in figure 5.17. When considered statistically, the two models give results in general agreement with each other (figure 5.18). However, when considered singularly the models are not longer in agreement. An example of which is shown in figure 5.19. The following table outlines the individual results of the parameters for both the FF and NFF model fits to examples in figures 5.19 and 5.20, with corresponding uncertainties.

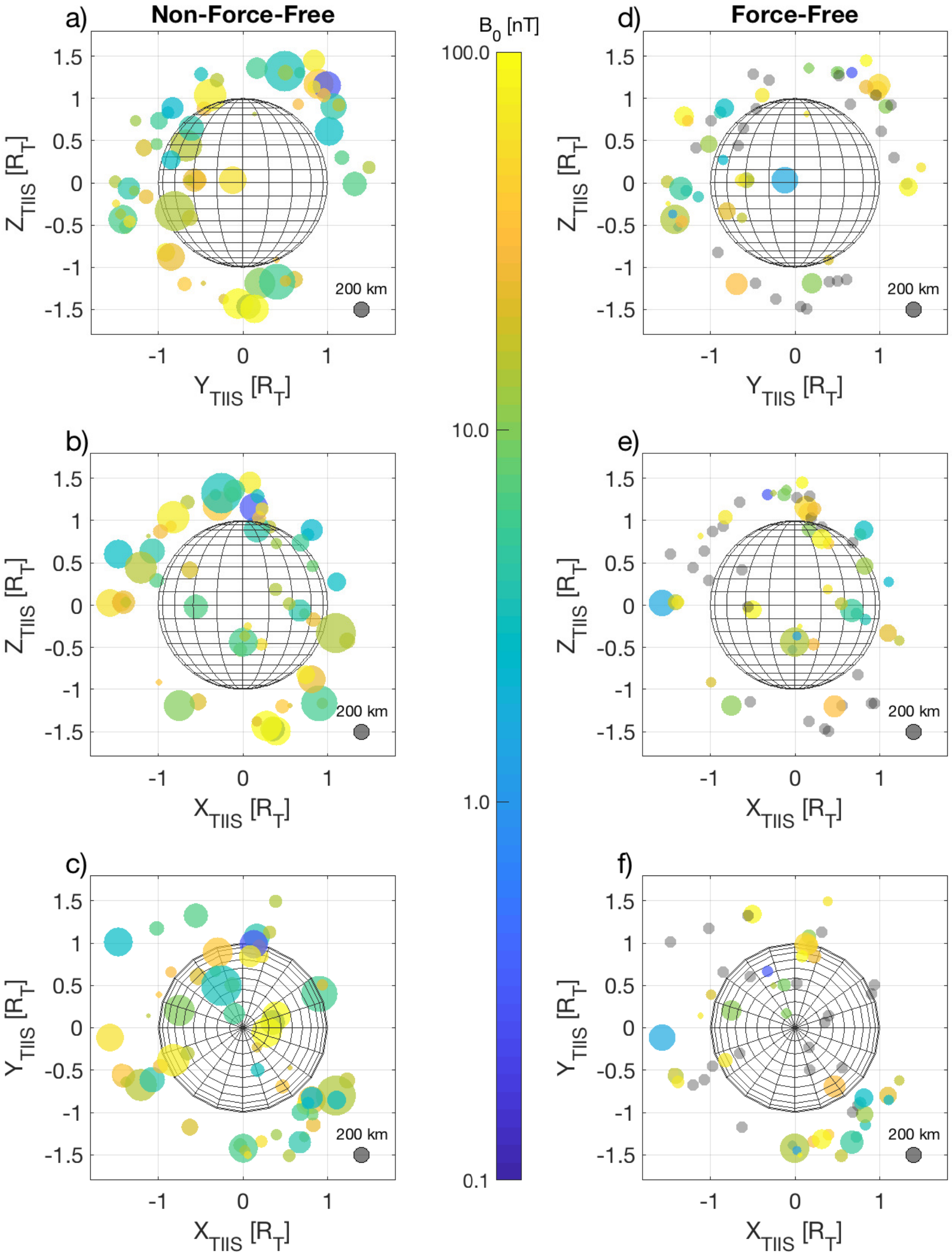

FIGURE 5.17: Flux rope characteristics from NFF model (left) and the FF model (right) where each plot shows a different positional perspective. Each flux rope is represented as a circle with colour representing the central field strength and a size representative of the radius of the flux rope.

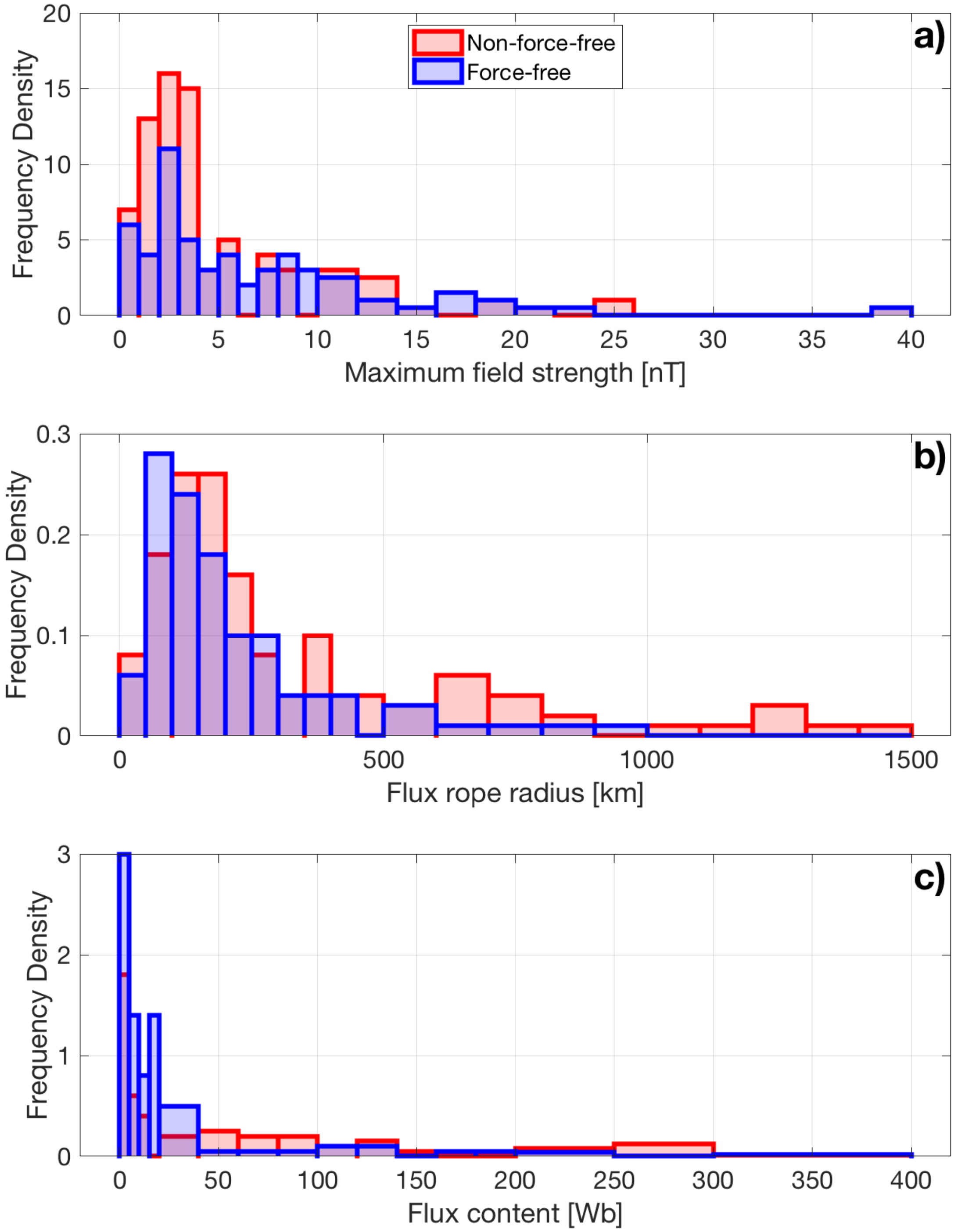

FIGURE 5.18: Flux rope characteristics derived from the FF model (blue) and the NFF model (red). a) maximum magnetic field b) flux rope radius and c) flux content

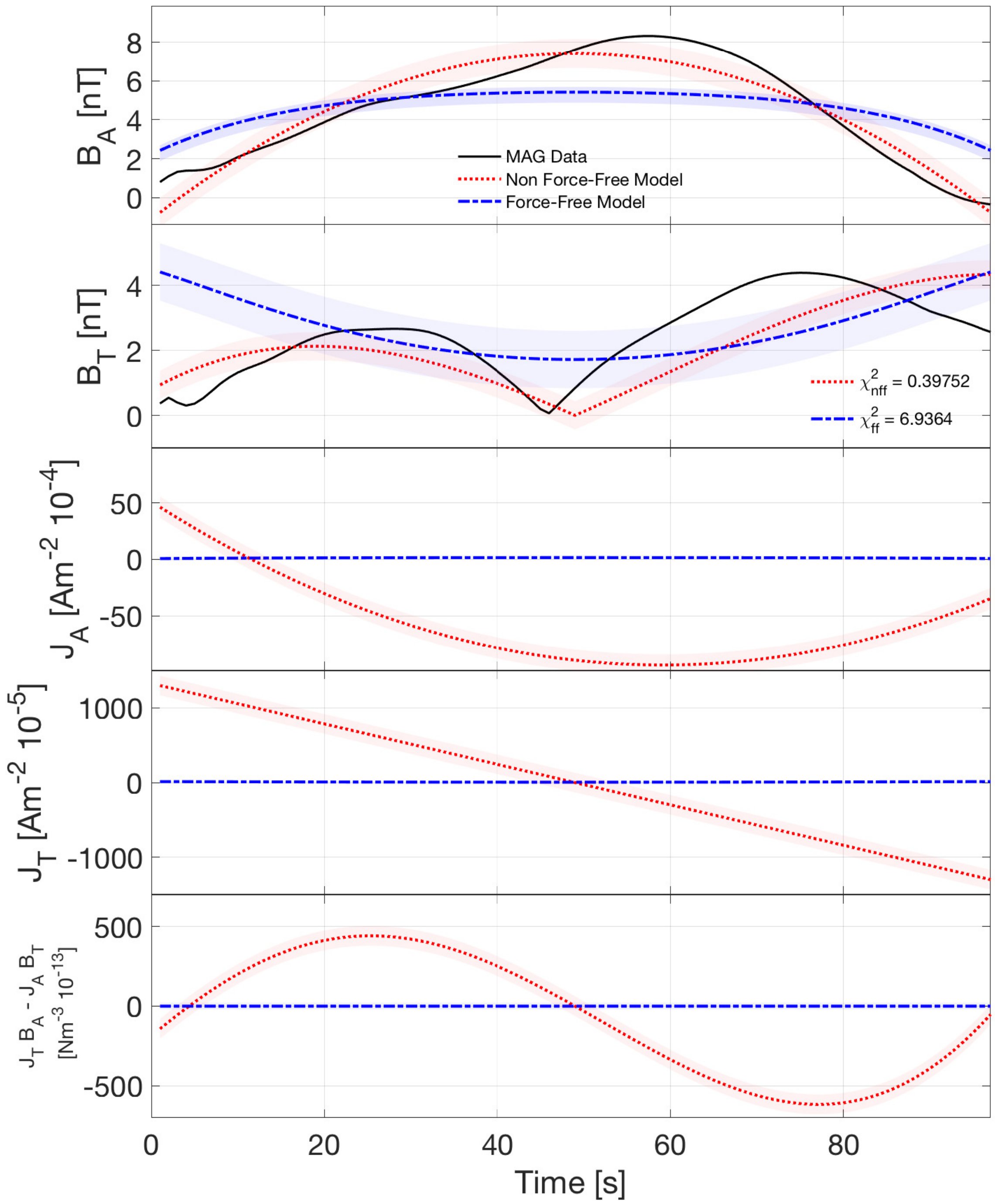

FIGURE 5.19: A fit of the FF model (blue) and the NFF model (red) with corresponding uncertainty bounds (shaded regions in corresponding colours). The figure shows axial magnetic field, tangential magnetic field, axial current density, tangential current density and force density where data is in black. The corresponding χ^2 values are shown for each fit. This flux rope is found at 13.6 SLT on T30 at 20:07 on 12/05/2007.

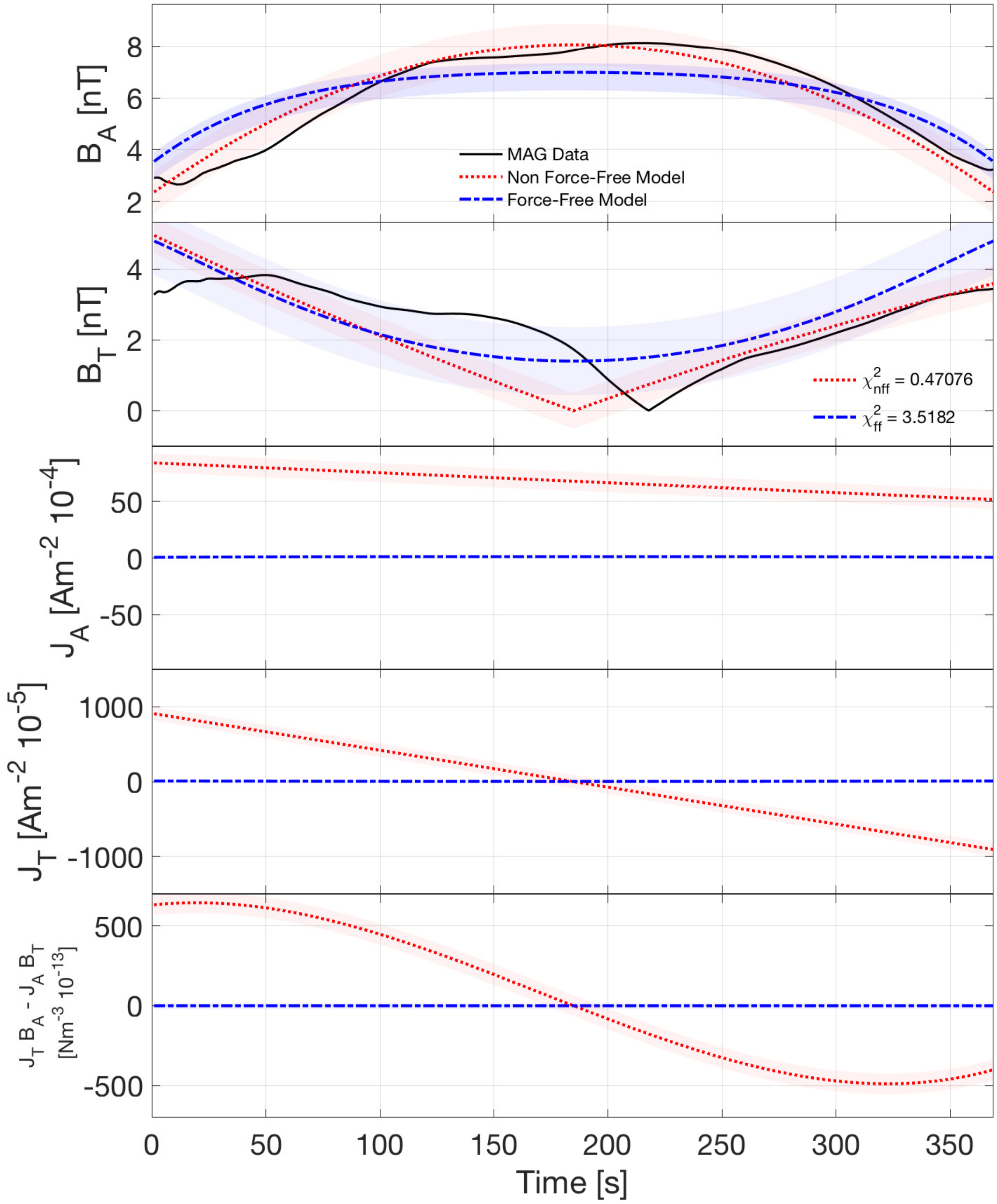

Figure 5.20: A fit of the FF model (blue) and the NFF model (red) with corresponding uncertainty bounds (shaded regions in corresponding colours). The figure shows axial magnetic field, tangential magnetic field, axial current density, tangential current density and force density where data is in black. The corresponding χ^2 values are shown for each fit. This flux rope is found at 5.3 SLT on T5 at 19:01 on 16/04/2005.

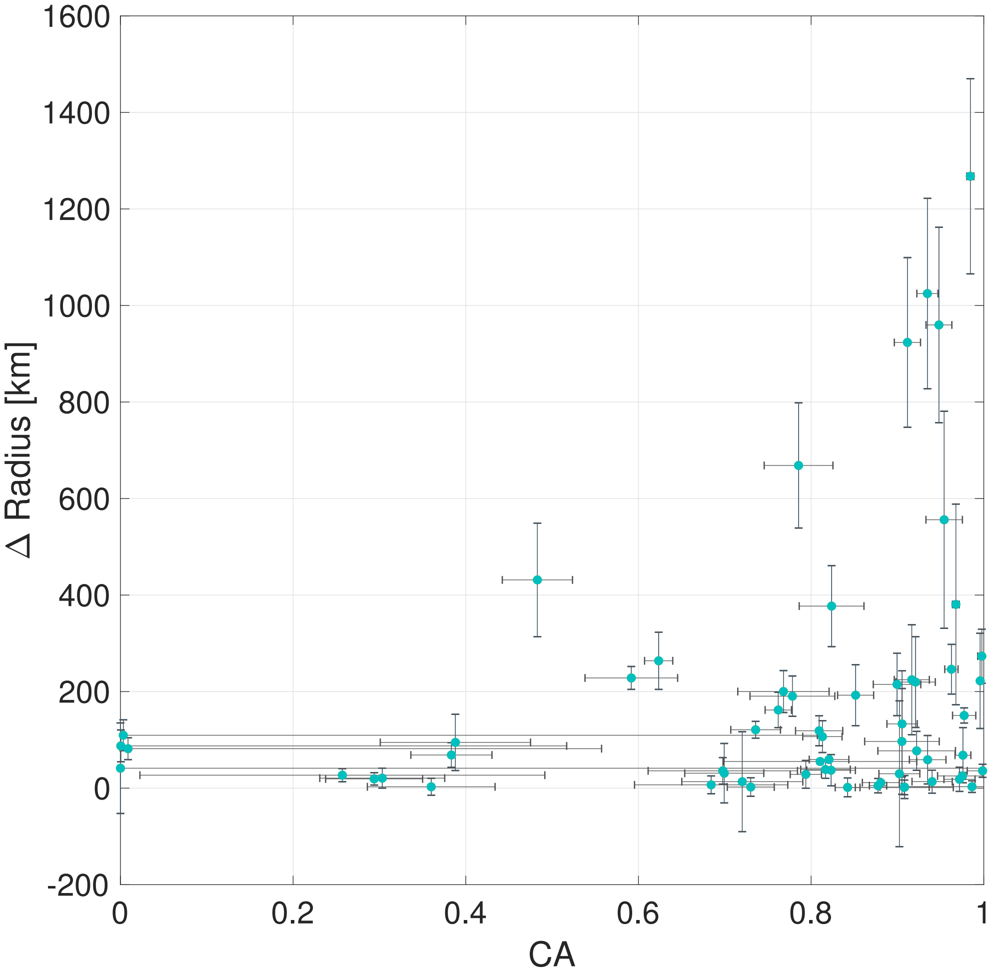

Figure 5.21: Figure showing the increased probability of a disparity between models and CA value.

The table (5.2) shows the parameters relating to two examples of fitted flux ropes, where the first has a large closest approach (CA) value (0.7) where CA describes the distance into the flux rope that the trajectory of Cassini penetrated. This first example shows a large disparity between the models, whereas example 2 shows a smaller CA and parameters that are in agreement within uncertainties, shown for all fitted flux ropes in figure 5.21. The figure shows that a larger closest approach value, i.e. Cassini is further from flux ropes axis, increases the magnitude of disagreement between the two models, along with increasing the chance of a disagreement.

Example 1 (figure 5.19) shows the comparison of FF and NFF for a flux rope on

	Example 1:	12/05/2007		Example 2:	16/04/2005	
Method	Radius [km]	Magnetic Field [nT]	CA	Radius [km]	Magnetic Field [nT]	CA
FF	53 ± 7	6.6 ± 2.3	0.7	115 ± 11	13.5 ± 2.2	0.3
NFF	132± 11	9.6 ±3.5	0.7	119 ± 11	14.1 ± 3.4	0.3

Table 5.2: Comparison of parameters corresponding to figures 5.19 (example 1) and 5.19 (example 2).

12/05/2017 in the noon sector. The FF model fits to a relatively satisfactory degree, with a χ^2 value of 6.9, however the NFF model fits with a χ^2 value of 0.39, which is lower than one due to the uncertainties on the fitting parameters. This example has a large CA value and a large disparity between the parameters fitted, however what is evident is the difference in the current densities (axial and tangential) in the third and fourth panels which shows large current density values when using the NFF model and a near zero value for the FF model. This results in a non-zero value for the force density (bottom panel) using the NFF method which has a symmetrical signature around the centre of the flux rope for NFF and an expected zero value (within uncertainties) for the FF model.

The current densities are as expected in a flux rope with a peak of axial current density near the centre of the flux rope which reduces to near zero at the edges, and the peak of tangential current density at the edge of the rope. The same can be said of example 2 (figure 5.20), where the only difference is a constant positive axial current density across the flux rope radius. Also noted that any break in assumptions during the traversal of a flux rope could cause a large change in the current density and force density signatures. For example, if the flux rope was not stationary or was evolving during the traversal, could cause an asymmetry or unexplained deviation from the model, to be explored more in section 5.6.4.

5.6.3 Comparison to Other Planetary Flux Ropes

A number of studies (see table 5.3) discuss flux ropes in Venus and Mars' ionospheres, we find that at Venus, flux ropes are generally on the order of 10-100 km in radius with a small flux content of 2-3 Wb. However Zhang et al. (2012) shows giant flux ropes are

Study	Planetary Body	Mean Radius [km]	Mean Field [nT]	Mean Flux Content [Wb]
This study (FF)	Titan	220 ± 260	6 ± 8	5 ± 54
This study (NFF)	Titan	210 ± 310	3 ± 10	5 ± 48
Wei et al. (2010)	Titan	100	10	15
Wei et al. (2011)	Titan	-	>37	-
Hara et al. (2015)	Mars	161.7	>50	>200
Hara et al. (2014)	Mars	30-670	-	-
Eastwood et al. (2012)	Mars	-	25.4,42.2	-
Beharrell and Wild (2012)	Mars	82.6,140,129	-	-
Briggs et al. (2011)	Mars	80-100	15	14-23
Morgan et al. (2011)	Mars	325-350	50-90	800-1700
Brain et al. (2010)	Mars	140	200	600
Vignes et al. (2004)	Mars	4-38	4-90	<20
Zhang et al. (2012)	Venus	>100	37-100	>1200
Wei et al. (2010)	Venus	20	7	0.4
Ledvina et al. (2002)	Venus	10-30	<50	<0.7-7
Kleeorin et al. (1994)	Venus	50-100	1-10	0.4-15
Luhmann and Elphic (1985)	Venus	-	<20-100	-
Elphic and Russell (1983*b*)	Venus	6-15	20-80	0.1- 2.7
Elphic et al. (1981)	Venus	20-30	100	6.0 - 14.0
Elphic et al. (1980)	Venus	15-20	100	3.5 - 6.0
DiBraccio et al. (2015)	Mercury	450	40	1250
Slavin et al. (2009) & (2010)	Mercury	240 - 1200	-	0.2 x 10^6
Russell and Walker (1985)	Mercury	400	40	1000

TABLE 5.3: Overview and comparison of flux rope parameters at Venus, Mars and Titan. Red values are calculated from mean radius and mean magnetic field given in other studies using the flux content calculation from the force-free method, black values are stated within the respective studies, and blue values are values from this study with a standard deviation.

present with radii on the order of 100's of km and flux content of 1000's Wb. This shows that the flux ropes at Titan are comparable is size to the giant flux ropes at Venus than the smaller more common flux ropes, but with a much smaller magnetic field.

Additionally, at Venus it is thought that flux ropes are formed near a zenith angle of 0° and travel away from their original site, hence more mature flux ropes are found at the terminator of Venus. More mature flux ropes appear more 'stable' and conform to the force-free flux rope idea, hence we conclude that flux ropes at Titan appear to be less developed on average than flux ropes at Venus, and are much larger in radii on average.

Additionally, we see flux ropes in Mars' ionosphere at around 200-400 km where at Titan we see flux ropes much higher up at around 800-1000km - a trajectory bias of limited closest approach of Cassini may be due to this difference along with the extended nature of Titan's atmosphere, and hence the ionosphere occurring at higher altitudes.

Also, there appears to be no altitude difference with field strength as at Venus where stronger flux ropes are detected lower in the atmosphere.

Table 5.3 gives an overview and comparison of previous flux rope results at numerous planetary bodies. It is noted that the standard deviations presented in this study are large, however this value represents the large spread of data from individual flux ropes and is not a representation of the uncertainties on the mean value.

Previous studies of flux ropes at Titan show a large variation in maximum magnetic field values from Wei et al. (2010) where the authors show a mean maximum magnetic field of 10 nT, to Wei et al. (2011) who present a flux rope with a lower bound of maximum magnetic field of 37 nT, which is a value much larger then the ambient magnetic field environment in Titan's ionosphere. This study found a similar mean maximum magnetic field to Wei et al. (2010) of 10 ± 8 nT. However Wei et al. (2010) presented two examples of flux ropes at Titan where the radii was on the order of 100 km, this study shows an average radii much larger (220 ± 260 km), the standard deviation however, includes this lower value of radii.

5.6.4 Deformations to Force-Free

As discussed earlier, the results of the FF-NFF model comparison show that the NFF method and assumptions give much lower χ^2 values and improved uncertainties over the FF method and assumptions. However, little physical background can be given to the assumption of the current density following a polynomial function. With increasing order of polynomial function of current density, an asymptotic improvement is seen in the fit of the NFF model to the data up to orders three and four for axial and tangential components respectively. This fact still does not present physical evidence of why the current density is modelled as a polynomial function.

It is evident that the FF model is symmetric around the 'peak' of the axial field (as expected when using a zeroth order Bessel function, see figures 5.11, 5.19 & 5.20), yet the magnetometer data itself is not symmetric around this point but often shifted or pulled to one side or the other forming a steeper decrease in magnetic field on one side of the rope than the other. In this section, deformations that can produce asymmetries in the force-free model are examined and case-studies are chosen to show improved fits to the force-free model.

5.6.4.1 Modelling a Bent Flux Rope

A bent flux rope is defined in this study as a flux rope which does not appear to have an axis that is straight, the flux ropes presented have a constant radius and axial field strength along the flux rope, however an asymmetry is present in the tangential and axial field strength with radius, a diagrammatic example of this is shown in figure 5.22. To model a bent flux rope, a force-free flux rope model utilised in the previous section is used. This model is then deformed using the TSY98 general deformation method (outlined in section 2.2.1).

The specific deformation used in this precess is as follows: the force-free Bessel function model is used as an undeformed magnetic field. A parabola is then used as the basis of the spatial deformation. The z-axis is deformed into the x-direction causing the axis of the flux rope to take the parabolic shape rather than a straight line.

$$z = a(x - c)^2 \tag{5.14}$$

The normal to the flux rope axis is then calculated by finding the derivatives of equation 5.14 to give:

$$\frac{dz}{dx} = 2a(x - c), \tag{5.15}$$

$$\frac{dz}{dy} = 2a(y - c), \tag{5.16}$$

where a is the leading co-efficient of the polynomial, describing how much the flux rope has bent and c is the offset from the y-axis that the centre of the flux rope has moved, in this analysis $c = 0$ as this difference can also be modelled by changing the position fo the simulated fly-through of the flux rope. Now, a unit normal (n_x, n_y, n_z) to the flux rope centre is found for the fly-though. The Y-vector (Y_x, Y_y, Y_z) is found as the undeformed y-axis and the X-vector (X_x, X_y, X_z) is found as the cross product of the normal and

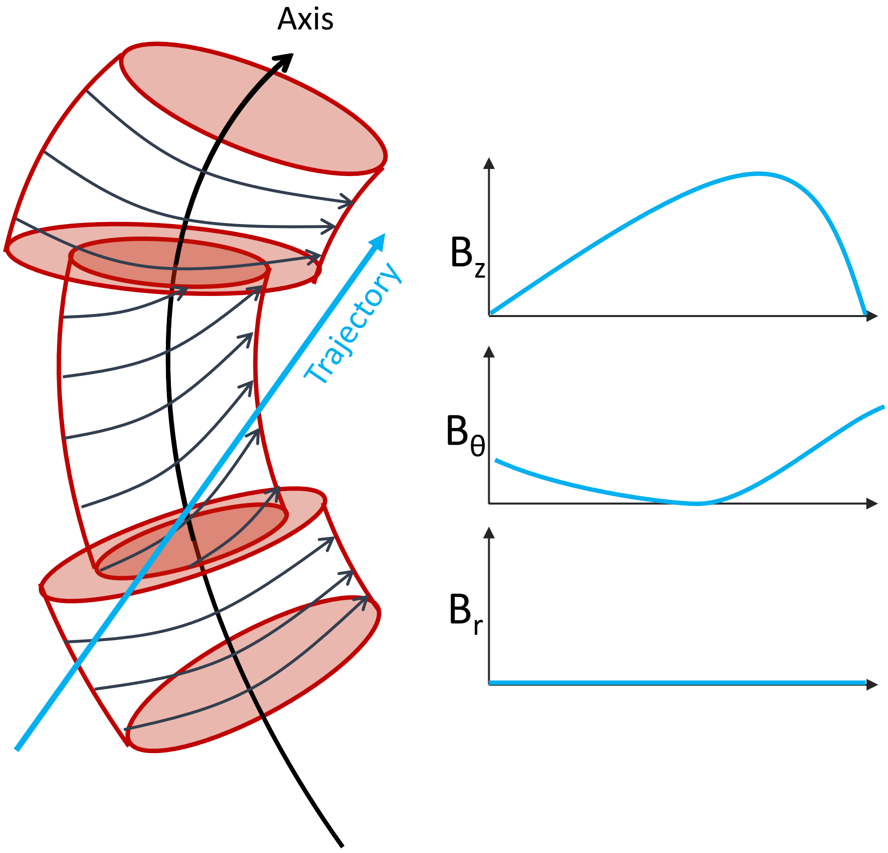

FIGURE 5.22: A bent flux rope, with simulated fly-through and expected cylindrical magnetic field components. Layers of the flux rope are cut away to view the inner structure.

the Y-vector. The new coordinate system is then found as:

$$x^* = xX_x + yX_y + zX_z \tag{5.17}$$

$$y^* = xY_x + yY_y + zY_z \tag{5.18}$$

$$z^* = xn_x + yn_y + zn_z \tag{5.19}$$

The new deformed magnetic field in the original undeformed coordinate system then reads:

$$B_z^* = B_0 J_0(\alpha r^*) + b_0, \tag{5.20}$$

$$B_x^* = -H B_0 J_1(\alpha r^*) \sin(\phi), \tag{5.21}$$

$$B_y^* = H B_0 J_1(\alpha r^*) \cos(\phi), \tag{5.22}$$

where the model is evaluated in cylindrical coordinates and converted to cartesian for plotting and simplicity in the following step. ϕ is calculated as the angle of the simulated spacecraft from the x-axis for each position. B_0 is the axial field, J_0 and J_1 are the zeroth and first order Bessel functions. α is the constant 2.40 and $r^* = \sqrt{x^{*2} + y^{*2}}$ is the radius. b_0 is the magnetic offset and H is the handedness.

The transformation matrix $\boldsymbol{T}$ (see section 2.2.1) can then be constructed to find the magnetic field in the new deformed system: $\boldsymbol{B'} = \boldsymbol{TB^*}$. Figure 5.23 shows an example of a comparison between an undeformed flux rope (grey) and a deformed flux rope (red) where a clear asymmetry can be seen in the axial (z) component and total field. The tangential components (x and y) show some asymmetry in the magnitude of each component before and after closest approach, but both still cross 0 at the 'centre' of the flux rope.

The main assumption of previous models is that using MVA (see section 2.2.2) will give the axial, tangential and radial field components. However, it is noted that at other planetary bodies (i.e. Mercury - Slavin et al. (2009)) the intermediate variance direction will give the axial direction and the maximum variance direction is found in the tangential direction, the opposite to what is found at Titan. If a completely undeformed, non-interacting, force-free flux rope is modelled the MVA process will find the maximum variance direction as the tangential direction, the intermediate variance direction as the axial direction and a zero valued minimum variance radial direction. In data, this is not the case at Titan.

Flux rope signatures at Titan will give the maximum variance direction as the axial field, the intermediate variance direction as the tangential field and a small - but non-zero- minimum variance radial field. It is found that adding a very slight bend will

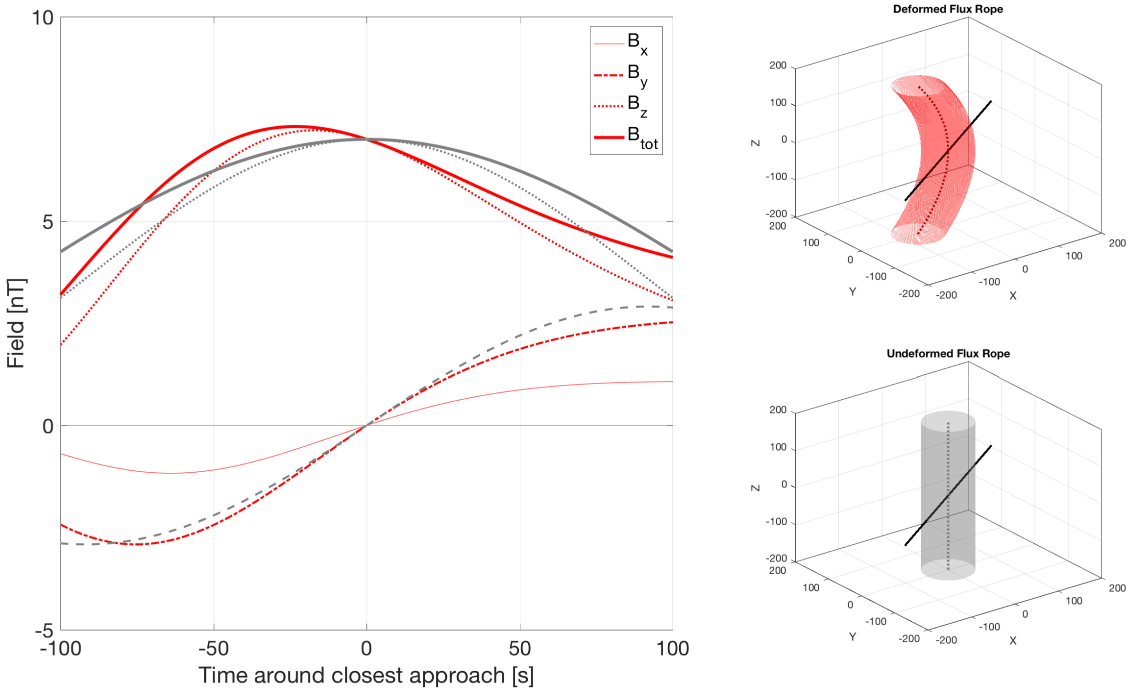

FIGURE 5.23: A comparison of an undeformed flux rope (grey) and a deformed flux rope (red) where the components are total field (thick solid), axial (dotted), y (dash-dot) and x (thin solid).

flip the variance directions from the standard seen at Mercury, to what is found in the data at Titan. However, further bending will increase the degeneracy of the variance directions and no solution may be found.

Figure 5.24 shows an undeformed and a deformed flux rope with calculated MVA directions in blue (maximum), yellow (intermediate) and green (minimum) when in the left-hand figure the flux rope is undeformed and the intermediate variance direction is along the central axis. In the right-hand figure the flux rope is deformed slightly, where the maximum variance direction is closest to the axial direction. This shows that MVA analysis is sensitive to changes in the flux rope which may lead to the method not correctly identifying variance directions. However, this does show that the flux ropes at Mercury are well modelled by a non-deformed force-free model.

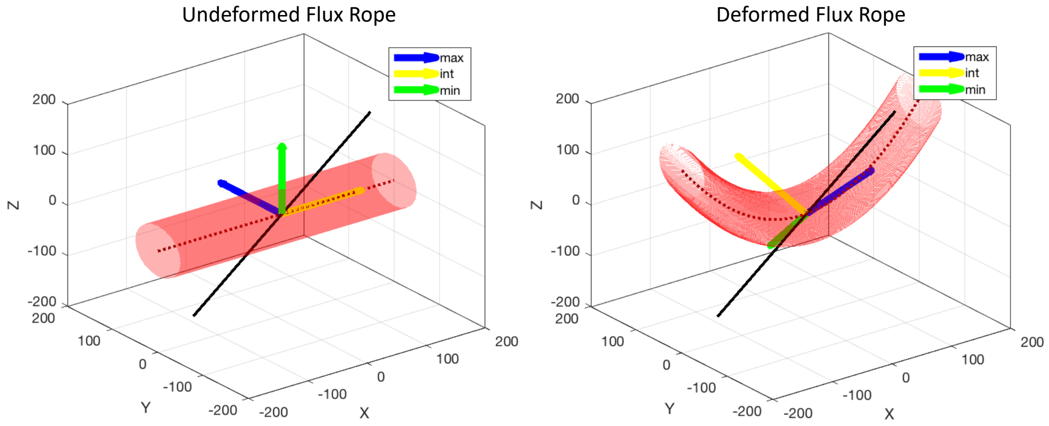

FIGURE 5.24: A comparison of an undeformed flux rope (left) and a deformed flux rope (right) where MVA is used on both and give maximum (blue), intermediate (yellow) and minimum (green) variance directions averaged for the whole fly-through.

5.6.4.2 Modelling an Elliptical Cross Section Flux Rope

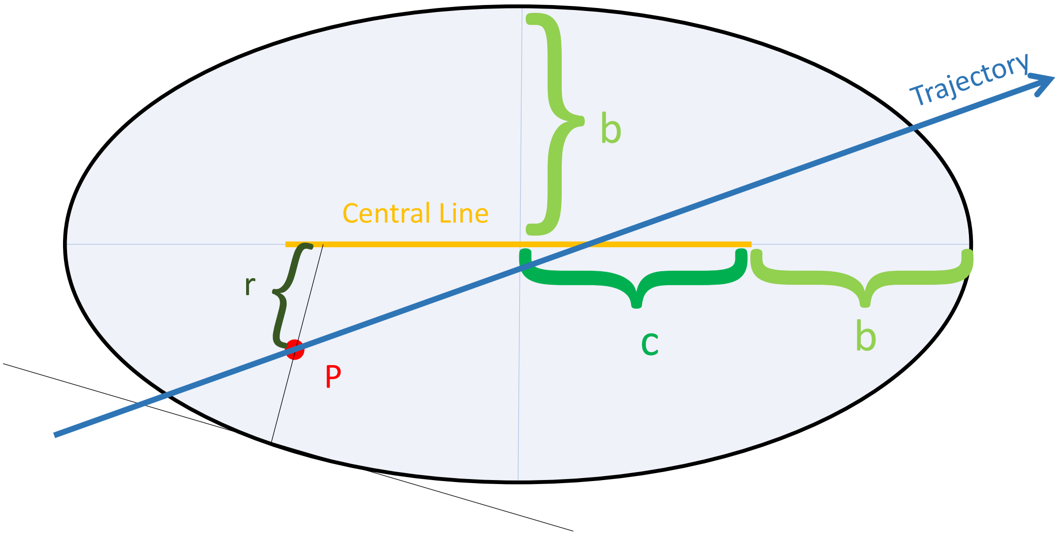

FIGURE 5.25: The cross-section of an elliptical flux rope with model parameters labeled.

Another possible asymmetry of a flux rope is that its cross-section is not a circle, as most models assume. However, evaluating the Bessel functions in elliptical coordinates is not straight forward and resembles the form of the Mathieu functions. However, with some simple geometry a circular flux rope model can be adapted into an elliptical model without the development of elliptical Bessel functions or the extended use of elliptical coordinates.

To begin, a 'central line' is constructed at the centre of an ellipse with semi-minor axis of b and a semi-major axis of $a(= b + c)$ where c is the half-length of the 'central line' (see figure 5.25). A simulated fly-through of the flux rope is then made with known trajectory, where each position P has its own unique value of r (radial distance from the central line position). However, this radial distance is not just the radial distance from the nearest point on the central line, but an extrapolation of the normal to the flux rope surface at the closest surface point to point P which goes through point P to the central line. This is shown as the thin black like through point P in figure 5.25.

This r is then used as the radial distance to be used in the Bessel function force-free model to evaluate the flux rope in elliptical co-ordinates. For simplicity, the magnetic offset b_0 is not used in this analysis but if need be can be easily added at a later stage.

$$B_z = B_0 J_0(\alpha r), \tag{5.23}$$

$$B_v = H B_0 J_1(\alpha r), \tag{5.24}$$

$$B_u = 0, \tag{5.25}$$

where the equations resemble the previously used force-free models, but with components in (u, v, z) which are described in appendix figure A4, where u is equivalent to a radial direction and v, tangential.

Figure 5.26 shows a fit to the elliptical flux rope model described above. This example is found on T29 at 21:34 on 26th April 2007 at 13.7 SLT. This model fits to the magnetometer data with a χ^2 value of 3.8, where the force-free model gives $\chi^2 = 6.7$ and non-force-free gives $\chi^2 = 6.5$. Along with comparable uncertainties of fit parameters, one can ascertain that the elliptical force-free model fits to the magnetometer data in this

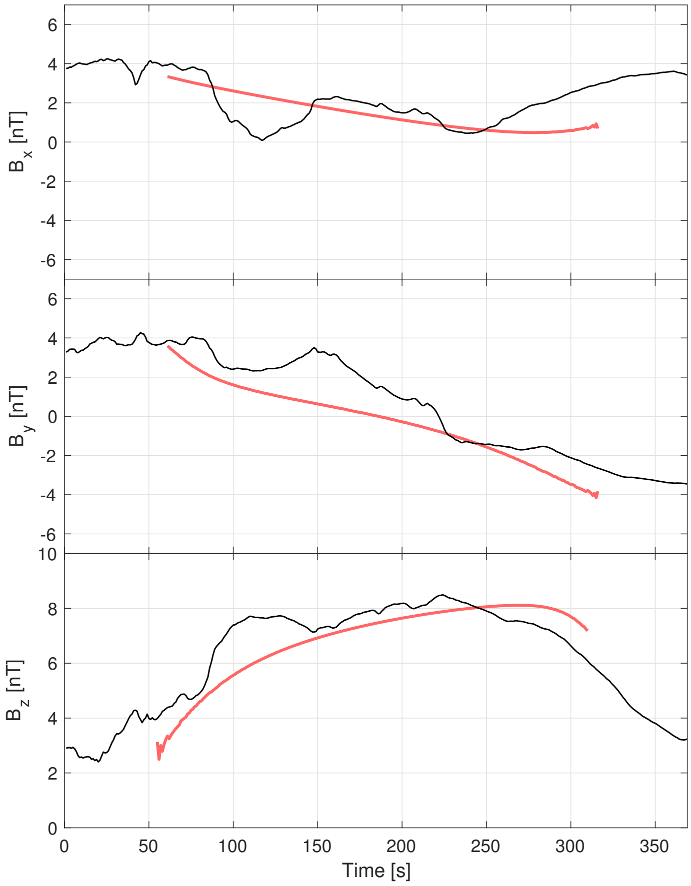

Figure 5.26: Figure showing magnetometer data (black) fitted with the elliptical flux rope model (red) in Cartesian coordinates.

example better than the circular force-free and non-force-free, leading to the hypothesis that this flux rope may be elliptical in cross-section, bent, or both. Figure 5.27 shows a diagram of the flux rope and trajectory of Cassini with the model that is fitted in figure 5.26. This example is fitted using the Bayesian inference method described in section 2.2.4 using angles of incidence on the flux rope rather than MVA analysis for all three methods (circular force-free, elliptical force-free and non-force-free).

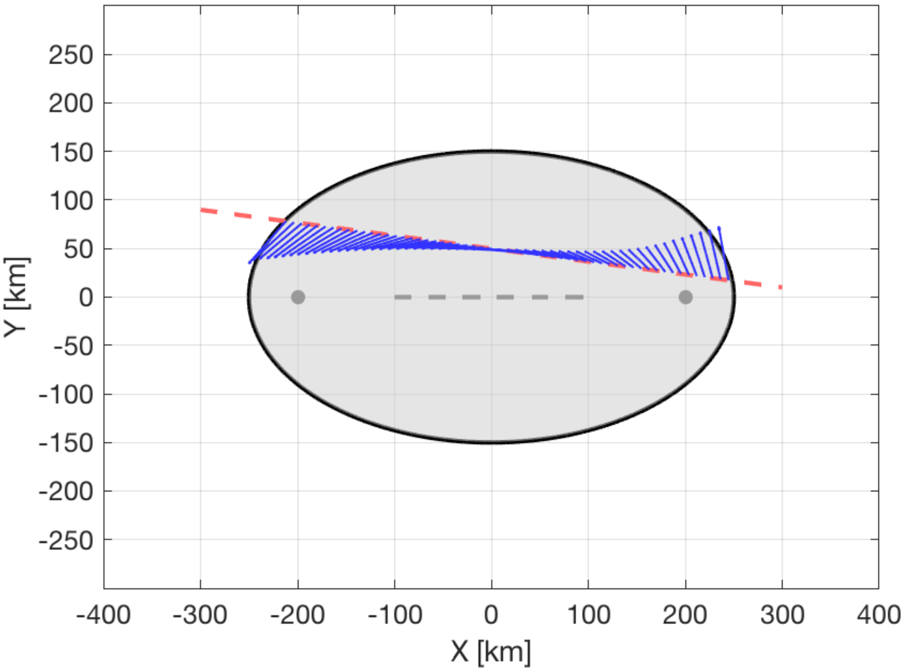

FIGURE 5.27: Figure showing schematic of set up of trajectory and elliptical flux rope corresponding to fitted magnetometer data in figure 5.26, where the red dashed line is the expected trajectory, the blue quiver is the model field direction in the x-y plane. The grey shaded area is inside the flux rope and the black solid line is the edge of the flux rope. A dashed grey line shows the central line as described in figure 5.25 with two grey dots showing the foci of the ellipse.

5.7 Conclusions

In conclusion, a statistical study was undertaken to determine the properties and location of flux ropes in Titan's ionosphere. The main findings of the studies outlined in this chapter are as follows:

- Flux ropes are mainly located in the noon sector of Saturn's magnetosphere, with a secondary peak at pre-midnight where the x-line from Vasyliunas cycle reconnection is expected. The only other positions that flux ropes are found, are when the current sheet is close to, and passing over Cassini frequently.
- With reference to position on Titan, the flux ropes are more common in the sunlit and ram-side of the moon rather than in shadow and in the tail region. A statistical

test of position is undertaken and shows a preference statistically for these regions. Some SLT bias in which hemisphere (sunlit or ram-side) is dominant in flux rope numbers however this is not statistically testable due to the changing nature of Titan's interaction with Saturn's magnetic field.

- A force-free flux rope model is fitted to magnetometer data and shows that the assumption of the force-free model give a good first approximation to the flux ropes at Titan, however the quality of the fits could be greatly improved.
- A non-force-free model is therefore fitted to the data which shows a much improved quality of fit and an improved number of flux ropes able to be fitted by the new model. However, the non-force-free model lacks the physical basis of the polynomial expansion of the current density.
- Hence, deformations to the force-free are explored to improve the fit of the force-free model. Explored are an elliptical cross-section and a bend in the flux rope. As both of these deformations introduce a larger number of parameters, singular flux ropes are explored to show that a small number of flux ropes can be fitted to a better degree using the elliptical cross section force-free model than the circular and non-force-free models.
- In comparison with other planetary bodies, Titan's flux ropes are much larger in radius, however much reduced in magnetic field strength. This is assumed to be due to the lower field strength in the surrounding area of Titan compared to the surroundings of the other planetary bodies.
- Deformations to flux ropes in the Titan system may make them not an applicable target for use of minimum variance analysis to determine the flux rope coordinate system needed for the various models.

This chapter has shown that Titan's ionospheric environment supports the development of flux ropes, in that over half of all flybys of Titan show flux rope signatures with a common occurrence being multiple flux ropes over the trajectory. However, the unsuccessful attempt to fit all flux rope signatures with a force-free flux rope model shows that the flux ropes can be considered as immature, or not in equilibrium. This conclusion shows that the flux ropes must therefore be initiated consistently in the ionospheric interaction with Saturn's magnetosphere, but not cultivated into mature flux ropes. Instead, they are disrupted and destroyed by the dynamical interaction with Saturn's magnetic field.

Chapter 6

Conclusions

This thesis has presented studies of small-scale magnetic phenomena from two very different but related locations in Saturn's magnetosphere. First, we explored the aperiodic waves present on Saturn's equatorial current sheet, their own controlling parameters and additionally what they can unveil about the current sheet itself. The aperiodic waves were used to map the current density of the equatorial current sheet and were also used as a current sheet crossing to allow for the analysis of the vertical structure.

Second, we diverted attention to Saturn's largest moon Titan, and the magnetic structures that reside in the ionosphere. A statistical study of the location and properties of the flux ropes found during flybys of the moon was presented.

Cassini magnetometer data has been the primary data source for this thesis, which was fitted to a number of flux rope models and a deformed model of the current sheet. A more in depth review of science results follows.

6.1 Review

To conclude effectively, we will proceed chapter by chapter.

To begin, a catalogue of the position and time of aperiodic wave events was created by identifying events in the Cassini magnetometer data that fitted the criteria of a time period of 1 - 30 minutes, a change in the magnetic field magnitude of over 1 nT and are not repeating or periodic. In total 1461 aperiodic events were found during Cassini's equatorial orbits that occurred between 2005 and 2012. These waves were found in all local time sectors and appear to be uniformly distributed spatially and temporally in Saturn's magnetosphere.

To extract more information on the current sheet and the waves themselves, a model is developed to fit to the magnetometer data. This model consists of a modified Harris current sheet that is deformed, using the general deformation method of TSY98, by a Gaussian wave pulse. Use of the Gaussian wave pulse came about due to its non-repeating nature and included physically-meaningful wave parameters.

The main science results from chapter 3 are:

- Scale height of the current sheet increases on average with radial distance from Saturn, an SLT asymmetry is present where the dusk current sheet is thicker than dawn, consistent with more limited results from previous studies.
- Wave amplitude increases with radial distance from Saturn. An analogy with water shoaling was used to argue for an increase in the amplitude as a consequence of the increasing scale height and decreasing mass density of the current sheet.
- Wave propagation in the radial and azimuthal directions were derived from the wave vectors in the Gaussian wave pulse equation. The dominant propagation direction is found to be radially outward.

Also explored are the possible sources of the waves, and concluded in this is that the waves are formed from a number of varying sources such as magnetopause compressions, dayside and nightside reconnection at the magnetopause, in the tail and on the current sheet. Additionally, interchange of plasma in the inner magnetosphere could also disturb the sheet to produce outward travelling waves. However, the main conclusion of this chapter is that, on average, the aperiodic waves are travelling outwards with increasing amplitude on a thickening current sheet implying that the source of the waves is in the inner magnetosphere, where we cannot probe due to a more dipolar field arrangement.

In chapter 4 we used the current sheet parameters obtained in chapter 3 to study the spatial variation in radial and azimuthal components. Both radial and azimuthal components of the current sheet varied with radial distance and had a pronounced local time asymmetry where current density peaks post-midnight and is at a minimum post-noon.

The divergence of the current densities in radius and azimuth are calculated and combined to give the divergence of the perpendicular current. This shows whether current is flowing from the higher latitudes into or out of the current sheet at the equator. We find that current is drawn out of the current sheet into the pre-noon sector of the magnetosphere and into the pre-midnight sector. By current continuity these currents flow as field-aligned currents into Saturn's ionosphere. The field-aligned currents in the pre-midnight sector correspond with downward electron precipitation into the ionosphere and we estimate an increase of 1-10 kR in auroral intensity in that sector, consistent with auroral investigations reported in the literature.

Finally, the aperiodic waves were used as a tool to resolve the vertical structure of the current sheet and examine the validity of the Harris current sheet assumption. The vertical current density structure is estimated using the value of B_a as a proxy for the distance to the current sheet centre, where a denotes the direction of largest change in the magnetic field just outside of the current sheet. The full time derivative $\left\langle \left| \frac{dB_a}{dt} \right| \right\rangle$ calculated numerically is used as a proxy for the current density in the current sheet. Hence, if the sheet is Harris-like, a discrete maximum is found at or near $B_a = 0$. Alternatively, if the sheet is bifurcated, two maxima are found either side of $B_a = 0$ and a local minimum is found at $B_a = 0$.

The structure of the current sheet is determined by fitting a three Gaussian model to the data, where if the central Gaussian is dominant then the sheet is Harris, or if the peripheral Gaussian's are dominant then the sheet is bifurcated, amongst other criteria. An striated category is also presented along with data for NaN and NED events. From the total number of events with enough data, it is found that 10% of events are classed as bifurcated, 78% are classified as Harris-like and the remaining 12% are striated, showing that the majority of current sheets sampled at Saturn are Harris-like, but a non-negligible number are bifurcated.

Titan's interaction with Saturn's magnetic field is a dynamic and unique interaction. Titan moves through the different regimes from current sheet to lobe magnetic field, from magnetosheath to solar wind, all of which have an effect on the thick ionosphere and draped magnetic field. A feature of Titan's interaction with its environment is the presence of magnetic flux ropes. Cassini magnetometer data was used to examine Titan flybys for the presence of flux ropes and a survey was presented in chapter 5. A total of 85 flux ropes signatures were identified. Flux ropes were found to be located, on average, in the sunlit hemisphere which is facing the incoming corotational plasma of Saturn's magnetosphere.

Removing the trajectory bias of the number of Titan flyby in each SLT sector, it is found that flux ropes are more common when Titan is in the noon sector of the magnetosphere. A secondary occurrence peak is found post-midnight. Additionally, outside of these two areas, flux ropes are only observed during flybys that also show that Titan is inside or is near the equatorial current sheet. Thus, we may conclude that the presence of flux ropes is indicative of a highly changeable environment which encourages flux rope formation.

To extract further information from the flux ropes, force-free and non-force-free models are fitted to the magnetometer data. To begin, the flux rope magnetic field signatures must be rotated into a 'flux rope coordinate system' which is where the axis of the flux rope is $\hat{A}$, and the other two components are the cylindrical radial $\hat{R}$ and tangential $\hat{T}$ components. This coordinate system is identified using two methods where MVA is used to establish the tangential and axial field where the maximum variance direction is the axial direction and the intermediate variance direction is the tangential direction, the other method being the fitting of angles of trajectory through the flux rope. The models are then fitted to the data using either a least-squares fitting or Bayesian inference regression - specified in each case.

The force-free model gives a good 'first approximation' to fitting the flux ropes; 49 flux ropes from the total 85 fitted the FF model with a χ^2 probability of less than 5%, whereas the NFF model fitted 84 from 85 flux ropes with a χ^2 probability of less than 5%. Thus showing that the flux ropes are better modelled by a non-force-free approach on average. Whilst the two models give similar statistical distributions of flux ropes radii, maximum field strength, and magnetic flux content, the actual values for individual flux ropes could be very different. We can conclude that the distance that Cassini was from the centre of the flux rope affected the agreement of the two models, where large CA values made a large difference between the models more likely.

However, the NFF model is dependent on a polynomial expansion of the current density in the flux rope. This assumption has no physical basis other than to fit the signatures. Additionally, both the FF and NFF models are symmetric around the centre of the flux rope, which is not necessarily true. Hence, deformations of the FF model were explored to search for asymmetries or bends in the flux rope that could yield better fits.

Firstly, a bending deformation was applied to the flux ropes, where a straight flux rope was deformed into a parabolic shape using the TSY98 general deformation method. The bending of the flux rope introduces an asymmetry in the axial and total magnetic field along with addition to the radial component from the axial and tangential components. Additionally, a test of MVA is used on a bent flux rope to examine if MVA is effective at finding the flux rope coordinate system. It is shown that in a straight force-free flux rope the maximum variance direction is identified as the tangential field and the intermediate variance direction is the axial direction - what is found with the flux ropes at Mercury. However, here at Titan the variance directions are switched. If a very slight bend is introduced, it is shown that the maximum variance direction is now the axial field (the same as what is seen in data at Titan) and the intermediate variance direction is the tangential direction. Showing that a slight bend can introduce the flux rope system seen at Titan, however, if a large bend is introduced the MVA analysis becomes degenerate and a coordinate system cannot be found.

Another deformation that was was to generate flux ropes with an elliptical cross-section. The elliptical FF model is described in section 5.6.4 where effectively the main change is the determination of the radial distance of Cassini from the *centre* of the flux rope, which in the elliptical sense is now a central line rather than point. The elliptical FF model is fitted to a select number of flux rope examples due to the number of fitted parameters in the new model, which is unsuitable for automatic fitting for all flux ropes. The elliptical FF model allows an asymmetry similar to the bendy model, however the elliptical model fits for a *plateau* in the axial direction which is due to the elongated flux rope centre. One example is presented, however only five flux rope are better fitted to the elliptical model than the non-force-free, but all flux ropes tested fit better to the elliptical FF model than the circular FF model.

Thus, the conclusion from this chapter is that the flux ropes sampled by Cassini are found in areas of changeable magnetic environment, can be considered not mature or not in equilibrium, which is emphasised by the better fitting of deformed models of a FF flux rope. Hence, Titan's environment can be considered an instigator of flux ropes, but it does not aid in the maturation or prevents maturation of flux ropes. In comparison with other planetary bodies where flux ropes are present, Titan's flux ropes are on average much larger in radius but much smaller in magnetic field magnitude.

This thesis has shown that the examination of the small-scale magnetic phenomena present in the Saturnian system can be a good indicator and surveyor of the system as a whole. They can also be indicators of much larger environmental changes and structures and be an important factor in the local environment, be it Titan's ionosphere or Saturn's equatorial current sheet.

6.2 Further Questions

There are a number of further research and open questions on the topics visited in this thesis, a fraction of which are outside the scope of the research produced within the thesis, however the rest are a subject for future further research. Kivelson (2016) outlined a number of currently unanswered questions on magnetodisc current sheets that have been touched on in this thesis, however the majority remain unsolved, or at least unresolved.

The larger questions in Saturn's current sheet revolve around finding a source of PPO related flapping, fully resolving the force balance which originally began the work presented in chapters 3 and 4 via Arridge et al. (2007). Additionally, the sources of pressure anisotropies in the current sheet is still an open question which is linked to the bifurcation process in chapter 4. Also addressed in this thesis are the dawn-dusk asymmetries in magnetic field and current density of the current sheet, which is highlighted as a large open question.

With regards to Titan, the main remaining magnetospheric interaction question is to what extent does Titan affect Saturn's magnetosphere with regards to a plasma torus or draped fields, currently it is hypothesised that Titan may influence the substorm-like behaviour in the night sector of the magnetosphere (Russell et al., 2008).

Produced directly from the work presented in this thesis, the following specific questions are open for future analysis:

- What are the sources of aperiodic waves, and in what proportions do they produce waves?
- What other wave forms may be used to effectively model the aperiodic waves, and how much can the model tell us about PPO flapping and other motions of the current sheet?
- Is there a solar wind or solar cycle effect on the current density in the current sheet?
- With highly biased trajectories, are there better methods for separating seasonal, solar cycle, and solar wind effects on the current sheet?
- What is the definitive source of bifurcations, are they related to velocity of the plasma in the radial direction?
- What other deformations can be made to a force-free flux rope model to more effectively model flux ropes in Titan's ionosphere?

- Is it possible to develop flux rope models with a more physically-meaningful analytical form for the current density, or an analytical form for the $\boldsymbol{j} \times \boldsymbol{B}$ force density?
- An overall question on methodology is, can improvements be brought to the Bayesian inference regression analysis so that it can easily and effectively be used on large models with a large number of variables?

The Cassini mission has given a limited, but expansive view into the Saturnian system and specifically the interaction of Titan and the dynamics of the current sheet. This thesis has presented novel techniques and models and addressed a number of previously unanswered questions and science objectives regarding the dynamics of the current sheet and the properties of flux ropes in Titan's ionosphere, however many areas deserve further investigation, and as always, more data and more coverage is always desired.

Appendices

A.1 Coordinate systems

This thesis presents a number of different coordinate systems, for reference all coordinate systems used are summarised below with diagrams for reference.

A.1.1 KSM

The KSM coordinate system or Kronocentric Solar Magnetospheric coordinates are a Cartisian system with Saturn at the origin. $\hat{\boldsymbol{x}}$ is a vector in the Saturn-Sun line, $\hat{\boldsymbol{z}}$ northward so that the rotation axis of Saturn is in the x-z plane. $\hat{\boldsymbol{y}}$ is therefore perpendicular to the z-axis, roughly in the anti-orbital direction and completes the right handed system.

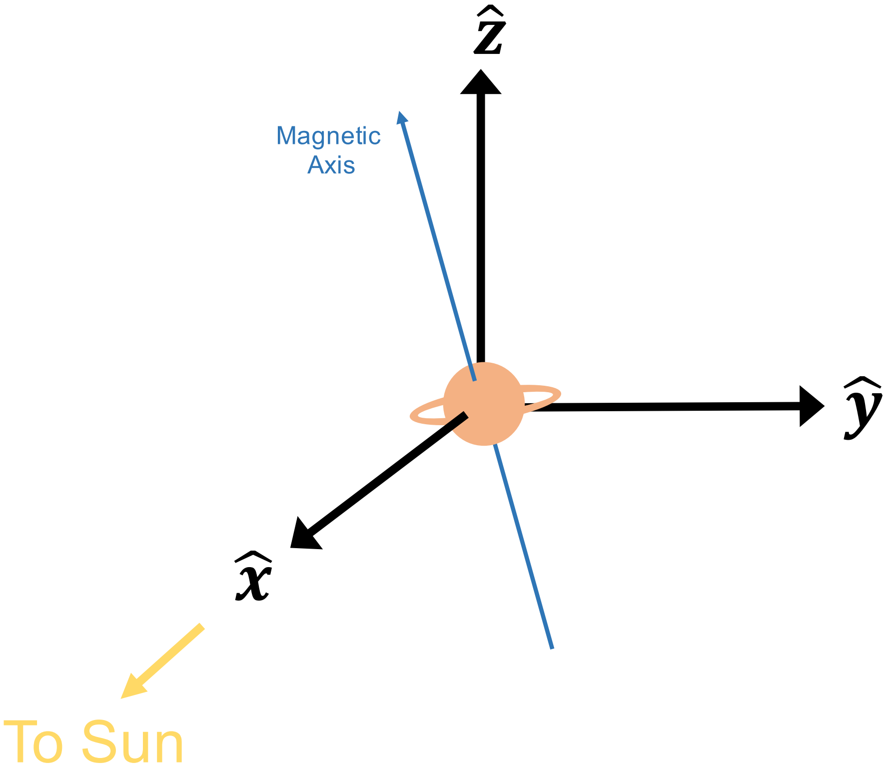

Figure A1: Figure depicting the KSM coordinate system

A.1.2 KRTP

The KRTP coordinate system, or Kronocentric Radial Theta Phi, is a spherical coordinate system centred at Saturn. This system is particularly useful when evaluating Saturn's stretched magnetic field. $\hat{\boldsymbol{r}}$ is radially outwards from Saturn, $\hat{\boldsymbol{\theta}}$ is southward at the equator. $\hat{\boldsymbol{\phi}}$ is in the direction of corotation.

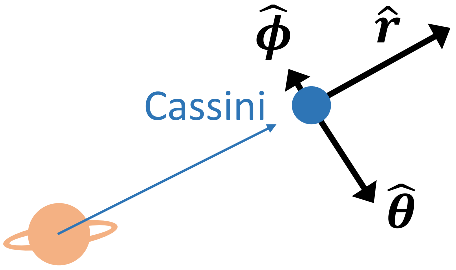

FIGURE A2: Figure depicting the KRTP coordinate system

A.1.3 Local Cassini-centric Cartesian

We define a local Cassini-centric Cartesian coordinate system for use in fitting models in the following chapters. This coordinate system is similar to the spherical KRTP system defined above, where $\hat{\boldsymbol{x}}$ is along the $\hat{\boldsymbol{r}}$ direction, $\hat{\boldsymbol{y}}$ is in the azimuthal direction and $\hat{\boldsymbol{z}}$ is positive northwards when at the equator.

A.1.4 Elliptical Cylindrical

An elliptical coordinate system is an orthogonal system where the lines of eqi-coordinate are either ellipses or hyperbolae. The z-axis is equivalent to the cylindrical z-axis which in figure A4 is out of the page. The u-coordinates increase with distance from the central focal line and the v-coordinates increase anti-clockwise with angle from the central focal line.

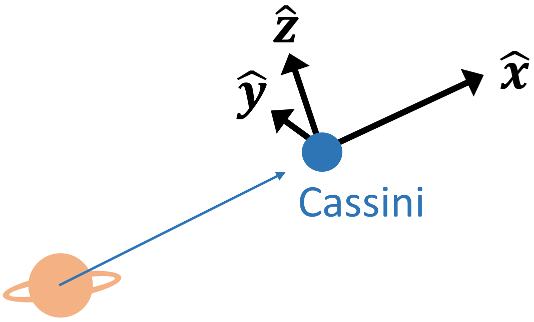

FIGURE A3: Figure depicting the local cartesian coordinate system

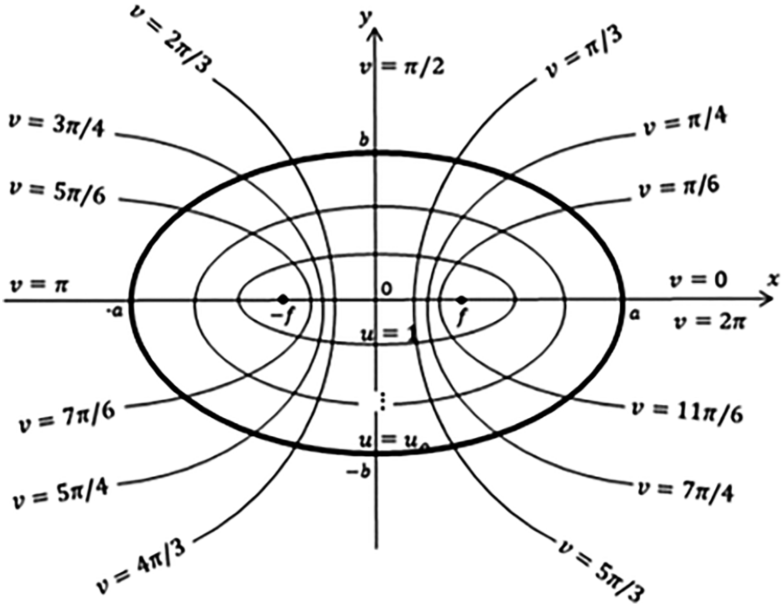

FIGURE A4: Figure depicting a 2-D elliptical cylindrical coordinate system. (Bryan, 2018)

A.1.5 TIIS

TIIS, or Titan ionospheric interaction system is a Titan-centred cartesian coordinate system where the x-axis points along the corotation direction, the y-axis points towards Saturn and the z-axis completes the right handed system and is roughly southward. Depicted in figure A5.

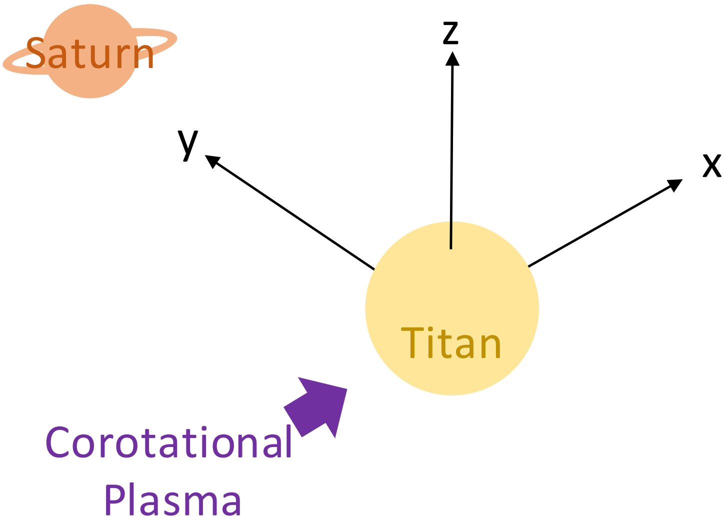

Figure A5: Figure depicting the Titan ionospheric interaction system

A.1.6 T-DRAP

T-DRAP is the coordinate system of the interaction of Saturn's magnetic field and Titan, however this coordinate system is an improvement on TIIS in that it uses the measured direction of plasma and doesn't assume corotation direction. X is in the direction of plasma flow, Y is the direction of magnetic field (roughly towards Saturn) and Z completes the system and is roughly southward.

A.1.7 TiCS

TiCS is the Titan-centric solar coordinate systems devised for the locational study of flux ropes. This system is an orthogonal Cartesian system where the x-direction is from Titan to the Sun, the z-axis is positive northward and y-axis completes the system.

A.1.8 Flux Rope Cylindrical

The flux rope cylindrical coordinate system has A-axis aligned with the axis of the flux rope (Axial), a R-axis aligned along the radial position of measurement from the centre of the flux rope (Radial) and a tangential component (T) that competes the right-handed

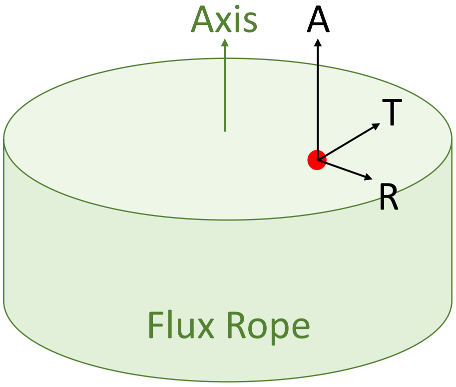

Figure A6: Figure depicting the flux rope cylindrical co-ordinate system.

system (R,T,A) and is tangential to the flux rope edge at the point of measurement, depicted in figure A6.

A.1.9 Flux Rope Cartesian-Trajectory

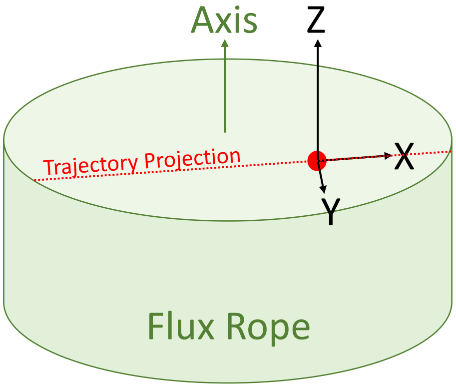

Figure A7: Figure depicting the flux rope cylindrical co-ordinate system.

A flux rope cartesian system has a Z-axis aligned with the flux rope axis, a X-axis aligned with the projection of the space craft trajectory in the plane perpendicular to the axis and Y-axis that completes the right handed (X,Y,Z) system.

A.1.10 Other

Other coordinate systems used are depicted in figure 4.8 in section 4.4 which shows the current sheet coordinate system aligned with the magnetic field and current density within the current sheet.

A.2 Bessel Function Solution to Force-Free Magnetic Fields

A.2.1 Force-free assumption

The MHD momentum equation neglecting gravity is:

$$-\nabla p + \mathbf{j} \times \mathbf{B} = 0 \tag{1}$$

With the assumption of a force free field, the gradient of plasma pressure is ignored:

$$\mathbf{j} \times \mathbf{B} = 0 \tag{2}$$

This equation physically shows that the current density must be parallel to the magnetic field or be equal to zero and hence with the known factor of $\nabla \cdot \mathbf{B} = 0$, Ampere's Law and the vector identity $\nabla \cdot (\nabla \times \mathbf{B}) = 0$:

$$\nabla \times \mathbf{B} = \mathbf{j} = \alpha \mathbf{B} \tag{3}$$

In a cylindrical coordinate system of a flux rope, the components of the magnetic field can be displayed as

$$\frac{dB_z}{d\rho} = -\alpha B_\phi, \tag{4}$$

$$\frac{1}{\rho}\frac{d(\rho B_\phi)}{d\rho} = \alpha B_z, \tag{5}$$

assuming no axial or azimuthal variation. Substituting one into the other and vice versa one can find that both components form a second order differential equation that resemble Bessel's equation with constant α where $\nu_z = 0$ and $\nu_\phi = 1$.

$$\rho^2\frac{d^2B_z}{d\rho^2} + \rho\frac{dB_z}{d\rho} + \alpha^2(\rho^2 - \nu_z^2)B_z = 0 \tag{6}$$

$$\rho^2\frac{d^2B_\phi}{d\rho^2} + \rho\frac{dB_\phi}{d\rho} + \alpha^2(\rho^2 - \nu_\phi^2)B_\phi = 0 \tag{7}$$

These ordinary differential equations can be solved using Bessel functions.

A.2.2 General Solution to Bessel Functions

In general terms Bessel's equation reads:

$$x^2\frac{d^2y}{dx^2} + x\frac{dy}{dx} + \alpha^2(x^2 - \nu^2)y = 0, \tag{8}$$

where α is a constant (equal to 1 in this example), ν is an integer constant relating to the order of the Bessel function.

Therefore, a solution is expected to take the form $y(x) = \sum_{n=0}^{\infty} a_n x^{(n+r)}$, and hence the components of the Bessel equation are as follows:

$$x^2y(x) = \sum_{n=0}^{\infty} a_n x^{(n+r+2)} \qquad \Rightarrow \qquad y(x) = \sum_{n=2}^{\infty} a_{n-2} x^{(n+r)} \tag{9}$$

$$x\frac{dy(x)}{dx} = \sum_{n=0}^{\infty}(n+r)a_n x^{(n+r)} \tag{10}$$

$$x^2\frac{d^2y(x)}{dx^2} = \sum_{n=0}^{\infty}(n+r)(n+r-1)a_n x^{(n+r)} \tag{11}$$

The differential equation then reads:

$$\sum_{n=0}^{\infty}(n+r)(n+r-1)a_n x^{(n+r)} + \sum_{n=0}^{\infty}(n+r)a_n x^{(n+r)} + \sum_{n=2}^{\infty} a_{n-2}x^{(n+r)} - \sum_{n=0}^{\infty}\nu^2 a_n x(n+r) = 0 \tag{12}$$

Group terms:

$$\sum_{n=0}^{\infty}\Big[(n+r)(n+r-1) + (n+r) - \nu^2\Big]a_n x^{(n+r)} + \sum_{n=2}^{\infty} a_{n-2}x^{(n+r)} = 0 \tag{13}$$

Simplify:

$$\sum_{n=0}^{\infty}\Big[(n+r)^2-\nu^2\Big]a_n x^{(n+r)}+\sum_{n=2}^{\infty}a_{n-2}x^{(n+r)}=0 \tag{14}$$

Split first term to allow for simplification of different orders:

$$(r^2+\nu^2)a_0x^r+\Big[(r+1)^2-\nu^2\Big]a_1x^{(r+1)}+\sum_{n=2}^{\infty}\Big[(n+r)^2-\nu^2\Big]a_nx^{(n+r)}+\sum_{n=2}^{\infty}a_{n-2}x^{(n+r)}=0 \tag{15}$$

Combine second summation order terms:

$$(r^2+\nu^2)a_0x^r+\Big[(r+1)^2-\nu^2\Big]a_1x^{(r+1)}+\sum_{n=2}^{\infty}\Bigg\{\Big[(n+r)^2-\nu^2\Big]a_n+a_{(n-2)}\Bigg\}x^{(n+r)}=0 \tag{16}$$

Each term must equal zero so one finds three recurrence relations:

$$(r^2+\nu^2)a_0x^r=0 \tag{17}$$

$$\Big[(r+1)^2-\nu^2\Big]a_1x^{(r+1)}=0 \tag{18}$$

and

$$\Big[(n+r)^2-\nu^2\Big]a_n+a_{(n-2)}=0 \text{ where } n\geq 2 \tag{19}$$

From equation 17 one can find that $r^2+\nu^2=0$ and hence $r=\pm\nu$. If this is true, then $(r+1)^2-\nu^2\neq 0$ and so a_1 must be equal to 0 and hence the first two recurrence relations are solved. The only remaining unknown is a_n for values greater than 2, and this is needed to solve the third recurrence relation by considering both $r=+\nu$ and $r=-\nu$. If we consider $r=+\nu$ we find:

$$(n^2+2n\nu)a_n+a_{(n-2)}=0 \tag{20}$$

$$n(n+2\nu)a_n=-a_{(n-2)} \tag{21}$$

Since $n\geq 2$ and $\nu\geq 0$, $n+2\nu$ will never be 0, and so:

$$a_n=-\frac{a_{(n-2)}}{n(n+2\nu)} \tag{22}$$

Equation 22 and $a_1 = 0$ imply that all odd coefficients are equal to 0, and we are left with only the even coefficients.

$$a_{2k} = \frac{(-1)^k a_0}{2^{2k}(k!)(1+\nu)(2+\nu)...(k+\nu)} \quad \text{where} \quad \nu \geq 0 \tag{23}$$

And hence when $a_0 = 1$, the solution is as follows:

$$J_\nu^+(x) = x^\nu \Big[1 + \sum_{k=1} \infty \frac{(-1)^k}{2^{2k}(k!)(1+\nu)(2+\nu)...(k+\nu)} \quad \text{where} \quad \nu \geq 0 \tag{24}$$

The same applies for $r = -\nu$:

$$J_\nu^-(x) = x^{-\nu} \Big[1 + \sum_{k=1} \infty \frac{(-1)^k}{2^{2k}(k!)(1-\nu)(2-\nu)...(k-\nu)} \quad \text{where} \quad \nu \geq 0 \tag{25}$$

So for magnetic field components B_z and B_ϕ, the solutions will be of the form:

$$B_z = c_1 J_0(\alpha\rho), \tag{26}$$

$$B_\phi = c_2 J_1(\alpha\rho), \tag{27}$$

Where J_0 and J_1 are the zeroth ($\nu = 0$) and first ($\nu = 1$) order Bessel functions of the first kind. Now, one must consider the physical implications of what the Bessel functions are modelling, i.e. form boundary conditions. Figure A8 shows the Bessel functions of the first kind with zeroth order (blue) and first order (red) with no scaling factors for positive and negative x.

The Bessel functions themselves are scaled between -1 and 1. One can see that the peak of the zeroth order function is at 1. If we postulate that this zeroth order function is describing the radial relationship of magnetic field along the axis of a flux rope, then the peak of the function will represent the field strength at the centre of the flux rope. Hence, one must scale the peak to the maximum axial magnetic field (B_0).

The first order Bessel function represents the tangential magnetic field of a flux rope, this too much be scaled to the maximum axial magnetic field (B_0), however the

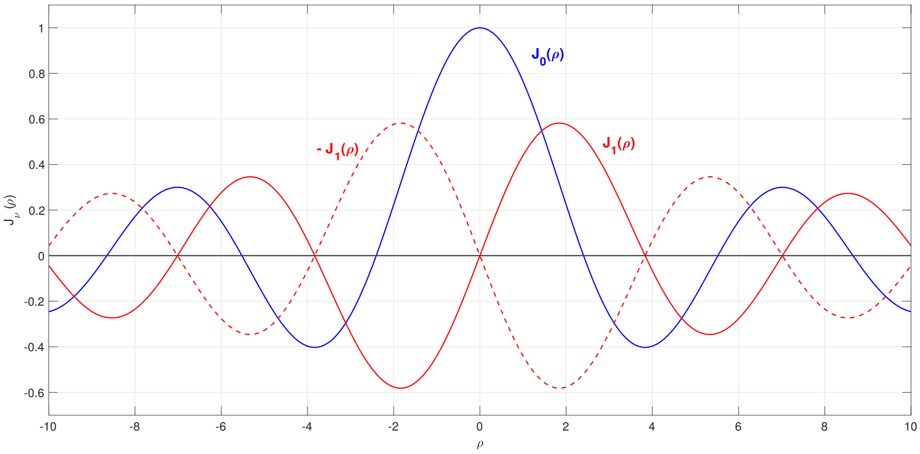

FIGURE A8: Figure showing the zeroth (blue) and first (red) order Bessel functions of the first kind

sign of this component is dependent on the 'handedness' (H) of the flux rope. This 'handedness' describes which way around the central field the magnetic field is twisting. Right handed flux ropes have a handedness value of 1, whereas left handed flux ropes have a handedness of -1. Figure A8 shows the first order Bessel function in red, with the negative function in dashed red.

We also must consider the surrounding plasma and magnetic environment that could have an effect on the magnetic field signatures of the flux rope. As most flux ropes are embedded in a plasma or magnetic field regime, an ambient background magnetic field component will be present and must be included, so an additional 'magnetic offset' is included in the axial component (b_0).

The remaining physical factor to include is to scale in the radial direction. The axial component of the flux rope will always be positive, and so the flux rope extends only to where the zeroth order function is positive, and hence the radius of the flux rope will be where the zeroth order function reaches zero. This can be scaled by finding the roots of the function, and using this value as a constant (α). The first root of the zeroth order Bessel functions is 2.4048.

The third component of the magnetic field, the radial component, should ideally equal 0 as the force free assumptions allude to the field either being axial (fully axial at the centre) or tangential (fully tangential at the outer edge) and hence one should not find any magnitude of radial magnetic field in a force free flux rope. And hence we find that an accurate description of a force free flux rope can be found using the Bessel equation solutions which results in field components as follows:

$$B_{Axial} = B_0 J_0(\alpha\rho) + b_0 \tag{28}$$

$$B_{Tangential} = B_0 H J_1(\alpha\rho) \tag{29}$$

$$B_{Radial} = 0 \tag{30}$$

A.3 Flux Content Derivation

$$\Phi = \int \boldsymbol{B} \cdot dS = \int B_A dS = B_0 \int J_0(\alpha r) 2\pi r dr, \tag{31}$$

Where Φ is flux content, B_0 is maximum magnetic field, J_0 is the zeroth order Bessel function from the axial field B_A, r is radius and α is 2.40.

$$\Phi = \frac{2\pi B_0}{\alpha^2} \int J_0(x) x dx, \tag{32}$$

where $x = \alpha R$

Completing the integral then gives:

$$\Phi = \frac{2\pi}{\alpha^2} B_0 \alpha R_0 J_1(\alpha R_0), \tag{33}$$

$$\Phi = \frac{2\pi}{\alpha} B_0 R_0^2 J_1(\alpha), \tag{34}$$

A.4 Field-Aligned Currents From Continuity of Currents

Using the continuity of currents and formulation from Vasyliunas (1984):

$$\nabla \cdot \boldsymbol{J_{\parallel}} = \nabla \cdot J_{\parallel} \frac{\boldsymbol{B}}{B} = \nabla \cdot \frac{J_{\parallel}}{B} \boldsymbol{B} \tag{35}$$

As $\nabla \cdot b\boldsymbol{A} = b\nabla \cdot \boldsymbol{A} + \boldsymbol{A} \cdot \nabla b$:

$$\nabla \cdot \frac{J_{\|}}{B}\boldsymbol{B} = \frac{J_{\|}}{B}\nabla \cdot \boldsymbol{B} + \boldsymbol{B} \cdot \nabla \frac{J_{\|}}{B} \tag{36}$$

The divergence of $\boldsymbol{B}$ is zero so:

$$\nabla \cdot \boldsymbol{J}_{\|} = \boldsymbol{B} \cdot \nabla \frac{J_{\|}}{B} \tag{37}$$

Divide both sides by B:

$$\frac{\nabla \cdot \boldsymbol{J}_{\|}}{B} = \frac{\boldsymbol{B}}{B} \cdot \nabla \frac{J_{\|}}{B} \tag{38}$$

We know $\frac{\boldsymbol{B}}{B} \cdot \nabla = \frac{\partial}{\partial s}$:

$$\frac{\nabla \cdot \boldsymbol{J}_{\|}}{B} = \frac{\partial}{\partial s}\frac{J_{\|}}{B} \tag{39}$$

$$\nabla \cdot \boldsymbol{J}_{\|} = B\frac{\partial}{\partial s}\frac{J_{\|}}{B} \tag{40}$$

We know $\nabla \cdot \boldsymbol{J}_{\|} = -\nabla \cdot \boldsymbol{J}_{\perp}$, hence:

$$\nabla \cdot \boldsymbol{J}_{\perp} = -B\frac{\partial}{\partial s}\frac{J_{\|}}{B} \tag{41}$$

A.5 Striated Current Density Examples

Additional plots to outline the shape of striated current density profiles.

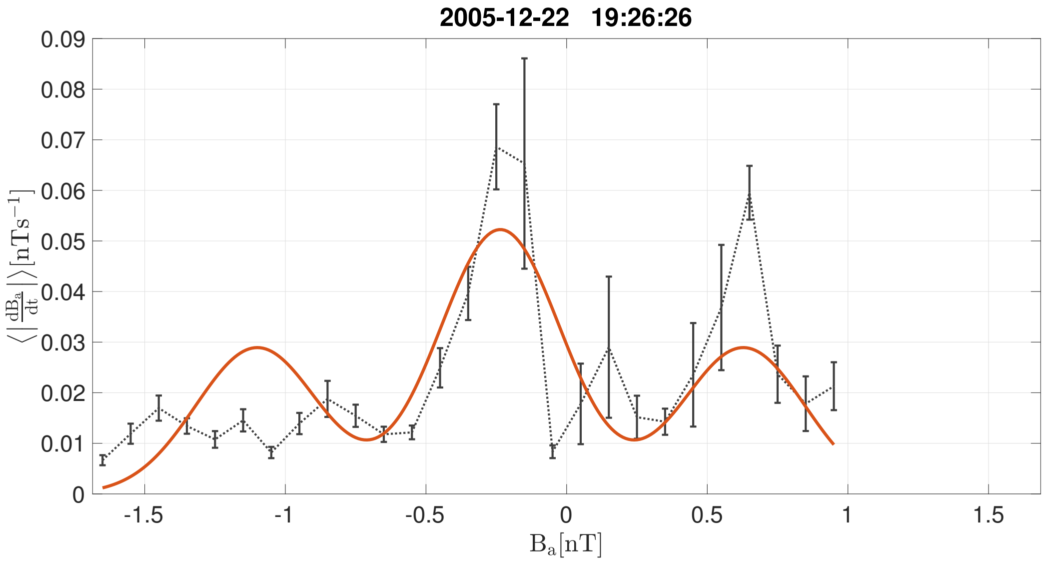

FIGURE A9: A current sheet with a 'striated' current density profile. The solid black lines show the spread in each B_a bin where the means of each bin are connected by the black dotted line. The solid orange line is the fitted model of three Gaussians.

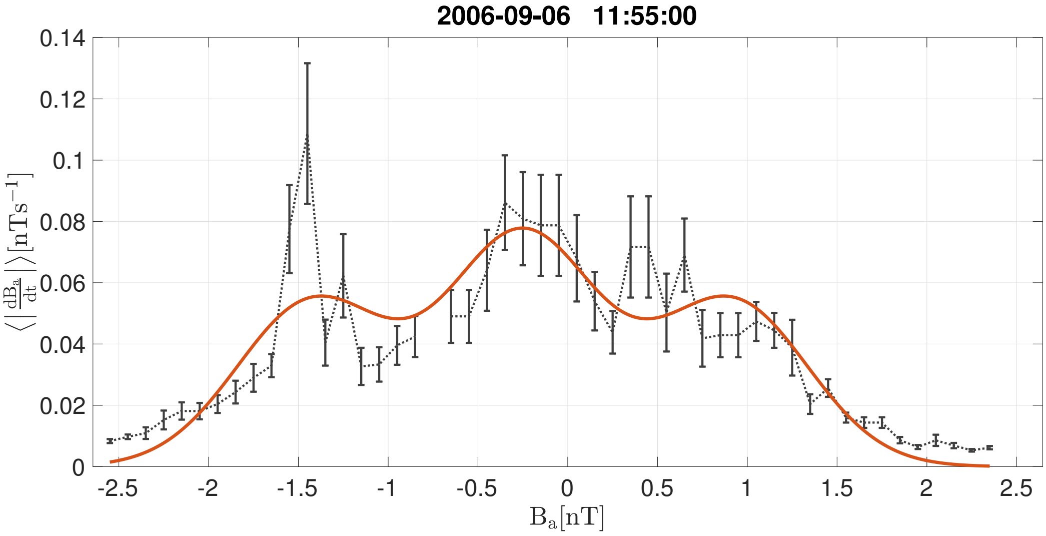

FIGURE A10: A current sheet with a 'striated' current density profile. The solid black lines show the spread in each B_a bin where the means of each bin are connected by the black dotted line. The solid orange line is the fitted model of three Gaussians.

A.6 Time Series for T30

This section outlines the surrounding magnetic field during T30. A flux rope is found during T30 which is plotted against altitude in figure 5.1. The following figures show a time series of the magnetic field during the flyby (figure A11), and the 4 hours before and after the flyby (figure A12).

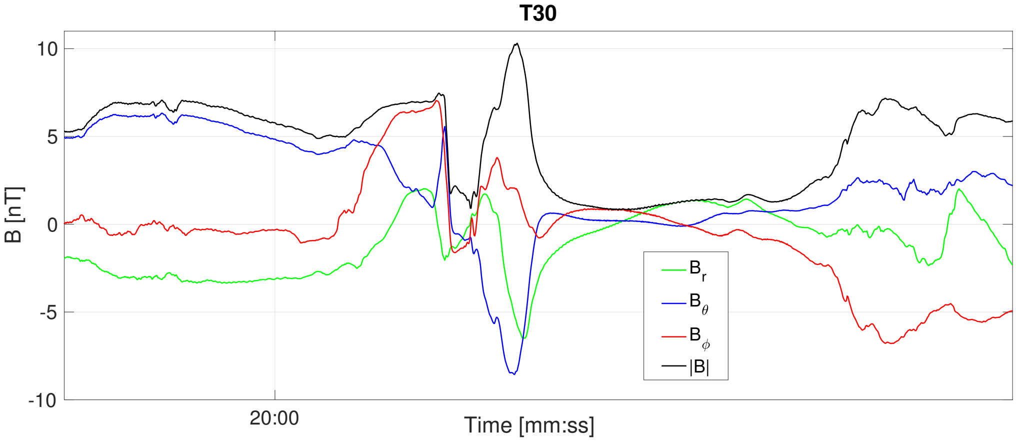

FIGURE A11: Magnetic field during the T30 flyby. Data is presented in the KRTP coordinate system.

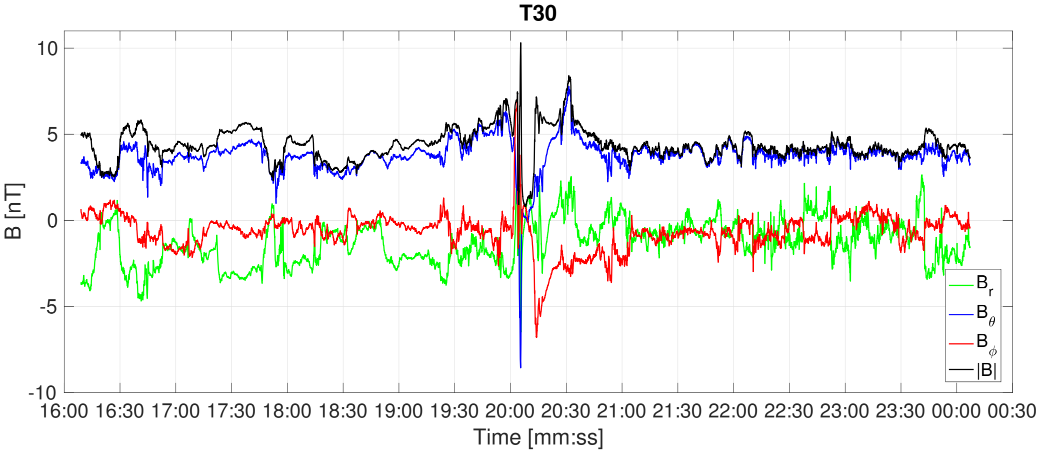

FIGURE A12: Magnetic field from 4 hours before the T30 flyby to 4 hours after. Data is presented in the KRTP coordinate system.

Bibliography

Achilleos, N., Arridge, C., Bertucci, C., Jackman, C., Dougherty, M., Khurana, K. and Russell, C. (2008), 'Large-scale dynamics of saturn's magnetopause: Observations by cassini', *Journal of Geophysical Research: Space Physics* **113**(A11209).

Acuna, M. H. (2002), 'Space-based magnetometers', *Review of scientific instruments* **73**(11), 3717–3736.

Acuna, M. and Ness, N. (1973), 'The pioneer 11 high-field fluxgate magnetometer'.

Ågren, K., Wahlund, J.-E., Garnier, P., Modolo, R., Cui, J., Galand, M. and Müller-Wodarg, I. (2009), 'On the ionospheric structure of titan', *Planetary and Space Science* **57**(14), 1821–1827.

Ågren, K., Wahlund, J.-E., Modolo, R., Lummerzheim, D., Galand, M., Müller-Wodarg, I., Canu, P., Kurth, W., Cravens, T., Yelle, R. et al. (2007), 'On magnetospheric electron impact ionisation and dynamics in titan's ram-side and polar ionosphere–a cassini case study', *Annales Geophysicae* **25**(11), 2359–2369.

Alfvén, H. (1942), 'Existence of electromagnetic-hydrodynamic waves', *Nature* **150**(3805), 405.

Andrews, D., Coates, A. J., Cowley, S., Dougherty, M., Lamy, L., Provan, G. and Zarka, P. (2010), 'Magnetospheric period oscillations at saturn: Comparison of equatorial and high-latitude magnetic field periods with north and south saturn kilometric radiation periods', *Journal of Geophysical Research: Space Physics* **115**(A12252).

Arridge, C., Achilleos, N., Dougherty, M., Khurana, K. and Russell, C. (2006), 'Modeling the size and shape of saturn's magnetopause with variable dynamic pressure', *Journal of Geophysical Research: Space Physics* **111**(A11), A11227.

Arridge, C., Kane, M., Sergis, N., Khurana, K. and Jackman, C. (2015), 'Sources of local time asymmetries in magnetodiscs', *Space Science Reviews* **187**(1-4), 301–333.

Arridge, C., Khurana, K., Russell, C., Southwood, D., Achilleos, N., Dougherty, M., Coates, A. and Leinweber, H. (2008b), 'Warping of saturn's magnetospheric and magnetotail current sheets', *Journal of Geophysical Research: Space Physics* **113**(A8), A012963.

Arridge, C., Russell, C., Khurana, K., Achilleos, N., André, N., Rymer, A., Dougherty, M. and Coates, A. (2007), 'Mass of saturn's magnetodisc: Cassini observations', *Geophysical research letters* **34**(9), L09108.

Arridge, C., Russell, C., Khurana, K., Achilleos, N., Cowley, S., Dougherty, M., Southwood, D. and Bunce, E. (2008a), 'Saturn's magnetodisc current sheet', *Journal of Geophysical Research: Space Physics* **113**(A4), A04214.

Arridge, C. S., André, N., Khurana, K., Russell, C., Cowley, S., Provan, G., Andrews, D., Jackman, C., Coates, A. J., Sittler, E. et al. (2011), 'Periodic motion of saturn's nightside plasma sheet', *Journal of Geophysical Research: Space Physics* **116**(A11), A11205.

Asano, Y., Nakamura, R., Baumjohann, W., Runov, A., Vörös, Z., Volwerk, M., Zhang, T., Balogh, A., Klecker, B. and Reme, H. (2005), 'How typical are atypical current sheets?', *Geophysical research letters* **32**(3), L03108.

Aschenbrenner, H. and Goubau, B. (1936), 'Eine anordnung zur registrierung rascher mag netischer strungen', *Hochfrequenztechnik und Elektroakustik* **47**, 177–181.

Bader, A., Badman, S., Kinrade, J., Cowley, S., Provan, G. and Pryor, W. (2018), 'Statistical planetary period oscillation signatures in saturn's uv auroral intensity', *Journal of Geophysical Research: Space Physics* **123**, 8459–8472.

Badman, S. and Cowley, S. (2007), 'Significance of dungey-cycle flows in jupiter's and saturn's magnetospheres, and their identification on closed equatorial field lines', *Annales Geophysicae* **25**(4), 941–951.

Badman, S. V., Achilleos, N., Arridge, C. S., Baines, K., Brown, R., Bunce, E., Coates, A. J., Cowley, S., Dougherty, M., Fujimoto, M. et al. (2012), 'Cassini observations of ion and electron beams at saturn and their relationship to infrared auroral arcs', *Journal of Geophysical Research: Space Physics* **117**(A1), A01211.

Bagenal, F. (1992), 'Giant planet magnetospheres', *Annual Review of Earth and Planetary Sciences* **20**(1), 289–328.

Balogh, A., Dunlop, M., Cowley, S., Southwood, D., Thomlinson, J., Glassmeier, K., Musmann, G., Lühr, H., Buchert, S., Acuna, M. et al. (1997), 'The cluster magnetic field investigation', *Space Science Reviews* **79**(1-2), 65–91.

Behannon, K., Acuna, M., Burlaga, L., Lepping, R., Ness, N. and Neubauer, F. (1977), 'Magnetic field experiment for voyagers 1 and 2', *Space Science Reviews* **21**(3), 235–257.

Beharrell, M. and Wild, J. (2012), 'Stationary flux ropes at the southern terminator of mars', *Journal of Geophysical Research: Space Physics* **117**(A12212).

Bertucci, C., Achilleos, N., Dougherty, M., Modolo, R., Coates, A., Szego, K., Masters, A., Ma, Y., Neubauer, F., Garnier, P. et al. (2008), 'The magnetic memory of titan's ionized atmosphere', *Science* **321**(5895), 1475–1478.

Bertucci, C., Hamilton, D., Kurth, W., Hospodarsky, G., Mitchell, D., Sergis, N., Edberg, N. J. and Dougherty, M. (2015), 'Titan's interaction with the supersonic solar wind', *Geophysical Research Letters* **42**(2), 193–200.

Birkeland, K. (1908), 'The norwegian aurora polaris expedition 1902-3, part 1', *A, Aschehoug, Christiania, Norway* .

Birn, J. and Hesse, M. (2014), 'Forced reconnection in the near magnetotail: Onset and energy conversion in pic and mhd simulations', *Journal of Geophysical Research: Space Physics* **119**(1), 290–309.

Box, G. E. and Tiao, G. C. (2011), *Bayesian inference in statistical analysis*, Vol. 40, John Wiley & Sons.

Brain, D., Baker, A., Briggs, J., Eastwood, J., Halekas, J. and Phan, T.-D. (2010), ‘Episodic detachment of martian crustal magnetic fields leading to bulk atmospheric plasma escape’, *Geophysical Research Letters* **37**(L14108).

Brice, N. M. and Ioannidis, G. A. (1970), ‘The magnetospheres of jupiter and earth’, *Icarus* **13**(2), 173–183.

Briggs, J., Brain, D., Cartwright, M., Eastwood, J. and Halekas, J. (2011), ‘A statistical study of flux ropes in the martian magnetosphere’, *Planetary and Space Science* **59**(13), 1498–1505.

Brown, M. E. (1994), ‘Observation of mass loading in the io plasma torus’, *Geophysical research letters* **21**(10), 847–850.

Bryan, A. (2018), ‘Free vibration of thin shallow elliptical shells’, *Journal of Vibration and Acoustics* **140**(1), 011004.

Bunce, E., Arridge, C., Cowley, S. and Dougherty, M. (2008), ‘Magnetic field structure of saturn’s dayside magnetosphere and its mapping to the ionosphere: Results from ring current modeling’, *Journal of Geophysical Research: Space Physics* **113**(A2), A02207.

Bunce, E., Cowley, S., Alexeev, I., Arridge, C., Dougherty, M., Nichols, J. and Russell, C. (2007), ‘Cassini observations of the variation of saturn’s ring current parameters with system size’, *Journal of Geophysical Research: Space Physics* **112**(A10202).

Burch, J., Goldstein, J., Hill, T., Young, D., Crary, F., Coates, A., Andre, N., Kurth, W. and Sittler Jr, E. (2005), ‘Properties of local plasma injections in saturn’s magnetosphere’, *Geophysical Research Letters: Saturn’s Magnetosphere: First Results From Cassini* **32**(14), L14SO2.

Burton, M., Dougherty, M. and Russell, C. (2010), ‘Saturn’s internal planetary magnetic field’, *Geophysical Research Letters* **37**(24).

Camporeale, E. and Lapenta, G. (2005), 'Model of bifurcated current sheets in the earth's magnetotail: Equilibrium and stability', *Journal of Geophysical Research: Space Physics* **110**(A07206).

Capone, L., Whitten, R., Dubach, J., Prasad, S. and Huntress, W. (1976), 'The lower ionosphere of titan', *Icarus* **28**(3), 367–378.

Carbary, J., Achilleos, N. and Arridge, C. (2012), 'Statistical ring current of saturn', *Journal of Geophysical Research: Space Physics* **117**(A6), A06223.

Case, N., Grocott, A., Haaland, S., Martin, C. and Nagai, T. (2018), 'Response of earth's neutral sheet to reversals in the imf b y component', *Journal of Geophysical Research: Space Physics* **123**, 8206–8218.

Chapman, S. and Ferraro, V. (1929), 'The electrical state of solar streams of corpuscles', *Monthly Notices of the Royal Astronomical Society* **89**, 470.

Connerney, J., Acuna, M. and Ness, N. (1981), 'Saturn's ring current and inner magnetosphere', *Nature* **292**, 724–726.

Connerney, J., Acuna, M. and Ness, N. (1983), 'Currents in saturn's magnetosphere', *Journal of Geophysical Research: Space Physics* **88**(A11), 8779–8789.

Coustenis, A. and Bézard, B. (1995), 'Titan's atmosphere from voyager infrared observations: Iv. latitudinal variations of temperature and composition', *Icarus* **115**(1), 126–140.

Coustenis, A., Bezard, B. and Gautier, D. (1989), 'Titan's atmosphere from voyager infrared observations: I. the gas composition of titan's equatorial region', *Icarus* **80**(1), 54–76.

Cowley, S. (1982), 'The causes of convection in the earth's magnetosphere: A review of developments during the ims', *Reviews of Geophysics* **20**(3), 531–565.

Cowley, S. and Bunce, E. (2001), 'Origin of the main auroral oval in jupiter's coupled magnetosphere–ionosphere system', *Planetary and Space Science* **49**(10-11), 1067–1088.

Cowley, S., Bunce, E. and O'Rourke, J. (2004), 'A simple quantitative model of plasma flows and currents in saturn's polar ionosphere', *Journal of Geophysical Research: Space Physics* **109**(A5), A05212.

Cowley, S. W. H., Provan, G., Hunt, G. and Jackman, C. (2017), 'Planetary period modulations of saturn's magnetotail current sheet: A simple illustrative mathematical model', *Journal of Geophysical Research: Space Physics* **122**(1), 258–279.

Cravens, T., Robertson, I., Ledvina, S., Mitchell, D., Krimigis, S. and Waite, J. (2008), 'Energetic ion precipitation at titan', *Geophysical Research Letters* **35**(3), L03103.

Cravens, T., Robertson, I., Waite, J. H., Yelle, R., Kasprzak, W., Keller, C., Ledvina, S., Niemann, H., Luhmann, J., McNutt, R. et al. (2006), 'Composition of titan's ionosphere', *Geophysical Research Letters* **33**(7), L07105.

Crookes, W. (1879), 'On the illumination of lines of molecular pressure, and the trajectory of molecules', *Philosophical Transactions of the Royal Society of London* **170**, 135–164.

Cui, J., Galand, M., Yelle, R., Wahlund, J.-E., Ågren, K., Waite, J. and Dougherty, M. (2010), 'Ion transport in titan's upper atmosphere', *Journal of Geophysical Research: Space Physics* **115**(A6), A06314.

Cui, J., Yelle, R. and Volk, K. (2008), 'Distribution and escape of molecular hydrogen in titan's thermosphere and exosphere', *Journal of Geophysical Research: Planets* **113**(E10004).

Dalena, S., Greco, A., Zimbardo, G. and Veltri, P. (2010), 'Role of oxygen ions in the formation of a bifurcated current sheet in the magnetotail', *Journal of Geophysical Research: Space Physics* **115**(A03213).

Davies, E., Masters, A., Dougherty, M., Hansen, K., Coates, A. and Hunt, G. (2017), 'Swept forward magnetic field variability in high-latitude regions of saturn's magnetosphere', *Journal of Geophysical Research: Space Physics* **122**, 12328–12337.

Delamere, P. and Bagenal, F. (2010), 'Solar wind interaction with jupiter's magnetosphere', *Journal of Geophysical Research: Space Physics* **115**(A10201).

Delamere, P. and Bagenal, F. (2013), 'Magnetotail structure of the giant magnetospheres: Implications of the viscous interaction with the solar wind', *Journal of Geophysical Research: Space Physics* **118**(11), 7045–7053.

Delamere, P., Otto, A., Ma, X., Bagenal, F. and Wilson, R. (2015), 'Magnetic flux circulation in the rotationally driven giant magnetospheres', *Journal of Geophysical Research: Space Physics* **120**(6), 4229–4245.

Delcourt, D., Ovodkov, D., Popov, V. Y., Malova, H. and Zelenyi, L. (2006), 'Do phase portraits resist current sheet bifurcation?', *Advances in Space Research* **37**(3), 547–551.

Desroche, M., Bagenal, F., Delamere, P. and Erkaev, N. (2013), 'Conditions at the magnetopause of saturn and implications for the solar wind interaction', *Journal of Geophysical Research: Space Physics* **118**(6), 3087–3095.

DiBraccio, G. A., Slavin, J. A., Imber, S. M., Gershman, D. J., Raines, J. M., Jackman, C. M., Boardsen, S. A., Anderson, B. J., Korth, H., Zurbuchen, T. H. et al. (2015), 'Messenger observations of flux ropes in mercurys magnetotail', *Planetary and Space Science* **115**, 77–89.

Dougherty, M. K., Cao, H., Khurana, K. K., Hunt, G. J., Provan, G., Kellock, S., Burton, M. E., Burk, T. A., Bunce, E. J., Cowley, S. W. et al. (2018), 'Saturns magnetic field revealed by the cassini grand finale', *Science* **362**(6410).

Dougherty, M., Kellock, S., Southwood, D., Balogh, A., Smith, E., Tsurutani, B., Gerlach, B., Glassmeier, K.-H., Gleim, F., Russell, C. et al. (2004), The cassini magnetic field investigation, *in* 'The Cassini-Huygens Mission', Springer, pp. 331–383.

Dougherty, M., Khurana, K., Neubauer, F., Russell, C., Saur, J., Leisner, J. and Burton, M. (2006), 'Identification of a dynamic atmosphere at enceladus with the cassini magnetometer', *Science* **311**(5766), 1406–1409.

Dryer, M. (1998), 'Multidimensional, magnetohydrodynamic simulation of solar-generated disturbances: space weather forecasting of geomagnetic storms', *AIAA journal* **36**(3), 365–370.

Dungey, J. (1963), 'The structure of the exosphere, or adventures in velocity space', *Geophysics, The Earth's Environment* .

Dungey, J. W. (1961), 'Interplanetary magnetic field and the auroral zones', *Physical Review Letters* **6**(2), 47.

Eastwood, J., Videira, J., Brain, D. and Halekas, J. (2012), 'A chain of magnetic flux ropes in the magnetotail of mars', *Geophysical Research Letters* **39**(L03104).

Edberg, N., Wahlund, J.-E., Ågren, K., Morooka, M. W., Modolo, R., Bertucci, C. and Dougherty, M. (2010), 'Electron density and temperature measurements in the cold plasma environment of titan: Implications for atmospheric escape', *Geophysical Research Letters* **37**(20), L20105.

Elphic, R., Luhmann, J., Russell, C. and Brace, L. (1981), 'Magnetic flux ropes in the venus ionosphere: In situ observations of force-free structures?', *Advances in Space Research* **1**(9), 53–58.

Elphic, R. and Russell, C. (1983*a*), 'Global characteristics of magnetic flux ropes in the venus ionosphere', *Journal of Geophysical Research: Space Physics* **88**(A4), 2993–3003.

Elphic, R. and Russell, C. (1983*b*), 'Magnetic flux ropes in the venus ionosphere: Observations and models', *Journal of Geophysical Research: Space Physics* **88**(A1), 58–72.

Elphic, R., Russell, C., Slavin, J. and Brace, L. (1980), 'Observations of the dayside ionopause and ionosphere of venus', *Journal of Geophysical Research: Space Physics* **85**(A13), 7679–7696.

Felici, M., Arridge, C. S., Coates, A., Badman, S. V., Dougherty, M., Jackman, C. M., Kurth, W., Melin, H., Mitchell, D. G., Reisenfeld, D. et al. (2016), 'Cassini observations of ionospheric plasma in saturn's magnetotail lobes', *Journal of Geophysical Research: Space Physics* **121**(1), 338–357.

Feyerabend, M., Simon, S., Neubauer, F. M., Motschmann, U., Bertucci, C., Edberg, N. J., Hospodarsky, G. B. and Kurth, W. S. (2016), 'Hybrid simulation of titan's interaction with the supersonic solar wind during cassini's t96 flyby', *Geophysical Research Letters* **43**(1), 35–42.

Fleshman, B., Delamere, P. and Bagenal, F. (2010a), 'Modeling the enceladus plume–plasma interaction', *Geophysical Research Letters* **37**(L03202).

Fleshman, B., Delamere, P. and Bagenal, F. (2010b), 'A sensitivity study of the enceladus torus', *Journal of Geophysical Research: Planets* **115**(E04007).

Fleshman, B., Delamere, P., Bagenal, F. and Cassidy, T. (2013), 'A 1-d model of physical chemistry in saturn's inner magnetosphere', *Journal of Geophysical Research: Planets* **118**(8), 1567–1581.

Fox, J. L. and Yelle, R. V. (1997), 'Hydrocarbon ions in the ionosphere of titan', *Geophysical research letters* **24**(17), 2179–2182.

Gan, L., Keller, C. and Cravens, T. (1992), 'Electrons in the ionosphere of titan', *Journal of Geophysical Research: Space Physics* **97**(A8), 12137–12151.

Génot, V., Mottez, F., Fruit, G., Louarn, P., Sauvaud, J.-A. and Balogh, A. (2005), 'Bifurcated current sheet: Model and cluster observations', *Planetary and Space Science* **53**(1-3), 229–235.

Geyger, W. A. (1964), *Nonlinear-magnetic control devices*, McGraw-Hill book Company.

Giampieri, G. and Dougherty, M. (2004), 'Modelling of the ring current in saturn's magnetosphere', *Annales Geophysicae* **22**(2), 653–659.

Gold, T. (1959), 'Motions in the magnetosphere of the earth', *Journal of Geophysical Research* **64**(9), 1219–1224.

Gombosi, T. I., Armstrong, T. P., Arridge, C. S., Khurana, K. K., Krimigis, S. M., Krupp, N., Persoon, A. M. and Thomsen, M. F. (2009), Saturn's magnetospheric configuration, *in* 'Saturn from Cassini-Huygens', Springer, pp. 203–255.

Greco, A., De Bartolo, R., Zimbardo, G. and Veltri, P. (2007), 'A three-dimensional kinetic-fluid numerical code to study the equilibrium structure of the magnetotail: The role of electrons in the formation of the bifurcated current sheet', *Journal of Geophysical Research: Space Physics* **112**(A06218).

Grodent, D., Waite, J. H. and Gérard, J.-C. (2001), 'A self-consistent model of the jovian auroral thermal structure', *Journal of Geophysical Research: Space Physics* **106**(A7), 12933–12952.

Guo, R., Yao, Z., Wei, Y., Ray, L. C., Rae, I., Arridge, C. S., Coates, A., Delamere, P., Sergis, N., Kollmann, P. et al. (2018), 'Rotationally driven magnetic reconnection in saturns dayside', *Nature Astronomy* p. 1.

Hanlon, P., Dougherty, M., Krupp, N., Hansen, K., Crary, F., Young, D. and Tóth, G. (2004), 'Dual spacecraft observations of a compression event within the jovian magnetosphere: Signatures of externally triggered supercorotation?', *Journal of Geophysical Research: Space Physics* **109**(A9).

Hara, T., Mitchell, D. L., McFadden, J. P., Seki, K., Brain, D. A., Halekas, J. S., Harada, Y., Espley, J. R., DiBraccio, G. A., Connerney, J. E. et al. (2015), 'Estimation of the spatial structure of a detached magnetic flux rope at mars based on simultaneous maven plasma and magnetic field observations', *Geophysical Research Letters* **42**(21), 8933–8941.

Hara, T., Seki, K., Hasegawa, H., Brain, D. A., Matsunaga, K. and Saito, M. H. (2014), 'The spatial structure of martian magnetic flux ropes recovered by the grad-shafranov reconstruction technique', *Journal of Geophysical Research: Space Physics* **119**(2), 1262–1271.

Harris, E. G. (1962), 'On a plasma sheath separating regions of oppositely directed magnetic field', *Il Nuovo Cimento (1955-1965)* **23**(1), 115–121.

Hidalgo, M., Cid, C., Vinas, A. and Sequeiros, J. (2002), 'A non-force-free approach to the topology of magnetic clouds in the solar wind', *Journal of Geophysical Research: Space Physics* **107**(A1), 1002.

Hill, T. (1979), 'Inertial limit on corotation', *Journal of Geophysical Research: Space Physics* **84**(A11), 6554–6558.

Hoshino, M., Nishida, A., Mukai, T., Saito, Y., Yamamoto, T. and Kokubun, S. (1996), 'Structure of plasma sheet in magnetotail: Double-peaked electric current sheet', *Journal of Geophysical Research: Space Physics* **101**(A11), 24775–24786.

Iijima, T., Potemra, T. and Zanetti, L. (1990), 'Large-scale characteristics of magnetospheric equatorial currents', *Journal of Geophysical Research: Space Physics* **95**(A2), 991–999.

Ingersoll, A. P. and Ewald, S. P. (2011), 'Total particulate mass in enceladus plumes and mass of saturns e ring inferred from cassini iss images', *Icarus* **216**(2), 492–506.

Ip, W.-H. (1990), 'Titan's upper ionosphere', *The Astrophysical Journal* **362**, 354–363.

Ishibashi, H. and Marubashi, K. (2004), 'Structure of interplanetary magnetic cloud on april 16, 1999 and its origin estimated by fitting the torus-shaped flux rope model', *Geophysical research letters* **31**(21), L21807.

Israelevich, P. and Ershkovich, A. (2006), 'Bifurcation of jovian magnetotail current sheet', **24**(6), 1479–1481.

Israelevich, P. and Ershkovich, A. (2008), 'Bifurcation of the tail current sheet and ion temperature anisotropy', *Annales geophysicae: atmospheres, hydrospheres and space sciences* **26**(7), 1759.

Israelevich, P., Ershkovich, A. and Oran, R. (2007), 'Bifurcation of the tail current sheet in jovian magnetosphere', *Planetary and Space Science* **55**(15), 2261–2266.

Jackman, C., Achilleos, N., Bunce, E., Cowley, S., Dougherty, M., Jones, G., Milan, S. and Smith, E. (2004), 'Interplanetary magnetic field at 9 au during the declining phase of the solar cycle and its implications for saturn's magnetospheric dynamics', *Journal of Geophysical Research: Space Physics* **109**, A11203.

Jasinski, J. M., Slavin, J. A., Arridge, C. S., Poh, G., Jia, X., Sergis, N., Coates, A. J., Jones, G. H. and Waite, J. H. (2016), 'Flux transfer event observation at saturn's dayside magnetopause by the cassini spacecraft', *Geophysical Research Letters* **43**(13), 6713–6723.

Jia, X., Kivelson, M. G. and Gombosi, T. I. (2012), 'Driving saturn's magnetospheric periodicities from the upper atmosphere/ionosphere', *Journal of Geophysical Research: Space Physics* **117**(A04215).

Jurac, S., McGrath, M., Johnson, R., Richardson, J., Vasyliunas, V. and Eviatar, A. (2002), 'Saturn: Search for a missing water source', *Geophysical research letters* **29**(24), 2172.

Kaplan, W. (1952), *Advanced Calculus*, Addison-Wesley.

Keller, C., Anicich, V. and Cravens, T. (1998), 'Model of titans ionosphere with detailed hydrocarbon ion chemistry', *Planetary and space science* **46**(9), 1157–1174.

Keller, C., Cravens, T. and Gan, L. (1992), 'A model of the ionosphere of titan', *Journal of Geophysical Research: Space Physics* **97**(A8), 12117–12135.

Kellett, S., Arridge, C. S., Bunce, E., Coates, A. J., Cowley, S., Dougherty, M., Persoon, A., Sergis, N. and Wilson, R. (2011), 'Saturn's ring current: Local time dependence and temporal variability', *Journal of Geophysical Research: Space Physics* **116**(A05220).

Kellett, S., Bunce, E., Coates, A. and Cowley, S. (2009), 'Thickness of saturn's ring current determined from north-south cassini passes through the current layer', *Journal of Geophysical Research: Space Physics* **114**(A4), A04209.

Khurana, K. K. (2001), 'Influence of solar wind on jupiter's magnetosphere deduced from currents in the equatorial plane', *Journal of Geophysical Research: Space Physics* **106**(A11), 25999–26016.

Khurana, K. K. and Kivelson, M. G. (1989*a*), 'On jovian plasma sheet structure', *Journal of Geophysical Research: Space Physics* **94**(A9), 11791–11803.

Khurana, K. K. and Kivelson, M. G. (1989*b*), 'Ultralow frequency mhd waves in jupiter's middle magnetosphere', *Journal of Geophysical Research: Space Physics* **94**(A5), 5241–5254.

Khurana, K., Kivelson, M., Vasyliunas, V., Krupp, N., Woch, J., Lagg, A., Mauk, B. and Kurth, W. (2004), 'The configuration of jupiters magnetosphere', *Jupiter: The planet, satellites and magnetosphere* **1**, 593–616.

Kidder, A., Winglee, R. and Harnett, E. (2008), 'Erosion of the dayside magnetosphere at mercury in association with ion outflows and flux rope generation', *Journal of Geophysical Research: Space Physics* **113**(A09223).

Kidder, A., Winglee, R. and Harnett, E. (2009), 'Regulation of the centrifugal interchange cycle in saturn's inner magnetosphere', *Journal of Geophysical Research: Space Physics* **114**(A2), A02205.

Kivelson, M. G. (2016), Planetary magnetodiscs: Some unanswered questions, *in* 'The Magnetodiscs and Aurorae of Giant Planets', Springer, pp. 5–21.

Kivelson, M. G., Khurana, K. K. and Walker, R. J. (2002), 'Sheared magnetic field structure in jupiter's dusk magnetosphere: Implications for return currents', *Journal of Geophysical Research: Space Physics* **107**(A7), 1116.

Kivelson, M. G. and Russell, C. T. (1995), *Introduction to Space Physics*, Cambridge University Press.

Kivelson, M., Khurana, K., Means, J., Russell, C. and Snare, R. (1992), 'The galileo magnetic field investigation', *Space Science Reviews* **60**(1-4), 357–383.

Kivelson, M. and Southwood, D. (2005), 'Dynamical consequences of two modes of centrifugal instability in jupiter's outer magnetosphere', *Journal of Geophysical Research: Space Physics* **110**(A12209).

Kleeorin, N., Rogachevskii, I. and Eviatar, A. (1994), 'A mechanism of magnetic flux rope formation in the ionosphere of venus', *Journal of Geophysical Research: Space Physics* **99**(A4), 6475–6481.

Kleindienst, G., Glassmeier, K.-H., Simon, S., Dougherty, M. and Krupp, N. (2009), 'Quasiperiodic ulf-pulsations in saturn's magnetosphere', **27**(2), 885–894.

Knight, S. (1973), 'Parallel electric fields', *Planetary and Space Science* **21**(5), 741–750.

Krupp, N., Dougherty, M., Woch, J., Seidel, R. and Keppler, E. (1999), 'Energetic particles in the duskside jovian magnetosphere', *Journal of Geophysical Research: Space Physics* **104**(A7), 14767–14780.

Krupp, N., Lagg, A., Woch, J., Krimigis, S., Livi, S., Mitchell, D., Roelof, E., Paranicas, C., Mauk, B., Hamilton, D. et al. (2005), 'The saturnian plasma sheet as revealed by energetic particle measurements', *Geophysical research letters* **32**(20), L20S03.

Kuiper, G. P. (1944), 'Titan: a satellite with an atmosphere.', *The Astrophysical Journal* **100**, 378.

Lamy, L., Cecconi, B., Prangé, R., Zarka, P., Nichols, J. and Clarke, J. (2009), 'An auroral oval at the footprint of saturn's kilometric radio sources, colocated with the uv aurorae', *Journal of Geophysical Research: Space Physics* **114**(A10), A10212.

Lassen, K. and Friis-Christensen, E. (1995), 'Variability of the solar cycle length during the past five centuries and the apparent association with terrestrial climate', *Journal of Atmospheric and Terrestrial Physics* **57**(8), 835–845.

Ledvina, S., Nunes, D., Cravens, T. and L Tinker, J. (2002), 'Pressure balance across magnetic flux ropes in the ionosphere of venus', *Journal of Geophysical Research: Space Physics* **107**(A6), 1074.

Lee, P. M. (2012), *Bayesian statistics: an introduction*, John Wiley & Sons.

Leisner, J., Russell, C., Dougherty, M., Blanco-Cano, X., Strangeway, R. and Bertucci, C. (2006), 'Ion cyclotron waves in saturn's e ring: Initial cassini observations', *Geophysical Research Letters* **33**(L11101).

Lepping, R., Berdichevsky, D. and Wu, C.-C. (2017), 'Average magnetic field magnitude profiles of wind magnetic clouds as a function of closest approach to the clouds axes and comparison to model', *Solar Physics* **292**(2), 27.

Levenberg, K. (1944), 'A method for the solution of certain non-linear problems in least squares', *Quarterly of applied mathematics* **2**(2), 164–168.

Leyser, R. P., Imber, S. M., Milan, S. E. and Slavin, J. A. (2017), 'The influence of imf clock angle on dayside flux transfer events at mercury', *Geophysical Research Letters* **44**(21), 10829–10837.

Li, Z., Chen, T. and Yan, G. (2016), 'New method for determining central axial orientation of flux rope embedded within current sheet using multipoint measurements', *Science China Earth Sciences* **59**(10), 2037–2052.

Luhmann, J. (1986), 'The solar wind interaction with venus', *Space Science Reviews* **44**, 241–306.

Luhmann, J. (1990), 'wave analysis of venus ionospheric flux ropes', *Physics of Magnetic Flux Ropes* **58**, 425–432.

Luhmann, J. and Elphic, R. (1985), 'On the dynamo generation of flux ropes in the venus ionosphere', *Journal of Geophysical Research: Space Physics* **90**(A12), 12047–12056.

Lundin, R. and Sandahl, I. (1978), 'Some characteristics of the parallel electric field acceleration of electrons over discrete auroral arcs as observed from two rocket flights', **135**.

Marquardt, D. W. (1963), 'An algorithm for least-squares estimation of nonlinear parameters', *Journal of the society for Industrial and Applied Mathematics* **11**(2), 431–441.

Martin, C. and Arridge, C. S. (2017), 'Cassini observations of aperiodic waves on saturn's magnetodisc', *Journal of Geophysical Research: Space Physics* **122**(8), 8063–8077.

Martz, H. F. (2014), 'Bayesian reliability analysis', *Wiley StatsRef: Statistics Reference Online* .

Masters, A. (2018), 'A more viscous-like solar wind interaction with all the giant planets', *Geophysical Research Letters* **45**(15), 7320–7329.

Matsui, T. and Daughton, W. (2008), 'Kinetic theory and simulation of collisionless tearing in bifurcated current sheets', *Physics of Plasmas* **15**(1), 012901.

McAndrews, H., Owen, C., Thomsen, M., Lavraud, B., Coates, A., Dougherty, M. and Young, D. (2008), 'Evidence for reconnection at saturn's magnetopause', *Journal of Geophysical Research: Space Physics* **113**(A4), A04210.

McComas, D. and Bagenal, F. (2007), 'Jupiter: A fundamentally different magnetospheric interaction with the solar wind', *Geophysical Research Letters* **34**(L20106).

McComas, D., Elliott, H., Schwadron, N., Gosling, J., Skoug, R. and Goldstein, B. (2003), 'The three-dimensional solar wind around solar maximum', *Geophysical research letters* **30**(10), 1517.

Mitchell, D., Carbary, J., Bunce, E., Radioti, A., Badman, S., Pryor, W., Hospodarsky, G. and Kurth, W. (2016), 'Recurrent pulsations in saturns high latitude magnetosphere', *Icarus* **263**, 94–100.

Mitchell, J. L. and Lora, J. M. (2016), 'The climate of titan', *Annual Review of Earth and Planetary Sciences* **44**, 353–380.

Mok, C., Ryu, C.-M., Yoon, P. H. and Lui, A. T. (2006), 'Global two-fluid stability of bifurcated current sheets', *Journal of Geophysical Research: Space Physics* **111**(A03203).

Moldwin, M., Ford, S., Lepping, R., Slavin, J. and Szabo, A. (2000), 'Small-scale magnetic flux ropes in the solar wind', *Geophysical research letters* **27**(1), 57–60.

Morgan, D., Gurnett, D., Akalin, F., Brain, D., Leisner, J., Duru, F., Frahm, R. and Winningham, J. (2011), 'Dual-spacecraft observation of large-scale magnetic flux ropes in the martian ionosphere', *Journal of Geophysical Research: Space Physics* **116**(A02319).

Nakamura, R., Baumjohann, W., Runov, A., Volwerk, M., Zhang, T., Klecker, B., Bogdanova, Y., Roux, A., Balogh, A., Reme, H. et al. (2002), 'Fast flow during current sheet thinning', *Geophysical research letters* **29**(23), 2140.

Nichols, J. D., Badman, S., Bunce, E., Clarke, J., Cowley, S. W. H., Hunt, G. and Provan, G. (2016), 'Saturns northern auroras as observed using the hubble space telescope', *Icarus* **263**, 17–31.

Nieves-Chinchilla, T., Linton, M., Hidalgo, M. A., Vourlidas, A., Savani, N. P., Szabo, A., Farrugia, C. and Yu, W. (2016), 'A circular-cylindrical flux-rope analytical model for magnetic clouds', *The Astrophysical Journal* **823**(1), 27.

Omidi, N., Sulaiman, A. H., Kurth, W., Madanian, H., Cravens, T., Sergis, N., Dougherty, M. and Edberg, N. J. (2017), 'A single deformed bow shock for titan-saturn system', *Journal of Geophysical Research: Space Physics* **122**, 11058–11075.

Osherovich, V., Farrugia, C. and Burlaga, L. (1993), 'Nonlinear evolution of magnetic flux ropes: 1. low-beta limit', *Journal of Geophysical Research: Space Physics* **98**(A8), 13225–13231.

Owens, M. J. and Forsyth, R. J. (2013), 'The heliospheric magnetic field', *Living Reviews in Solar Physics* **10**(1), 5.

Paissan, G., Rovira, M. and Stenborg, G. (2005), 'Study of an expanding magnetic cloud', *Boletin de la Asociacion Argentina de Astronomia La Plata Argentina* **48**, 97–101.

Palmaerts, B., Roussos, E., Krupp, N., Kurth, W. S., Mitchell, D. G. and Yates, J. N. (2016), 'Statistical analysis and multi-instrument overview of the quasi-periodic 1-hour pulsations in saturns outer magnetosphere', *Icarus* **271**, 1–18.

Parker, E. N. (1957), 'Sweet's mechanism for merging magnetic fields in conducting fluids', *Journal of Geophysical Research* **62**(4), 509–520.

Parker, E. N. (1958), 'Dynamics of the interplanetary gas and magnetic fields.', *The Astrophysical Journal* **128**, 664.

Parker, E. N. (1970), 'The origin of solar magnetic fields', *Annual Review of Astronomy and Astrophysics* **8**(1), 1–30.

Piddington, J. H. (1969), 'Cosmic electrodynamics', *Coelum Periodico Bimestrale per la Divulgazione dell'Astronomia* .

Pilkington, N., Achilleos, N., Arridge, C., Guio, P., Masters, A., Ray, L., Sergis, N., Thomsen, M., Coates, A. and Dougherty, M. (2015*a*), 'Asymmetries observed in saturn's magnetopause geometry', *Geophysical Research Letters* **42**(17), 6890–6898.

Pilkington, N. M., Achilleos, N., Arridge, C. S., Guio, P., Masters, A., Ray, L., Sergis, N., Thomsen, M. F., Coates, A. and Dougherty, M. (2015*b*), 'Internally driven large-scale changes in the size of saturn's magnetosphere', *Journal of Geophysical Research: Space Physics* **120**(9), 7289–7306.

Pontius, D. and Hill, T. (2006), 'Enceladus: A significant plasma source for saturn's magnetosphere', *Journal of Geophysical Research: Space Physics* **111**(A09214).

Press, W. H., Press, W. H., Flannery, B. P., Flannery, B. P., Teukolsky, S. A., Vetterling, W. T. and Vetterling, W. T. (1989), *Numerical recipes in Pascal: the art of scientific computing*, Vol. 1, Cambridge University Press.

Primdahl, F. (1979), 'The fluxgate magnetometer', *Journal of Physics E: Scientific Instruments* **12**(4), 241.

Provan, G., Andrews, D. J., Arridge, C. S., Coates, A. J., Cowley, S., Cox, G., Dougherty, M. and Jackman, C. (2012), 'Dual periodicities in planetary-period magnetic field oscillations in saturn's tail', *Journal of Geophysical Research: Space Physics* **117**(A1), A01209.

Ray, L., Galand, M., Delamere, P. and Fleshman, B. (2013), 'Current-voltage relation for the saturnian system', *Journal of Geophysical Research: Space Physics* **118**(6), 3214–3222.

Ray, L., Su, Y.-J., Ergun, R., Delamere, P. and Bagenal, F. (2009), 'Current-voltage relation of a centrifugally confined plasma', *Journal of Geophysical Research: Space Physics* **114**(A04214).

Rego, D., Prangé, R. and Gérard, J.-C. (1994), 'Auroral lyman α and h2 bands from the giant planets: 1. excitation by proton precipitation in the jovian atmosphere', *Journal of Geophysical Research: Planets* **99**(E8), 17075–17094.

Ricci, P., Lapenta, G. and Brackbill, J. (2004), 'Structure of the magnetotail current: Kinetic simulation and comparison with satellite observations', *Geophysical research letters* **31**, L06801.

Ridler, N. M. and Salter, M. J. (2002), 'An approach to the treatment of uncertainty in complex s-parameter measurements', *Metrologia* **39**(3), 295.

Rind, D., Lean, J., Lerner, J., Lonergan, P. and Leboissitier, A. (2008), 'Exploring the stratospheric/tropospheric response to solar forcing', *Journal of Geophysical Research: Atmospheres* **113**(D24), D24103.

Romashets, E. and Vandas, M. (2005), 'Asymmetric magnetic field inside a cylindrical flux rope', *Advances in Space Research* **35**(12), 2167–2171.

Runov, A., Nakamura, R., Baumjohann, W., Zhang, T., Volwerk, M., Eichelberger, H.-U. and Balogh, A. (2003), 'Cluster observation of a bifurcated current sheet', *Geophysical Research Letters* **30**(2), 1036.

Russell, C. (1990), 'Magnetic flux ropes in the ionosphere of venus', *Physics of Magnetic Flux Ropes* pp. 413–423.

Russell, C. and Dougherty, M. (2010), 'Magnetic fields of the outer planets', *Space Science Reviews* **152**(1-4), 251–269.

Russell, C., Huddleston, D., Khurana, K. and Kivelson, M. (1999), 'Structure of the jovian magnetodisk current sheet:: initial galileo observations', *Planetary and space science* **47**(8), 1101–1109.

Russell, C., Jackman, C., Wei, H., Bertucci, C. and Dougherty, M. (2008), 'Titans influence on saturnian substorm occurrence', *Geophysical Research Letters* **35**, L12105.

Russell, C., Leisner, J., Arridge, C., Dougherty, M. and Blanco-Cano, X. (2006), 'Nature of magnetic fluctuations in saturn's middle magnetosphere', *Journal of Geophysical Research: Space Physics* **111**(A12205).

Russell, C. T. (2007), The coupling of the solar wind to the earth's magnetosphere, *in* V. Bothmer and I. A. Daglis, eds, 'Space weather: physics and effects', Springer Science & Business Media, p. 113.

Russell, C. T. (2013), *The Cassini-Huygens Mission: Volume 1: Overview, Objectives and Huygens Instrumentarium*, Springer Science & Business Media.

Russell, C. T. and Elphic, R. (1978), 'Initial isee magnetometer results: Magnetopause observations', *Space Science Reviews* **22**(6), 681–715.

Russell, C. T. and Elphic, R. (1979), 'Observation of magnetic flux ropes in the venus ionosphere', *Nature* **279**(5714), 616–618.

Russell, C. and Walker, R. (1985), ‘Flux transfer events at mercury’, *Journal of Geophysical Research: Space Physics* **90**(A11), 11067–11074.

Saito, M. (2015), ‘Themis two-point measurements of the cross-tail current density: A thick bifurcated current sheet in the near-earth plasma sheet’, *Journal of Geophysical Research: Space Physics* **120**(8), 6258–6275.

Sanny, J., McPherron, R., Russell, C., Baker, D., Pulkkinen, T. and Nishida, A. (1994), ‘Growth-phase thinning of the near-earth current sheet during the cdaw 6 substorm’, *Journal of Geophysical Research: Space Physics* **99**(A4), 5805–5816.

Seber, G. A. and Wild, C. (2003), ‘Nonlinear regression (wiley series in probability and statistics)’.

Seki, K., Nagy, A., Jackman, C., Crary, F., Fontaine, D., Zarka, P., Wurz, P., Milillo, A., Slavin, J., Delcourt, D. et al. (2015), ‘A review of general physical and chemical processes related to plasma sources and losses for solar system magnetospheres’, *Space science reviews* **192**(1-4), 27–89.

Sergeev, V., Mitchell, D., Russell, C. and Williams, D. (1993), ‘Structure of the tail plasma/current sheet at 11 re and its changes in the course of a substorm’, *Journal of Geophysical Research: Space Physics* **98**(A10), 17345–17365.

Sergeev, V., Runov, A., Baumjohann, W., Nakamura, R., Zhang, T., Balogh, A., Louarnd, P., Sauvaud, J.-A. and Reme, H. (2004), ‘Orientation and propagation of current sheet oscillations’, *Geophysical research letters* **31**(5), L05807.

Sergeev, V., Runov, A., Baumjohann, W., Nakamura, R., Zhang, T., Volwerk, M., Balogh, A., Reme, H., Sauvaud, J., André, M. et al. (2003a), ‘Current sheet flapping motion and structure observed by cluster’, *Geophysical research letters* **30**(1327).

Sergis, N., Arridge, C. S., Krimigis, S., Mitchell, D., Rymer, A., Hamilton, D., Krupp, N., Dougherty, M. and Coates, A. J. (2011), ‘Dynamics and seasonal variations in saturn’s magnetospheric plasma sheet, as measured by cassini’, *Journal of Geophysical Research: Space Physics* **116**(A4), A04203.

Sergis, N., Jackman, C., Thomsen, M., Krimigis, S., Mitchell, D., Hamilton, D., Dougherty, M., Krupp, N. and Wilson, R. (2017), 'Radial and local time structure of the saturnian ring current, revealed by cassini', *Journal of Geophysical Research: Space Physics* **122**(2), 1803–1815.

Sergis, N., Krimigis, S., Mitchell, D., Hamilton, D., Krupp, N., Mauk, B., Roelof, E. and Dougherty, M. (2009), 'Energetic particle pressure in saturn's magnetosphere measured with the magnetospheric imaging instrument on cassini', *Journal of Geophysical Research: Space Physics* **114**(A2), A02214.

Simon, S., Motschmann, U., Kleindienst, G., Saur, J., Bertucci, C., Dougherty, M., Arridge, C. and Coates, A. (2009), 'Titan's plasma environment during a magnetosheath excursion: Realtime scenarios for cassini's t32 flyby from a hybrid simulation', *Annales geophysicae: atmospheres, hydrospheres and space sciences* **27**(2), 669.

Simon, S., van Treeck, S. C., Wennmacher, A., Saur, J., Neubauer, F. M., Bertucci, C. L. and Dougherty, M. K. (2013), 'Structure of titan's induced magnetosphere under varying background magnetic field conditions: Survey of cassini magnetometer data from flybys ta–t85', *Journal of Geophysical Research: Space Physics* **118**(4), 1679–1699.

Simon, S., Wennmacher, A., Neubauer, F. M., Bertucci, C. L., Kriegel, H., Saur, J., Russell, C. T. and Dougherty, M. K. (2010), 'Titan's highly dynamic magnetic environment: A systematic survey of cassini magnetometer observations from flybys ta–t62', *Planetary and Space Science* **58**(10), 1230–1251.

Sitnov, M., Guzdar, P. and Swisdak, M. (2003), 'A model of the bifurcated current sheet', *Geophysical research letters* **30**(13), 1712.

Sitnov, M. and Merkin, V. (2016), 'Generalized magnetotail equilibria: Effects of the dipole field, thin current sheets, and magnetic flux accumulation', *Journal of Geophysical Research: Space Physics* **121**(8), 7664–7683.

Sitnov, M., Swisdak, M., Drake, J., Guzdar, P. and Rogers, B. (2004), 'A model of the bifurcated current sheet: 2. flapping motions', *Geophysical research letters* **31**(L09805).

Sittler, E., Ali, A., Cooper, J., Hartle, R., Johnson, R., Coates, A. and Young, D. (2009), 'Heavy ion formation in titan's ionosphere: Magnetospheric introduction of free oxygen and a source of titan's aerosols?', *Planetary and Space Science* **57**(13), 1547–1557.

Slavin, J. A., Acuña, M. H., Anderson, B. J., Barabash, S., Benna, M., Boardsen, S. A., Fraenz, M., Gloeckler, G., Gold, R. E., Ho, G. C. et al. (2009), 'Messenger and venus express observations of the solar wind interaction with venus', *Geophysical Research Letters* **36**(9), L09106.

Slavin, J. A., Imber, S. M., Boardsen, S. A., DiBraccio, G. A., Sundberg, T., Sarantos, M., Nieves-Chinchilla, T., Szabo, A., Anderson, B. J., Korth, H. et al. (2012), 'Messenger observations of a flux-transfer-event shower at mercury', *Journal of Geophysical Research: Space Physics* **117**(A12), A00M06.

Slavin, J. A., Lepping, R. P., Wu, C.-C., Anderson, B. J., Baker, D. N., Benna, M., Boardsen, S. A., Killen, R. M., Korth, H., Krimigis, S. M. et al. (2010), 'Messenger observations of large flux transfer events at mercury', *Geophysical Research Letters* **37**(2), L02105.

Slavin, J., Smith, E., Spreiter, J. and Stahara, S. (1985), 'Solar wind flow about the outer planets: Gas dynamic modeling of the jupiter and saturn bow shocks', *Journal of Geophysical Research: Space Physics* **90**(A7), 6275–6286.

Smith, E., Davis Jr, L., Jones, D., Coleman Jr, P., Colburn, D., Dyal, P., Sonett, C. and Frandsen, A. (1974), 'The planetary magnetic field and magnetosphere of jupiter: Pioneer 10', *Journal of Geophysical Research* **79**(25), 3501–3513.

Smith, E., Davis, L., Jones, D., Coleman, P., Colburn, D., Dyal, P. and Sonett, C. (1980), 'Saturn's magnetic field and magnetosphere', *Science* **207**(4429), 407–410.

Snekvik, K., Østgaard, N., Tenfjord, P., Reistad, J. P., Laundal, K. M., Milan, S. E. and Haaland, S. E. (2017), 'Dayside and nightside magnetic field responses at 780 km altitude to dayside reconnection', *Journal of Geophysical Research: Space Physics* **122**(2), 1670–1689.

Snodgrass, H. B. and Ulrich, R. K. (1990), 'Rotation of doppler features in the solar photosphere', *The Astrophysical Journal* **351**, 309–316.

Sonnerup, B. Ö. and Cahill, L. (1967), 'Magnetopause structure and attitude from explorer 12 observations', *Journal of Geophysical Research* **72**(1), 171–183.

Sonnerup, B. U. and Scheible, M. (1998), 'Minimum and maximum variance analysis', *Analysis methods for multi-spacecraft data* pp. 185–220.

Southwood, D. and Cowley, S. W. H. (2014), 'The origin of saturn's magnetic periodicities: Northern and southern current systems', *Journal of Geophysical Research: Space Physics* **119**(3), 1563–1571.

Southwood, D. and Kivelson, M. (2001), 'A new perspective concerning the influence of the solar wind on the jovian magnetosphere', *Journal of Geophysical Research: Space Physics* **106**(A4), 6123–6130.

Stern, D. P. (1987), 'Tail modeling in a stretched magnetosphere: 1. methods and transformations', *Journal of Geophysical Research: Space Physics* **92**(A5), 4437–4448.

Thompson, S., Kivelson, M., El-Alaoui, M., Balogh, A., Reme, H. and Kistler, L. (2006), 'Bifurcated current sheets: Statistics from cluster magnetometer measurements', *Journal of Geophysical Research: Space Physics* **111**(A3), A03212.

Thomsen, M., Jackman, C., Cowley, S. W. H., Jia, X., Kivelson, M. and Provan, G. (2017), 'Evidence for periodic variations in the thickness of saturn's nightside plasma sheet', *Journal of Geophysical Research: Space Physics* **122**(1), 280–292.

Tokar, R., Johnson, R., Thomsen, M., Delapp, D., Baragiola, R., Francis, M., Reisenfeld, D., Fish, B., Young, D., Crary, F. et al. (2005), 'Cassini observations of the thermal plasma in the vicinity of saturn's main rings and the f and g rings', *Geophysical research letters* **32**(L14S04).

Tsyganenko, N. (1998), 'Modeling of twisted/warped magnetospheric configurations using the general deformation method', *Journal of Geophysical Research: Space Physics* **103**(A10), 23551–23563.

Tsyganenko, N. and Fairfield, D. (2004), 'Global shape of the magnetotail current sheet as derived from geotail and polar data', *Journal of Geophysical Research: Space Physics* **109**(A03218).

Vandas, M., Romashets, E. and Watari, S. (2005), 'Magnetic clouds of oblate shapes', *Planetary and Space Science* **53**(1), 19–24.

Vasyliunas, V. M. (1983), 'Plasma distribution and flow', *Physics of the Jovian magnetosphere* pp. 395–453.

Vasyliunas, V. M. (1984), 'Fundamentals of current description', *Magnetospheric currents* **28**, 63–66.

Vignes, D., Acuña, M., Connerney, J., Crider, D., Rème, H. and Mazelle, C. (2004), 'Magnetic flux ropes in the martian atmosphere: Global characteristics', *Space Science Reviews* **1**(111), 223–231.

Vogt, M. F., Bunce, E. J., Nichols, J. D., Clarke, J. T. and Kurth, W. S. (2017), 'Long-term variability of jupiter's magnetodisk and implications for the aurora', *Journal of Geophysical Research: Space Physics* pp. 12090–12110.

Vogt, M. F., Kivelson, M. G., Khurana, K. K., Joy, S. P. and Walker, R. J. (2010), 'Reconnection and flows in the jovian magnetotail as inferred from magnetometer observations', *Journal of Geophysical Research: Space Physics* **115**(A6), A06219.

von Papen, M. and Saur, J. (2016), 'Longitudinal and local time asymmetries of magnetospheric turbulence in saturn's plasma sheet', *Journal of Geophysical Research: Space Physics* **121**(5), 4119–4134.

von Papen, M., Saur, J. and Alexandrova, O. (2014), 'Turbulent magnetic field fluctuations in saturn's magnetosphere', *Journal of Geophysical Research: Space Physics* **119**(4), 2797–2818.

Waite, J., Cravens, T., Kozyra, J., Nagy, A., Atreya, S. and Chen, R. (1983), 'Electron precipitation and related aeronomy of the jovian thermosphere and ionosphere', *Journal of Geophysical Research: Space Physics* **88**(A8), 6143–6163.

Wei, H., Russell, C., Dougherty, M., Ma, Y., Hansen, K., McAndrews, H., Wellbrock, A., Coates, A., Thomsen, M. and Young, D. (2011), 'Unusually strong magnetic fields in titans ionosphere: T42 case study', *Advances in Space Research* **48**(2), 314–322.

Wei, H., Russell, C., Zhang, T. and Dougherty, M. (2010), 'Comparison study of magnetic flux ropes in the ionospheres of venus, mars and titan', *Icarus* **206**(1), 174–181.

Went, D., Hospodarsky, G., Masters, A., Hansen, K. and Dougherty, M. (2011b), 'A new semiempirical model of saturn's bow shock based on propagated solar wind parameters', *Journal of Geophysical Research: Space Physics* **116**(A07202).

Went, D., Kivelson, M., Achilleos, N., Arridge, C. S. and Dougherty, M. (2011a), 'Outer magnetospheric structure: Jupiter and saturn compared', *Journal of Geophysical Research: Space Physics* **116**(A04224).

Yates, J., Southwood, D., Dougherty, M., Sulaiman, A., Masters, A., Cowley, S., Kivelson, M., Chen, C., Provan, G., Mitchell, D. et al. (2016), 'Saturn's quasiperiodic magnetohydrodynamic waves', *Geophysical Research Letters* **43**(21), 11102–11111.

Zelenyi, L., Delcourt, D., Malova, H. and Sharma, A. (2002), 'aging of the magnetotail thin current sheets', *Geophysical research letters* **29**(12), 1608.

Zelenyi, L. M., Malova, H. V. and Popov, V. Y. (2003), 'Splitting of thin current sheets in the earths magnetosphere', *Journal of Experimental and Theoretical Physics Letters* **78**(5), 296–299.

Zhang, T., Baumjohann, W., Teh, W., Nakamura, R., Russell, C., Luhmann, J., Glassmeier, K., Dubinin, E., Wei, H., Du, A. et al. (2012), 'Giant flux ropes observed in the magnetized ionosphere at venus', *Geophysical Research Letters* **39**(23), L23103.